Electrochemical Sensor Development for Robust Amino Acid Biosensing

Siba Moussa

A thesis submitted to McGill University
in partial fulfillment of the requirements for the degree of
Doctor of Philosophy

Department of Chemistry, McGill University
Montreal, Quebec, Canada
August 2021

To Mama, Baba, Batoul, Yaso and Mo - *I could have never gotten this far without you, alhamduliallah.*

Abstract

The field of biosensors has been growing since the development of the widely used commercial glucose oxidase sensors. By definition, a biosensor is an analytical device where the sensing element consists of a biological component, typically an enzyme. Currently, there are many challenges in the fabrication of enzymatic biosensors including enzyme selectivity, stability, and pH sensitivity. As a result, there is a limited pool of enzymes currently in use for electrochemical biosensing. One way to unlock the potential of electrochemical biosensors is by discovering a wider range of enzymes suitable for use in biosensor development.

This thesis focuses on the design improvements of D-amino acid oxidase-based electrochemical biosensors. Limitations in biosensor performance attributed to the bioreceptor component are discussed. The methodology used to tackle these challenges, which includes generating D-amino acid oxidase variants through single point mutations for use in biosensor development is presented. It is possible to alter enzyme selectivity and sensitivity to develop biosensors with desired performance properties. Moreover, the application of DAAO biosensors, focusing on D-serine detection through *ex vivo* and in *vivo* measurements from Xenopus, is discussed in this thesis. The application of D-serine detecting biosensors allowed to measure neurochemical release in model animal systems. Finally, biosensor development is extended to other oxidase enzymes, such as glycine oxidase. This extension makes the application of biosensors highly attractive for multiple real-time chemical detection, not necessarily limited to biological applications.

Résumé

Le domaine des biocapteurs s'est développé depuis le développement du utilisé des capteurs commerciaux de glucose oxydase. Par définition, un biocapteur est un dispositif où l'élément de détection est constitué d'un composant biologique, généralement une enzyme.Actuellement, il existe de nombreux défis dans la fabrication de ces capteurs, y compris les enzymes sélectivité, stabilité et sensibilité au pH. En conséquence, il existe un pool limité d'enzymes actuellement utilisé pour ces types d'appareils. Une façon de libérer le potentiel de ces biocapteurs est en découvrant une gamme plus large d'enzymes adaptées à une utilisation dans les biocapteurs développement.

Cette thèse discute des efforts déployés pour améliorer la conception de l'-aminoacide oxydase Biocapteurs électrochimiques à base de (DAAO). Dans cette thèse, certains des les limitations du composant enzymatique du biocapteur, telles que la sélectivité enzymatique, sont discutées. La méthodologie utilisée pour relever ces défis, qui comprend la génération de DAAO des variantes par mutations ponctuelles à utiliser dans le développement de biocapteurs sont présentées. Les résultats montrent qu'il est possible de modifier la sélectivité et la sensibilité des enzymes pour developer biocapteurs avec les propriétés de performance souhaitées. De plus, l'application de biocapteurs DAAO, axés sur la détection de la D-sérine par ex vivo et in vivo mesures de Xenopus, est discuté dans cette thèse. L'application de biocapteurs de détection de -sérine a permis de démêler des informations importantes sur la libération neurochimique dans des systèmes animaux modèles. Enfin, le développement de biocapteurs est étendu à l'utilisation d'autres enzymes oxydase, telles que la glycine oxy-

dase. Cette extension rend l'application des biocapteurs très attrayante pour de multiples détection chimique en temps réel, pas nécessairement pour les seules applications biologiques.

Acknowledgments

Being a PhD student was definitely not what I expected it to be. I started in Janine's lab thinking that I was going to change the world during my PhD, only to realize that no one can change the world in five years. That being said, I would like to thank my supervisor, Janine, for being a key player in helping me make this realization. Instead, the biggest thing that my PhD changed was myself.

First and foremost, I'd like thank Janine, for having the largest impact on me throughout these years. Thank you Janine, for teaching me that I can't do a million things at the same time. Over the past five years, Janine was an amazing supervisor and mentor. Without Janine I would have never been able to make it to the finish line. Thank you Janine, for always being available, especially when I sent crazy excited emails about a research idea I had. Thank you for helping me navigate through this puzzle called graduate school. Thank you for working with me to improve my writing skills. I always walked into our meetings in panic, and you always managed to make me leave a much calmer version of myself. More importantly, thank you for all the opportunities you have made possible for me throughout these five years.

Being part of the Mauzeroll lab is like being part of a science family. Yani, you make working in the lab so much more fun. Lisa, thank you for all the smart questions and always being ready to pick up a scientific discussion with me. Jeremy, thanks for all the laughs and long office chats - I am certainly going to miss walking in the office only to find you looking up another random city on the world map. Danny, thanks for making those extra

long thesis writing days more endurable. Yuanjiao, Nathaniel, Sara, Reza, Emmanuel, and Hu- without you guys this journey would have never been the same. Isa, you are the glue to our lab, thanks for the million and one things you do for all of us.

I'd also like to thank my second science family at University of Insubria. Dr. Pollegioni, thank you for being welcoming, hosting me your lab and teaching me everything there is to learn about enzymes. The three months I spent in Italy were some of the best times of my PhD and your lab made the three months beyond memorable. Antonio, Giulia, Valentina, Elena, Elisa, Laura - there are many memorable things to say and I will always remember all the good times we had on the yellow floor!

To the people at the Montreal Neurological Institute (Marion, Daryan, Marjda, Dr. Ruthazer)- thank you for teaching me all there is to know about neuroscience and working with tadpoles and rat cells. Without you all, this biosensor journey would have been very different.

My journey to McGill would not have been made possible without some of my undergraduate professors. Without them, I would have never considered doing a PhD. To my professors at AM: Dr. Bazzi, Dr. Nounou and Dr. Salama - you three have been role models and I am lucky to have been taught and mentored by you.

On a more personal note, working in Pulp and Paper was a real joy thanks to all my fellow graduate school friends. Haiyan, Simone, Hassan, Hatim, Roberto, Kevin, Yeganeh, Sally and Linda - thank you guys. Friday dinners have always been the best way to end a long week, especially when we all left Pulp and Paper together. You guys are family. Aya, thank you for being the shoulder to cry on during the bad times but also being the one to

celebrate with during the good - I am glad to have found a close friend in you.

To my friends who never understood the journey of an academic - thank you for your endless support regardless. Ehsan, whom I have known since 10th grade and has listened to me complain about every class we took together since we were 14 - thank you for always picking up the phone when I was in need for a chat. Finally, none of this would have been remotely possible without my real family who have always continuously pushed me to strive for the best version of myself, especially my father, Khaled, and mother, Rana. Thank you for being role models, my backbone and number one cheerleaders.

Contents

List of Figures

List of Tables

List of Equations

List of Abbreviations

Table 1: List of Abbreviations.

Abbreviation	Full Name
aCSF	artificial Cerebrospinal Fluid
Ag/AgCl	Silver / Silver Chloride
ATP	Adenosine Triphosphate
AMPA	α-amino-3-hydroxy-5-methyl-4-isoxazolepropionic acid
BSA	Bovine Serum Albumin
CF	Carbon Fibre
CFME	Carbon Fibre Microelectrode
CV	Cyclic Voltammetery
CM	Conditioned Medium
DAAO	D-amino acid oxidase
DA	Dopamine
DMEM	Dulbecco's Modified Eagle Medium
DLS	Dynamic Light Scattering
EIS	Electrochemical Impedance Spectroscopy
ESI	Electrospray Ionization
FAD	Flavin Adenosine Dinucleotide
FTIR	Fourier transform infrared
GO	Glycine Oxidase
hDAAO	human D-amino acid oxidase
HEPES	4-(2-hydroxyethyl)-1-piperazineethanesulfonic acid
H_2O_2	Hydrogen Peroxide
KPi	Potassium Phosphate (buffer)
ME	Microelectrode

Table 1: List of Abbreviations.

Abbreviation	Full Name
LC-MS	Liquid Chromatography - Mass Spectrometery
LOD	Limit of Detection
LOQ	Limit of Quantification
NaPPi	Sodium Phosphate (buffer)
NE	Norepinephrine
o-DNS	ortho-Dianisidine
O	Oxidized Species
PBS	Phosphate Buffered Saline (buffer)
Pt	Platinum
PDMS	Polydimethylsiloxane
PPD	Poly-m-phenylenediamine
PDL	poly-d-lysine
QRE	Quasi Reference Electrode
R	Reduced Species
*Rg*DAAO	Rhodotorula gracilis D-amino acid oxidase
RSD	Relative Standard Deviation
$RgDAAO_{free}$	Free Rhodotorula gracilis D-amino acid oxidase
$RgDAAO_{immob}$	Immobilized Rhodotorula gracilis D-amino acid oxidase
S.E.M	Standard Error of the Mean
SD	Standard Deviation
ZT	Zeitgeber Time
1D	One dimensional

List of Symbols

Table 2: List of Symbols.

Symbol	SI Units	Meaning
α	-	Mass Transfer Coefficient
a	a	Electroactive radius (microelectrode)
β	-	Microelectrode Parameter
C_k	mol L^{-1}	Concentration of Species k
$C_{k,bulk}$	mol L^{-1}	Bulk Concentration of Species k
di/dt	A/s	Rate of Current Change
D_k	m^2 s^{-1}	Diffusion coefficient of species k
D_0	m^2 s^{-1}	Bulk diffusion Coefficient
D_{app}	m^2 s^{-1}	Apparent Diffusion Coefficient
$\frac{dC_{H_2O_2}}{dt}$	mol.s^{-1}	Rate of Change of H_2O_2 Concentration
E	V	Electrode Potential
E_{app}	V	Applied Potential
E^0	V	Formal Electrode Potential
f_{NP}	-	Collision Frequency
F	C m^{-1}	Faraday's Constant
i	A	Current
i_{red}	A	Reduction Current
i_{ox}	A	Oxidation Current
i_{max}	A	Maximum Steady-State Current at Saturating Conditions
i_{net}	A	Net Current
i_{ss}	A	Steady-State Current at a Microelectrode
i_T	A	Current at the Microelectrode Tip

Table 2: List of Symbols

Symbol	SI Units	Definition
i_{norm}	A	Buffer normalized current
J_k	mol L^{-1}	Flux of Species k
j	A m^{-2}	Current Density
k_{ox}	mol.m^{-2} s^{-1}	Electrode Oxidation Reaction Rate
k_{red}	mol.m^{-2} s^{-1}	Electrode Reduction Reaction Rate
k_0	m s^{-1}	Standard Rate Constant
K_m	-	Number of Individual Replicates
k_{cat}	s^{-1}	Rate of Catalysis
K_d	s^{-1}	Rate of Dissociation
L	cm	Length
$n_{electrons}$	-	Number of Electrons
n_e	-	number of electrodes
n	-	number of individual replicates
N_A	mol^{-1}	Avogadro's Number
$p-value$	-	Hypothesis Testing (Statistics)
Q	C	Electric Charge
R_f	-	Roughness Factor
R	J mol^{-1} C^{-1}	Gas constant
R_g	-	Normalized Microelectrode Glass Radius (r_{glass}/a)
r	-	Cylindrical Coordinate (COMSOL)
R^2	-	Correlation Coefficient
SEA	U. mg^{-1}	Specific Electrochemical Activity
$[S]$	M	Substrate Concentration
t	s	Time
T	K	Temperature

Table 2: List of Symbols

Symbol	SI Units	Definition
t_{calc}	-	T-Statistic (Student's t-Test)
$t_{critical}$	-	Critical t-value (Student's t-Test)
x	m	Position relative to the electrode surface
z_R	-	Charge of species R
z	-	Cylindrical Coordinate (COMSOL)
τ	-	Tortousity
ϕ	-	Porosity
δ	mm	Diffusion Layer Thickness

Contributions

The work in this thesis was performed under the supervision of Professor Janine Mauzeroll. She provided guidance on all projects and corrections on all manuscripts.

Chapter 1

Author Contributions: This chapter was written by Siba Moussa (SM) and reviewed by Janine Mauzeroll (JM).

Contributions to Original Knowledge: Chapter 1 provides an introduction to microelectrodes, their theory, and applications. Recent developments of microelectrodes tailored for custom bioanalytical applications are discussed. Chapter 1 serves as a practical guide to be used for rapid assessment of experimental possibilities and to make informed decisions about experimental design with microelectrodes.

Publication Information: Portions of this text have been reproduced from: Moussa, S., Mauzeroll, J. Microelectrodes: An Overview of Probe Development and Bioelectrochemistry Applications from 2013 to 2018. *Journal of the Electrochemical Society* **2019**, 166(6), G25-G38.

Chapter 2

Author Contributions: SM designed the experimental methodology, performed experiments, COMSOL simulations and wrote the manuscript. Danny Chhin contributed to the writing and formatting of the manuscript. Loredano Pollegioni (LP) provided the enzyme and reviewed the manuscript. JM edited and reviewed the manuscript.

Contributions to Original Knowledge: Current quantitative methods for analysis of the activity of immobilized enzymes are limited. This is especially true for non-redox enzymes

that generate a redox-active product. Lack of quantitative methods is partially owing to the inability of quantifying the true amount of active immobilized enzyme onto a solid support. Chapter 2 presents a methodology to assess the activity of immobilized enzymes using PPD-modified microelectrodes using *Rhodotorula gracilis* D-amino acid oxidase (DAAO) as a model enzyme. This approach may be used for other non-redox enzymes, especially for exploring the crosslinker effect on enzyme activity.

Publication Information: Chapter 2 is reproduced from: Moussa, S., Chhin, D., Pollegioni, L., Mauzeroll J., Quantitative measurements of free and immobilized *Rg*DAAO Michaelis-Menten constant using an electrochemical assay reveal the impact of covalent crosslinking on substrate specificity, *Analytical and Bioanalytical Chemistry* **2021**, 1-10.

Chapter 3

Author Contributions: SM designed the experimental methodology and performed experiments. Marion Van Horn (MVH) and Aryah Shah performed animal manipulations and animal tracking experiments. Christopher J. Thibodeaux (CJT) helped with the LC-MS experiments. The writing and manuscript correction were performed by SM, MVH, ESR, CJT, JM and LP. LP provided the enzyme.

Contributions to Original Knowledge: Disrupted levels of D-serine in the brain have been associated with neurological disorders, including schizophrenia, depression, and Alzheimer's disease. The work in Chapter 3 addresses factors for successful and reproducible miniature biosensor fabrication required to measure D-serine in biological samples, pharmacological evaluation, and designing point of care devices.

Publication Information: Chapter 3 is reproduced from: Moussa S., Van Horn M.,

Shah A., Pollegioni L., Thibodeaux C.J., Ruthazer E.S., Mauzeroll J., A Miniaturized Enzymatic Biosensor For Detection of Sensory-Evoked D-serine Release in the Brain, *Journal of the Electrochemical Society* **2021**,168(02).

Chapter 4

Author Contributions: SM designed the experimental methodology, performed experiments, and wrote the manuscript. Giulia Murtas provided training for the experimental work. LP provided the enzyme, reviewed and edited the manuscript. JM reviewed and edited the manuscript.

Contributions to Original Knowledge: The design of selective DAAO-based enzymatic biosensors remains a challenge for real-world biosensor application. DAAO enzymes do not have a unique selectivity for D-serine and are influenced by interference effects from D-alanine presence. Chapter 4 addresses DAAO-based biosensor selectivity towards D-serine by introducing point mutations into DAAO and using the mutants to build biosensors with enhanced D-serine detection properties. Chapter 3 also presents a close study of the DAAO immobilization process using various characterization methods, leading to an unexpected biosensor regeneration strategy.

Publication Information: Chapter 4 is reproduced from: Moussa, S., Murtas, G., Pollegioni, L., Mauzeroll J., Enhancing Electrochemical Biosensor Selectivity with Engineered -amino acid Oxidase Enzymes for D-serine and D-alanine Quantification, *ACS Applied Biomaterials* **2021**,4(7),5598-5604.

Chapter 5

Author Contributions: SM designed the experimental methodology, performed experi-

ments, developed the software and wrote the manuscript. Elena Rosini provided training for the experimental work for the high-throughput enzyme screenings. Daryan Chitsaz provided the primary astrocyte cultures.LP provided the enzyme. Timothy Kennedy, JM, and LP reviewed and edited the manuscript(s).

Contributions to Original Knowledge: The design of oxidase-based enzymatic biosensors has been limited to detect a select number of substrates. Lack of stable enzymes with high substrate activity usable for immobilization remains a challenge for biosensor development. Chapter 5 extends the substrate scope of oxidase biosensors by using mutagenesis and screening for enzymes with glycine activity. Glycine Oxidase (GO) H244K, the enzyme with the highest potential for application as a glycine biosensor was used for biosensor development and application. Moveover, this chapter presents the development of a data analysis software purposed to reduce time spent on biosensor data analysis.

Publication Information: Chapter 5 is reproduced from:

Moussa, S., Rosini, E.,Chitsaz, D., Pollegioni, L., Kennedy, T., Mauzeroll J., A High-throughput Strategy for Glycine Oxidase Biosensor Development Reveals Glycine Release from Cultured Cells , *Analytical Chemistry* **2021** *(Accepted).*

Moussa, S., Mauzeroll J., Sensorlyze: A Software for Biosensor Data Analysis , *Manuscript in preparation* **2021**.

Thesis Outline

Biosensors have significant potential in monitoring diseases, enabling huge developments in personalized healthcare. For example, the conception of glucometers has transformed the life of diabetics whom rely on measuring their blood sugar levels regularly. This thesis contributes to the field of biosensing by developing robust and rapid methodology for real-time amino acid detection, beginning with biosensor optimization and application to data analysis simplification. This thesis demonstrates the advancements made towards robust enzymatic electrochemical biosensor development and application for real-time amino acid monitoring in neurological environments.

Chapter 1 presents an introduction to microelectrode-based sensors typically used for analyte detection in various fields and their specific application for biological sensing. In particular, the theory and equations behind analyte quantification using microelectrodes are introduced. The literature surrounding microelectrodes as biosensors was reviewed over the 2013-2018 period and is presented in this chapter.

Chapter 2 presents a methodology for the characterization of immobilized *Rg*DAAO study the activity of crosslinked *Rg*DAAO on fixed supports. The methodology is validated using literature methods and the effect of immobilization on enzyme specificity is further explored.

Chapter 3 focuses on the application of *Rg*DAAO biosensors in biological settings for D-serine detection. The biosensors were tested in different complex tadpole matrices to asses their usability for D-serine detection in pre-clinical research. The application of these biosensors may be extended to other model organisms and detection media.

Chapter 4 applies protein engineering strategies to improve the sensitivity and selectivity of D-serine detecting enzymatic biosensors. Mutant yeast and human D-amino acid oxidase were expressed, characterized and used to develop D-serine biosensors with varying D-serine selectivity. The biosensor may then be used in different environments based on their D-serine selectivity.

Chapter 5 extends the application of microelectrode- based biosenors to probe glycine. Through the use of mutagenesis and highthroughput screening, the search for GO variants with high glycine activity was optimized. Based on the screening results, GO H244K was identified as an enzyme with high potential for biosensor development and glycine detection. GO H244K biosensors were characterized and compared against GO WT biosensors and demonstrate excellent glycine detection properties. GO H244K biosensors were also applied in real sample analysis by measuring real-time glycine release from HEK293 cells as well as astrocytes.

Chapter 1

Introduction: An Overview of Microelectrode Development and Bioelectrochemistry Applications

Chapter Preface

Chapter 1 introduces the theory, experimental design, and existing literature on microelectrode (ME) development and application. Chapter 1 consists of three sections:

- The first section introduces the theory behind ME measurements and analytical quantification of analytes. The fundamental equations that link concepts to experimentally measurable quantities are presented.
- The second section ties in the theory with application by introducing an experimental design guide for planning and executing experiments using ME.
- The third section presents recent literature examples where MEs were applied for biological analyte detection.

Portions of the work presented in Chapter 1 have been adapted from: Moussa, S.; Mauzeroll, J. Microelectrodes: An Overview of Probe Development and Bioelectrochemistry Applications from 2013 to 2018. *Journal of the Electrochemical Society* 2019, 166(6), G25-G38.

1.1 Introduction to Microelectrodes

MEs are small scale electrodes with a critical parameter of at least one dimension being on the micron scale and are used for electroanalytical detection. They were first introduced by William Hyde Wollaston in 1801[1], and employed as early as the 1900s to measure the release of dopamine.[2] ME development has led to exciting research in the electrochemical detection of molecules across confined spaces such as isolated bio-membrane and cells.[3] Smaller electrodes allow for localized recordings of concentration profiles as well as of analytes of interest. MEs have found application in a wide variety of research areas including biology[4–12], corrosion[13,14], energy[14,15], kinetics[14], instrumental development[9,16], and surface modification[17,18] due to their small size, high sensitivity, fast steady-state response, low double-layer charging current and minimal ohmic loss.[19] Advantages of MEs include reduced ohmic resistance (iR) due to low faradaic currents ($\leq$ nA), higher current densities and improved signal-to-noise ratios.[2,9]

Chapter 1 presents a summary of the theory and experimental parameters used for bio-electrochemistry applications of MEs. A review of select ME bio-analytical applications from 2013 to 2018 is also discussed along with a discussion on future research directions with MEs.

1.1.1 Theory of Microelectrodes

Consider a solution in which an electrode reaction (Equation 1.1) involving charge transfer between the electrode and an electroactive species occurs, such as the reactions listed in Table 1.3:

$$R \underset{k_{ox}}{\overset{k_{red}}{\rightleftharpoons}} O + e^- \tag{1.1}$$

Where k_{ox} is rate of reaction for the oxidation of species R and k_{red} is rate of reaction for the reduction of species O, also known as the reverse of the oxidation reaction rate.

Application of a potential to the electrode tip such that a reaction may now occur at the electrode surface (Equation 1.1) results in a time-dependent concentration gradient of species R at a certain distance from the electrode surface towards the solution bulk (Figure 1.1).

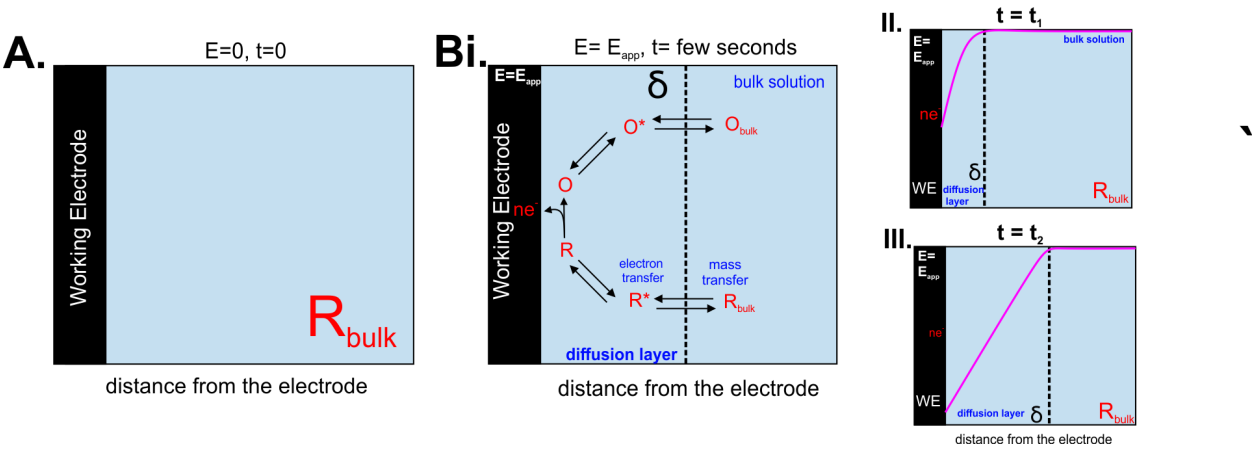

Figure 1.1: Schematic of the time-dependent concentration gradient that occurs with electrode presence in a solution under application of a potential. A) No concentration gradient is present the solution at t=0, only species R is present at the bulk and of the electrode surface B) i) In a few seconds following the application of a potential,the concentration of R changes as it is consumed and converted into O. Mass transport of R from the bulk towards the electrode surface where electrons are transferred as part of the oxidation process. O is formed and diffuses away from the surface of the electrode towards the bulk. As a result of this process a diffusion layer, with thickness δ, forms. ii) At the beginning of the oxidation process, where $t = t_1$ the diffusion layer begins to form. iii) After a time, where $t = t_2$, the thickness of the diffusion layer grows.

The transport of species R towards the electrode surface is governed by diffusion, migration and convection as given by the electrode geometry independent, Nernst-Plank equation (Equation 1.2) :

$$J_R(x,t) = -D_R \Delta C_R(x,t) - \frac{z_R F D_R}{RT} C_R(x,t) \Delta\phi + v C_R(x,t) \tag{1.2}$$

Where J_R is the time and location dependent mass transfer flux, D_R the diffusion coefficient, F is Faraday's constant, R is the universal gas constant, T is the temperature, C_R the concentration, z_R the charge of species R, v is the solution velocity, and $\Delta\phi$ is the electrostatic potential difference between two points.

Equation 1.2 can be simplified in many cases depending on the experimental setup. For instance, in diffusion limited systems where no external mixing occurs, the convection term $[vC_R(x,t)]$ is neglected. In presence of high electrolyte concentrations, the migration term $[\frac{z_R F D_R}{RT} C_R(x,t)\Delta\phi]$ is also considered negligible due to an electric potential gradient of approximately zero. In the more specific case of one-dimensional linear diffusion, under experimental conditions with no convection and migration, the Nernst-Planck equation simplifies to Fick's First Law of Diffusion[20]:

$$J_R(x,t) = -D_R \Delta C_R(x,t) \tag{1.3}$$

Equation 1.3 states that the mass transfer flux is proportional to the concentration gradi-

ent that develops from electrochemical reactions at the electrode surface, causing diffusional flux of reactants, R, towards the electrode surface. By relating Fick's laws of diffusion[20] to electrochemical measurements, it is possible to extract the relationship between reactant flux, J_R, at the electrode surface and the net current, i_{net}, measured at the electrode surface:

$$\sum_R z_R J_R = \frac{i_{net}}{n_{electrons} F A} \tag{1.4}$$

Where i_{net} is the total current measured at the tip of a ME, A is the ME cross-sectional area that is dictated by the ME geometry, $n_{electron}$ is the number of electrons involved in the reaction.

The net current measured at the electrode surface is a contribution of both oxidation and reduction processes at the electrode:

$$i_{net} = i_{ox} - i_{red} \tag{1.5}$$

Where i_{ox} is the current associated with the oxidation reaction and i_{red} is the current associated with the reduction reaction

Macroscopic Electron Transfer Kinetics

The current measured at the electrode surface is dependent upon many parameters, one of which is the kinetics of electron transfer. For instance, the oxidation current depends on the

kinetics of oxidation of species R:

$$i_{ox} = k_{ox} C_R(0,t) n_{electrons} F A \tag{1.6}$$

Where $C_R(0,t)$ is the concentration of species R at the electrode surface at time, t.

Similarly, for a reduction reaction:

$$i_{red} = k_{red} C_O(0,t) n_{electrons} F A \tag{1.7}$$

Where $C_O(0,t)$ is the concentration of species O at the electrode surface at time, t.

The net overall electrochemical reaction with both oxidation and reduction reactions occurring simultaneously can be expressed in terms of oxidation and reduction reaction rates:

$$i_{net} = i_{red} - i_{ox} = n_{electron} F A [k_{ox} C_R(0,t) - k_{red} C_O(0,t)] \tag{1.8}$$

The potential of an electrode impacts the kinetics of a reaction occurring at the electrode surface. In the case where the electrode interface is at equilibrium with the solution, the forward and backward reactions have the same rate constants, making Equation 1.6 and Equation 1.7 representative of the oxidation and reduction currents. In cases where the

electrode potential is not at equilibrium, such that a potential is applied at the electrode surface, the reaction rates, k_{ox} and k_{red}, no longer have equal rates and can be expressed as a function of E, the electrode potential, and k_0, the standard rate constant. For the oxidation reaction:

$$k_{ox} = k_0^{[1-\alpha f(E-E^{0'})]} \tag{1.9}$$

Where α is the mass transfer coefficient, E is the electrode potential, $E^{0'}$ is the formal electrode potential and f is the product of nRT/F.

Similarly, the reduction reaction:

$$k_{red} = k_0^{[-\alpha f(E-E^{0'})]} \tag{1.10}$$

The complete current-potential characteristics can now be expressed as:

$$i = FAk_0[C_O(0,t)^{[-\alpha f(E-E^0)]} - C_R(0,t)^{[(1-\alpha)f(E-E^{0'}])}] \tag{1.11}$$

Equation 1.11 is also known as the equation for Butler-Volmer kinetics. Butler-Volmer kinetics for electron transfer are important in studying electrochemical redox reactions, specifically in conditions where the electron transfer rate at the interface is rate-determining. In

the case of electrochemical biosensors, however, steady state currents are typically correlated to the analyte concentrations. As such, as long as the potentials are high enough to oxidize or reduce the electron transfer kinetics are not important enough to be a significant consideration. One exception is the need to consider electron transfer kinetics for electrochemical biosensors in simulations of reactions as is the case in Chapter 2.

Marcus Theory for Microscopic Electron Transfer

While Butler-Volmer kinetics explain macroscopic electron transfer for electrode reactions, microscopic theories are important to describe the relationship between a biomolecule and the electrode. Originally developed by Ruldolph Marcus, Marcus theory explains the rates of electron transfer reactions. For a one electron transfer reaction, the donor molecule donates the electron and the acceptor accepts the electron (Equation 1.12).

$$Donor + Acceptor \rightleftharpoons Donor^{+} + Acceptor^{-} \tag{1.12}$$

This process is dependent on overcoming the energy barrier for the reaction to occur (ΔG^{o}) which dictates the rate of electron transfer, k_{ET}. Marcus theory states that the calculation of k_{ET} requires the knowledge of $\Delta G^{\ddagger}$, which is the free energy difference between the activated donor complex and the precursor acceptor complex. For electron transfer to occur in the first place, such that a redox reaction is favorable, the Fermi level of the electrode must not be at equilibrium. Moreover, a potential large enough to enable electron

transfer must be applied to overcome the energy barrier and form the transition state complex (Figure 1.2).

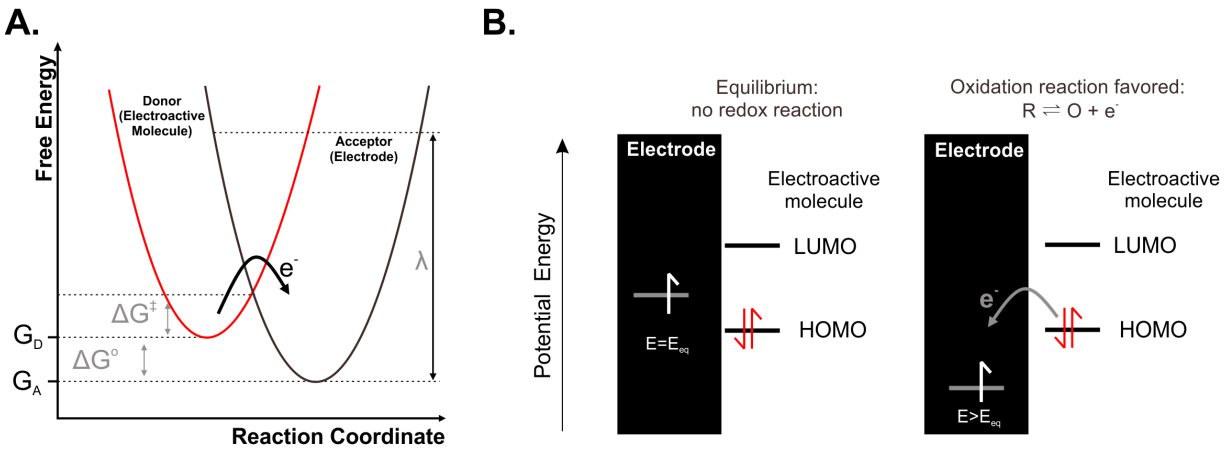

Figure 1.2: Theory behind electron transfer between the electrode and the electroactive molecule. A) Marcus energy model for electron transfer between the donor electroactive molecule (i.e. redox mediator or enzyme) and the acceptor (electrode). The rate of electron transfer is dependent on the free energy required for the electron transfer to occur. B) To overcome the energy barrier for electron transfer, the Fermi level of the electrode must be lowered (for an oxidation reaction).

1.1.2 Electron Transfer Nature to the ME Surface

While the rate of electron transfer does not need to be strictly considered in electrochemical biosensor design, understanding the nature of electron transfer between an electrode and a biomolecule is important for rational biosensor design. Effective electronic coupling between a biomolecule and an electrode occurs through one of the three possible mechanisms. Electron transfer may be achieved indirectly through an electroactive intermediate, which is the substrate or product of the biomolecule based reaction (1^{st} generation biosensors, Figure 1.3Ai) and through artificially mediated electron transfer (MET) by introducing elec-

troactive mediators (2^{nd} generation "single-use" biosensors, Figure 1.3Aii) or directly through direct electron transfer (DET) between the biomolecule's active site and the electrode surface (3^{rd} generation biosensors, Figure 1.3B).

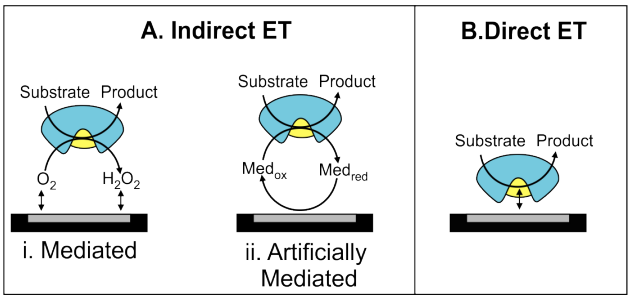

Figure 1.3: Electron transfer mechanisms between a biomolecule and the ME surface.

The electrode and the electroactive molecule can be considered as an electron-donor pair and as such, Marcus theory can be used to describe the electron transfer rate between them.[20] For enzyme mediated reactions (1^{st} and 2^{nd} generation biosensors), the electron transfer distance between the enzyme and the electrode is rather long (> 14 Å) preventing direct electron transfer from occurring.[21]

Microelectrode Geometries

An essential component to understanding electrode measurements is an analysis of the electrode geometry and the way in which the electrode geometry impacts the diffusion profile. Various ME geometries have been developed including but not limited to disk[22–26] (Figure 1.4A), cylindrical[27] (Figure 1.4B), hemispherical[28–30] (Figure 1.4C), beveled[31] (Figure 1.4D), and band[32] (Figure 1.4E). Parameters such as recession/protrusion, bluntness, aspect ratio, insulation angle, off-center positioning of the metal wire, uneven insulation, and

cracks may strongly influence MEs of certain geometries.[18] Due to their ease of fabrication, maintenance, as well as the simple analytical expressions describing their electrochemical behavior, disk-shaped MEs are the most commonly used ME geometry.[33,34] Disk ME designs consist of an electroactive material surrounded by a concentric coplanar insulating layer.[35]

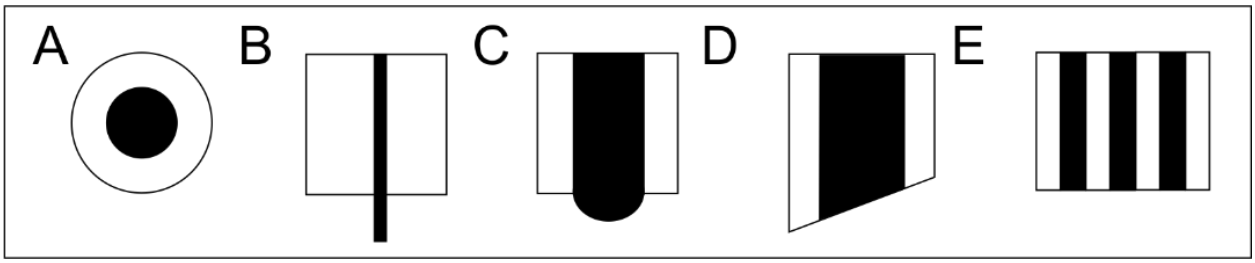

Figure 1.4: Common ME shapes: A) disk B) cylinder C) hemisphere D) bevel E) band

Disk-Shaped Specific Microelectrode Theory

Two electrode properties affect the diffusion profile of reactants towards the electrode surface: 1) the electrode size and 2) the electrode geometry. While for macroelectrodes planar diffusion dominates, the behavior of MEs is governed by the presence of radial diffusion fields Figure 1.5.

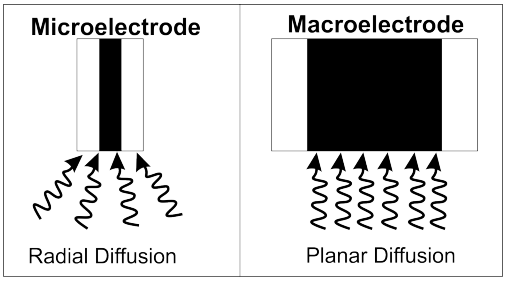

Figure 1.5: Schematic of the diffusion profiles for both micro (left) and macro(right) electrodes.

The Cottrell equation is a well studied equation used in diffusion controlled experiments to describe the change in current over time measured at a polarized electrode. This equation has been modified for MEs that reach a diffusion-dependent steady state response, and the steady-state limiting current is given by[36]:

$$I_{ss} = kn_{electrons}FD_R C_R^* a\beta \tag{1.13}$$

Where k is a shape related geometric constant (disk, $k = 4$), C_R^* is the bulk concentration of dissolved redox species, a is the electroactive surface radius, and β is a tabulated factor dependent on the R_g of the ME.[36,37] The R_g, defined as the ratio between the radius of the insulating sheath (r_{ME}) and the radius of the electroactive surface critical geometric parameter affecting the overall ME quality. Smaller R_g values are preferred in bioelectrochemical experiments, especially in imaging due to increased spatial resolution and reduced diffusion induced interferences.[35] Moreover, MEs reach steady state currents at shorter timescales, t, due to the diffusion dependent diffusion layer thickness δ[36]:

$$\delta = \sqrt{\pi D_R t} \tag{1.14}$$

For MEs where the geometry is not disk shaped, the timescale of the applied potential is short, or the size is not on the micron scale, the diffusion profile varies and it may be difficult to derive analytical expressions for the limiting current, as is in the case of nanowires, which

have 3D geometries.[2] Simulations by O'Riordan and coworkers demonstrate the differences that may result in the diffusion profiles from varying the electrode size and geometry.[36,38]

1.2 Experimental Design with Microelectrodes

MEs are especially useful in the detection of biomolecules. Biomolecules often have limited lifespans and are present at low concentrations in complex media, making them difficult to detect. The ability to probe biomolecules using MEs is tied to the ME selectivity, stability and biocompatibility. Often, MEs are used as the backbone of more complex sensor designs which enable detection of the desired biomolecule. To optimize the performance of ME-based sensors, the ME material, size, R_g value, as well as type of surface pretreatment and modification must be carefully chosen. It is imperative that ME design be compatible with both the applied electrochemical methodology and experimental conditions (i.e. electrolyte concentration, temperature and pH.[39] A comprehensive summary of reported ME-based sensors is listed in Table 1.1.

Table 1.1: List of microelectrode-based sensors from 2013-2018 and their applications.

Analyte	Physiological role	ME Material*	ME Size (um)	Geometry*	Array? (Y/N)	Pretreated? (Y/N)	Surface Modif?* (Y/N)	Ref.
Acetylcholine	Cholinergic receptor function regulation	C	30	Cy	N	Y	N	39
Adenosine	Cellular energy transfer	NM	50x150	B	Y	N	Y(Ch,B)	31
Ascorbate	Neuromodulator	C	5-7	Cy	N	Y	Y(Ch),N	40,41
Bacteria	Diseases and food intoxication	C, NM, O	2-3, 8-25, 3350 x 100	D, B, O	Y, N	N	Y(Ch),N	27,42–48
Catalase	Oxidative damage cell protection	C	10	D	N	N	N	49
Cells	Building block of all organisms	C,NM,O	2-4,10-60	D, Be, O	Y, N	Y, N	Y(Ch),N	50–56
Cholesterol	Basal activity regulation	C, NM	1,10-50	R, D	N	N	Y(Ch,B)	57–59
DNA	Hereditary material	C,NM	$\leq$ 0.15, 7-50	Cy, D	N	Y, N	Y(Ch),N	22,60–62
Dopamine	Neurotransmitter	C, M	7-33	Cy, D	N	Y, N	Y(Ch,B)	63,64
D-serine	Gliotransmitter	NM	25	D	N	N	Y(Ch,B)	65,66
Estradiol	Reproductive function	NM	50	Cy	N	N	Y(Ch)	67
Ex-vivo tissue slices	Composition of organs	C, O, NM	25.5 x 20.4, 30	O	Y	N	Y(Ch),N	68,69
Glucose	Metabolism	C,NM	7,10,25, 33	Cy, D	N	N	Y(Ch,B)	65,70–72
Glutamate	Neurotransmitter	NM	20-50	D	Y, N	N	Y(Ch,b)	65,73–75
Hydrazine	Nervous system toxin	NM, O	10	D	N	N	Y(Ch)	28,29
Hydrogen Peroxide	Redox signaling and oxidative stress	NM	10-100	Cy, D	Y, N	Y, N	Y(Ch,B),N	39,76–79
Insulin	Blood sugar regulation	C	7	Cy	N	Y	Y(Ch)	80
Lactate	Energy production	NM	10,50	D	N	N	Y(Ch,B)	72,79
MicroRNA	RNA silencing and gene expression	NM, O	25	D	N	Y	N	81
Mitochondria	Energy production	NM	20	D	Y	N	Y(Ch)	78
Neural cell culture	Signal transmission	C, NM, M	10-50	B, O	Y	N	Y(Ch),N	82–87
Oxygen	Metabolism	C, NM	8-50	Cy,D	N	Y, N	Y(Ch,N)	88,89
RONS	Neurotransmitters, Oxidative stress	C, NM	1.54,5-50,90	D, Be	Y, N	N	Y(Ch)	90–96
Tumor necrosis factor	Inflammatory cells marker	NM	5 x 3200	B,Cy	Y,N	N	N	97
Viruses	Viral diseases	C, NM	1, 7-33	D,Cy	Y, N	N	Y(Ch)	25,98–100

*C=carbon, NM=noble metals,O=not noble metals,semiconductors,mercury;R=ring,D=disk,

Cy=cylindrical, Be=beveled, B=band, O=other, Ch=chemical, B=biomolecular

1.2.1 Microelectrode Materials

Asides from the geometry, choosing the most appropriate ME material is dependent on the bioanalyte of interest as well as the intrinsic properties of the available ME materials.[101] Factors such as cost, conductivity, ease of ME fabrication, surface area, biocompatibility, and material potential window play a significant role in material selection as shown in Table 1.2.[25,102]

Table 1.2: List of Advantages and Disadvantages for Common Microelectrode Materials.

Material	Advantages	Drawbacks
Noble Metals	Stable in air and aqueous solvents, high conductivities, high surface areas (nanoparticles), electrocatalytic, biocompatible, malleable	Expensive, Formation of oxide layer
Carbon Materials (excluding graphene)	Biocompatible, low cost, chemically stable, biofouling resistant, mechanically robust	Low conductivity (0.01 S · cm-1- 103 S · cm-1)
Non-noble Metals and Semiconductors	Antimicrobial, fast electron transfer abilities, high surface areas (∼100-500 g.m^2)	Diamond-based materials are expensive

Noble metals. Due to their corrosion resistance, stability in air and electrical conductivity ($\sim 10^5 S \cdot cm^{-1}$), noble metals have been used as electrode materials since the inception of MEs. Gold (Au), platinum (Pt) and silver (Ag) have been studied and used extensively.[25] Approximately 60% of the publications surveyed in 2013–2018 have relied on metal-based MEs as opposed to other materials due to their chemical stability and ease of surface functionalization.[103]

Carbon materials. Carbon materials are the second most used ME material in the 2013–2018 period. They exhibit favorable features such as structural polymorphism, which is

useful for tailoring sensor electrochemical properties, high chemical stability, low cost, wide potential windows, relatively inert electrochemistry, rich surface chemistry and electrocatalytic activities for a variety of redox reactions. Carbon materials are often biocompatible, a prerequisite for in vivo bio-electroanalytical measurements.

Graphene. Graphene is a two-dimensional carbon-based nanomaterial.[104] Graphene-based MEs[21,84] take advantage of graphene's remarkably large surface areas ($> 2000 m^2 g^{-1}$), resulting in enhanced adsorptive capabilities and electric conductivity.[105,106] These properties lead to sensors having lower limits of detection, higher sensitivities and the capability of direct electron transfer. In the 2013–2018 period, graphene-based ME sensors have been used for the detection of DNA, protein and pathogens as well as in the design of cell nanodevices and for neural electrodes (Table 1.1).[106]

Carbon nanotubes (CNTs). The unique electric, thermal, optical mechanical and biocompatibility properties associated with CNTs make them excellent materials for biomedical applications.[105] In fact, CNT-based MEs have found use in bioanalyte detection such as viruses, DNA, antigens and disease markers.[107] Surface modifications of carbon MEs using CNTs have also been applied in neurotransmitter (NT) detection as they are less susceptible to biofouling.[108] In a review by Grumezescu and co-workers, the properties of CNTs and their biomedical applications are thoroughly discussed.[10]

Diamond. Boron-doped diamond (BDD) presents metal-like conductivities whilst retaining the chemical stability, hardness and biocompatibility inherent to diamond and desired during bioelectroanalysis. BDD has a much larger potential window (-1.2 V to 2.5 V vs. 0.1 M Ag/AgCl) compared to other materials (i.e. Pt: -1.0 V to 0.96 V vs. 0.1 M Ag/AgCl).[9]

This is due to high oxygen and hydrogen evolution overpotentials in aqueous media, mainly attributed to the lack of surface sites for intermediate species adsorption.[9] The electrochemical properties of BDD electrodes can be tuned by changing the level and type of dopant and surface termination.[105] BDD modified MEs are fabricated using techniques similar[9] andf have been used for both *in vivo* and *in vitro* neural studies from 2013-2018.[109–113]

1.2.2 Microelectrode Surface Modifications

Surface modification of MEs is required to clean[39,62,95], activate[42,114] , chemically modify[87,115,116], alter the aspect/ratio[117,118], block interferences[66,119], or immobilize biomolecules.[80,120] These techniques may either be manual or electrochemical. For example, removal of the surface oxide layer from platinum electrodes be may achieved through manual polishing with alumina powder or electrochemical cycling in sulfuric acid. Manual techniques such as dip-coating and drop-casting are simple and are commonly used for ME-based sensor fabrication.

Nonetheless, there is a tradeoff between simplicity and reproducibility for these surface modification techniques.[121,122] Some commonly used materials for ME surface modifications over 2013–2018 include Pt black (PtBK)[79,83,91], polymers[123], carbon nanoubes[81], polelectrolytes[124], Nafion[125], Prussian blue[80,126], chitosan[75], enzymes[60,127,128], aptamers[129], self- monolayers (i.e cystamines)[10], nucleic acids[130], collagen[56] and nanoparticles[65,131,132]. Though each of these materials has their use, we will focus on enzyme modified MEs in the remainder of this chapter given their prominent applications in live cell and neuronal studies.

In this thesis, enzyme-modified MEs are defined as biosensors. Although other biorecognition elements have been used for biosensor construction, enzymes are the oldest since

their first reported use by Clark and Lyons in 1962[133] and remain the most commonly used. Electrochemical biosensors are used to address electrochemical challenges in selectivity and non-electroactive species detection.

The focus of the reviewed biosensor research has been mainly on their bioanalytical applications, yet several studies have explored biosensor design strategies. The motivation for these studies was biosensor performance evaluation and enhancement.[71–73,134] The most investigated aspect of biosensor design is the process of enzyme immobilization onto the ME-backbone. This is because the fabrication procedure may significantly impact the biosensor performance[126,135] This step is designed to maximize the active enzyme loading onto the ME backbone without significantly affecting the enzyme activity and selectivity.

Common enzyme loading and stabilization methods include entrapment within a matrix[72] (Figure 1.6A) or behind an analyte permeable membrane (Figure 1.6B) covering the ME surface[23] (i.e. polyvinyl alcohol, poly-acetonitrile, agar gel, redox hydrogels) and covalent binding on a bare[73] or surface functionalized ME using non-specific binders[135] (Figure 1.6Ci/Cii), bifunctional groups[63] (Figure 1.6Ciii) bio-specific interactions[68] (i.e. antibody-analyte) (Figure 1.6Civ).

For stable and reproducible biosensors, covalent attachment within a crosslinked matrix is the most commonly used immobilization technique. The enzyme is usually dissolved in bovine serum albumen (BSA) prior to deposition and crosslinking.[136] Glutaraldehyde, a nonspecific binder with an amine condensing-carbonyl group, is the conventional crosslinker in biosensor design. Studies suggest that using alternatives such as poly(ethylene glycol) (PEG) may actually yield better performing biosensors due to the spacer arm length, which

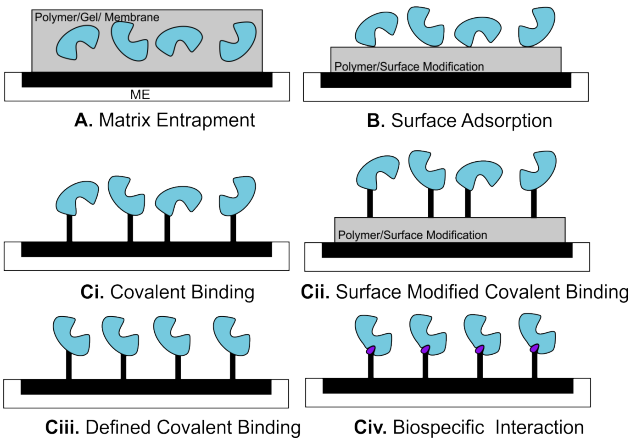

Figure 1.6: Enzyme Loading Strategies.

affect the enzyme conformational behavior and mobility, as well as the reactive side chain differences, which may distort the enzyme active site.[71] In fact, it has been shown that glutaraldehyde immobilization is comparatively harsh and modifies the enzyme selectivity toward the substrate of interest.[71,74]

Most biosensor architectures detect H_2O_2 produced through an oxidoreductase enzymatic reaction with the substrate of interest. Application of high potentials (+400 to +700 mV vs Ag/AgCl) will oxidize the H_2O_2 present at the surface of the electrode, resulting in indirect electron transfer.[137] Common substrates detected using biosensors are glutamate, acetylcholine, choline and adenosine.[108] As many other biomolecules are also oxidized in same potential region as H_2O_2, the sensors must be designed to maximize H_2O_2 selectivity over other interferences. For the electrochemical reactions associated with the detection of various bioanalytes using MEs and biosensors, refer to Table 1.3.

Table 1.3: Electrochemical reactions associated with amperometric bioanalyte detection.

Bioanalyte(s)	Redox Mediator	Redox Reaction	E_{app} (V vs Ag/AgCl)	References
Glutamate, D-serine, Lactate, Glucose, Adenosine, Ascorbate	Hydrogen Peroxide	$H_2O_2 \rightarrow O_2 + 2H^+ + 2e^-$	0,0.005,0.30, 0.45,0.50, 0.60,0.70	31,40,41,64,65 72,74,78,138,139
Dopamine	Direct	Dopamine $\rightarrow 2e^- + 2H^+ +$ Dopaminoquinone	0.185	129
Oxygen, catalase	Oxygen	$O_2 + 2H^+ + 4e^- \rightarrow 2H_2O$	-0.20	49,88
Nitric Oxide	Direct	$NO\bullet + O_2 + 2H_2O \rightarrow 4NO_2^- + 4H^+$	0.80	92,93,95
Peroxynitrite	Direct	ONOO- $\rightarrow$ ONOO$\bullet + e^-$	-0.10	92
Catalase	Direct	Heme[Fe (III)] $\rightarrow$ Heme[Fe (IV)] + e^-	-0.13	49

Another challenge with biosensor use is biocompatibility and in turn, lifetime. Biocompatible films used for biosensor may delaminate or lose their structural integrity over time. During the first few hours of use, proteins or biomolecules may adsorb onto the surface of the biosensor, resulting in reduced detection sensitivity. The maximum lifetime of biosensors from literature surveyed in recent years is limited to a few days.[73] To improve both the

biosensor selectivity and working lifetime, protective barriers such as an outer membrane to prevent large molecule interferences and/or diffusional outer barriers of thin membranes to control the diffusion toward the enzyme increasing the enzyme stability may be applied. Examples of outer layer materials include collagen, polycarbonates, cellulose or conductive polymers.[136] Nafion and polyurethane can also be drop-casted on the surface as outer diffusion-limiting membranes.[115]

1.2.3 Microelectrode Arrays (MEAs)

Compared to individual MEs, MEAs present certain advantages over MEs as they generate greater faradaic responses ($\geq$ nA) while maintaining their high spatiotemporal resolution.[97,108,115] For instance, MEAs have been developed for spatially resolved studies of single cell exocytosis.[52] Moreover, MEAs offer multiplexing capabilities useful in probing the behavior of large cell populations, particularly neural networks.[138,139]

State-of-the-art fabrication techniques such as photolithography[52,140], thin film deposition[52,141], and reactive ion etching[93,141] have made the development and application of these reproducible arrays conceivable. Since the first report on MEA use for cell studies by Thomas and coworkers in 1972[142], developments in surface and bulk micromachining methods have made possible ME standardization and downsizing with well-defined sizes and spacings. This has addressed accuracy and reproducibility concerns commonly encountered with single ME use.[142] While the first MEA sensor was glass-based, recent and more common MEA sensors are silicon-based.[103,143] Typically, microfabrication tools are used to sputter metal layers onto a silicon wafer with a thermally grown layer of silica (SiO_2). These arrays can then

be surface treated for enhanced applications. TiN, PtBK and conductive polymers such as polypyrrole (PPy) are some of the most commonly used materials for surface modification of MEAs.[144] Details on the fabrication processes can be found elsewhere in literature.[142] Most MEAs are developed for *in vitro*, *in vivo* and *ex vivo* neuroscientific research and for clinical diagnosis of bacteria and virus presence Table (Table 1.1).[145]

1.2.4 Electrochemical Methods.

A typical bio-electrochemical experiment uses standard electrochemical cells.[65] Figure 1.7 presents a visual representation of the distribution of methods applied in literature from the 2013–2018 period.

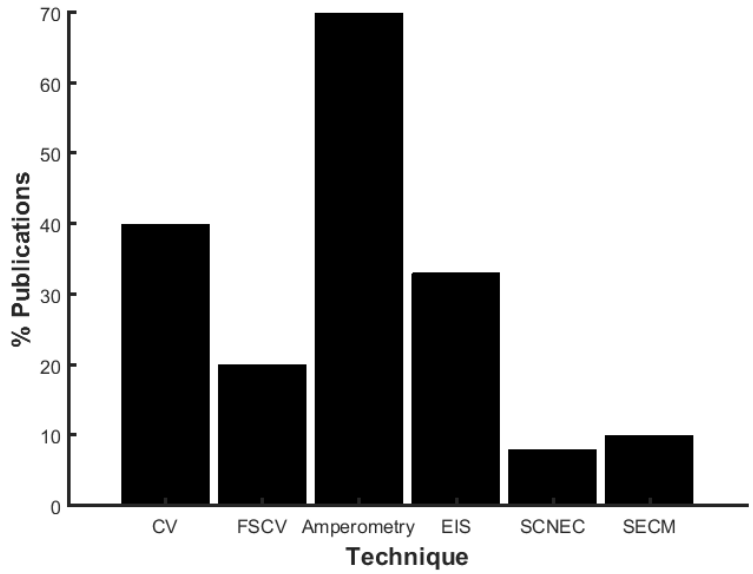

Figure 1.7: Distribution of the electrochemical techniques used over 2013–2018. (CV = cyclic voltammetry, FSCV = fast-scan cyclic voltammetry, EIS = electrochemical impedance spectroscopy, SCNEC = stochastic collision nanoelectrochemistry, SECM = scanning electrochemical microscopy)

Voltammetry

Of the applied voltammetry-based techniques, cyclic voltammetry (CV) and fast scan cyclic voltammetry (FSCV) are the most commonly used for bioelectroanalysis. Other techniques include square wave voltammetry (SWV) and double pulse potential voltmmetry (DPV).[20]

Cyclic Voltammetry. Cyclic voltammetry is used in 40% of ME-based measurements reviewed between 2013–2018 where it was the standard method for electrochemical characterization of ME performance.[24,146–148] On the other hand, it is rarely used for chemical analysis in complex media to due the limited chemical resolution it offers.

Fast Scan Cyclic Voltammetry. FSCV is one of the most common methods for sub-second transient measurements of electroactive neurotransmitter concentration changes, used in 20% of the surveyed literature.[119] Carbon-fiber microelectrodes (CFMEs) are the electrodes of choice for this technique, especially since they are biocompatible and are more resistant to biofouling than metal electrodes.[6] FSCV is a technique comparable to CV but uses rapid cyclic potential sweeps (>100 Vs^{-1}) to separate and quantify electroactive analytes with varying but similar current-potential characteristics. Each sweep can take less than 10 milliseconds.[5] The CVs produced serve as "fingerprints" for compound identification to ensure chemical selectivity.[108] Rapid scanning allows *in situ* detection of electroactive chemical fluctuations while simultaneously producing large background currents due to the charging of the electric double layer. As a result, background current subtraction post-experimentation is required. Calibration curves are used for peak currents to be converted into concentration values.[108]

Amperometry

Another common technique, applied in 70% of recent literature, amperometry relies on the measurement of a current resulting from the application of a constant potential large enough to oxidize or reduce a molecule of interest.[136] Due to continuous sampling and a sampling frequency limited only by the data acquisition system and the current amplifier filter, a much higher temporal resolution is obtained with amperometry than with other techniques. As such amperometry is the method of choice to study biochemical events occurring on short timescales.[5] Challenges in interferences from electroactive molecules in samples are addressed through ME surface modifications for analyte selectivity.[6]

Electrochemical Impedance Spectroscopy (EIS)

EIS is a technique that relies on resistance measurements under the application of a varying voltage or frequency (10^{-3} to 10^{5} Hz).[3,6] EIS was employed in 33% of the reviewed literature. It was typically used for cell culture studies where arrays of microelectrodes are constructed beneath the cell attachment platform and an alternating current is applied between the electrodes while the potential is monitored.[144,149–151] If no cells are on the surface, then the current flows freely. The presence of cell growth on the electrodes results in an impeded current flow, and thus the increase in the system resistance can be measured. Changes in cell behavior, causing growth disturbances will result in measurable impedance changes.[152]

Stochastic Collision Nanoelectrochemistry (SCNEC)

SCNEC has been applied in numerous studies that work toward probing single molecules. This stems from the desire to obtain molecular information such as molecular heterogeneities in fundamental studies as well as the drive for the development of very low concentration assays.[137,152] Recent years have seen numerous publications of SCENC bio-applications[152], comprising about 8% of the literature on ME bioapplications from 2013–2018. In a typical SCNEC system, the ME surface hosts the electrochemical reaction while various types of nanoparticles (NPs) collide with it, producing a sharp current change. Typically, the ME is immersed in a dilute solution of NPs and amperometry is used to drive the detection of NP stochastic collisions at the ME surface. Assuming steady state diffusion-limited flux of the NPs, the collision frequency is given by:

$$f_{NP} = 4D_{np}C_{np}aN_A \tag{1.15}$$

Where f_{NP} is the collision frequency, D_{NP} is the bulk diffusion coefficient of the NP, C_{NP} is the NP concentration, a is the radius of the UME, and N_A is Avogadro's number. As NP electrochemical behavior mainly depends on their composition, diameter and geometry, their selection is an important consideration in designing SCNEC experiments.

There are three main approaches to SCNEC-based experiments (Figure 1.8)[152]:

1. Blockage: An inert NP collides with the ME surface and blocks it, resulting in a step decrease in the current.

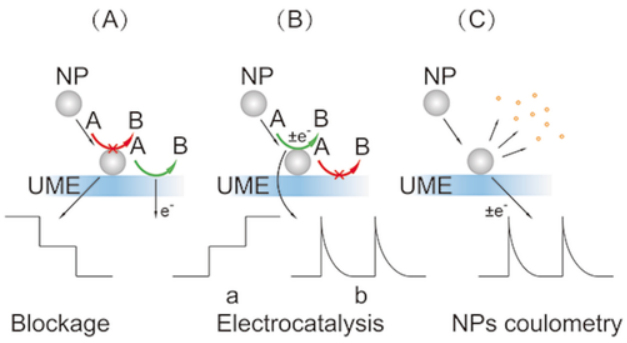

Figure 1.8: Typical SCNEC modes a) insulating particle blockage b) nanoparticle electrocatalysis c) nanoparticle coulometry. Reprinted with permission from Ref. 166. Copyright Wiley 2017.

2. Electrocatalysis: Catalytically active NPs collide with the ME surface, resulting in a step increase in the current.

3. Coulometry: Direct NP electrolysis occurs when a constant potential to oxidize or reduce the NP is applied at the ME surface. The NP size distribution can be obtained from the integrated charge of the current spikes.

Scanning Electrochemical Microscopy (SECM)

SECM is a scanning electroanalytical ME-based measurement technique applied in 10% of the review literature. SECM relies on scanning a ME across the surface of sample immersed in electrolyte. The signal recorded at the ME is influenced by the sample topography and reactivity as well as the distance between the ME and the sample surface.[153] In essence, SECM is used for high spatiotemporal resolution (submicron, millisecond) material flux quantification from surfaces.[6,18]

1.3 Bioanalytical Applications

In the 2013–2018 period reviewed, there have been significant developments in ME design and optimization for biological applications. Some examples include sensor miniaturization[65,73], the development of novel fabrication strategies[64,77] and surface modification enhancements for sensitivity and selectivity.[73,81] While 40% of the published literature has been aimed at *in vivo* neurotransmitter detection on model systems, the remaining literature focuses on ME modification for clinical sample applications and molecular biology studies. In the following sections, the various bio-applications of MEs from 2013 to 2018 will be discussed with an emphasis on their applications in probing dissolved and adhered bioanalytes as well as in bioanalyte collisions Figure 1.9. Table 1.4 lists examples of the bioanalytes and their classes discussed in this text.

Table 1.4: Examples of Bioanalytes and Their Classes Studied with Microelectrodes from 2013–2018.

Bioanalyte Class	Bioanalyte Examples
Cells	HeLa[154], Neurons[55,60,83–85,87,118,139], PC12[52,141], Cardiomyocytes[54,90], Chromaffin[41,154], Mast[57], MFC-7[77]
Cell Metabolites	Lactate[73,155], Glucose[65,73]
Nucleic Acids	DNA[23,63,154] , RNA[82], Aptamers[120,131]
Bacteria	Gram negative *(Escherichia coli)*[44,45,156], Gram positive (*Staphylococcus epidermis*)[44,49]
Enzymes	Glucose Oxidase[65,73] , Cholesterol oxidase[58,157]
Neurochemicals	Dopamine[64,65], Acetylcholine[40,70]
Viruses	Murine Cytomegalovirus (MCMV)[26,158]

Figure 1.9: Schematic of the bio-analytical microelectrode applications.

Detection of Dissolved Bioanalytes

In Vivo Neurochemicals. For the past century, researchers have been relying on the use of MEs for both in *vitro* and *in vivo* detection of neurotransmitters. Typically, FSCV in combination with 7–10 μm CFMEs, are used for these experiments, given the many advantages of using carbon as an electrode material such as the ability to alter the CF electrochemical properties.[5,159]

Dopamine. Abnormal dopamine (DA) levels have been associated with neurological dysfunction, making DA an important biomarker for disease related mechanistic studies.[160] In recent literature, MEs have been applied for dopamine quantification in anesthetized rats[64], new born fetal calf serum[129], and *Drosophila melanogaster* (fruit flies).[161] Modified carbon surfaces have been used extensively for these experiments due to enhanced electrochemical surface properties.[24,64,105,107,159,162–164] CNT modifications are most common for DA detection due to their intrinsic cationic selectivity at physiological pH and biocompatibility.[64,165] In fact, a study by Venton et al. on the performance of various CNT fiber ME structures demonstrated structure-dependent bioelectrochemical responses.[24] The authors concluded that variations in the fabrication protocol can drastically affect the sensitivity, selectivity, and the electrochemical response to FSCV frequency. In a separate publication, the same group used CNT-Niobium (Nb) MEs for *in vivo* detection of pulse-stimulated dopamine release from male Sprague-Dawley anaesthetized rats. Using these MEs, they were able to improve their limit of detection toward dopamine by two folds as compared to bare carbon fibers to 11 $\pm 1nM$.[64]

Glutamate. Glutamate detecting biosensors have been mostly used for the detection of concentration changes associated with the forebrain and cognitive and memory processes.[136] Glutamate is present in neurons at intracellular concentrations of $\approx$ 10 mM.[165] Extracellular concentrations are usually much lower and elevated concentrations are characteristic of pathological states. Functionalized biosensors, rather than bare MEs, are typically used for its detection. The biosensors are generally Pt based modified MEs with polymer and immobilized glucose oxidase films.[71,74,136] For instance, Monbouquette and coworkers developed

an implantable Pt based-iridium oxide (IrOx) PPy GOx modified MEA with an integrated Ag/AgCl reference electrode for glutamate detection.[75]

Nitric Oxide. Nitric oxide ($NO\bullet$) is another important signaling molecule in living organisms.[95] It can exert beneficial or deleterious effects depending on the site, rate of production, concentration and redox environment. Its reactivity and relatively short lifetime ($\sim$ 1 s) make $NO\bullet$ particularly challenging to detect in biological systems.[166] CFMEs were used to quantify $NO\bullet$ concentration changes upon exposure to $NO\bullet$ synthase-targeting pharmacological agents.[31] The spatial distribution of $NO\bullet$ release in different parts of the zebrafish intestine was also observed using these CFMEs. This work served as a unique approach for real-time quantitative measurements of $NO\bullet$ modulation and investigation of RONS (reactive oxygen/nitrogen species) biochemical pathways *in vivo*. $NO\bullet$ levels were also detected in rat kidneys[96] and breast cancer cell lines[92].

Other Neurotransmitters. MEs have been employed to identify the presence of many other neurochemicals including ascorbate[41,42], oxygen (O_2)[90,142], acetylcholine (ACh)[40,70], and glucose[65,71–73] For instance, Mao and co-workers developed a vertically aligned CNT-CFME for *in vivo* monitoring ascorbate levels (Figure 1.10).[122] To stimulate ascorbate release, 2.0 μL of 100 μM glutamate was infused into the brain. The group noticed an increase in the current response compared to the artificial cerebrospinal fluid (aCSF) injection response, demonstrating the utility of these sensors for *in vivo* measurements useful for physiological and pathological investigations.

O_2 fluctuations *in vivo* were measured using the same sensor with an added Nafion coating and PtNP surface modifications for reduced surface fouling as well as increased

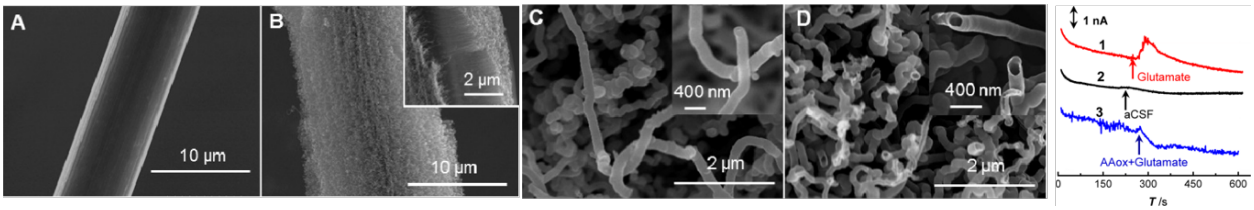

Figure 1.10: Left: SEM images of (A) CF, (B) VACNT-CF, and the tips of VACNT-CF (C) before and (D) after electrochemical treatment in 1.0 M NaOH. Right: Amperometric responses for ascorbate recorded *in vivo* with VACNT-CF microelectrode during local microinfusion of 2.0 μL of 100 μM glutamate (curve 1), 2.0 μL of aCSF (curve 2), and 2.0 μL of 100 μM glutamate containing AAox (40 units $\cdot\, mL^{-1}$) (curve 3), with 1.0 μL $\cdot\, min^{-1}$ into rat striatum. The electrode was polarized at +0.05 V. Arrows represent the beginning of the microinfusion. Reprinted with permission from Ref. 123. Copyright American Chemical Society 2014.

surface area.[89] The sensor was inserted into the rat hippocampus to record O_2 levels. The O_2 level was shown to decrease very quickly during global ischemia, a condition associated with inadequate blood supply to an organ, and then returned to baseline after reperfusion, the restoration of blood flow to an organ (Figure 1.11).

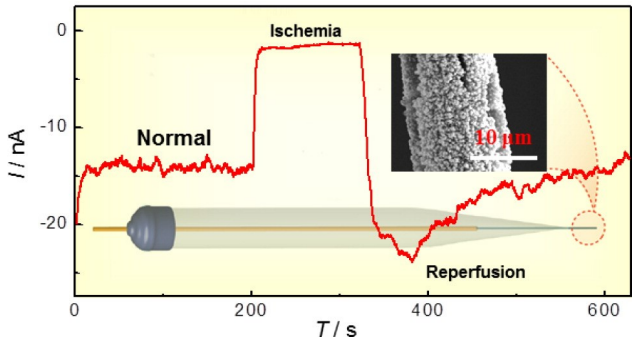

Figure 1.11: Amperometric response for the hippocampus O_2 recorded in anesthetized rats during global ischemia/reperfusion. The electrode was polarized at -0.5 V vs Ag/AgCl (aCSF) Top Right: SEM image of the Pt/VACNT-CF. Many densely packed Pt nanoparticles homogeneously distributed on the surface of VACNTs are shown. Reprinted with permission from Ref. 89. Copyright American Chemical Society 2014.

Cans and coworkers developed a proof-of-concept amperometric biosensor for co-detection of two neurotransmitters, glucose and dopamine using a CFME at the millisecond scale.[65] The working principle behind the co-detection is the indirect, enzymatic detection of glucose and the direct direction of dopamine. This sensor has not yet been applied *in vivo*.

CFMEs have also been used for the indirect detection of ACh levels in rats.[40] Experimental data suggest that *in vivo* signal modifications may represent modifications of ACh-dependent processes in the striatum, a cluster of neurons which serve as a critical component of the brain's motor and reward systems. The methodology developed in this work presents possibilities in the assessment of disease-modifying pharmacological treatments.

Cells and their Dissolved Molecules

MEs have been applied in single cell analysis for many different types of studies, most of which involve monitoring the flux of dissolved molecules from cells such as cholesterol, reactive oxygen/nitrogen species (RONS) and other small metabolites.

ROS Release from Cells. MEs are useful electroanalytical tools for detection of RONS species formation such as H_2O_2 and NO$\bullet$. Amatore's group detected the production of RONS by cells upon incubation with ferrocifen molecules in hopes of exploring a potential breast cancer treatment.[92] Induced depolarization stimulated RONS release for RONS detection and quantification at the single-cell level using a platinized CFME positioned in close proximity ($\sim 5\ \mu$m).

Huang's group also developed a hybrid nanoporous Au ME decorated with PtNPs for H_2O_2 release detection from single cells.[77] Phorbol myristate acetate (PMA) was added to the

cells to stimulate cellular H_2O_2 release. The group also demonstrated the sensor capability for H_2O_2 detection from multiple and single cells.

For RNS-specific release detection, MEs have been implemented in the simultaneous sensing of NO• and peroxynitrite ($ONOO^-$) release from cultured cells.[94] MEAs with over 2400 single Au MEs were fabricated and used for amperometric release measurements.[93] The same research group also collaborated on the development of Au and Pt based superoxide (O_2^-)and NO•-detecting cytochrome c-modified biosensors.

Cholesterol Efflux. Cholesterol is a tightly regulated major structural component of the cell plasma membrane (PM). The plasma membrane consists of cholesterol with both high and weak escape tendencies, also known as "inactive" and "active" cholesterol, respectively. While the past few years have not seen much work for this application due to the extensive exploration in earlier years[167–169], a small number of recent publications have demonstrated the application of cholesterol oxidase based biosensors for quantification of cholesterol efflux from the PM.[58,60,128]

Burgess and coworkers developed a biosensor for indirect cholesterol efflux determination from a single cell obtained from buccal ganglia from *Aplysia californica* (sea slug).[60] Toward clinical application, the same group demonstrated proof of concept biosensor-based experiments as a diagnostic tool for cystic fibrosis.[58] The measured cholesterol efflux rate from the mucosae suggests that cholesterol is elevated in the inflamed airway tissue of humans suffering from cystic fibrosis. Chen and coworkers used an alternative approach for measuring cholesterol efflux.[170] A hollow capillary with a Pt sputtered ring of 1 μm tip aperture was filled with a solution of cholesterol oxidase and Triton-X 100 to permeabilize the cell

membrane and measure a cholesterol efflux rate from the PM.

Other Metabolites. MEs have been broadly employed in monitoring the metabolic activity of cells and are finding further applications for single cell level metabolic activity measurements. Of these, the most commonly studied substrates are glucose and lactate. Other metabolites released from cultured cells include oxygen[90], ascorbate[171], and hormones.[68,81,172] While glucose and lactate sensors have been around since the late 19^{th} century[173,174], recent work has been oriented toward sensor optimizations with a focus on sensitivity and spatiotemporal resolution. Rapino and coworkers performed a comparative study to demonstrate sensor miniaturization for metabolite monitoring at the single cell level from MCF10A cells (human breast epithelial cells).[73] The authors conducted an extensive study on the parameters affecting biosensor for SECM studies on cells. They provide a decision matrix offering insight on suitable biosensor fabrication protocols for desired biosensor performance (Figure 1.12). Stralfor's group also designed a biosensor for potentiometric probing of intracellular glucose release from human adipocytes (fat cells).[175]

Criteria → / Protocols ↓	*Sensitivity LOD Biosensor Efficiency*	*Linear Range Response time*	*Spatial Resolution*	*Selectivity & Permeability*	*Reproducibility & Stability*
Crosslinking with GDA	+	=	=	−	=
Poly-*o*-aminophenol	−	+	+	=	+
Poly-pyrrole	−	+	+	=	+
Cathodic EDP	−	−	−	=	−

Figure 1.12: The Decision Matrix - a green cross means a positive score for the criteria (thicker cross: very positive), yellow equal sign means comparable responses, and red line means negative score for the criteria of the several investigated protocols. Reprinted with permission from Ref. 73. Copyright American Chemical Society 2017.

Tsuneda et al. measured the dissolved oxygen (DO) levels in cell culture media using Clark type Pt-based O_2 permeable membrane coated MEs.[90] The MEs were manipulated with 1 μm precision high resolution, real time detection of local DO cell consumption and spatiotemporal distribution in culture media of confluent monolayers (CMs) from neonatal rat cardiomyocytes (heart muscle cells) and human induced pluripotent stem cell (hiPSC)-CMs. Their work demonstrated the ability to use MEs to measure local rather than global DO concentration profiles to mimic *in vivo* heterogenous microenvironments. Cellular release of bioanalytes was further explored through monitoring ascorbate exocytosis. Using pretreated CFMEs for selective ascorbate detection, the accelerated ascorbate electrochemical oxidation was achieved.[41] The experimental results provided the first description of exocytosis kinetics of endogenous ascorbate from single chromaffin cells (adrenal gland cells) using single cell amperometry using single cell amperometry. The quantitative information on endogenous ascorbate exocytosis obtained from this study is useful for understanding the physiological and pathological transport kinetics mechanisms of ascorbate.

Electrochemical assays for hormone detection are a quick and straightforward method in clinical diagnosis as compared to other time consuming and expensive current methods such as chromatography[176], immunoassays[177] and spectrometry[177], MEs have been used to measure insulin levels as a tool for diabetes mellitus diagnosis by Songmao's group.[81] Moreover, an extensive review on sensors designed for cortisol detection in point of care applications can be found in literature.[172] Hoa and co-workers also developed an enzyme-linked immunosorbent assay (ELISA) ME to assay estradiol and serum estradiol presence.[68]

Nucleic Acid Biosensors

Nucleic acid-based biosensors have only been around since the 1990s as compared to the conventional electrochemical enzymatic biosensors, which were developed in the 1970s. Their development spans over hundreds of published papers in the last five years and comprehensive discussions on these biosensors can be accessed in references.[7,178,179] For the sake of brevity, only select publications will be discussed but readers must keep in mind that there is a plethora of remarkable published work on this topic.[154,180–184] DNA sensors have great potential in quick clinical diagnosis of genetic and pathogenic diseases as well as monitoring of food safety. Various designs have been developed for DNA-based sensing, using various electrode materials from carbon[63] to noble metals.[23,62] As a diagnostic tool, Josowicz and co-workers developed a proof-of-concept label-free electrochemical methylated DNA detector as opposed to the conventional metal-complex based DNA methylation detection approach for prostate cancer diagnosis.[62,185] Bedioui and coworkers studied the long range electron transfer of their developed DNA biosensors.[23] They were able to achieve mediated electron transfer through Fe III/ Fe II redox process of intercalated mediators was used to rapidly probe DNA hybridization in small volumes of 50 μL. DNA sensors based on CFMEs were also developed ty Arikan et al. to detect DNA hybridization.[63]

Detection of Adhered Bioanalytes

Cells. Cells are commonly integrated on MEAs for their analysis. As a cancer model, MCF-7 cells were deposited on the center of a collagen-modified MEA with 400 single sites by

Matsue and co-workers.[56] Cell adhesion blocks the electrochemical oxidation of potassium ferrocyanide ($K_4[Fe(CN)_6] \cdot 3H_2O$) and ferrocene methanol ($FcCH_2OH$), resulting in a decreased oxidation signal at the sensors in a cell-dependent manner. Another collagen adhesion dependent MEA sensor was developed by Ewing and coworkers for spatiotemporally resolved amperometric detection of neurotransmitter release across a single PC-12 cell.[52] The authors developed a micro-well-based MEA consisting of 36 2-μm-width square MEs. The MEA was used to image the spatial distribution of exocytosis at the cell surface. Signals were successfully recorded from eight independent 2 μm-wide MEs from a single cell, showing the MEA capability to probe subcellular heterogeneity, a feature which is inherent to exocytosis (Figure 1.13).

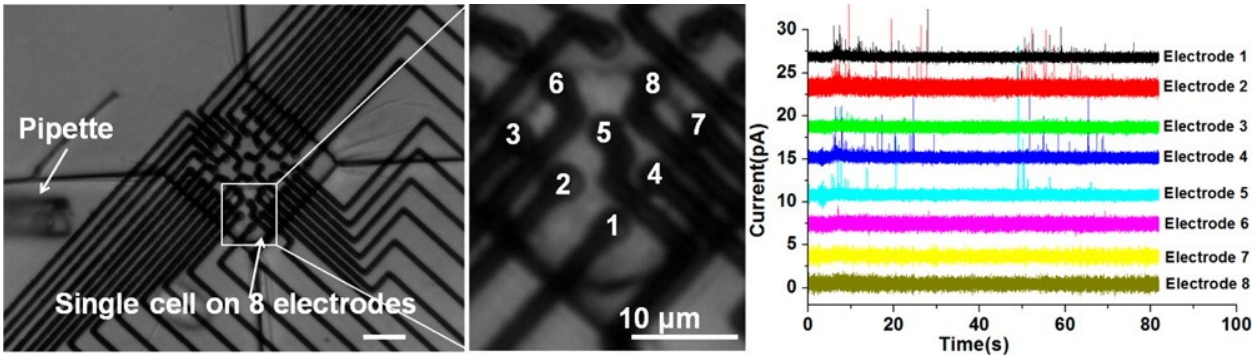

Figure 1.13: Left to Right: Micrograph of the setup, showing the 36-electrode array partially covered by a single PC12 cell (scale bar: 10 μm); Expanded view of the electrode array showing a single cell identified in a red dotted circle and the labeling of the electrodes (scale bar: 10 μm); Representative amperometric traces of exocytotic release from a PC12 cell recorded at 8 electrodes for 25 s stimulations of the cell. Reprinted with permission from Ref. 51. Copyright American Chemical Society 2014.

Pancrazio and co-workers used neuronal cultures grown on a poly-D-lysine coated 60-ME planar MEAs with diameters of 10–30 μm to assay the neurotoxicity of amyloid-β

1–42 (Aβ42).[86] Aβ42 is a bioanalyte implicated in Alzheimer's disease. Cultured neurons characteristically form dense networks on MEAs and become spontaneously active within three weeks of seeding on the MEAs. Methylene blue and memantine, two model therapeutics for Aβ42, were tested with the MEA-based assay and almost full recovery in the spiking activity was shown within 24 h after administration in the cultures.

Bacteria. Many techniques have been applied to study biofilm formation including fluorescence microscopy[117], scanning electrochemical microscopy[45], and confocal laser scanning microscopy.[46] The disadvantage of these methods is the need for fixation or labeling, all of which have damaging effects on the samples.[48]

Lei and co-workers observed *Shewanella oneidensis* MR-1 bacterial biofilm growth on an Au macroelectrode using Pt ME.[186] The film thickness was monitored by approaching the ME tip to the biofilm outer later at different periods of development. MEAs were also developed by Flandre and coworkers developed for the detection of bacterial cells, based on impedimetric techniques.[187] In their work, the authors used lytic enzymes to selectively destroy bacteria anchored on the sensor surface from synthetic urine samples, namely *Staphylococcus epidermis* and *Enterococcus faecium*. *Escherichia coli (E.coli)* was detected in human urine samples for urinary tract infection diagnosis using Au MEAs.[48] Through detecting changes in impedance, growth of *E.* coli growth was monitored during a 12-hour culture.

Au MEAs were also used for impedance based detection of gram-positive bacteria, bacteria which contains a thick peptidoglycan layer in the cell wall (Figure 1.14).[187] Using thiol-based covalent immobilization, Kaur and co-workers functionalized the MEA with Leucocin A, a naturally occurring antimicrobial peptide. The sensor responded through

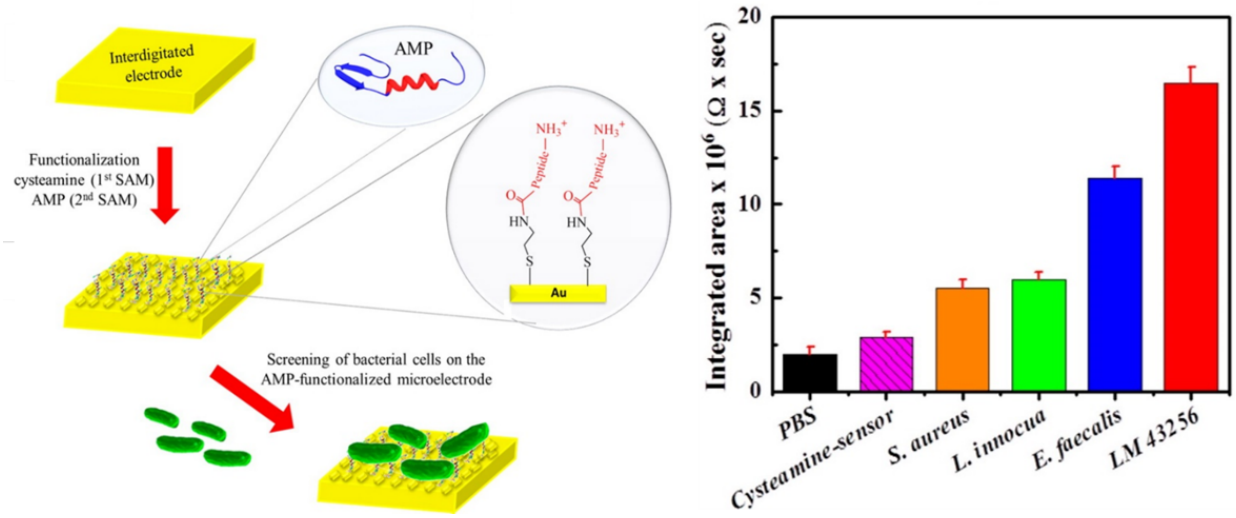

Figure 1.14: Left: Graphic depiction of the AMP-based biosensor showing a simulated cartoon denoting the interdigitated microelectrode, AMP immobilized on the microelectrode array, and bacterial detection achieved via binding of the target cells to the immobilized AMP. Right: The binding curve parameter (integrated area under the curve) for impedance sensor responses to the corresponding strains. Reprinted with permission from Ref. 196. Copyright American Chemical Society 2014.

an impedance change to the presence of gram-positive bacteria to detect *Listeria monocytogenes* (*L*.monocytogenes) at clinically relevant concentrations. The sensor was also tested in *L*.monocytogenes contaminated dilute milk samples. Although selective *L*.monocytogenes binding was not achieved with the sensor when tested with other Gram-positive bacteria, there was a clear discrimination of the sensor toward the various bacterial species of the same concentration- with the highest impedance response toward *L*.monocytogenes. To detect bacteria in more concentrated milk samples, a piezoelectric ME array system was designed by Huang's group.[156] The sensor was tested against fifty fresh milk samples contaminated with five different bacterial species and has potential as an identification tool in the food industry.

Collision-Based Detection of Bioanalytes

Collisions of NPs on ME surfaces have attracted much interest in the past decade.[152] The Bard, Compton and Crooks groups have demonstrated much of the pioneering work in this field.[29,30,61,188–190] One of the earliest work on collisions was done by Bard's group. The group proposed that each collision produces a unique current–time profile related to the particle size, particle residence time, and the nature of particle interaction with the electrode surface, thus opening many possibilities in single molecule electrochemistry.[188] Using $Fe(CN)_6^{4-}$ as a redox mediator, discrete blocking-based collision events of electrochemically inert bioanalytes on a ME were probed.[61] This specific study demonstrated the application of collision based-measurements in the detection of antibody, enzyme, DNA, and polystyrene nanosphere adsorption events (Figure 1.15).

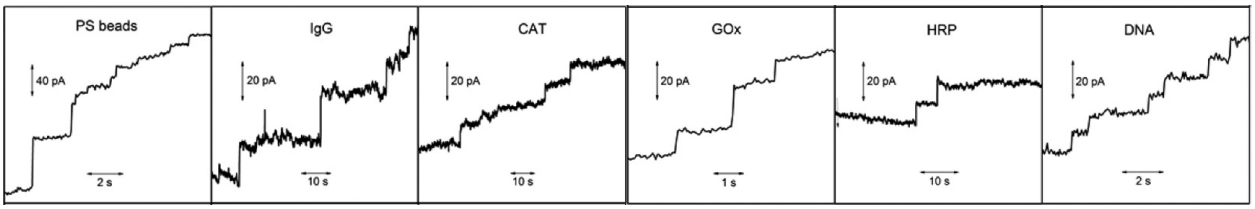

Figure 1.15: i-t curves recorded in the presence of 7 pM polystyrene beads, 2 pM IgG, 2 pM CAT, 2 pM GOx, 2 pM HRP, and 300 pM DNA. Pt UME biased at 0.8 V vs Ag/AgCl in a solution of 400 mM ferrocyanide was used. each experiment, a data point was taken every 50 ms. Reprinted with permission from Ref. 61. Copyright American Chemical Society 2015

Viruses. Single virus impacts on a ME surface were one of the recently explored SCNEC-based research avenues.[26] For instance, low concentrations of murine cytomegalovirus (MCMV) were measured through irreversible blockage-based SCNEC absorption at ME surface. This work was extended to detect the presence of viruses in biological samples such as urine.[158]

Moreover, Compton and coworkers presented a proof of concept method toward the detection of individual viruses using carbon MEs and AgNP-decorated viruses.[191] The group showed that the virus concentration could be rapidly quantified, even at the single virus level, and the electrochemical signal could be distinguished from a bacterial collision signal.

Bacteria. The presence of single, living, 2 μm long bacterial cells on MEs through blocking collisions using a combination of electrochemical and optical methods was demonstrated by Park and coworkers (Figure 1.16).[192] $[Fe(CN)_6]^{4-}$ was used as the redox mediator to attract negatively charged *E.* coli to the positive electric field from the oxidation reaction. This work was extended by Thorgaard and coworkers where the adsorption events of both *E.* coli and *Bacillus subtilis (B.subtilis)* bacteria were detected through probing blocking collisions at the surface of UMEs.[44] While *E.*coli collisions resulted in "step" shaped transients, the presence of *B.*subtiltis was distinguished through "blip" shaped transients. Simultaneous fluorescence microscopy was used to correlate the current transients to the collision events of the fluorescently labeled bacteria.

Nucleic Acids, Cells and Enzymes. Advancing into the use of more complex bioanalytes, Crooks and coworkers used DNA modified ME surfaces for electrocatalytic amplification (ECA) applications in biological target detection using hydrazine (N_2H_4) mediated electron transfer.[193] The key findings from this work were that while immobilizing ssDNA on MEs had little to no impact on the collision current transients, DNA modification of the NPs severely affected the collision frequency and current transient magnitude. The Crooks group built on this methodology to detect the presence of DNA.[194] This study established useful protocols for future ECA-based biosensing applications. More recently, the group applied

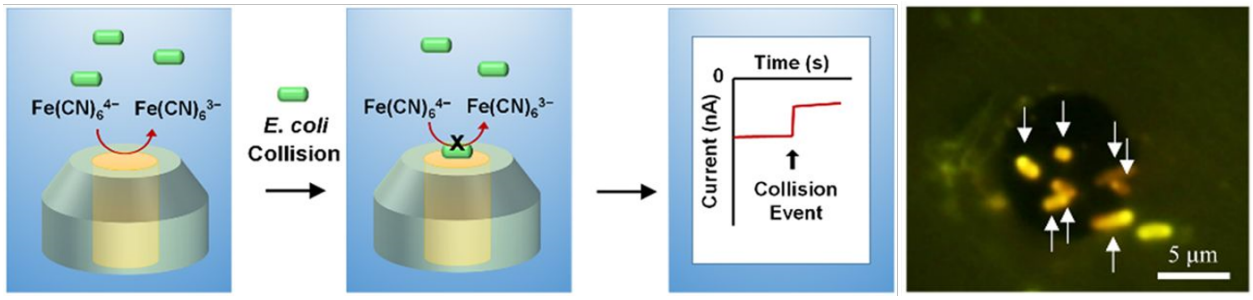

Figure 1.16: Left: Schematic diagram of E.coli detection by collision event on a UME. Bottom: i-t curves and relevant fluorescent images of *E.*coli on C-UME. Right: Fluorescent image after multiple *E.*coli collisions. The solutions contained 53 fM *E.*coli and 20 mM $K_4Fe(CN)_6$. The C-UME (10 μm diameter) was biased at +0.6V vs Ag/AgCl. Black circles in the fluorescent images indicate the surface of the C-UME.Reprinted with permission from Ref. 201. Copyright Nature 2016.

a similar framework for microRNA (miRNA) detection.[82] Dysregulation of the expression levels of one or more miRNAs is associated with various pathological diseases, including cancer, and therefore certain miRNAs may serve as important diagnostic biomarkers.

Other bioanalytical research contributions in this field consisted of enzyme and cell collision studies based on direct electron transfer. To demonstrate the possibility of direct electron transfer using single-catalase enzyme detection, enzyme collisions at BBD MEs were observed.[195] Also using direct electron transfer, the ability to differentiate between healthy and cancer cells was demonstrated.[196] This detection was achieved through monitoring the consumption of a single cell's contents when it collided with a ME in the presence of a surfactant. The electrochemical response between acute lymphoblastic lymphoma T-cells (cancerous white blood cells) and healthy thymocytes was shown to vary by two orders of magnitude.

1.4 Future Prospects of Microelectrodes

More than two centuries after their inception, MEs have been developed with new shapes, geometries and designs to solve problems associated with spatially and temporally resolved bioanalyte detection and long chemical release events. Today, MEs are routinely used for both *in vivo* and *in vitro* bioelectrochemistry. Yet, several significant challenges remain in their application. Difficulties in signal discrimination between various redox active molecules, lowering limits of detection and quantification, as well as invasiveness-associated challenges are faced with ME use. While ME miniaturization into the nanoscale size regime for nanopore fabrication is attractive because it offers several benefits including the ability to carry out electrochemistry in smaller spaces, this approach includes additional operational challenges.

The applications of MEs are likely to continue expanding in the future toward single-molecule electrochemical detection, especially through collision-based electrochemistry. Another attractive area of research is ME commercialization for clinical diagnostics. Foreseeable developments of MEs for biological applications and commercialization purposes include the development of:

1. Cost efficient nanoparticle-based nanoscale ME designs
2. 3-D structured MEs for increased sensitivities
3. Biosensor based home testing kits for various applications
4. Practical MEs with prolonged lifetimes

5. MEs with simultaneous multichemical sensing

6. High throughput, environmentally and cost-friendly biosensor fabrication technology

MEs also have potential implications in providing unprecedented insight into the chemical basis of biological behavior and disease onset. Currently, the biggest challenge standing between unlocking the full potential of MEs is the design of highly reliable and reproducible MEs which can be used over prolonged periods of time. In the case of enzyme-based MEs, uncovering methods to produce and engineer enzymes in a cost and time efficient manner will significantly contribute toward clinical implementation of the sensors.

1.5 Summary

In general, enzyme-based MEs have been used mainly for neurochemical detection. In combination with amperometric techniques, these sensors have allowed for real time analyte detection. Currently, there remain to be challenges in the fabrication and design of enzymatic electrochemical biosensors, including enzyme selectivity, stability, and pH sensitivity, limiting their potential for commercialization. More importantly, there is a limited pool of enzymes currently in use for these types of devices, serving as a bottleneck in the detection of many analytes of interest. One way to unlock the potential of these biosensors is by discovering a wider range of enzymes suitable for use in biosensor development.

This thesis addresses the bottlenecks in robust biosensor development and application by bridging the gap between biotechnology, engineering and neuroscience. Using a multidisciplinary approach, the design of enzymatic electrochemical biosensors is optimized and their

applications in model animal systems demonstrate their suitability for analyte quantification, more specifically D-serine. This thesis also expands the application of these biosensors to other fields where real-time analyte quantification is required by developing a general biosensor design strategy. Overall, these biosensors may be used for both localized and global analyte detection using micro- and macro-electrochemical methods.

Chapter 2 describes the development of microelectrode based approach to study the activity of immobilized enzymes using RgDAAO as a model enzyme and revealing the effect of enzyme immobilization and cross-linking on substrate specificity.

Chapter 3 explores enzymatic electrochemical D-serine detecting biosensor characterization, LC-MS validation of biosensor measurements and the application of miniaturized biosensors *ex vivo* and *in vivo* in stage 48 *Xenopus Laevis*, a model animal system.

Chapter 4 investigates the relationship between mutant DAAO enzymes and D-serine biosensor performance (i.e. selectivity and sensitivity) to develop biosensors with improved D-serine detection properties.

Chapter 5 expands upon and incorporates lessons learned from D-amino acid biosensor design to expand the scope of enzymatic biosensors to other oxidase enzymes. This chapter discusses the development of an automated methodology to build and apply biosensors for glycine quantification by integrating highthroughput enzyme screening with a software-based data treatment approach.

References

(1) Bard, A.; Michael, A. The Rise of Voltammetry: From Polarography to the Scanning Electrochemical Microscope. *J. Chem. Educ.* **2007**, *84*, 644–651.

(2) Tiwari, A.; Patra, H.; Turner, A.; Ronkainen, N., Micro-and Nanoelectrodes in Protein- Based Electrochemical Biosensors for Nanomedicine and Other Applications In *Adv. Bioelectron. Mat.* 2015, pp 1–34.

(3) Eliaz, N., *Applications Electrochemistry and Nanotechnology in Biology and Medicine II In Modern Aspects of Electrochemistry No. 53*; Springer: New York, NY, 2012.

(4) Sekretaryova, A.; Eriksson, M.; Turner, A. Bioelectrocatalytic Systems for Health Applications. *Biotechnol. Adv.* **2016**, *34*, 177–197.

(5) Wang, Y.; Mao, L. Recent Advances in Analytical Methodology for In Vivo Electrochemistry in Mammals. *Electroanal.* **2016**, *28*, 265–276.

(6) Sismaet, H.; Goluch, E. Electrochemical Probes of Microbial Community Behavior. *Annu. Rev. Anal. Chem* **2018**, *11*, 441–461.

(7) Abi, A.; Mohammadpour, Z.; Zuo, X.; Safavi, A. Nucleic Acid-Based Electrochemical Nanobiosensors. *Biosens. Bioelectron.* **2018**, *102*, 479–489.

(8) Ferapontova, E. Electrochemical Analysis of Dopamine: Perspectives of Specific In Vivo Detection. *Electrochim. Acta* **2017**, *245*, 664–671.

(9) Kranz, C. Diamond as Advanced Material for Scanning Probe Microscopy Tips. *Electroanal.* **2016**, *28*, 35–45.

(10) Meliţă, E.; Purcel, G.; Grumezescu, A. Carbon Nanotubes for Cancer Therapy and Neurodegenerative Diseases. *Rom. J. Morphol. Embryol.* **2015**, *56*, 349–356.

(11) Fekete, Z.; Pongrácz, A. Multifunctional Soft Implants to Monitor and Control Neural Activity in the Central and Peripheral Nervous System: A Review. *Sens. Actuat. B. Chem* **2017**, *243*, 1214–1223.

(12) Rodeberg, N.; Sandberg, S.; Johnson, J.; Phillips, M.; E., P.; Mark Wightman, R. Hitchhiker's Guide to Voltammetry: Acute and Chronic Electrodes for In Vivo Fast-Scan Cyclic Voltammetry. *ACS Chem. Neurosci.* **2017**, *8*, 221–234.

(13) Payne, N.; Stephens, L.; Mauzeroll, J. The Application of Scanning Electrochemical Microscopy to Corrosion Research. *Corrosion* **2017**, *73*, 759–780.

(14) Dauphin-Ducharme, P.; Mauzeroll, J. Surface Analytical Methods Applied to Magnesium Corrosion. *Anal. Chem.* **2015**, *87*, 7499–7509.

(15) Syuto, M.; Kusakabe, T.; Honda, D. Determination of D -Serine in Several Model Organisms Used for Metabolic , Developmental and / or Genetic Researches by Liquid Chromatography / Fluorescence Detection and Tandem Mass Spectrometry. *Mem. Konan Univ., Sci. Eng. Ser.* **2013**, *1*, 11–19.

(16) Zhang, W.; Zhu, S.; Luque, R.; Han, S.; Hu, L.; Xu, G. Recent Development of Carbon Electrode Materials and Their Bioanalytical and Environmental Applications. *Chem. Soc. Rev.* **2016**, *45*, 715–752.

(17) Graaf, M.; Moeller, K. Introduction to Microelectrode Arrays, the Site-Selective Functionalization of Electrode Surfaces, and the Real-Time Detection of Binding Events. *Langmuir* **2015**, *31*, 7697–7706.

(18) Polcari, D.; Dauphin-Ducharme, P.; Mauzeroll, J. Scanning Electrochemical Microscopy: A Comprehensive Review of Experimental Parameters from 1989 to 2015. *Chem. Rev.* **2016**, *116*, 13234–13278.

(19) Oh, J.-M.; Chow, K.-F. Recent Developments in Electrochemical Paper-Based Analytical Devices. *Anal. Methods* **2015**, *7*, 7951–7960.

(20) Bard, A.; Faulkner, L., *Electrochemical Methods:Fundamentals and Applications*; John Wiley and Sons: New York, NY, 2015; Vol. 8.

(21) Sekretaryova, A.; Eriksson, M.; Turner, A. Bioelectrocatalytic Systems for Health Applications. *Biotechnol. Adv.* **2016**, *34*, 177–197.

(22) Lee, W.; Wahman, D.; Pressman, J. Monochloramine-Sensitive Amperometric Microelectrode: Optimization of Gold, Platinum, and Carbon Fiber Sensing Materials for Removal of Dissolved Oxygen Interference. *Ionicsl* **2015**, *21*, 2663–2674.

(23) Nassi, A.; Guillon, F.-X.; Amar, A.; Hainque, B.; Amriche, S.; Maugé, D.; Markova, E.; Tsé, C.; Bigey, P.; Lazerges, M.; Bedioui, F. Electrochemical DNA-Biosensors Based on Long-Range Electron Transfer: Optimization of the Amperometric Detection in the Femtomolar Range Using Two-Electrode Setup and Ultramicroelectrode. *Electrochim. Acta* **2016**, *209*, 269–277.

(24) Yang, C.; Trikantzopoulos, E.; Jacobs, C.; Venton, B. Evaluation of Carbon Nanotube Fiber Microelectrodes for Neurotransmitter Detection: Correlation of Electrochemical Performance and Surface Properties. *Anal. Chim. Acta* **2017**, *965*, 1–8.

(25) Zhang, L.; Wang, J.; Tian, Y. Electrochemical In-Vivo Sensors Using Nanomaterials Made from Carbon Species, Noble Metals, or Semiconductors. *Microchim. Acta* **2014**, *181*, 1471–1484.

(26) Dick, J.; Hilterbrand, A.; Boika, A.; Upton, J.; Bard, A. Electrochemical Detection of a Single Cytomegalovirus at an Ultramicroelectrode and Its Antibody Anchoring. *PNAS* **2015**, *112*, 5303–5308.

(27) Thuy, T.; Tseng, T. A Micro-Platinumwire Biosensor for Fast and Selective Detection of Alanine Aminotransferase. *Sensors* **2016**, *16*, 1–14.

(28) Rudolph, D.; Bates, D.; DiChristina, T.; Mizaikoff, B.; Kranz, C. Detection of Metal-Reducing Enzyme Complexes by Scanning Electrochemical Microscopy. *Electroanal.* **2016**, *28*, 2459–2465.

(29) Alligrant, T.; Dasari, R.; Stevenson, K.; Crooks, R. Electrocatalytic Amplification of Single Nanoparticle Collisions Using DNA-Modified Surfaces. *Langmuir* **2015**, *31*, 11724–11733.

(30) Castã Neda, A.; Robinson, D.; Stevenson, K.; Crooks, R. Electrocatalytic Amplification of DNA-Modified Nanoparticle Collisions via Enzymatic Digestion. *Chem. Sci.* **2016**, *7*, 6450–6457.

(31) Dumitrescu, E.; Wallace, K.; Andreescu, S. Real Time Electrochemical Investigation of the Release, Distribution and Modulation of Nitric Oxide in the Intestine of Individual Zebrafish Embryos. *Nitric Oxide* **2018**, *74*, 32–38.

(32) Hinzman, J.; Gibson, J.; Tackla, R.; Costello, M.; Burmeister, J.; Quintero, J.; Gerhardt, G.; Hartings, J. Real-Time Monitoring of Extracellular Adenosine Using Enzyme-Linked Microelectrode Arrays. *Biosens. Bioelectron.* **2015**, *74*, 512–517.

(33) Daniele, S.; Bragato, C., *From Macroelectrodes to Microelectrodes: Theory and Electrode Properties. In Environmental Analysis by Electrochemical Sensors and Biosensors*; Springer: New York, NY, 2014, pp 373–401.

(34) Molina, A.; Gonzalez, J.; Barnes, E.; Compton, R. Simple Analytical Equations for the Current-Potential Curves at Microelectrodes: A Universal Approach. *J. Phys. Chem. C* **2014**, *118*, 346–356.

(35) Danis, L.; Polcari, D.; Kwan, A.; Gateman, S.; Mauzeroll, J. Fabrication of Carbon, Gold, Platinum, Silver, and Mercury Ultramicroelectrodes with Controlled Geometry. *Anal. Chem.* **2015**, *87*, 2565–2569.

(36) Fangt, Y.; Leddy, J. Cyclic Voltammetric Responses for Inlaid Microdisks with Shields of Thickness Comparable to the Electrode Radius: A Simulation of Reversible Electrode Kinetics. *Anal. Chem.* **1995**, *67*, 1259–1270.

(37) Lefrou, C.; Cornut, R. Analytical Expressions for Quantitative Scanning Electrochemical Microscopy. *ChemPhysChem* **2010**, *11*, 547–556.

(38) Wahl, A.; Barry, S.; Dawson, K.; MacHale, J.; Quinn, A.; O'Riordan, A. Electroanalysis at Ultramicro and Nanoscale Electrodes: A Comparative Study. *J. Electrochem. Soc.* **2013**, *161*, 3055–3060.

(39) Ronkainen, N., Micro- and Nanoelectrodes in Protein-Based Electrochemical Biosensors for Nanomedicine and Other Applications In *Advanced Bioelectronic Materials*; John Wiley and Sons, Inc: Hoboken, NJ, USA, 2015, pp 1–34.

(40) Crespi, F. Hydrogen Peroxide Monitored in Vivo, in Situ and in Real Time in Rat Brain, Is It a Marker of Central Cholinergic Dynamics? *Anal. Methods* **2014**, *6*, 1174–1181.

(41) Wang, K.; Xiao, T.; Yue, Q.; Wu, F.; Yu, P.; Mao, L. Selective Amperometric Recording of Endogenous Ascorbate Secretion from a Single Rat Adrenal Chromaffin Cell with Pretreated Carbon Fiber Microelectrodes. *Anal. Chem* **2017**, *89*, 9502–9507.

(42) Xiang, L.; Yu, P.; Hao, J.; Zhang, M.; Zhu, L.; Dai, L.; Mao, L. Vertically Aligned Carbon Nanotube-Sheathed Carbon Fibers as Pristine Microelectrodes for Selective Monitoring of Ascorbate in Vivo. *Anal. Chem* **2014**, *86*, 3909–3914.

(43) Li, Z.; Fu, Y.; Fang, W.; Li, Y. Electrochemical Impedance Immunosensor Based on Self-Assembled Monolayers for Rapid Detection of Escherichia Coli O157:H7 with Signal Amplification Using Lectin. *Sensors* **2015**, *15*, 19212–19224.

(44) Ronspees, A.; Thorgaard, S. E. C. o. S. E.; B. Subtilis Bacteria at Ultramicroelectrodes Elucidated Using Simultaneous Fluorescence Microscopy. *Electrochim. Acta* **2018**, *278*, 412–420.

(45) Lee, J.; Kim, B.-K.; Kang, M.; Park, J. Label-Free Detection of Single Living Bacteria via Electrochemical Collision Event. *Sci. Rep.* **2016**, 1–10.

(46) Bao, H.; Zheng, Z.; Yang, B.; Liu, D.; Li, F.; Zhang, X.; Li, Z.; Lei, L. In Situ Monitoring of Shewanella Oneidensis MR-1 Biofilm Growth on Gold Electrodes by Using a Pt Microelectrode. *Bioelectrochem.* **2016**, *109*, 95–100.

(47) Brosel-Oliu, S.; Abramova, N.; Bratov, A.; Vigués, N.; Mas, J.; Muñoz, F.-X. Sensitivity and Response Time of Polyethyleneimine Modified Impedimetric Transducer for Bacteria Detection. *Electroanal.* **2015**, *27*, 656–662.

(48) Settu, K.; Chen, C.-J.; Liu, J.-T.; Chen, C.-L.; Tsai, J.-Z. Impedimetric Method for Measuring Ultra-Low E. Coli Concentrations in Human Urine. *Biosens. Bioelectron.* **2014**, *66*, 244–250.

(49) Etayash, H.; Jiang, K.; Thundat, T.; Kaur, K. Impedimetric Detection of Pathogenic Gram-Positive Bacteria Using an Antimicrobial Peptide from Class IIa Bacteriocins. *Anal. Chem* **2014**, *86*, 1693–1700.

(50) Jiang, L.; Santiago, I.; Foord, J. Observation of Nanoimpact Events of Catalase on Diamond Ultramicroelectrodes by Direct Electron Transfer. *Chem. Commun.* **2017**, *53*, 8332–8335.

(51) Dick, J. Electrochemical Detection of Single Cancer and Healthy Cell Collisions on a Microelectrode. *Chem. Commun.* **2016**, *52*, 10906–10909.

(52) Wang, J.; Dunevall, J.; Ewing, A. Spatial Resolution of Single-Cell Exocytosis by Microwell-Based Individually Addressable Thin Film Ultramicroelectrode Arrays. *Anal. Chem* **2014**, *86*, 4515–4520.

(53) Wang, L.; Xu, S.-W.; Xu, H.-R.; Song, Y.-L.; Liu, J.-T.; Luo, J.-P.; Cai, X.-X. Spatio-Temporally Resolved Measurement of Quantal Exocytosis from Single Cells Using Microelectrode Array Modified with Poly L-Lysine and Poly Dopamine. *Chinese Chem. Lett.* **2016**, *27*, 738–744.

(54) Study of the Union Method of Microelectrode Array and AFM for the Recording of Electromechanical Activities in Living Cardiomyocytes. *Eur. Biophys. J.* **2017**, *46*, 495–507.

(55) Wu, H.-C.; Lyau, J.-B.; Lin, M.-H.; Chuang, Y.-J.; Chen, H. Multilayer Microfluidic Systems with Indium-Tin-Oxide Microelectrodes for Studying Biological Cells. *J. M. M.* **2017**, *27*, 1–15.

(56) Abe, H.; Kanno, Y.; Ino, K.; Inoue, K.; Suda, A.; Kunikata, R.; Matsudaira, M.; Shiku, H.; Matsue, T. Electrochemical Imaging for Single-Cell Analysis of Cell Adhesion Using a Collagen-Coated Large-Scale Integration (LSI)-Based Amperometric Device. *Electrochem. Soc. Japan* **2016**, *84*, 364–367.

(57) Manning, B.; Meyer, A.; Gruba, S.; Haynes, C. Single-Cell Analysis of Mast Cell Degranulation Induced by Airway Smooth Muscle-Secreted Chemokines. *Biochim. Biophys. Acta* **2015**, *1850*, 1862–1868.

(58) Yu, X.; Kelley, T.; Chiel, H.; Burgess, J. Communication-Microelectrode Detection of Cholesterol Efflux from the Human Buccel Mucosa. *J. Electrochem. Soc.* **2016**, *163*, 453–455.

(59) Xu, H.; Zhou, S.; Jiang, D.; Chen, H.-Y. Cholesterol Oxidase/Triton X-100 Parked Microelectrodes for the Detection of Cholesterol in Plasma Membrane at Single Cells. *Anal. Chem* **2018**, *90*, 1054–1058.

(60) West, R.; Lu, H.; Shaw, K.; Chiel, H.; Kelley, T.; Burgess, J. Double Potential Pulse Chronocoulometry for Detection of Plasma Membrane Cholesterol Efflux at Disk Platinum Microelectrodes. *J. Electrochem. Soc.* **2014**, *161*, 111–116.

(61) Dick, J.; Renault, C.; Bard, A. Observation of Single-Protein and DNA Macromolecule Collisions on Ultramicroelectrodes. *J. Am. Chem. Soc.* **2015**, *137*, 8376–8379.

(62) Saheb, A.; Patterson, S.; Josowicz, M. Probing for DNA Methylation with a Voltammetric DNA Detector. *Analyst* **2014**, *139*, 786–792.

(63) Doğru, E.; Erhan, E.; Arikan, O. The Using Capacity of Carbon Fiber Microelectrodes in DNA Biosensors. *Electroanal.* **2017**, *29*, 287–293.

(64) Yang, C.; Jacobs, C.; Nguyen, M.; Ganesana, M.; Zestos, A.; Ivanov, I.; Puretzky, A.; Rouleau, C.; Geohegan, D.; Venton, B. Carbon Nanotubes Grown on Metal Microelectrodes for the Detection of Dopamine. *Anal. Chem.* **2016**, *88*, 645–652.

(65) Bergman, J.; Mellander, L.; Wang, Y.; Cans, A.-S. Co-Detection of Dopamine and Glucose with High Temporal Resolution. *Catalysts* **2018**, *8*, 1–10.

(66) Polcari, D.; Kwan, A.; Van Horn, M.; Danis, L.; Pollegioni, L.; Ruthazer, E.; Mauzeroll, J. Disk-Shaped Amperometric Enzymatic Biosensor for in Vivo Detection of D-Serine. *Anal. Chem.* **2014**, *86*, 3501–3507.

(67) Polcari, D.; Perry, S.; Pollegioni, L.; Geissler, M.; Mauzeroll, J. Localized Detection of D-Serine by Using an Enzymatic Amperometric Biosensor and Scanning Electrochemical Microscopy. *ChemElectroChem* **2017**, *4*, 920–926.

(68) Tseng, T.-C.; Gusviputri, A.; Hoa, L. Sensitive and Compact Electrochemical ELISA for Estradiol Based on Chitosan Deposited Platinum Wire Microelectrodes. *J. Electroanal. Chem.* **2015**, *758*, 59–67.

(69) Tedjo, W.; Nejad, J.; Feeny, R.; Yang, L.; Henry, C.; Tobet, S.; Chen, T. Electrochemical Biosensor System Using a CMOS Microelectrode Array Provides High Spatially and Temporally Resolved Images. *Biosens. Bioelectron.* **2018**, *114*, 78–88.

(70) Hermann, D.; Amsterdam, C. Analysis of Spontaneous Hippocampal Activity Allows Sensitive Detection of Acetylcholine-Mediated Effects. *J. Pharmacol. Toxicol. Meth.* **2015**, *71*, 54–60.

(71) Vasylieva, N.; Maucler, C.; Meiller, A.; Viscogliosi, H.; Lieutaud, T.; Barbier, D.; Marinesco, S. Immobilization Method to Preserve Enzyme Specificity in Biosensors: Consequences for Brain Glutamate Detection. *Anal. Chem* **2013**, *85*, 2507–2515.

(72) Donahue, C.; Miller, D.; Beger, T.; Johann, T.; Keithley, R. Improved Formation of Electrically-Deposited Enzyme-Embedded Chitosan Coatings onto Carbon Fiber Microelectrodes. *Anal. Methods* **2018**, *10*, 1565–1567.

(73) Soldà, A.; Valenti, G.; Marcaccio, M.; Giorgio, M.; Pelicci, P.; Paolucci, F.; Rapino, S. Glucose and Lactate Miniaturized Biosensors for SECM-Based High-Spatial Resolution Analysis: A Comparative Study. *ACS Sensors* **2017**, *2*, 1310–1318.

(74) Burmeister, J.; Davis, V.; Quintero, J.; Pomerleau, F.; Huettl, P.; Gerhardt, G. Glutaraldehyde Cross-Linked Glutamate Oxidase Coated Microelectrode Arrays: Selectivity and Resting Levels of Glutamate in the CNS. *ACS Chem. Neurosci.* **2013**, *4*, 721–728.

(75) Tolosa, V.; Wassum, K.; Maidment, N.; Monbouquette, H. Electrochemically Deposited Iridium Oxide Reference Electrode Integrated with an Electroenzymatic Glutamate Sensor on a Multi-Electrode Array Microprobe. *Biosens. Bioelectron.* **2013**, *42*, 256–260.

(76) Li, Z.; Song, Y.; Xiao, G.; Gao, F.; Xu, S.; Wang, M.; Zhang, Y.; Guo, F.; Liu, J.; Xia, Y.; Cai, X. Bio-Electrochemical Microelectrode Arrays for Glutamate and Electrophysiology Detection in Hippocampus of Temporal Lobe Epileptic Rats. *Anal. Biochem.* **2018**, *550*, 123–131.

(77) Xiao, C.; Liu, Y.-L.; Xu, J.-Q.; Lv, S.-W.; Guo, S.; Huang, W.-H. Real-Time Monitoring of H_2O_2 Release from Single Cells Using Nanoporous Gold Microelectrodes Decorated with Platinum Nanoparticles. *Analyst* **2015**, *140*, 3753–3758.

(78) Ehsan Salamifar, S.; Lee, S.; Lai, R. Electrochemical Hydrogen Peroxide Sensors Fabricated Using Cytochrome c Immobilized on Macroelectrodes and Ultramicroelectrodes. *Col. Surf. B Biointerfaces* **2014**, *123*, 866–869.

(79) Ben-Amor, S.; Vanhove, E.; Sékli Belaïdi, F.; Charlot, S.; Colin, D.; Rigoulet, M.; Devin, A.; Sojic, N.; Launay, J.; Temple-Boyer, P.; Arbault, S. Enhanced Detection of Hydrogen Peroxide with Platinized Microelectrode Arrays for Analyses of Mitochondria Activities. *Electrochim. Acta* **2014**, *126*, 171–178.

(80) Radulescu, M.-C.; Bucur, M.-P.; Alecu, A.; Bucur, B.; Radu, G. Electrochemical Determination of Hydrogen Peroxide Using a Prussian Blue-Copper Modified Platinum Microelectrode. *Anal. Lett.* **2016**, *49*, 2006–2017.

(81) Lu, L.; Liang, L.; Xie, Y.; Tang, K.; Wan, Z.; Chen, S. A Nickel Nanoparticle/Carbon Nanotube-Modified Carbon Fiber Microelectrode for Sensitive Insulin Detection. *J. Solid State Electrochem.* **2018**, *22*, 825–833.

(82) Castañ Eda, A.; Brenes, N.; Kondajji, A.; Crooks, R. Detection of MicroRNA by Electrocatalytic Amplification: A General Approach for Single-Particle Biosensing. *J. Am. Chem. Soc.* **2017**, *139*, 7657–7664.

(83) Kim, J.-H.; Kang, G.; Nam, Y. Electrochemical Layer-by-Layer Approach to Fabricate Mechanically Stable Platinum Black Microelectrodes Using a Mussel-Inspired Polydopamine Adhesive. *J. Neural Eng.* **2015**, *12*, 1–10.

(84) Collaert, N.; Mora Lopez, C.; Cott, D.; Cools, J.; Braeken, D.; De Volder, M. In Vitro Recording of Neural Activity Using Carbon Nanosheet Microelectrodes. *Carbon N. Y* **2014**, *67*, 178–184.

(85) Napoli, A.; Obeid, I. Comparative Analysis of Human and Rodent Brain Primary Neuronal Culture Spontaneous Activity Using Micro-Electrode Array Technology. *J. Cell. Biochem.* **2016**, *117*, 559–565.

(86) Charkhkar, H.; Meyyappan, S.; Matveeva, E.; Moll, J.; Mchail, D.; Peixoto, N.; Cliff, R.; Pancrazio, J. Amyloid Beta Modulation of Neuronal Network Activity In Vitro. *Brain Res.* **2015**, 1–9.

(87) Koutsouras, D.; Hama, A.; Pas, J.; Gkoupidenis, P.; Hivert, B.; Faivre-Sarrailh, C.; Di Pasquale, E.; Owens, R.; Malliaras, G. PEDOT:PSS Microelectrode Arrays for Hippocampal Cell Culture Electrophysiological Recordings. *MRS. Commun.* **2017**, *7*, 259–265.

(88) Nguyen, A.; Mattiassi, S.; Loeblein, M. Biocompatibility of Nanostructured Boron Doped Diamond for the Attachment and Proliferation of Human Neural Stem Cells. *J. Neural Eng.* **2015**, *12*, 1–12.

(89) Xiang, L.; Yu, P.; Zhang, M.; Hao, J.; Wang, Y.; Zhu, L.; Dai, L.; Mao, L. Platinized Aligned Carbon Nanotube-Sheathed Carbon Fiber Microelectrodes for In Vivo Amperometric Monitoring of Oxygen. *Anal. Chem.* **2014**, *86*, 5017–5023.

(90) Kagawa, Y.; Matsuura, K.; Shimizu, T.; Tsuneda, S. Direct Measurement of Local Dissolved Oxygen Concentration Spatial Profiles in a Cell Culture Environment. *Biotechnol. Bioeng.* **2015**, *112*, 1263–1274.

(91) Li, Y.; Meunier, A.; Fulcrand, R.; Sella, C.; Amatore, C.; Thouin, L.; Lemaître, F.; Guille-Collignon, M. Multi-Chambers Microsystem for Simultaneous and Direct Electrochemical Detection of Reactive Oxygen and Nitrogen Species Released by Cell Populations. *Electroanal.* **2016**, *28*, 1865–1872.

(92) Lu, C.; Heldt, J.-M.; Guille-Collignon, M.; Lemaître, F.; Jaouen, G.; Vessières, A.; Amatore, C. Quantitative Analyses of ROS and RNS Production in Breast Cancer Cell Lines Incubated with Ferrocifens. *ChemMedChem* **2014**, *9*, 1286–1293.

(93) Thi Kim, L.; Escriou, V.; Griveau, S.; Girard, A.; Griscom, L.; Razan, F.; Bedioui, F. Array of Ultramicroelectrodes for the Simultaneous Detection of Nitric Oxide and Peroxynitrite in Biological Systems. *Electrochim. Acta* **2014**, *140*, 33–36.

(94) Gómez-Mingot, M.; Griveau, S.; Bedioui, F.; Banks, C.; Montiel, V.; Iniesta, J. Electrochemical Devices for Monitoring Biomarkers in Embryo Development. *Electrochim. Acta* **2014**, *140*, 42–48.

(95) Dumitrescu, E.; Wallace, K.; Andreescu, S. Real Time Electrochemical Investigation of the Release, Distribution and Modulation of Nitric Oxide in the Intestine of Individual Zebrafish Embryos. *Nitric Oxide* **2018**, *74*, 32–38.

(96) Ramirez-Garcia, G.; Martinez-Alfaro, M.; Gutierrez-Granados, S.; Alatorre-Ordaz, A.; Griveau, S.; Bedioui, F. Electrochemical Assessment of Possible Melatonin Effect On Nitric Oxide Production From Kidneys Of Sub-Acute Lead Treated Rats. *Electrochim. Acta* **2015**, *166*, 88–92.

(97) Elliott, J.; Duay, J.; Simoska, O.; Shear, J.; Stevenson, K. Gold Nanoparticle Modified Transparent Carbon Ultramicroelectrode Arrays for the Selective and Sensitive Electroanalytical Detection of Nitric Oxide. *Anal. Chem.* **2017**, *89*, 1267–1274.

(98) Kongsuphol, P.; Ng, H.; Pursey, J.; Arya, S.; Wong, C.; Stulz, E.; Park, M. EIS-Based Biosensor for Ultra-Sensitive Detection of TNF- from Non-Diluted Human Serum. *Biosens. Bioelectron.* **2014**, *61*, 274–279.

(99) Sepunaru, L.; Plowman, B.; Sokolov, S.; Young, N.; Compton, R. Rapid Electrochemical Detection of Single Influenza Viruses Tagged with Silver Nanoparticles. *Chem. Rev.* **2016**, *7*, 3892–3899.

(100) Lin, J.; Wang, R.; Jiao, P.; Li, Y.; Li, Y.; Liao, M.; Yu, Y.; Wang, M. An Impedance Immunosensor Based on Low-Cost Microelectrodes and Specific Monoclonal Antibodies for Rapid Detection of Avian Influenza Virus H5N1 in Chicken Swabs. *Biosens. Bioelectron.* **2015**, *67*, 546–552.

(101) Elgrishi, N.; Rountree, K.; Mccarthy, B.; Rountree, E.; Eisenhart, T.; Dempsey, J. A Practical Beginner's Guide to Cyclic Voltammetry. *J. Chem. Ed.* **2018**, *95*, 197–206.

(102) Baudler, A.; Schmidt, I.; Langner, M.; Greiner, A.; Schröder, U. Does It Have to Be Carbon? Metal Anodes in Microbial Fuel Cells and Related Bioelectrochemical Systems. *Energy Environ. Sci.* **2015**, *8*, 2048–2055.

(103) Pancrazio, J.; Deku, F.; Ghazavi, A.; Stiller, A.; Rihani, R.; Frewin, C.; Varner, V.; Gardner, T.; Cogan, S. Thinking Small: Progress on Microscale Neurostimulation Technology. *Neuromodulation Technol. Neural Interface* **2017**, *20*, 745–752.

(104) Wang, G.; Yang, J.; Park, J.; Gou, X.; Wang, B.; Liu, H.; Yao, J. Facile Synthesis and Characterization of Graphene Nanosheets. *J. Phys. Chem. C* **2008**, *112*, 8192–8195.

(105) Zhang, W.; Zhu, S.; Luque, R.; Han, S.; Hu, L.; Xu, G. Recent Development of Carbon Electrode Materials and Their Bioanalytical and Environmental Applications. *Chem. Soc. Rev.* **2016**, *45*, 715–752.

(106) Jorfi, M.; Skousen, J.; Weder, C. Electroactive Biocompatible Materials for Nerve Cell Stimulation. *Mater. Res. Express* **2015**, *2*, 1–10.

(107) Mirzaei, M.; Sawan, M. Microelectronics-Based Biosensors Dedicated to the Detection of Neurotransmitters: A Review. *Sensors* **2014**, *14*, 17981–18008.

(108) Bucher, E.; Wightman, R. Electrochemical Analysis of Neurotransmitters. *Annu. Rev. Anal. Chem.* **2015**, *8*, 239–261.

(109) Park, J.; Quaiserová-Mocko, V.; Patel, B.; Novotný, M.; Liu, A.; Bian, X.; Galligan, J.; Swain, G. Diamond Microelectrodes for In Vitro Electroanalytical Measurements: Current Status and Remaining Challenges. *Analyst* **2008**, *133*, 17–24.

(110) Ruan, J.; Zhang, W.; Zhang, H.; Chen, Y.; Rehman, F.; Jiang, H.; Strehle, S.; Pasquarelli, A.; Wang, X. Highly Sensitive Electrochemical Detection of Living Cells Based on Diamond Microelectrode Arrays. *Chinese Chem. Lett.* **2018**, *29*, 919–921.

(111) Hébert, C.; Warnking, J.; Depaulis, A.; Garçon, L.; Mermoux, M.; Eon, D.; Mailley, P.; Omnès, F. Characterization and in Vivo MRI Compatibility of Diamond Microelectrodes Array for Neural Interfacing. *Mater. Sci. Eng. C* **2015**, *46*, 25–31.

(112) Cobb, S.; Ayres, Z.; Macpherson, J. Boron Doped Diamond: A Designer Electrode Material for the Twenty-First Century. *Annu. Rev. Anal. Chem.* **2018**, *11*, 463–484.

(113) Nguyen, A.; Mattiassi, S.; Loeblein, M. Biocompatibility of Nanostructured Boron Doped Diamond for the Attachment and Proliferation of Human Neural Stem Cells. *J. Neural Eng* **2015**, *2*, 1–12.

(114) Stevenson, K.; Tschulik, K. A Materials Driven Approach for Understanding Single Entity Nano Impact Electrochemistry. *Curr. Opin. Electrochem* **2017**, *6*, 38–45.

(115) Gunderson, C.; Zhang, B. Massive Electrochemical Arrays of Uniform Ultramicroelectrodes. *J. Electroanal. Chem.* **2016**, *781*, 174–180.

(116) Maerten, C.; Jierry, L.; Schaaf, P.; Boulmedais, F. Review of Electrochemically Triggered Macromolecular Film Buildup Processes and Their Biomedical Applications. *ACS Appl. Mater. Interfaces* **2017**, *9*, 28117–28138.

(117) Kamaraj, A.; Murali, S.; M., M.; R. Ultra High Aspect Ratio Penetrating Metal Microelectrodes for Biomedical Applications. *Microsyst. Technol* **2013**, *19*, 179–186.

(118) Nick, C.; Quednau, S.; Sarwar, R.; Schlaak, H.; Thielemann, C. High Aspect Ratio Gold Nanopillars on Microelectrodes for Neural Interfaces. *Microsyst. Technol.* **2014**, *20*, 1849–1857.

(119) Mirzaei, M.; Sawan, M. Microelectronics-Based Biosensors Dedicated to the Detection of Neurotransmitters: A Review. *Sensors* **2014**, *14*, 17981–18008.

(120) Cui, H.; Wu, J.; Eda, S.; Chen, J.; Chen, W.; Zheng, L. Rapid Capacitive Detection of Femtomolar Levels of Bisphenol A Using an Aptamer-Modified Disposable Microelectrode Array. *Microchim. Acta* **2015**, *182*, 2361–2367.

(121) Jorfi, M.; Skousen, J.; Weder, C. Electroactive Biocompatible Materials for Nerve Cell Stimulation Related Content Modification of Surface/Neuron Interfaces for Neural Cell-Type Specific Responses. *Mater. Res. Express* **2015**, *2*, 1–10.

(122) Xiang, L.; Yu, P.; Hao, J.; Zhang, M.; Zhu, L.; Dai, L.; Mao, L. Vertically Aligned Carbon Nanotube-Sheathed Carbon Fibers as Pristine Microelectrodes for Selective Monitoring of Ascorbate In Vivo. *Anal. Chem.* **2014**, *86*, 3909–3914.

(123) Ates, M. A Review Study of (Bio)Sensor Systems Based on Conducting Polymers. *Mater. Sci. Eng. C* **2013**, *33*, 1853–1859.

(124) Castañ Eda, A.; Alligrant, T.; Loussaert, J.; Crooks, R. Electrocatalytic Amplification of Nanoparticle Collisions at Electrodes Modified with Polyelectrolyte Multilayer Films. *Langmuir* **2015**, *31*, 876–885.

(125) Choi, S.; Choi, J.; Kim, Y.; Kim, S.; Dwivedi, P.; Sharma, A.; Goel, S.; Kim, G. Enzyme Immobilization on Microelectrode Arrays of CNT/Nafion Nanocomposites Fabricated Using Hydrogel Microstencils. *Microelectron. Eng* **2015**, *141*, 193–197.

(126) Pribil, M.; Cortés-Salazar, F.; Andreyev, E.; Lesch, A.; Karyakina, E.; Voronin, O.; Girault, H.; Karyakin, A. Rapid Optimization of a Lactate Biosensor Design Using Soft Probes Scanning Electrochemical Microscopy. *J. Electroanal. Chem* **2014**, *731*, 112–118.

(127) Donahue, C.; Miller, D.; Beger, T.; Johann, T.; Keithley, R. Improved Formation of Electrically-Deposited Enzyme-Embedded Chitosan Coatings onto Carbon Fiber Microelectrodes. *Anal. Methods* **2018**, *10*, 1565–1576.

(128) Li, L.; Lu, B.; Jiang, D.; Shin, M.; Kelley, T.; Burgess, J. Review Article Cell Plasma Membrane Cholesterol as a Diagnostic. *Curr. Opin. Electrochem.* **2017**, *2*, 82–87.

(129) Lvarez-Martos, I.; Ferapontova, E. Electrochemical Label-Free Aptasensor for Specific Analysis of Dopamine in Serum in the Presence of Structurally Related Neurotransmitters. *Anal. Chem* **2016**, *88*, 3608–3616.

(130) Doğru, E.; Erhan, E.; Arikan, O. A Recent Approach for Monitoring Interactions Between Methylene Blue and DNA Using Carbon Fiber Based DNA Biosensor. *Int. J. Electrochem. Sci.* **2016**, *11*, 829–839.

(131) Xu, Q.-C.; Zhang, Q.-Q.; Sun, X.; Guo, Y.-M.; Wang, X.-Y. Aptasensors Modified by Antimony Tin Oxide Nanoparticle-Chitosan Based on Interdigitated Array Microelectrodes for Tetracycline Detection. *RSC Adv.* **2016**, *6*, 17328–17335.

(132) Lin, J.; Xin, Q.; Gao, X. Real-Time Detection of Hydrogen Peroxide Using Microelectrodes in an Ultrasonic Enhanced Heterogeneous Fenton Process Catalyzed by Ferrocene. *Environ. Sci. Pollut. Res.* **2015**, *22*, 11170–11174.

(133) Clark, L.; Lyons, C. Electrode Systems for Continuous Monitoring in Cardiovascular Surgery. *Ann. N. Y. Acad. Sci.* **1962**, *102*, 29–45.

(134) Datta, S.; Christena, L.; Rajaram, Y. Enzyme Immobilization: An Overview on Techniques and Support Materials. *3 Biotech.* **2013**, *3*, 1–9.

(135) Polcari, D.; Perry, S.; Pollegioni, L.; Geissler, M.; Mauzeroll, J. Localized Detection of Dfi-Serine by Using an Enzymatic Amperometric Biosensor and Scanning Electrochemical Microscopy. *ChemElectroChem* **2017**, *4*, 920–926.

(136) Hamdan, S.; A, M. Z. In Vivo Electrochemical Biosensor for Brain Glutamate Detection: A Mini Review. *Malays. J. Med. Sci.* **2014**, *21*, 12–26.

(137) Mathwig, K.; Albrecht, T.; Goluch, E.; Rassaei, L. Challenges of Biomolecular Detection at the Nanoscale: Nanopores and Microelectrodes. *Anal. Chem* **2015**, *87*, 5470–5475.

(138) Hébert, C.; Scorsone, E.; Bendali, A.; Kiran, R.; Cottance, M.; Girard, H.; Degardin, J.; Dubus, E.; Lissorgues, G.; Rousseau, L.; Mailley, P.; Picaud, S.; Bergonzo, P. Boron Doped Diamond Biotechnology: From Sensors to Neurointerfaces. *Faraday Discuss.* **2014**, *172*, 47–59.

(139) Cell Specific Electrodes for Neuronal Network Reconstruction and Monitoring. *Analyst* **2014**, *139*, 3191–3482.

(140) Tsopela, A.; Lale, A.; Vanhove, E.; Reynes, O.; Séguy, I.; Temple-Boyer, P.; Juneau, P.; Izquierdo, R.; Launay, J. Integrated Electrochemical Biosensor Based on Algal Metabolism for Water Toxicity Analysis. *Biosens. Bioelectron.* **2014**, *61*, 290–297.

(141) Tian, H.-C.; Liu, J.-Q.; Kang, X.-Y.; Tang, L.-J.; Wang, M.-H.; Ji, B.-W.; Yang, B.; Wang, X.-L.; Chen, X.; Yang, C.-S. Enhanced Flexible Tubular Microelectrode with Conducting Polymer for Multi-Functional Implantable Tissue-Machine Interface. *Sci. Rep.* **2016**, *6*, 1–10.

(142) Fekete, Z. Recent Advances in Silicon-Based Neural Microelectrodes and Microsystems: A Review. *Sens. Actuat. B* **2015**, *215*, 300–315.

(143) Xu, Y.; Xie, X.; Duan, Y.; Wang, L.; Cheng, Z.; Cheng, J. A Review of Impedance Measurements of Whole Cells. *Biosens. Bioelectron.* **2017**, *77*, 824–836.

(144) Monaco, A.; Giugliano, M. Carbon-Based Smart Nanomaterials in Biomedicine and Neuroengineering. *Beilstein J. Nanotechnol.* **2014**, *5*, 1849–1863.

(145) Lee, J.; Kim, H.; Hun, J.; Ac, K.; Lee, S.-H. From Chip-in-a-Lab to Lab-on-a-Chip: Towards a Single Handheld Electronic System for Multiple Application-Specific Lab-on-a-Chip (ASLOC. *Lab Chip* **2016**, *16*, 2168–2176.

(146) Hébert, C.; Warnking, J.; Depaulis, A.; Garçon, L.; Mermoux, M.; Eon, D.; Mailley, P.; Omnès, F. Characterization and in Vivo MRI Compatibility of Diamond Microelectrodes Array for Neural Interfacing. *Mater. Sci. Eng. C* **2015**, *46*, 25–31.

(147) Xiang, L.; Yu, P.; Zhang, M.; Hao, J.; Wang, Y.; Zhu, L.; Dai, L.; Mao, L. Platinized Aligned Carbon Nanotube-Sheathed Carbon Fiber Microelectrodes for In Vivo Amperometric Monitoring of Oxygen. *Anal. Chem.* **2014**, *86*, 5017–5023.

(148) Lima, A.; Luz, G.; Batista, N.; Longo, E.; Cavalcante, L.; Santos, R. Determination of Ethambutol in Aqueous Medium Using an Inexpensive Gold Microelectrode Array as Amperometric Sensor. *Electroanal.* **2016**, *28*, 985–989.

(149) Das, D.; Ahmad Kamil, F.; Biswas, K.; Das, S. Evaluation of Single Cell Electrical Parameters from Bioimpedance of a Cell Suspension. *RSC Adv.* **2014**, *4*, 181–188.

(150) Anh-Nguyen, T.; Tiberius, B.; Pliquett, U.; Urban, G. An Impedance Biosensor for Monitoring Cancer Cell Attachment, Spreading and Drug-Induced Apoptosis. *Sens. Actuat. A* **2016**, *241*, 231–237.

(151) Lei, K. Review on Impedance Detection of Cellular Responses in Micro/Nano Environment. *Micromachines* **2014**, *5*, 1–12.

(152) Peng, Y.; Qian, R.; Hafez, M.; Long, Y. Stochastic Collision Nanoelectrochemistry: A Review of Recent Developments. *ChemElectroChem* **2017**, *4*, 977–985.

(153) Kranz, C. Recent Advancements in Nanoelectrodes and Nanopipettes Used in Combined Scanning Electrochemical Microscopy Techniques. *Analyst* **2014**, *139*, 336–352.

(154) Rasouli, E.; Shahnavaz, Z.; Basirun, W.; Rezayi, M.; Avan, A.; Ghayour-Mobarhan, M.; Khandanlou, R.; Johan, M. Advancements in Electrochemical DNA Sensor for Detection of Human Papilloma Virus - A Review. *Anal. Biochem.* **2018**, *556*, 136–144.

(155) Weltin, A.; Kieninger, J.; Enderle, B.; Gellner, A.-K.; Fritsch, B.; Urban, G.-B. Flexible Glutamate and Lactate Microsensors for in Vivo Applications. *Biosens. Bioelectron.* **2014**, *61*, 192–199.

(156) Ren, J.; Zhou, Y.; Zhou, Y.; Zhou, C.; Li, Z.; Lin, Q.; Huang, H. A Piezoelectric Microelectrode Arrays System for Real-Time Monitoring of Bacterial Contamination in Fresh Milk. *Food Bioprocess. Technol.* **2015**, *8*, 228–237.

(157) Xu, H.; Zhou, S.; Jiang, D.; Chen, H.-Y. Cholesterol Oxidase/Triton X-100 Parked Microelectrodes for the Detection of Cholesterol in Plasma Membrane at Single Cells. *Anal. Chem.* **2018**, *90*, 1054–1058.

(158) Dick, J.; Hilterbrand, A.; Strawsine, L.; Upton, J.; Bard, A. Enzymatically Enhanced Collisions on Ultramicroelectrodes for Specific and Rapid Detection of Individual Viruses. *PNAS* **2016**, *113*, 6403–6408.

(159) Rodeberg, N.; Sandberg, S.; Johnson, J.; Phillips, M.; E., P.; Mark Wightman, R. Hitchhiker's Guide to Voltammetry: Acute and Chronic Electrodes for in Vivo Fast-Scan Cyclic Voltammetry. *ACS Chem. Neurosci.* **2017**, *8*, 221–234.

(160) E, S.; Miller, T.; Macpherson, J.; Unwin, P. Controlled Functionalisation of Single-Walled Carbon Nanotube Network Electrodes for the Enhanced Voltammetric Detection of Dopamine. *Phys. Chem. Chem. Phys.*, *2639, 17*, 26394–26402.

(161) Rees, H.; Anderson, S.; Privman, E.; Bau, H.; Venton, B. Carbon Nanopipette Electrodes for Dopamine Detection in Drosophila. *Anal. Chem.* **2015**, *87*, 3849–3855.

(162) E, S.; Miller, T.; Macpherson, J.; Unwin, P. Controlled Functionalisation of Single-Walled Carbon Nanotube Network Electrodes for the Enhanced Voltammetric Detection of Dopamine. *Phys. Chem. Chem. Phys.* **2015**, *17*, 26394–26402.

(163) Jaquins-Gerstl, A.; Michael, A. A Review of the Effects of FSCV and Microdialysis Measurements on Dopamine Release in the Surrounding Tissue. *Analyst* **2015**, 3696–3708.

(164) Strakosas, X.; Wei, B.; Martin, D.; Owens, R. Biofunctionalization of Polydioxythiophene Derivatives for Biomedical Applications. *J. Mater. Chem. B* **2016**, *4*, 4952–4968.

(165) Weltin, A.; Kieninger, J.; Urban, G.; Amperometric Enzyme-Based Biosensors for In Vivo Applications. *Anal. Bioanal. Chem.* **2016**, *408*, 4503–4521.

(166) Bryan, N.; Grisham, M. Methods to Detect Nitric Oxide and Its Metabolites in Biological Samples. *Free Radic. Biol. Med* **2007**, *43*, 645–657.

(167) Koseoglu, S.; Love, S.; Haynes, C. Cholesterol Effects on Vesicle Pools in Chromaffin Cells Revealed by Carbon-Fiber Microelectrode Amperometry. *Anal. Bioanal. Chem.* **2011**, *400*, 2963–2971.

(168) Devadoss, A.; Burgess, J. Steady-State Detection of Cholesterol Contained in the Plasma Membrane of a Single Cell Using Lipid Bilayer-Modified Microelectrodes Incorporating Cholesterol Oxidase. *J. Am. Chem. Soc.* **2004**, *126*, 10214–10215.

(169) Sinner, A.; Offenhäusser, A. The Electrical Characterization of Supported Phospholipid Bilayers Using Titanium/Titanium Oxide Microelectrodes. *Thin Solid Films* **1998**, 327–329, 758–761.

(170) Xu, H.; Zhou, S.; Jiang, D.; Chen, H.-Y. Cholesterol Oxidase/Triton X-100 Parked Microelectrodes for the Detection of Cholesterol in Plasma Membrane at Single Cells. *Anal. Chem.* **2017**, *90*, 1054–1058.

(171) Wang, K.; Xiao, T.; Yue, Q.; Wu, F.; Yu, P.; Mao, L. Selective Amperometric Recording of Endogenous Ascorbate Secretion from a Single Rat Adrenal Chromaffin Cell with Pretreated Carbon Fiber Microelectrodes. *Anal. Chem.* **2017**, *89*, 9502–9507.

(172) Kaushik, A.; Vasudev, A.; Arya, S.; Pasha, S.; Bhansali, S. Recent Advances in Cortisol Sensing Technologies for Point-of-Care Application. *Biosens. Bioelectron.* **2014**, *53*, 499–512.

(173) Kenausis, G.; Chen, Q.; Heller, A. Electrochemical Glucose and Lactate Sensors Based on "Wired" Thermostable Soybean Peroxidase Operating Continuously and Stably at 37 °C. *Anal. Chem.* **1997**, *69*, 1054–1060.

(174) Giulbault, G.; Lubrano, G. An Enzyme Electrode for the Amperometric Determination of Glucose. *Analytica Chim. Acta* **1973**, *64*, 439–455.

(175) Ul Hasan, K.; Asif, M.; Hassan, M.; Sandberg, M.; Nur, O.; Willander, M.; Fagerholm, S.; Strålfors, P. A Miniature Graphene-Based Biosensor for Intracellular Glucose Measurements. *Electrochim. Acta* **2015**, *174*, 574–580.

(176) Lo, A.; Guibal, P.; Doummar, D.; Rodriguez, D.; Hautem, J.-Y.; Couderc, R.; Billette De Villemeur, T.; Roze, E.; Chaminade, P.; Moussa, F. Single-Step Rapid Diagnosis of Dopamine and Serotonin Metabolism Disorders. *ACS Omega* **2017**, *2*, 5962–5972.

(177) Hows, M.; Lacroix, L.; Heidbreder, C.; Organ, A.; Shah, A. High-Performance Liquid Chromatography/Tandem Mass Spectrometric Assay for the Simultaneous Measurement of Dopamine, Norepinephrine, 5-Hydroxytryptamine and Cocaine in Biological Samples. *J. Neurosci. Methods* **2004**, *138*, 123–132.

(178) Ho, T.; Guillon, F.-X.; Bigey, P.; Bedioui, F.; Lazerges, M. Analysis of the Evolution of the Detection Limits of Electrochemical Nucleic Acid Biosensors II. *Anal. Bioanal. Chem* **2017**, *409*, 4335–4352.

(179) Wang, L.; Wu, A.; Wei, G. Graphene-Based Aptasensors: From Molecule-Interface Interactions to Sensor Design and Biomedical Diagnostics. *Analyst* **2018**, *143*, 526–1543.

(180) Tian, L.; Qi, J.; Ma, X.; Wang, X.; Yao, C.; Song, W.; Wang, Y. A Facile DNA Strand Displacement Reaction Sensing Strategy of Electrochemical Biosensor Based on N-Carboxymethyl Chitosan/-Molybdenum Carbide Nanocomposite for MicroRNA-21 Detection. *Biosens. Bioelectron.* **2018**, *122*, 43–50.

(181) Teengam, P.; Siangproh, W.; Tuantranont, A.; Vilaivan, T.; Chailapakul, O.; Henry, C. Electrochemical Impedance-Based DNA Sensor Using Pyrrolidinyl Peptide Nucleic Acids for Tuberculosis Detection. *Anal. Chim. Acta* **2018**, *1044*, 102–109.

(182) Sani, N.; Heng, L.; Marugan, R.; Rajab, N. Electrochemical DNA Biosensor for Potential Carcinogen Detection in Food Samples. *Food Chem* **2018**, *269*, 503–510.

(183) Nazari-Vanani, R.; Sattarahmady, N.; Yadegari, H.; Delshadi, N.; Hatam, G.; Heli, H. Electrochemical Quantitation of Leishmania Infantum Based on Detection of Its KDNA Genome and Transduction of Non-Spherical Gold Nanoparticles. *Anal. Chim. Acta* **2018**, *1041*, 40–49.

(184) Yang, Y.; Fu, Y.; Su, H.; Mao, L.; Chen, M. Sensitive Detection of MCF-7 Human Breast Cancer Cells by Using a Novel DNA-Labeled Sandwich Electrochemical Biosensor. Biosens. *Bioelectron.* **2018**, *122*, 175–182.

(185) Saheb, A.; Patterson, S.; Josowicz, M. Probing for DNA Methylation with a Voltammetric DNA Detector. *Analyst* **2014**, *139*, 786–792.

(186) Bao, H.; Zheng, Z.; Yang, B.; Liu, D.; Li, F.; Zhang, X.; Li, Z.; Lei, L. In Situ Monitoring of Shewanella Oneidensis MR-1 Biofilm Growth on Gold Electrodes by Using a Pt Microelectrode. *Biochem.* **2016**, *109*, 95–100.

(187) Etayash, H.; Jiang, K.; Thundat, T.; Kaur, K. Impedimetric Detection of Pathogenic Gram-Positive Bacteria Using an Antimicrobial Peptide from Class IIa Bacteriocins. *Anal. Chem.* **2014**, *86*, 1693–1700.

(188) Santos, G.; Melo, A.; Crespilho, F. Magnetically Controlled Single-Nanoparticle Detection via Particle–electrode Collisions. *Phys. Chem. Chem. Phys.* **2014**, *16*, 8012–8018.

(189) Alligrant, T.; Anderson, M.; Dasari, R.; Stevenson, K.; Crooks, R. Single Nanoparticle Collisions at Microfluidic Microband Electrodes: The Effect of Electrode Material and Mass Transfer. *Langmuir* **2014**, *30*, 13462–13469.

(190) Stuart, E.; Tschulik, K.; Batchelor-Mcauley, C.; Compton, R. Electrochemical Observation of Single Collision Events: Fullerene Nanoparticles. *ACS Nano* **2014**, *8*, 7648–7654.

(191) Sepunaru, L.; Plowman, B.; Sokolov, S.; Young, N.; Compton, R. Rapid Electrochemical Detection of Single Influenza Viruses Tagged with Silver Nanoparticles. *Chem. Sci.* **2016**, *7*, 3892–3899.

(192) Lee, J.; Kim, B.-K.; Kang, M.; Park, J. Label-Free Detection of Single Living Bacteria via Electrochemical Collision Event. *Sci. Rep.* **2016**, *6*, 1–10.

(193) Alligrant, T.; Dasari, R.; Stevenson, K.; Crooks, R. Electrocatalytic Amplification of Single Nanoparticle Collisions Using DNA-Modified Surfaces. *Langmuir* **2015**, *31*, 11724–11733.

(194) Castã Neda, A.; Robinson, D.; Stevenson, K.; Crooks, R. Electrocatalytic Amplification of DNA-Modified Nanoparticle Collisions via Enzymatic Digestion. *Chem. Sci.* **2016**, *7*, 6450–6457.

(195) Jiang, L.; Santiago, I.; Foord, J. Observation of Nanoimpact Events of Catalase on Diamond Ultramicroelectrodes by Direct Electron Transfer. *Chem. Commun.* **2017**, *53*, 8332–8335.

(196) Dick, J. Electrochemical Detection of Single Cancer and Healthy Cell Collisions on a Microelectrode. *Chem. Commun* **2016**, *52*, 10906–10909.

Chapter 2

Quantitative Measurements of Free and Immobilized *Rg*DAAO Michaelis-Menten Constant using an Electrochemical Assay Reveal the Impact of Covalent Crosslinking on Substrate Specificity

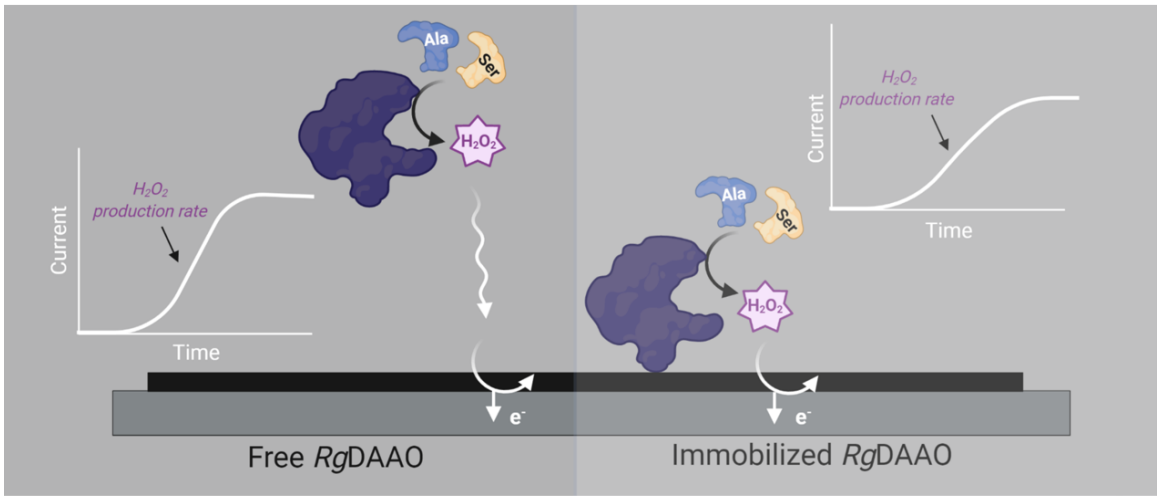

Chapter Preface

Challenges facing enzyme-based electrochemical sensors include substrate specificity, batch to batch reproducibility and lack of quantitative metrics related to the effect of enzyme immobilization. This chapter presents a quick, simple and general approach for measuring the effect of immobilization and crosslinking on enzyme activity and substrate specificity. The method can be generalized for electrochemical biosensors using an enzyme that releases H_2O_2 during its catalytic cycle. Using as proof of concept *Rg*DAAO-based electrochemical biosensors, we found that the Michaelis-Menten constant (K_m) decreases post immobilization, hinting at alterations in the enzyme kinetic properties and thus substrate specificity. We confirm the decrease in K_m electrochemically by characterizing the substrate specificity of the immobilized *Rg*DAAO using chronoamperometry. Our results demonstrate that enzyme immobilization affects enzyme substrate specificity and this must be carefully evaluated during biosensors development.

The work presented in Chapter 2 is reproduced from:

Moussa, S., Chhin, D., Pollegioni, L., Mauzeroll J., Quantitative measurements of free and immobilized *Rg*DAAO Michaelis-Menten constant using an electrochemical assay reveal the impact of covalent cross-linking on substrate specificity, *Analytical and Bioanalytical Chemistry* **2021**, 1-10.

2.1 Introduction

Enzyme immobilization on solid supports is a cost reduction technique that has been widely adopted in biosensing[1–7] and biocatalysis.[8–10] Yet, the catalytic performance of an immobilized enzyme will change based on the chosen method i.e. nature of the substrate, enzyme loading and concentration.[11–14] For biosensors based on redox-active enzymes, there are established quantitative analytical expressions to evaluate the enzyme activity but they do not apply to non-redox enzymes.[15–19] Techniques such as AFM[20], SECM[21–23], SEM[24] and FTIR[25,26], employed to characterize non-redox enzymatic biosensors, are neither quantitative nor representative of the final device structure. There is no simple and analytically valid method to quantify the activity of immobilized non-redox enzymes. Thus it is difficult to compare performance between different biosensor designs and fabrication methods. Traditionally, enzymes are immobilized through a range of methods. The key immobilization methods are either chemical (i.e. covalent attachment and crosslinking) or physical (i.e. adsorption and entrapment).[27] Depending on their application, which ranges from the pharmaceuticals to the cosmetic industries, support materials for enzyme immobilization are either organic (i.e. natural or synthetic polymers) or inorganic (i.e. silica and glass) based.[27–29] Support type and immobilization impact enzyme stability, a desired property for enzyme industrial application. Covalent-based enzyme immobilization is the most commonly used technique due to the resulting high enzyme stability. Covalent crosslinking based on linker functional group reactivity with enzyme reactive residues to form stable bonds impacts enzyme conformation and gives rise increased enzyme stability.[30] In addi-

tion to enzyme stability, enzyme activity is an important parameter in assessing enzyme performance. Studies using optical oxygen assays and electrospray ionization- mass spectrometry have shown that immobilization may either reduce[31], maintain[32,33] or improve enzyme activity[34]. Herein, we propose to immobilize an enzyme to the surface of a poly-m-phenylenediamine modified microelectrode (PPD-ME) and measure the chronoamperometric current of the enzyme electroactive byproduct to quantify its catalytic activity. As a proof of concept, the microelectrode-based electrochemical characterization approach (MECA) is applied to *Rg*DAAO, which has significant potential for applications as a D-amino acid detecting biosensor.[21,35–38] *Rg*DAAO is involved in the degradation of D-amino acids such as D-serine[31], which regulates neurotransmission in the central nervous system. Hence, changes in DAAO function and D-amino acid levels are linked to the onset of chronic diseases such as depression, schizophrenia, Alzheimer's, and gut inflammation.[32–35] Biosensors are simple, low-cost tools that allow for real-time analyte detection: employing *Rg*DAAO biosensors is an attractive approach for probing D-amino acids.[36] Furthermore, in oxidase enzymes like *Rg*DAAO, the electroactive enzyme catalysis byproduct is H_2O_2, which is oxidizable at platinum ME surfaces.[37] As such, the MECA method is applicable to enzymes producing an electroactive product. In this work, MECA is used to measure the kinetics for both free and ME-immobilized *Rg*DAAO. The Michaelis–Menten constant (K_m) obtained using MECA is compared to spectrophotometric assays for free *Rg*DAAO and the Shu and Wilson method for immobilized *Rg*DAAO. The MECA was also applied to study *Rg*DAAO substrate specificity. Finally, we build on these findings by discussing the effect of the presence of dual substrates (D-alanine and D-serine) on *Rg*DAAO biosensor response.

2.2 Experimental Section

2.2.1 Materials and Chemicals

D-serine (99%), D-alanine (99%), D-aspartate (99%), glycine (≥98.5%) m-phenylenediamine flakes (99%), bovine serum albumin (BSA, ≥98%), glycerol (≥99%), o-dianisidine (o-DNS), H_2O_2 (30% vol/vol in H_2O), 2-mercaptoethanol were all purchased from Sigma-Aldrich. Glutaraldehyde (50% in H_2O) was purchased from Fischer Scientific.

2.2.2 Enzyme Purification and Expression

Recombinant *Rg*DAAO wild type (WT) was prepared as reported in the literature.[39] Briefly, recombinant *Rg*DAAO WT was expressed in BL21(DE3)pLysS *E.* coli cells using the pT7-HisDAAO expression vector and purified by HiTrap Chelating chromatography (GE Healthcare Bio-sciences). The final preparation of *Rg*DAAO WT was stored in 20 mM Tris-HCl (pH 8.0), 100 mM NaCl, 10% v/v glycerol, and 5 mM 2-β-mercaptoethanol. The enzyme purity was confirmed by SDS-PAGE. The final enzyme solution was concentrated to 56.8 mg mL^{-1} protein in 0.01 M phosphate-buffered saline (PBS, pH 7.4) containing 1% v/v glycerol and 25 mg mL^{-1} BSA.

2.2.3 Spectrophotometric Characterization of *Rg*DAAO$_{free}$

H_2O_2 production was detected using a coupled enzyme o-DNS activity assay as discussed in the literature.[40] Briefly, H_2O_2 produced from the enzymatic reaction is reduced by horseradish

peroxidase that simultaneously oxidizes o-DNS to give a colored compound with an absorption maxima at 440 nm. To explore pH effects on the specific activity of *Rg*DAAO$_{free}$, activity assays were carried out in both 100 mM sodium pyrophosphate (NaPPi, pH=8.5) and 100 mM potassium phosphate (KPi, pH=7.4) with various substrates (D-serine, D-alanine and glycine). One unit of enzyme is defined as the amount of enzyme that converts 1 µmol of substrate per minute at 25^{o}C.[41]

2.2.4 PPE-ME and *Rg*DAAO-PPD-ME Preparation

Pt disk MEs (10 µm) were prepared according to the literature.[42] Briefly, a soda-lime glass capillary was pulled and a Pt wire was inserted into the capillary, which was then sealed. The ME was polished until the Pt wire was exposed, revealing a disk-shaped surface geometry. This was followed by rinsing the ME with Millipore MilliQ water (18.2 M$\Omega \cdot$ cm), 70% ethanol, and acetone. The R_g, defined as the glass sheath to the exposed platinum diameter ratio, was confirmed with optical microscopy using a customized Axio Vert.A1 inverted microscope (Zeiss, Oberkochen, Germany). The R_g was 5 for all MEs. A permselective polymer was then electrodeposited on the microelectrode surface using cyclic voltammetry (0 to +1000 mV, 5 cycles) with 0.1 M PPD prepared in 0.01 M PBS (pH=7.4).[43] To fabricate the full biosensor, 2 µL of the enzyme (56.8 mg mL^{-1} in 25 mg mL^{-1} BSA) was drop-casted onto a polydimethylsiloxane coated glass slide. This was done to ensure hydrophobicity of the surface, which facilitated enzyme deposition onto the PPD-ME tip. The PPD-ME was immersed in the enzyme droplet for five seconds and then removed to dry for 4 minutes. The immersion process was repeated four times until a small amount of enzyme had adsorbed onto

the PPD-ME, confirmed with optical microscopy. Glutaraldehyde vapor-based crosslinking of the PPD layer with the enzyme layer was achieved by placing the biosensor in a sealed chamber containing 10 mL of glutaraldehyde solution (50% v/v in H_2O) for 10 minutes. Glutaraldehyde is a non-specific fixating crosslinker which reacts primarily with amino groups of proteins in DAAO.

2.2.5 Electrochemical Measurements

For chronoamperometry, the biosensor was biased at 0.5V vs. Ag/AgCl. Measurements were performed using an Electrochemical Probe Scanner 3 (HEKA Elektronik, Lambrecht, Germany). All potentials were recorded relative to a chloridized silver (Ag/AgCl) wire (fabricated in-house, radius=0.250 mm) quasi-reference electrode (QRE).[42] All solutions were prepared in phosphate-buffered saline (PBS, 0.01 M, pH 7.4). Similarly, cyclic voltammetry experiments using the *Rg*DAAO$_{immob}$ PPD-ME (biosensor) immersed in individual solutions of D-serine and D-alanine were performed (-0.1–0.6 V vs. Ag/AgCl wire, 0.1 $V \cdot s^{-1}$).

2.2.6 Electrochemical Characterization of *Rg*DAAO$_{free}$ and *Rg*DAAO$_{immob}$

H_2O_2 production from free *Rg*DAAO reaction with D-serine using a PPD-ME was measured to assess *Rg*DAAO$_{free}$ activity. *Rg*DAAO was thawed on ice and then warmed to room temperature for 5 mins. An oxidative potential step of (0.5 V vs. Ag/AgCl) was applied to a solution of 200 μL of D-serine (0.01 M PBS, pH=7.4), then 1 μL of *Rg*DAAO (56.8 $mg \cdot mL^{-1}$) was added during mixing. The increase in current following the addition of *Rg*DAAO was used to calculate the specific activity of *Rg*DAAO towards D-serine at a

given concentration. To study the effect of enzyme immobilization on the biosensor specific activity, the current response from a biosensor was measured using a potential step of 0.5 V vs Ag/AgCl in D-serine solutions (0.01 M PBS, pH=7.4) at different concentrations.

2.2.7 Numerical Simulations

A 2D axisymmetric model was built using COMSOL Multiphysics version 5.3a. COMSOL was used to simulate the steady state current following the oxidation of H_2O_2 at the ME tip. A parametric sweep was applied to determine the current value (i) at various concentrations to generate a calibration curve for the *Rg*DAAO-PPD-ME with D-serine. The diffusion coefficient (D_{app}) was also parameterized to determine the apparent diffusion coefficient of H_2O_2 through the PPD layer. Following the minimization of the sum of squared residuals between the simulated and experimental calibration curve data, the diffusion coefficient was extracted. To ensure that both calibration curves were similar, the slopes of the regression lines were compared with a two-tailed student's t-test ($t(4)=0.27$, $p=.800$) (See Appendix A for full model details).

2.2.8 Data Analysis

All experimental data presented are the mean of triplicate measurements unless otherwise stated. Error bars represent standard deviation (± S.D.) unless otherwise stated. A two-tailed student's t-test was used for statistical testing ($\alpha=0.05$). Data were analyzed and treated on Matlab R2016b (Mathworks, Natick, USA). Kinetic curves were built using an in-house developed code on Matlab R2016b(See Appendix A for full code details). All other

data were imported into Rx64 3.5.2 (Windows version) for visualization. All electrochemical currents were normalized by the blank signal.

2.3 Results and Discussion

2.3.1 A Method to Probe Redox Molecule Formation Kinetics from Enzyme Catalysis

For neutral and basic D-amino acids, *Rg*DAAO's reaction produces H_2O_2, ammonia and α-keto acid (Figure 2.1).[40,44] The rate of product formation is typically determined using spectrophotometric methods i.e. o-DNS assays where absorbance changes are measured corresponding to enzymatic H_2O_2 production (Figure 2.1A). However, they have limited sensitivity, are prone to optical interferences (such as solution turbidity)[45] and cannot be applied to immobilized enzymes. Alternatively, *Rg*DAAO oxygen consumption can be measured with electrochemical assays (Figure 2.1B). Electrochemical oxygen consumption assays do not suffer from spectrophotometric method disadvantages. Yet, oxygen consumption assays do not quantify H_2O_2 product formation and do not represent the final biosensor device architecture.[40] The proposed MECA approach (Figure 2.1C) enables direct measurement of redox active molecules formed from immobilized enzyme catalysis; an approach free of optical interferences. Using amperometric PPD-modified MEs, the MECA measures the reagent-free enzymatic rate of H_2O_2 formation. Direct enzyme activity quantification is achieved by measuring the rate of current change ($\frac{di}{dt}$) from H_2O_2 oxidizing under a fixed potential (0.5V

vs. Ag/AgCl) (Figure 2.1C).

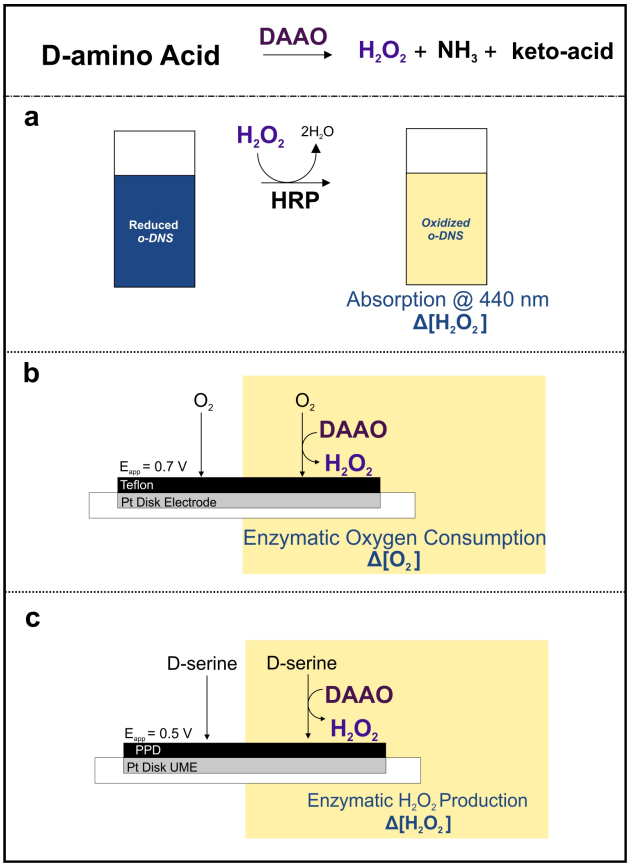

Figure 2.1: The a) spectrophotometric, b) electrochemical and c) the proposed MECA method used to determine the activity of the *Rg*DAAO$_{free}$ and *Rg*DAAO$_{immob}$ form of the enzymes. The MECA method directly quantifies H_2O_2 production.

2.3.2 Analytical Equations for H_2O_2 Detection at the ME Surface

Under diffusion limited regimes (V 0.5 V vs Ag/AgCl), the H_2O_2 oxidative steady state current (i) at a disk ME is defined by[46]:

$$i = \beta(R_g)4nFaD_{app}C \tag{2.1}$$

Where $\beta(R_g)$ is a parameter associated with the R_g of the disk ME $\beta(R_g)$ =1.04 for R_g=5)[47], n is the number of electrons involved in the rate-determining reaction, F is Faraday's number, C is the H_2O_2 concentration (M), D_{app} is the apparent H_2O_2 diffusion coefficient towards the electroactive ME surface and a is the radius of the electroactive area (m). Optical microscopy is used to evaluate a and β. Using the relationship between concentration and current measured at the microelectrode surface, the rate of H_2O_2 detection ($\frac{dC_{H_2O_2}}{dt}$) is as follows:

$$\frac{dC_{H_2O_2}}{dt} = \frac{di}{dt} * \frac{1}{4nFD_{app}(R_g)a} \tag{2.2}$$

2.3.3 Contribution of a Permeable Polymer Layer at the ME Surface to H_2O_2 Detection

To solve for $dC_{H_2O_2}/dt$, an approximation of the apparent H_2O_2 diffusion coefficient, D_{app} is required. Due to the presence of a permeable PPD layer at the Pt surface, transport across the PPD layer must be considered in the D_{app} value. To extract D_{app} corresponding to H_2O_2 diffusion from the bulk through the PPD and towards the ME surface, a numerical model in COMSOL Multiphysics was built to generate simulated calibration curves at various D_{app} values. (See Appendix A for full model details). Next, the simulated calibration curves were fit to experimental calibration curves. The experimental calibration was generated by

extracting i_{ss} from the oxidation current profile for H_2O_2 produced by the *Rg*DAAO reaction with 0-25 µM D-serine (Figure A.4). This concentration range is relevant to D-serine levels in brain extracellular spinal fluid (0-10 µM) from quantification studies performed in human and animal models.[35,43,48,49]

2.3.4 Contribution of Enzyme Kinetics to H_2O_2 Detection

Enzyme kinetics play a dominating role in H_2O_2 detection at the PPD-modified ME surface. To demonstrate that the signal detected at the ME surface is associated with enzymatic H_2O_2 production, a calibration curve of the PPD-ME immersed in H_2O_2 solutions was generated. The PPD-ME calibration curve was compared to calibration curves of the biosensor immersed in D-serine solutions. The two different calibrations showed good agreement with one another (A.2). As such, the electrochemical enzyme activity (EA) in µmol $min^{-1}mL^{-1}$ can be related to the H_2O_2 current at the PPD-ME (Equation 2.2). The enzyme reaction-dependent increase in H_2O_2 production is proportional to the current transient measured at the ME surface. To compare *Rg*DAAO$_{free}$ and *Rg*DAAO$_{immob}$, the EA values are normalized by the enzyme concentration (mgDAAO/mL), total solution volume (mL_{total}) and enzyme volume used for the assay (mL_{DAAO}). Normalization yields the specific electrochemical activity (SEA) expressed as U/mgDAAO as follows:

$$SEA = \frac{U}{mg_{DAAO}} = EA * \frac{mL_{total}}{mL_{DAAO}} * \frac{mL}{mg_{DAAO}} \tag{2.3}$$

2.3.5 MECA Derived K_m values for *Rg*DAAO$_{free}$ and *Rg*DAAO$_{immob}$

To determine the SEA at different D-serine concentrations, the current transient ($\frac{di}{dt}$) was calculated from chronoamperograms. Using a PPD-ME immersed in D-serine solutions ranging from 0.1-25 mM, chronoamperograms were recorded at 0.5 V vs Ag/AgCl for each concentration (Figure 2.2A). The initial current transient at D-serine concentrations lower than 0.1 mM was not used due to the PPD-ME response time and instrument resolution. In the first 400 s, a background current was recorded. At 400 s, the addition of *Rg*DAAO$_{free}$ under solution mixing led to the observed current transient from H_2O_2 production. Time-dependent current changes in the initial linear range (30 s) of the *Rg*DAAO$_{free}$ reaction were used to determine SEA values at each D-serine concentration. By fitting SEA values to the Michaelis-Menten equation using a non-linear least squares regression hyperbolic model (Figure 2.2B), the K_m for D-serine of *Rg*DAAO$_{free}$ is calculated (Equation 2.4).

$$SEA = \frac{SEA_{max}[S]}{K_m + [S]} \tag{2.4}$$

Similarly, the SEA for *Rg*DAAO$_{immob}$ was determined. Briefly, a biosensor poised at 0.5V vs Ag/AgCl, was immersed in a solution of PBS for 300 s where a background current was observed. At 300s, a standard D-serine solution (0-25 mM) replaced the PBS solution, where mixing resulted in several current transients. An increase in H_2O_2 oxidation current is observed upon D-serine addition (Figure 2.2C). The first 15 s of the linear portion of the current profile of the *Rg*DAAO$_{immob}$ reaction was used to calculate $\frac{di}{dt}$. Using a modified ver-

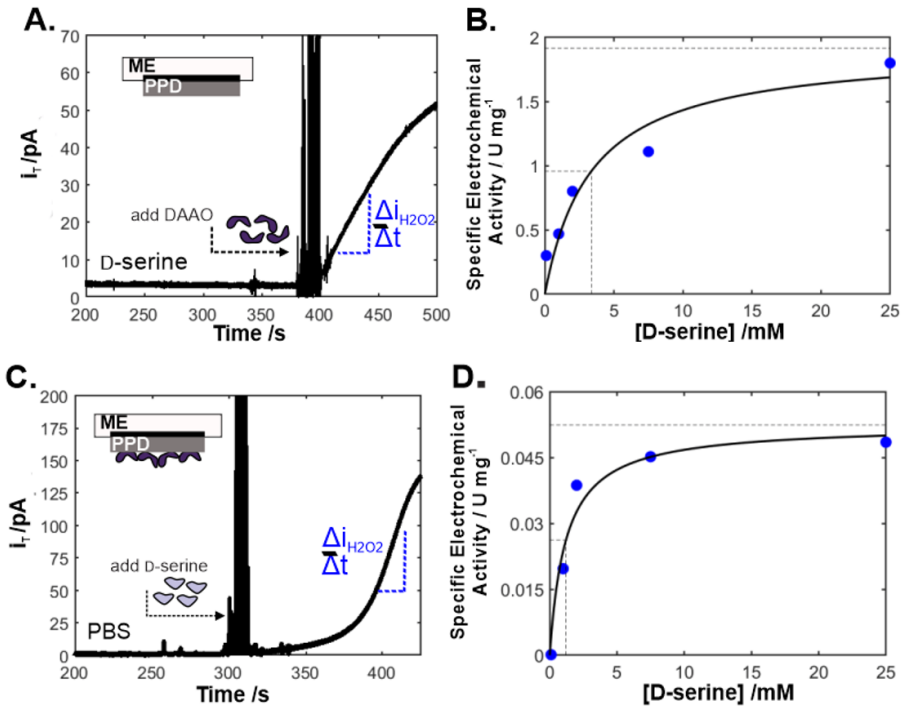

Figure 2.2: a) Schematic of experiment (in 25 mM D-serine) used to build the MM curve for the *Rg*DAAO$_{free}$. b) MM curve used to determine K_m value for the free *Rg*DAAO$_{free}$ (3.69 mM). c) Schematic of experiment used to build the MM curve for the immobilized enzyme. d MM curve used to determine K_m value for *Rg*DAAO$_{immob}$ (1.21 mM).

sion of Equation 2.3 where mL_{total}/mL_{DAAO} =1, EA was normalized to the concentration of enzyme immobilized on the PPD-ME surface (56.8 mg mL^{-1}). Then, individual SEA values were fit to a Michaelis Menten model (Figure 2.2B). For fitting the data points to a Michealis-Menten model, we recommend using a minimum of four data points. However, to improve the fit of a Michaelis Menten model, we recommend using nine data points over a wide range of substrate concentrations. From the Michaelis Menten model fit, the *Rg*DAAO$_{immob}$ K_m value obtained by MECA (Figure 2.2BD) is 3-fold lower than for *Rg*DAAO$_{free}$, suggesting an increase in apparent D-serine affinity. From the MM curves in Figure 2.2, both *Rg*DAAO

forms exhibit substrate saturation at 25 mM. Moreover, cyclic voltammograms (CVs) of the biosensor in D-serine and D-alanine solutions show changes in substrate selectivity as a function of substrate concentration for *Rg*DAAO$_{immob}$ (Figure A.5). Both results suggest the possibility of tuning the enzyme's substrate specificity through immobilization as previously demonstrated for other enzymes such as lipase[50] and ester hydrolase[51]. Substrate specificity changes are tied to the crosslinker nature which affects enzyme orientation, substrate access to the enzyme active site and the altered surface chemistry of the support matrix.[52] While the MECA does not determine all enzyme kinetic parameters, it is suitable for comparisons of surface-immobilized enzymes unlike conventional methods such as spectrophotometric assays. The MECA is applicable for biosensors where an electroactive product is probed. For practical MECA application, we recommend consistency in enzyme concentrations for immobilization: this enables valid comparisons across biosensor design strategies.

2.3.6 Validation of the MECA Method

To determine the validity of MECA, its results were compared against established methods namely the standard o-DNS spectrophotometric assay[40] and an electrochemical method, defined in this work as the Shu and Wilson method.[35,53–55] The Shu and Wilson method (Equation 2.5), derived for the rotating enzyme disk electrode, has been applied in the past as an analytical method to determine the K_m value for electrode surf immobilized enzymes.[35,53,56–58] This method uses steady state current measurements for analysis and is usually applied only for surface bound enzymes. Spectrophotometric assays, on the other hand, use rates of absorbance changes and are typically employed with free enzymes.

$$i_{ss} = \frac{i_{max}[S]}{K_m + [S]} \tag{2.5}$$

The Shu and Wilson method is based on the theory of Levich rotating disk electrodes.[53] The method demonstrates that the Levich electrode equation is consistent with the steady state current trend of amperometric enzyme electrodes. Chronoamperometry is used to extract i_{ss} corresponding to H_2O_2 oxidation at different substrate concentrations. The Km is calculated using the measured i_{ss} for each D-serine concentration as follows:[59,60]

Where i_{max} is the maximum H_2O_2 oxidative current at substrate saturating conditions and [S] is the substrate concentration. For *Rg*DAAODAAO$_{free}$, the Shu and Wilson method underestimate the K$_m$ by a factor of $\approx$ 30 compared to the spectrophotometric method. In comparison, the MECA approach underestimates the K$_m$ by a factor of $\approx$ 0.12. The difference between the spectrophotometric and MECA derived Km is ascribed to the rejection of approximately 80% of the produced H_2O_2 by the permselective PPD-layer: the PPD layer induces hindered diffusion towards electroactive ME surface.[21] This hindered diffusion masks the original rate of H_2O_2 production, causing a deviation in matching the K_m determined with spectrophotometry. For *Rg*DAAO$_{immob}$, the Km value is lower than for *Rg*DAAO$_{free}$ for both the MECA and Shu and Wilson methods. Moreover, when comparing MECA to the Shu and Wilson method, the latter method gave a lower K$_m$ value for *Rg*DAAO$_{immob}$ suggesting that the Shu and Wilson method also underestimates this kinetic parameter. Using the MECA, the*Rg*DAAO$_{immob}$ K_m value (1.21 mM) is less than the *Rg*DAAO$_free$ K_m

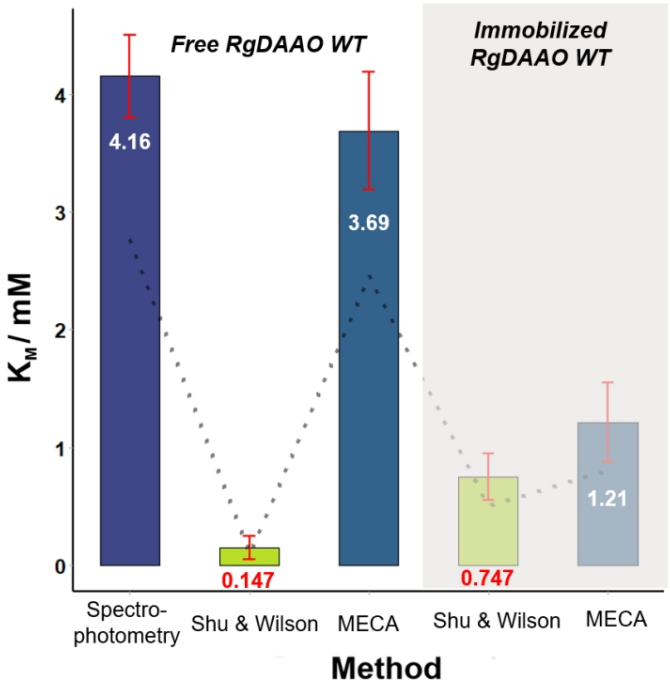

Figure 2.3: K_m values derived from non-linear least squares fit of the individual activity values using the spectrophotometric assay, the Shu and Wilson method, and the MECA approach for both the free and immobilized *Rg*DAAO$_{free}$ and *Rg*DAAO$_{immob}$ WT at pH=7.4.

(3.69 mM). The change in the K_m is due to alterations in the rate of enzyme catalysis (k_{cat}) and/or dissociation (K_d) as both impacts the overall K_m value.[55,61] Variations in K_m values for the same enzyme represent changes in enzyme substrate specificity.

2.3.7 Immobilization Alters *Rg*DAAO Substrate Specificity

To identify *Rg*DAAO's most electrochemically active substrates, four different amino acids (D-serine, D-alanine, D-aspartate and glycine) were tested with *Rg*DAAO$_{free}$. Chronoamperometric measurements monitoring the current profile from the incubation of *Rg*DAAO$_{free}$ in 100 μM of each substrate were performed. The steady state current responses demon-

strated that D-serine and D-alanine were the preferred substrates of *Rg*DAAO (Figure A.4). Accordingly, D-serine and D-alanine were tested with both *Rg*DAAO$_{free}$ and *Rg*DAAO$_{immob}$ using spectrophotometry and electrochemistry, respectively. The spectrophotometric and electrochemical measurements were used to quantify concentration dependent D-alanine:D-serine specific activity ratios (Figure 2.4A&B). The ratios allow to evaluate the effect of enzyme immobilization on enzyme selectivity. For *Rg*DAAO$_{free}$, *Rg*DAAO is generally more

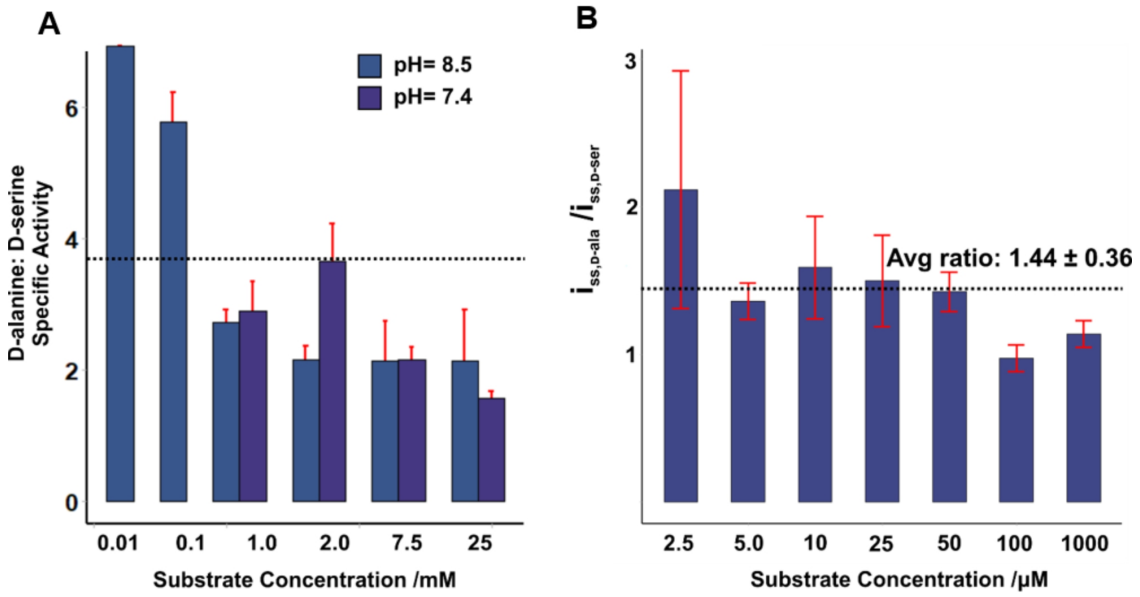

Figure 2.4: a The specific activity of *Rg*DAAO was measured at various concentrations of D-alanine and D-serine individually using the o-DNS assay in NaPPi buffer (pH=8.5) and KPi buffer (pH=7.4). The specific activity at each concentration was used to calculate the D-alanine:D-serine specific activity ratio of *Rg*DAAO$_{free}$. Each bar shows the average specificity ratio of three ratios derived from measurements for each concentration. B) Ratio of biosensor response (i_{ss}) at various concentrations towards D-ala and D-ser (n=3). Error bars represent ±SD. The biosensor steady state response was not measured at higher substrate concentrations due to a substrate inhibition effect masking i_{ss}.

selective towards D-alanine (Figure 2.4A). Moreover, the *Rg*DAAO$_{free}$ specific activity ratios highlighted two main points: the ratios are on average ≥ 2 and the ratio increases drasti-

cally below 7.5 mM substrate concentration. Taken together, the results emphasize that the enzyme specificity depends on substrate concentration in the biosensor linear range.[56] Additionally, a pH change has no significant effect on *Rg*DAAO specificity ratio (Fig. 4A) as confirmed with a Welch's t-test (for specific activity ratio values at pH 7.4 and 8.5, tcalc =0.5774 ¡ $t_{critical}$=3.182). In contrast to *Rg*DAAO$_{free}$, the average *Rg*DAAO$_{immob}$ D-alanine/D-serine specificity ratio is < 2 (Figure 2.4B). While for both enzyme forms there is preferential selectivity of D-alanine over D-serine, enzyme immobilization results in a lower dependence on the substrate concentration, apparently increasing *Rg*DAAO selectivity towards D-serine.

2.3.8 Dual Substrate Presence Impact on *Rg*DAAO$_{immob}$ Response

Typically, a single amino acid is probed with biosensors and the presence of unwanted amino acids interferes with biosensor responses.[29,57,62] To explore the extent of the interference effect, the *Rg*DAAO biosensor was calibrated in standard D-serine (2.5 – 25 µM) (Figure 2.5A, yellow), D-alanine (Figure 2.5A, purple), and equimolar D-serine and D-alanine solutions (Figure 2.5A, black). Using chronoamperometry, the i_{ss} for D-serine and D-alanine mixtures was larger than for pure D-alanine and D-serine solutions. For example, a mixture of 2.5 µM D-serine and 2.5 µM D-alanine generates an $i_{ss} = 3$ pA, compared to an $i_{ss} < 2.5$ pA for pure solutions of 5 µM D-alanine or D-serine. Subpicoamp currents measured with the sensors developed in this chapter are relevant in comparison to subpicoamp currents measured with larger biosensors of alternative architectures. In this work, changes in subpicoamp currents correspond to different analyte concentrations compared to the latter where they correspond

to noise or measurement artifacts. The i_{ss} increase is attributed to substrate specific reaction velocity (SEA) with *Rg*DAAO.[63] The results suggest that both amino acids are depleted by *Rg*DAAO, resulting in increased H_2O_2 production and making it challenging to attribute the biosensor response to a single D-amino acid. Consequently, in conditions where D-serine and D-alanine co-localize, such as the plasma and the pituitary gland, the biosensor may not accurately quantify a single D-amino acid. Nonetheless, D-serine may still be quantified in the presence of constant D-alanine levels as evidenced by the linear current increase in standard D-serine solutions (Figure 2.5B). Indeed, most biological environments do not have constant or equimolar concentrations of D-alanine and D-serine and the level of one or both D-amino acids may change following a release process. To simulate time-dependent release, D-serine and D-alanine were added sequentially instead of simultaneously. The addition of D-alanine to a D-serine solution increased the i_{ss} by more than 100% whereas the addition of D-serine to a D-alanine solution increased the i_{ss} by less than 20% (Figure 2.5C) this allowing a valid evaluation of D-serine level changes. Hence, constant D-alanine levels enable quantification of D-serine level changes. Conversely, time-dependent release of both D-serine and D-alanine do not allow individual D-amino acid quantification.

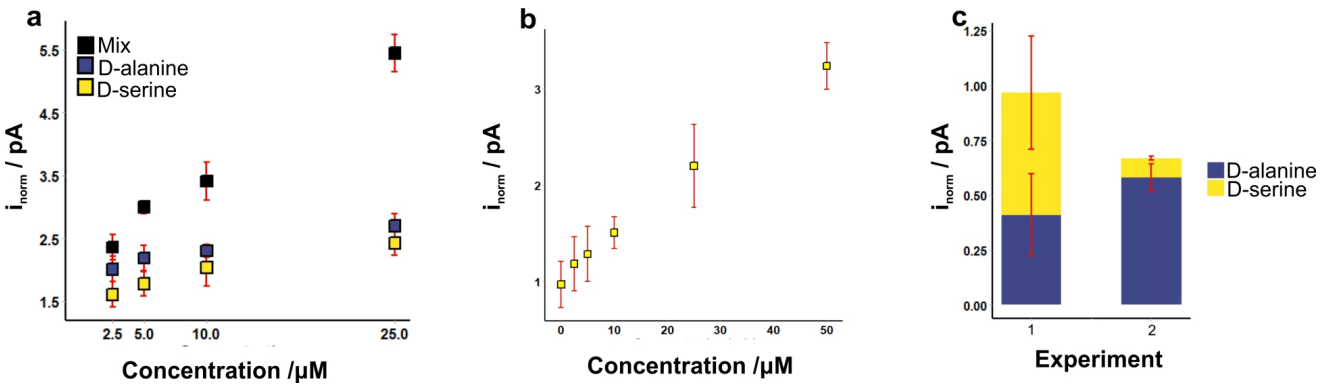

Figure 2.5: *Rg*DAAO$_{immob}$ production of H_2O_2 from various substrate conditions. A) Biosensor steady state currents (n=3 ±S.D.) for standard solutions of D-serine (yellow), D-alanine (blue) and equimolar D-serine/D-alanine mixtures (black) in PBS (pH=7.4). B) The steady state current measured with the biosensor immersed in a solution of 0-25 µM D-serine, combined with 2.5 µM D-alanine (n=3 ±S.E.M). The response increases linearly despite the presence of 2.5 µM D-alanine. C) Effect of adding equimolar amounts (2.5 µM) of one -amino acid to a solution containing the other on the oxidative steady state current. The average of three measurements is shown ±S.D. The current is normalized to remove the capacitive contribution from the PBS buffer.

2.4 Conclusion

We report an analytical method (MECA) to characterize the kinetics of H_2O_2 production from free and immobilized enzymes using PPD-modified MEs. Using *Rg*DAAO for proof of concept, we validated the MECA by comparing K$_m$ values for *Rg*DAAO$_{free}$ determined by a spectrophotometric assay, the Shu and Wilson method and the MECA method. The MECA method enabled us to study enzyme selectivity differences between free and immobilized *Rg*DAAO forms. As such, the MECA is a useful tool for the characterization of other non-redox enzymatic biosensors that rely on quantification of electrochemical products. The development of such biosensors often employs glutaraldehyde crosslinking of *Rg*DAAO to a

modified electrode surface.[35,37] To assess alternative safe and sustainable crosslinkers such as poly(ethylene glycol) diglycidyl ether (PEDGE)[23], the MECA is used to extract generalized assessment metrics for various enzymatic biosensor architectures. Thus, the MECA could be useful to address questions concerning the crosslinking and crosslinker efficiency and their effect on enzyme activity. We also demonstrate that substrate concentration modifies enzyme selectivity for free and immobilized *Rg*DAAO: modifications in enzyme selectivity are advantageous for biosensor application in selective analyte measurements. The effect of an unwanted D-alanine presence on D-serine quantification was also evaluated showing that under fixed D-alanine levels, biosensors remain useful for D-serine quantification. Increasing the pool of methods to characterize immobilized enzymes on solid supports is beneficial to wide a range of fields, most prominently for biofuel cell and biosensor design. Future extensions to this work include exploring alternative crosslinker methodologies and the use of variant enzymes with altered substrate selectivity for improved accuracy in quantitative D-amino acid *in situ* measurements.

References

(1) Ehret, F.; Wu, H.; Alexander, S.; Devaraj, N. Electrochemical Control of Rapid Bioorthogonal Tetrazine Ligations for Selective Functionalization of Microelectrodes. *J. Am. Chem. Soc.* **2015**, *137*, 8876–8879.

(2) Schneider, E.; Clark, D. Cytochrome P450 (CYP) Enzymes and the Development of CYP Biosensors. *Biosens. Bioelectron.* **2013**, *39*, 1–13.

(3) Tak-Shing Ching, C.; Chang, J.-W.; Sun, T.-P.; Shieh, H.-L.; Tsai, C.-L.; Huang, H.-W.; Liu, W.-H.; Liu, C.-M.; Yeh, W.-C.; Li, J.-H. An Amperometric Biosensor Array for Precise Determination of Homocysteine. *Sens. Actuat. B* **2010**, *152*, 94–98.

(4) Li, Z.; Yu, Y.; Li, Z.; Wu, T.; Yin, J. The Art of Signal Transforming: Electrodes and Their Smart Applications in Electrochemical Sensing. *Anal. Methods* **2015**, *7*, 9732–9743.

(5) Feng, W.; Ji, P. Enzymes Immobilized on Carbon Nanotubes. *Biotechnol. Adv.* **2011**, *29*, 889–895.

(6) Pundir, C.; Lata, S.; Narwal, V. Biosensors for Determination of D and L- Amino Acids: A Review. *Biosens. Bioelectron.* **2018**, *117*, 373–384.

(7) Vasylieva, N.; Barnych, B.; Meiller, A.; Maucler, C.; Pollegioni, L.; Lin, J.-S.; Barbier, D.; Marinesco, S. Covalent Enzyme Immobilization by Poly(Ethylene Glycol) Diglycidyl Ether (PEGDE) for Microelectrode Biosensor Preparation. *Biosens. Bioelectron.* **2011**, *26*, 3993–4000.

(8) Andler, S.; Goddard, J. Transforming Food Waste: How Immobilized Enzymes Can Valorize Waste Streams into Revenue Streams. *npj Sci. Food* **2018**, *2*, 1–11.

(9) Rehm, F.; Chen, S.; Rehm, B. Bioengineering toward Direct Production of Immobilized Enzymes: A Paradigm Shift in Biocatalyst Design. *Bioengineering* **2018**, *9*, 6–11.

(10) Neira, H.; Herr, A. Kinetic Analysis of Enzymes Immobilized in Porous Film Arrays. *Anal. Chem.* **2017**, *89*, 10311–10320.

(11) Barlett, P.; Cooper, J. A Review of the Immobilization of Enzymes in Electropolymerized Films. *J. Electroanal. Chem.* **1993**, *362*, 1–12.

(12) D'souza, S. Immobilization and Stabilization of Biomaterials for Biosensor Applications. *Applied Biochemistry and Biotechnology* **2001**, *96*, 225–238.

(13) Kim, D.; Herr, A. Protein Immobilization Techniques for Microfluidic Assays. *Biomicrofluidics* **2013**, *7*.

(14) Marangoni, A., Immobilized Enzymes In *Enzyme Kinetics*; John Wiley Sons, Inc: Hoboken, NJ, USA, pp 116–120.

(15) Anne, A.; Cambril, E.; Chovin, A.; Demaille, C. Touching Surface-Attached Molecules with a Microelectrode: Mapping the Distribution of Redox-Labeled Macromolecules by Electrochemical-Atomic Force Microscopy. *Anal. Chem.* **2010**, *82*, 6353–6362.

(16) Jensen, U.; Ferapontova, E.; Sutherland, D. Quantifying Protein Adsorption and Function at Nanostructured Materials: Enzymatic Activity of Glucose Oxidase at GLAD Structured Electrodes. *Langmuir* **2012**, 11106–11114.

(17) Bourdillon, C.; Demaille, C.; Moiroux, J.; Savéant, J.-M. Activation and Diffusion in the Kinetics of Adsorption and Molecular Recognition on Surfaces. Enzyme-Amplified Electrochemical Approach to Biorecognition Dynamics Illustrated by the Binding of Antibodies to Immobilized Antigens. *P. Curr. Opin. Biotechnol.* **1998**, *70*, 2401–2408.

(18) Limoges, B.; Savéant, J.-M.; Yazidi, D. Quantitative Analysis of Catalysis and Inhibition at Horseradish Peroxidase Monolayers Immobilized on an Electrode Surface. *J. Am. Chem. Soc.* **2003**, *125*, 9192–9203.

(19) Limoges, B.; Marchal, D.; Mavré, F.; Savéant, J. Electrochemistry of Immobilized Redox Enzymes: Kinetic Characteristics of NADH Oxidation Catalysis at Diaphorase Monolayers Affinity Immobilized on Electrodes. *J. Am. Chem. Soc.* **2006**, *128*, 2084–2092.

(20) Nguyen, B.; Nguyen, B.; Van Vu, H.; Van Nguyen, C.; Nguyen, D.; Nguyen, L.; Vu, T.; Tran, L. Development of Label-Free Electrochemical Lactose Biosensor Based on Graphene/Poly(1,5-Diaminonaphthalene) Film. *Curr. Appl. Phys.* **2016**, *16*, 135–140.

(21) Polcari, D.; Perry, S.; Pollegioni, L.; Geissler, M.; Mauzeroll, J. Localized Detection of D-Serine by Using an Enzymatic Amperometric Biosensor and Scanning Electrochemical Microscopy. *ChemElectroChem* **2017**, *4*, 920–926.

(22) Pribil, M.; Cortés-Salazar, F.; Andreyev, E.; Lesch, A.; Karyakina, E.; Voronin, O.; Girault, H.; Karyakin, A. Rapid Optimization of a Lactate Biosensor Design Using Soft Probes Scanning Electrochemical Microscopy. *J. Electroanal. Chem* **2014**, *731*, 112–118.

(23) Soldà, A.; Valenti, G.; Marcaccio, M.; Giorgio, M.; Pelicci, P.; Paolucci, F.; Rapino, S. Glucose and Lactate Miniaturized Biosensors for SECM-Based High-Spatial Resolution Analysis: A Comparative Study. *ACS Sensors* **2017**, *2*, 1310–1318.

(24) Campos-Beltrán, D.; Konradsson-Geuken, Å.; Quintero, J.; Marshall, L. Amperometric Self-Referencing Ceramic Based Microelectrode Arrays for D-Serine Detection. *Biosensors* **2018**, *8*, 28–34.

(25) Sri Kaja, B.; Lumor, S.; Besong, S.; Taylor, B.; Ozbay, G. Investigating Enzyme Activity of Immobilized Candida Rugosa Lipase. *J. Food Qual.* **2018**, 1–9.

(26) Baghayeri, M.; Zare, E.; Lakouraj, M.; Biosensor, H.; Fe, N. A Simple Hydrogen Peroxide Biosensor Based on a Novel Electro-Magnetic Poly(p-Phenylenediamine)@Fe 3 O 4 Nanocomposite. *Biosens. Bioelectron.* **2014**, *55*, 259–265.

(27) Ottone, C.; Romero, O.; Urrutia, P.; Bernal, C.; Illanes, A.; Wilson, L., Enzyme Biocatalysis and Sustainability In *Nanostructured Catalysts for Environmental Applications*; Springer International Publishing: 2021, pp 383–413.

(28) Abolpour Homaei, A.; Sariri, R.; Vianello, F.; Stevanato, R. Enzyme Immobilization: An Update. *J. Chem. Biol.* **2013**, 185–205.

(29) Nanomaterials for Enzyme Immobilization In *Green Synthesis of Nanomaterials for Bioenergy Applications*; Wiley: 2020, pp 165–190.

(30) Bolivar, J.; Nidetzky, B. On the Relationship between Structure and Catalytic Effectiveness in Solid Surface-Immobilized Enzymes: Advances in Methodology and the Quest for a Single-Molecule Perspective. *Biochimica et Biophysica Acta* **2020**, *1*, 1–12.

(31) Bolivar, J.; Schelch, S.; Mayr, T.; Nidetzky, B. Mesoporous Silica Materials Labeled for Optical Oxygen Sensing and Their Application to Development of a Silica-Supported Oxidoreductase Biocatalyst. *ACS Catal.* **2015**, *5*, 5984–5993.

(32) Grasso, G.; Fragai, M.; Rizzarelli, E.; Spoto, G.; Yeo, K. A New Methodology for Monitoring the Activity of CdMMP-12 Anchored and Freeze-Dried on Au (111. *J. Am. Soc. Mass Spectrom.* **2007**, *18*, 961–969.

(33) Grasso, G.; D'agata, R.; Rizzarelli, E.; Spoto, G.; D'andrea, L.; Pedone, C.; Picardi, A.; Romanelli, A.; Fragai, M.; Yeo, K. Activity of Anchored Human Matrix Metalloproteinase-1 Catalytic Domain on Au (111) Surfaces Monitored by ESI-MS †. *J. MASS Spectrom. J. Mass Spectrom.* **2005**, *40*, 1565–1571.

(34) Meridor, D.; Gedanken, A. Enhanced Activity of Immobilized Pepsin Nanoparticles Coated on Solid Substrates Compared to Free Pepsin. *Enzyme Microb. Technol.* **2014**, *67*, 67–76.

(35) Zain, Z.; O'Neill, R.; Lowry, J.; Pierce, K.; Tricklebank, M.; Dewa, A.; Ghani, S. Development of an Implantable D-Serine Biosensor for in Vivo Monitoring Using Mammalian d-Amino Acid Oxidase on a Poly (o-Phenylenediamine) and Nafion-Modified Platinum-Iridium Disk Electrode. *Biosens. Bioelectron.* **2010**, *25*, 1454–1459.

(36) Maucler, C.; Pernot, P.; Vasylieva, N.; Pollegioni, L.; Marinesco, S. In Vivo D-Serine Hetero-Exchange through Alanine-Serine-Cysteine (ASC) Transporters Detected by Microelectrode Biosensors. *ACS Chem. Neurosci.* **2013**, *4*, 772–781.

(37) Zain, Z.; Ghani, S.; O'Neill, R. Amperometric Microbiosensor as an Alternative Tool for Investigation of D-Serine in Brain. *Amino Acids* **2012**, *43*, 1887–1894.

(38) Papouin, T.; Haydon, P. D-Serine Measurements in Brain Slices or Other Tissue Explants. *Bio-Protocol* **2018**, *8*, 1–10.

(39) Cappelletti, P.; Piubelli, L.; Murtas, G.; Caldinelli, L.; Valentino, M.; Molla, G.; Pollegioni, L.; Sacchi, S. Structure–Function Relationships in Human d-Amino Acid Oxidase Variants Corresponding to Known SNPs. *Biochim. Biophys. Acta* **2015**, *1854*, 1150–1159.

(40) Rosini, E.; Caldinelli, L.; Piubelli, L. Assays of D-Amino Acid Oxidase Activity. *Front. Mol. Biosci.* **2018**, *4*, 1–12.

(41) Caligiuri, A.; D'Arrigo, P.; Rosini, E.; Pedrocchi-Fantoni, G.; Tessaro, D.; Molla, G.; Servi, S.; Pollegioni, L. Activity of Yeast D-Amino Acid Oxidase on Aromatic Unnatural Amino Acids. *J. Mol. Catal. B Enzym.* **2008**, *50*, 93–98.

(42) Danis, L.; Polcari, D.; Kwan, A.; Gateman, S.; Mauzeroll, J. Fabrication of Carbon, Gold, Platinum, Silver, and Mercury Ultramicroelectrodes with Controlled Geometry. *Anal. Chem.* **2015**, *87*, 2565–2569.

(43) Polcari, D.; Kwan, A.; Van Horn, M.; Danis, L.; Pollegioni, L.; Ruthazer, E.; Mauzeroll, J. Disk-Shaped Amperometric Enzymatic Biosensor for in Vivo Detection of D-Serine. *Anal. Chem.* **2014**, *86*, 3501–3507.

(44) Spehar-Délèze, A.-M.; Anastasova, S.; Vadgama, P. Electropolymerised Phenolic Films as Internal Barriers for Oxidase Enzyme Biosensors. *Electroanal.* **2014**, *26*, 1335–1344.

(45) Kangas, M.; Burks, R.; Atwater, J.; Lukowicz, R.; Williams, P.; Holmes, A. Colorimetric Sensor Arrays for the Detection and Identification of Chemical Weapons and Explosives. *Critical Reviews in Analytical Chemistry* **2017**, *4*, 138–153.

(46) Bard, A.; Faulkner, L., *Electrochemical Methods:Fundamentals and Applications*; John Wiley and Sons: New York, NY, 2015; Vol. 8.

(47) Lefrou, C.; Cornut, R. Analytical Expressions for Quantitative Scanning Electrochemical Microscopy. *ChemPhysChem* **2010**, *11*, 547–556.

(48) Biemans, E.; Verhoeven-Duif, N.; Gerrits, J.; Claassen, J.; Kuiperij, H.; Verbeek, M. CSF D-Serine Concentrations Are Similar in Alzheimer's Disease, Other Dementias, and Elderly Controls. *Neurobiol. Aging* **2016**, *42*, 213–216.

(49) Kumashiro, S.; Hashimoto, A.; Nishikawa, T. Free D-Serine in Post-Mortem Brains and Spinal Cords of Individuals with and without Neuropsychiatric Diseases. *Brain Res* **1995**, *681*, 117–125.

(50) Dos Santos, J.; Rueda, N.; Torres, R.; Barbosa, O.; Gonçalves, L.; Fernandez-Lafuente, R. Evaluation of Divinylsulfone Activated Agarose to Immobilize Lipases and to Tune Their Catalytic Properties. *Process Biochem.* **2015**, *50*, 918–927.

(51) Coscolín, C.; Beloqui, A.; Martínez-Martínez, M.; Bargiela, R.; Santiago, G.; Blanco, R.; Delaittre, G.; Márquez-Álvarez, C.; Ferrer, M. Controlled Manipulation of Enzyme Specificity through Immobilization-Induced Flexibility Constraints. *Appl. Catal. A Gen.* **2018**, *565*, 59–67.

(52) Barbosa, O.; Torres, R.; Ortiz, C.; Berenguer-Murcia, Á.; Rodrigues, R.; Fernandez-Lafuente, R. Heterofunctional Supports in Enzyme Immobilization: From Traditional Immobilization Protocols to Opportunities in Tuning Enzyme Properties. *Biomacromolecules. August* **2013**, *12*, 2433–2462.

(53) Shu, F.; Wilson, G. Rotating Ring-Disk Enzyme Electrode for Surface Catalysis Studies. *Anal. Chem.* **1976**, *48*, 1679–1686.

(54) Gonzalez-Navarro, F.; Stilianova-Stoytcheva, M.; Renteria-Gutierrez, L.; Belanche-Muñoz, L.; Flores-Rios, B.; Ibarra-Esquer, J. Glucose Oxidase Biosensor Modeling and Predictors Optimization by Machine Learning Methods. *Sensors* **2016**, *16*, 16–22.

(55) Fortier, G.; Brassard, E.; Bélanger, D. Optimization of a Polypyrrole Glucose Oxidase Biosensor. *Biosens. Bioelectron.* **1990**, *5*, 473–490.

(56) Vasylieva, N.; Barnych, B.; Meiller, A.; Maucler, C.; Pollegioni, L.; Lin, J.-S.; Barbier, D.; Marinesco, S. Covalent Enzyme Immobilization by Poly(Ethylene Glycol) Diglycidyl Ether (PEGDE) for Microelectrode Biosensor Preparation. *Biosens. Bioelectron.* **2011**, *26*, 3993–4000.

(57) Li, J.; Xiao, L.-T.; Liu, X.-M.; Zeng, G.-M.; Huang, G.-H.; Shen, G.-L.; Yu, R.-Q. Amperometric Biosensor with HRP Immobilized on a Sandwiched Nano-Au / Polymerized m-Phenylenediamine Film and Ferrocene Mediator. *Anal. Bioanal. Chem.* **2003**, *376*, 902–907.

(58) Shoja, Y.; Rafati, A.; Ghodsi, J. Enzymatic Biosensor Based on Entrapment of d -Amino Acid Oxidase on Gold Nanofilm/MWCNTs Nanocomposite Modified Glassy Carbon Electrode by Sol-Gel Network: Analytical Applications for d -Alanine in Human Serum. *Enzyme Microb. Technol.* **2017**, *100*, 20–27.

(59) Kornienko, N.; Ly, K.; Robinson, W.; Heidary, N.; Zhang, J.; Reisner, E. Advancing Techniques for Investigating the Enzyme–Electrode Interface. *Acc. Chem. Res.* **2019**, *52*, 1439–1448.

(60) Kueng, A.; Kranz, C.; Lugstein, A.; Bertagnolli, E.; Mizaikoff, B. Integrated AFM–SECM in Tapping Mode: Simultaneous Topographical and Electrochemical Imaging of Enzyme Activity. *Angew. Chemie Int. Ed.* **2003**, *42*, 3238–3240.

(61) Baleizão, C.; Berberan-Santos, M. Enzyme Kinetics with a Twist. *J. Math Chem.* **2011**, *49*, 1949–1960.

(62) Shimekake, Y.; Furuichi, T.; Abe, K.; Kera, Y.; Takahashi, S. A Novel Thermostable D-Amino Acid Oxidase of the Thermophilic Fungus Rasamsonia Emersonii Strain YA. *Sci. Rep.* **2019**, *9*, 1–12.

(63) Kaki, S.; Adlercreutz, P. Quantitative Analysis of Enzymatic Fractionation of Multiple Substrate Mixtures. *Biotechnol. Bioeng.* **2013**, *110*, 78–86.

Chapter 3

A Miniaturized Enzymatic Biosensor for Detection of Sensory-Evoked D-serine Release in the Brain

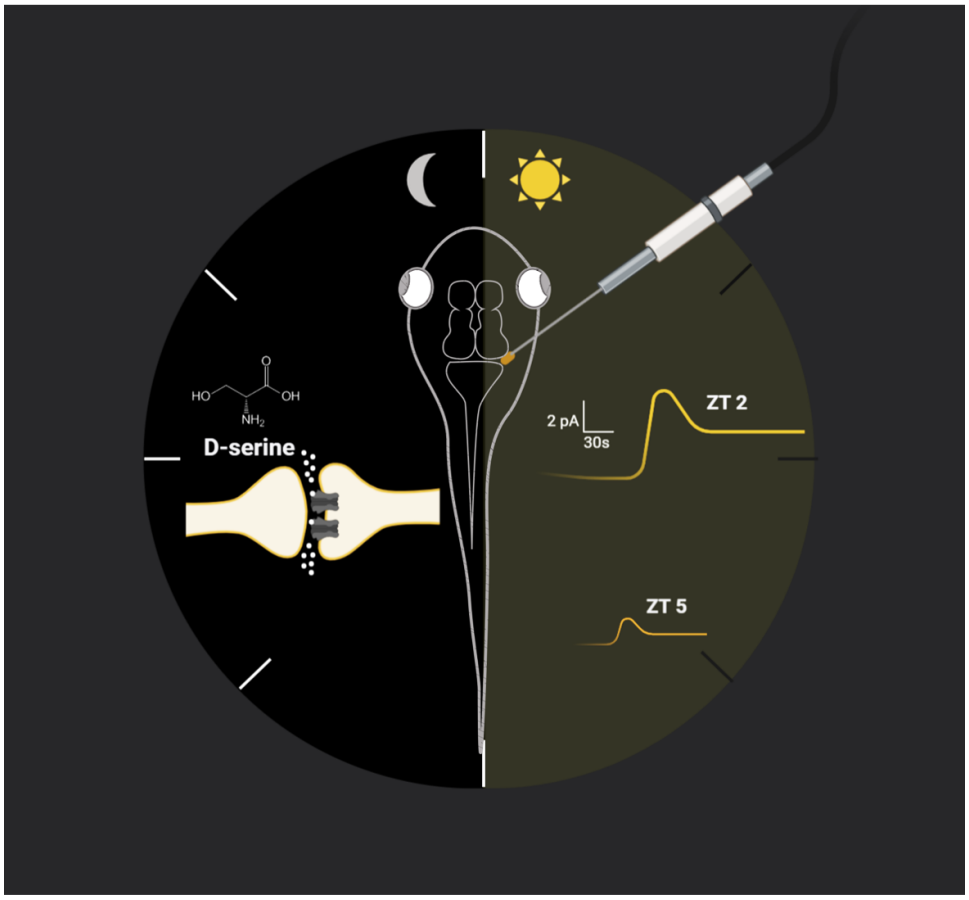

Chapter Preface

D-serine has been implicated as a brain messenger with central roles in neural signaling and plasticity. Disrupted levels of D-serine in the brain have been associated with neurological disorders, including schizophrenia, depression and Alzheimer's disease. Electrochemical biosensors are attractive tools for measuring real-time *in vivo* D-serine concentration changes. Current biosensors suffer from relatively large sizes ($\geq$ 25 μm) making localized cellular measurements challenging, especially for single cell studies.

Chapter 3 presents a robust methodology for the fabrication of a reproducible miniaturized 10 μm D-serine detecting amperometric biosensorkkkkkk. The miniature biosensor incorporated yeast D-amino acid oxidase immobilized on a PPD modified 10 μm Pt disk microelectrode. The biosensor offered a limit of detection of 0.361 μM (RSD <10 %) with high sensitivity (283 μA cm^{-2} mM^{-1}, $R^2 = 0.983$). The biosensor was stable for over four hours of continuous use, demonstrated a storage stability of four days and high analyte selectivity. Biosensor selectivity was validated with LC-MS and interferences with yeast D-amino acid oxidase were evaluated using drugs believed to stimulate D-serine release. *Ex vivo* D-serine measurements were made from Xenopus laevis tadpole brains, demonstrating the utility of the biosensors for measurements on living tissue. We observed that D-serine levels in the brain fluctuate with sensory experience. The biosensors were also used *in vivo* successfully. Taken together, this study addresses factors for successful and reproducible miniature biosensor fabrication for measuring D-serine in biological samples, for pharmacological evaluation, and for designing point of care devices.

The work presented in Chapter 3 is reproduced from:

Moussa S., Van Horn M., Shah A., Pollegioni L., Thibodeaux C.J., Ruthazer E.S., Mauzeroll J., A Miniaturized Enzymatic Biosensor For Detection of Sensory-Evoked D-serine Release in the Brain, *Journal of the Electrochemical Society*, **2021**,168(02),1-10.

3.1 Introduction

Free D-serine is a commonly occurring D-amino acid, detected in many organisms from bacteria to mammals.[1,2] In the brain, D-serine is DAAO[3,4] and has been identified for its role as a co-agonist of N-methyl-α-aspartate type glutamate receptors.[5–8] D-serine levels are disrupted in many neurological diseases including schizophrenia, depression and Alzheimer's disease, making it an important biomarker of diseased states.[9,10] Classical D-serine detection methods include immunostaining,[8] electrophysiology,[11] and analytical detection.[12] Many of these tools are indirect, time-consuming, costly, and lack quantitative information.[13,14] For example, D-serine concentration measurements in biological samples often rely on high-pressure liquid chromatography[15] and liquid chromatography-mass spectrometry (LC-MS)[16–18] based techniques.[19,20] While these methods offer high sensitivities, they are costly, require well trained users and do not allow for real time measurements.[21] Biosensors are a relatively low cost and simple alternative for quantitative D-serine measurements.[22–29] D-serine detection using electrochemical biosensors requires the specific reaction of DAAO immobilized onto a 10 μm PPD-modified Pt ME (Figure 3.1). The reaction of DAAO with D-serine generates stoichiometric amounts of H_2O_2, which is oxidizable at the Pt tip under constant potential application (0.5 V vs Ag/AgCl), as well as hydroxypyruvate and ammonia. Successful detection of D-serine with respect to sensor miniaturization relies on the rates of 1) mass transport of D-serine towards DAAO 2) substrate turnover with H_2O_2 production by DAAO 3) H_2O_2 diffusion through the permeable PPD layer and 4) H_2O_2 reaction at the electroactive Pt surface.

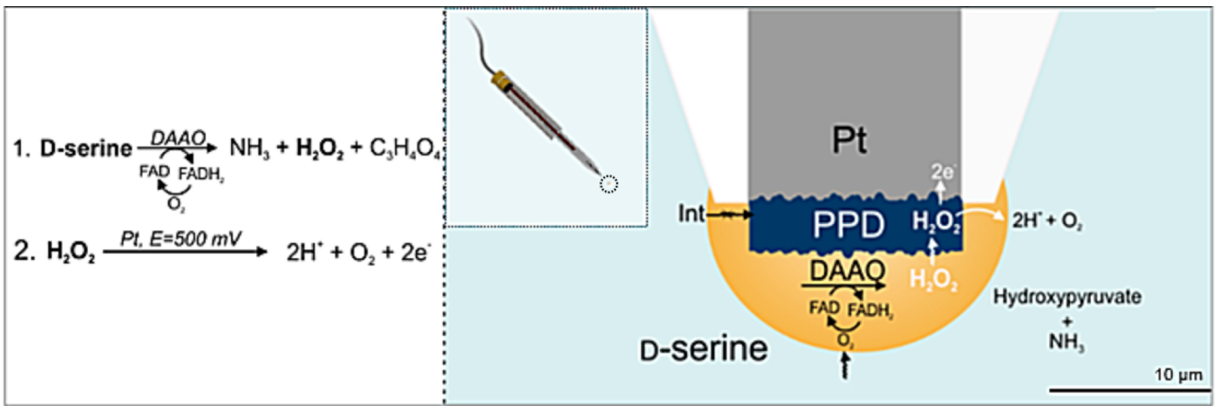

Figure 3.1: D-serine detection strategy using a disk-shaped amperometric enzymatic. Left: Mechanism of D-serine detection. Step 1- D-serine reacts with immobilized *Rg*DAAO with tightly bound flavin adenosine dinucleotide (FAD), and is oxidized into hydroxypyruvate and ammonia in the presence of oxygen. Molecular oxygen oxidizes $FADH_2$ back to FAD, producing equimolar H_2O_2. Step 2- The H_2O_2 diffuses through the permselective PPD layer, blocking out interferences (Int.), and is oxidized at the polarized Pt surface. Right: Schematic representation of the final biosensor tip geometry. Inset: Schematic of full biosensor geometry.

While D-serine sensors of various shapes and sizes have been designed,[30–33] there is still significant demand to further miniaturize these sensors for minimally invasive recordings. We previously demonstrated larger biosensor application to probe D-serine release from Xenopus laevis brains where the ventricular and pial surfaces of the optic tectum were exposed to the biosensor.[34] Due to the larger biosensor size, it was not possible to implant the biosensor directly in the brain of a live intact animal. Improving the ability to more precisely localize physiological changes in D-serine levels is tied to the spatial resolution of these sensors and remains vital for studies investigating the mechanisms regulating D-serine release and uptake. The goal of this work is to demonstrate that miniaturized electrochemical biosensors may be applied for *in vivo* D-serine detection in Xenopus as well as for single cell imaging.

We present the development and comparison of a biosensor that is two orders of magnitude smaller than previously reported. The stability, sensitivity, reproducibility, optimal storage conditions and applicability of this biosensor are reported. We also identified pharmacological drugs thought to simulate D-serine release that interfere with DAAO. Results were validated using elctrospray ionization (ESI)-LS-MS. To deduce biologically relevant information from biosensor application in complex biological environments, Xenopus laevis tadpoles were used as a vertebrate model, where D-serine has been shown to play an important role in promoting synapse maturation.[35] The biosensor was used *ex vivo* to determine if D-serine levels in the tadpole brain fluctuate across the day, a finding recently reported in mice.[36] Biosensor application in Xenopus brain confirmed circadian fluctuation of D-serine levels, especially during light-to-dark transitions when tadpole locomotor activity was found to be increased. Following biosensor response validation with complementary LC-MS experiments, the first-ever reported biosensor measurement inside the brain of live Xenopus was performed, suggesting these biosensors as a promising method for studying the mechanisms underlying D-serine release in Xenopus *in vivo* as well at the single cell level.

3.2 Experimental Section

3.2.1 Materials and Chemicals

Calcium chloride, calcium nitrate, glucose, HEPES, magnesium chloride, magnesium sulfate, potassium chloride, sodium chloride, and sodium bicarbonate were purchased from

VWR (Mississauga, Canada). All other reagents were purchased from either Fisher Scientific (Ottawa, Canada) or Sigma-Aldrich (Oakville, Canada).

3.2.2 Enzyme Preparation

*Rg*DAAO WT (*Rg*DAAO WT, EC 1.4.3.3) was overexpressed in *E.*coli cells and purified to homogeneity as previously reported.[37] The final enzyme solution was concentrated to 56.8 $mg.mL^{-1}$ protein in PBS (0.01 M, pH 7.4) containing 1 % glycerol and 25 $mg.mL^{-1}$ BSA. Pure *Rg*DAAO had a specific activity of $\approx$ 75 $U \cdot mg^{-1}$ on D-serine based on an oxygen consumption assay.

3.2.3 Microelectrode Preparation and Characterization

MEs were fabricated according to a published protocol[38] using carbon fibre (d=7 or 10 μm) or platinum wire (d=10 or 25 μm) (Goodfellow, Huntington, U.K.). The glass portion of the final ME tip was removed with a No.10 surgical scalpel blade (Sigma). The resulting tip was mechanically polished (240 rpm, 4000 grit Silicon carbide grinding paper, 10 min) using a TegraPol-25 grinder/polisher (Struers Ltd., Mississauga, Canada) to expose the Pt disk-shaped surface. The ME was then washed and sonicated in 18.2 MΩ water, 70 % ethanol, and acetone. The R_g of the MEs was characterized optically using a customized Axio Vert.A1 inverted microscope. The fabricated electrodes had an R_g between 2-3. The roughness factor (R_f) of the MEs associated with the polishing protocol was determined by cyclic voltammetry in degassed (N_2 bubbling) 1M H_2SO_4 according to a published protocol (0.02 Vs^{-1}, -0.30 V – 0.75 V vs. commercial saturated mercury-mercurous sulfate reference

electrode, CH instruments USA).[39]

3.2.4 Pt Microelectrode Surface Modification and Stability

The Pt surface was coated with 100 mM PPD in PBS (0.01 M, pH 7.4) through cyclic voltammetry-based electropolymerization (5 cycles, -0.10 V to +1.0 V, 0.10 V s^{-1}). To remove residual surface bound monomer, the PPD-ME was cycled in PBS (20 cycles, -0.1 to 0.5 V, 0.10 V s^{-1}). For PPD stability testing, the PPD-ME was subjected to an electrochemical stress test in 100 μM H_2O_2 for over 300 cycles using cyclic voltammetry. The long-term stability of the PPD layer under dry storage at 4^{o}C was examined using chronoamperometry where the response to the oxidation of 10 µM H_2O_2 (0.5 V) was monitored over a period of four weeks.

3.2.5 Final Biosensor Fabrication

To fabricate the full biosensor, 2 μL of *Rg*DAAO (56.8 mg mL^{-1} in 25 mg mL^{-1} BSA) was dropcasted onto a PDMS coated glass slide (2-part kit, SYLGARD 184 Silicone Elastomer, Dow Chemicals). This was done to improve the hydrophobicity of the surface to facilitate enzyme deposition onto the PPD-ME tip. The PPD-ME was immersed in the enzyme droplet for five seconds and then removed to dry for 4 min. This was repeated four times until approximately 0.5 µL of enzyme had adsorbed onto the PPD-ME surface. The biosensor was then placed in a desiccator containing 10 mL of glutaraldehyde (50 % v/v in H_2O) to vapor crosslink the *Rg*DAAO for 10 min. Null biosensors were produced using the exact same protocol described above with the exception of the *Rg*DAAO enzyme. The biosensors were

left in PBS for 20 min to stabilize the electrochemical signal and rehydrate the enzyme/PPD layers before use.

3.2.6 LC-MS Validation Experiments

For biosensor validation with LC-MS, conditioned medium (CM) from ATP-stimulated *ex vivo* brain preparations were derivatized with Marfey's reagent according to modified version of a literature protocol.[40] Briefly 50 µL of each sample was derivatized with 25 µL 0.5 % Marfey's reagent (wt/vol in acetone) and 50 µL 0.125 mol/L anhydrous disodiumtetraborate (in milli-Q-water) for 30 min at 40^oC under drying with a nitrogen steam. The reaction was stopped by addition of 12.5 µL 4 M HCl. The resulting solution was diluted (1:10) with eluent buffer (250 mg ammonium formate in 1 L milli-Q-water; pH adjusted to 4.6 with formic acid). The resulting sample was centrifuged (BioRad, 4000 rpm, 10 mins) and 10 µL of the supernatant were subjected to LC-MS using electrospray ionization (ESI) in negative ion mode. MassLynx software, which included QuanLynx (Waters), was used for instrument control, data acquisition, and data processing to obtain the area under the curve of the peaks and their retention times. Full instrumentation details are provided in Appendix C.

Chromatographic Conditions.

Samples were chromatographically resolved on Waters BEH C18 UPLC column (130 Å, 1.7 µm, 1x100 mm) using a 4 mM ammonium formate (mobile phase solvent A, pH=4.6)/acetonitrile (solvent B) system with a linear gradient of 3-100 % solvent B applied over 10 min. The flow rate was 50 µL/min.

Mass Spectrometric Conditions.

A triple quadrupole mass spectrometer (Waters) was used in the negative ESI mode. For analysis, extracted ion chromatograms were generated using the $[M\text{-}H]^{1-}$ ion of the dinitrophenyl-L-alanine-amide (Marfey) adduct of serine (m/z=356.1). Raw m/z values were corrected with a Leuenkephalin external standard.

3.2.7 Husbandry

All procedures were approved by the Animal Care Committee of the Montreal Neurological Institute at McGill University in accordance with Canadian Council on Animal Care guidelines. Albino Xenopus laevis frogs (RRID:$NXR_{0.0082}$) were injected with human chorionic gonadotropin (Sigma) and pregnant mare serum gonadotropin (Sigma) to induce mating. Eggs were collected and raised in 0.1x Modified Barth's Solution with HEPES (MBS-H; 88 mM NaCl, 1 mM KCl, 2.4 mM $NaHCO_3$, 0.82 mM $MgSO_4$ $7H_2O$, 0.33 mM $Ca(NO_3)_2$, $4H_2O$, 0.41 mM $CaCl_2$, 10 mM HEPES, pH 7.4). Animals were raised under a 12-h/12-h light-dark cycle at 20^oC until stage 48. All animals were reared under these conditions unless otherwise stated.

3.3 Electrochemical Experiments

Electrochemical measurements were performed using either an Electrochemical Probe Scanner 3 (ELP3, Heka Elektronik, Lambrecht, Germany, bipotentiostat model PG340) or an

Axopatch 200B amplifier (Molecular Devices, Sunnyvale, U.S.A.) enclosed in a Faraday cage and on a vibration dampening table (Micro 60, Halcyonics, Ames, IA, USA). All potentials were recorded relative to an in-house fabricated Ag/AgCl QRE at room temperature.[38] To select the potential of H_2O_2 oxidation in the amperometry experiments, the onset of H_2O_2 oxidation was determined using cyclic voltammetry (0.10 V.s^{-1}, 0 - 1.0 V, 20 cycles). To confirm the selectivity of the PPD-ME backbone towards H_2O_2 over other interferences, chronoamperometric measurements were performed (+0.5 V vs. Ag/AgCl). To confirm the effect of drugs used for evoked D-serine release, PPD-MEs were used.

The full biosensor was calibrated *in vitro* against 0-50 µM D-serine in PBS (0.01 M, pH 7.4) using chronoamperometry (5 min, 0.5 V). Fully fabricated biosensors were also tested for their storage stability post application in six hour-long experiments. The sensors were stored either dry or in PBS at 4^{o}C or in PBS and calibrated against standard solutions of D-serine (0-50 µM, in PBS, pH=7.4).

ELP 3 data was collected at a sampling frequency of 100 Hz and analog filtered (Current: Bessel 0.067 kHz, Voltage: 10 Hz, Stimulus: 1 kHz, Notch Filters: On). A smoothing digital filter was applied pre-data processing. All presented potentials are against an Ag/AgCl QRE.

3.3.1 Brain Preparations and *Ex Vivo* Measurements

Following anesthesia by immersion in 0.02 % MS222 0.1× MBS-H were dissected out from stage 48 tadpoles at different times of the day. Five brains were dissected at each time point and placed in a single Eppendorf with 200 µL artificial cerebrospinal fluid (aCSF), containing

115 mM NaCl, 2 mM KCl, 3 mM $CaCl_2$, 3 mM $MgCl_2$, 5 mM HEPES, 10 mM glucose, at pH 7.4. The brains were incubated for 90 min prior to electrochemical D-serine detection. To explore the effect of ATP stimulation on D-serine release, 1 mM adenosine triphosphate (ATP) was added to the aCSF prior to incubation.

A separate set of tadpoles were raised in complete darkness for 7-8 days. To study the effect of light on these animals, a group was subjected to two hours of light. Brains were dissected from the two groups at the same time and each sample was incubated for 90 min prior to electrochemical D-serine detection. Prior to electrochemical detection, biosensors were calibrated in standard solutions of 0-25 µM D-serine.

3.3.2 Recording Xenopus Laevis Tadpole Behaviour

Stage 48 tadpoles were tested individually in 6-well microtiter plates. The movement of each tadpole was monitored with a DanioVision Observation Chamber for 1 h (Noldus Information Technology). The experimental set-up provided visible (430-700 nm) and infrared (800-950 nm) light and was manually changed every 10 min to record the behavior in either light or dark, respectively. Video was recorded from a Basler GenICam (Basler acA1300-60) that fed into a standard PC (Dell Precision Tower 3620) for real-time tracking. Ethovision XT 13 (Noldus Information Technology) was used to extract locomotion data including distance travelled and velocity. The sampling rate was 25 frames per second. Statistics were averaged between the 6-wells over multiple days of experiments (n=5 experiments) monitored at the same time of day.

3.3.3 Whole Animal Preparations and *In Vivo* Measurements

Tadpoles were immobilized by immersion in 0.2 mM pancuronium bromide in 0.1 MBS-H rearing solution and placed in HEPES-buffered extracellular saline. The animal was pinned to a Sylgard block and a small incision was made in ventricle space at the caudal optic tectum to allow for biosensor placement in the brain tissue. While pinned to the Sylgard, the animal was placed in recording chamber with room temperature aCSF.

A Narishige micromanipulator was used to immerse the biosensor, held at a constant potential of 0.5 V, in aCSF and away from the animal in the recording chamber. The biosensor stabilized in aCSF for 10-15 minutes in this configuration prior to implanting the biosensor into the brain tissue. After 10 minutes of biosensor electrochemical signal recording in the brain tissue, the animal was simulated with light pulses for 5 minutes. The electrochemical signal was recorded inside the animal brain for a period of 10 minutes. Similar experiments were also repeated with null sensors. Close attention was paid to ensure that the angle and orientation of the biosensor were consistent between experiments.

3.3.4 Data Analysis and Statistics

Data sets were analyzed using Matlab R2016a (Mathworks, Natick, U.S.A.Results). Matlab was also used to generate figures. Error propagation calculations were performed with in-house Matlab code. The steady state current (i_{ss}) is defined as the maximum current response at which the current is static. Data are presented as mean ± standard error of the mean (S.E.M). n values refer to the number of individual experiments. ne refer to the number

of individual electrodes. Normalized current values (i_{norm}) are presented as blank corrected currents. Digital filtering of the electrochemical data to remove noise was performed using a smoothing digital filter on Matlab (Savitzky-Golay).

The limit of detection (LOD) is defined as 3 times the standard deviation of the blank divided by the slope of the regression line. The limit of quantitation (LOQ) is defined as 10 times the standard deviation of the blank divided by the slope of the regression line. The relative standard deviation (RSD) is defined as the standard deviation of the mean divided by the mean value times 100. Comparisons between two groups were performed using the Student's t-test (significance level of $p < 0.05$).

3.4 Results and Discussion

3.4.1 Backbone Biosensor Miniaturization and Characterization

Single mammalian brain cells are between 4-100 µm in diameter.[41] Previous electrode designs for D-serine detection are no smaller than 80-100 µm in diameter post-enzyme immobilization, making it difficult to achieve localized single cell measurements.[12] Moreover, *in vivo* measurements with larger sensors, especially cylindrical-shaped sensors, result in reduced sensor implantation accuracy[42] and increased stress associated H_2O_2 levels from tissue damage[43–45]. To explore whether biosensor miniaturization was feasible using the current design, disk-shaped MEs of different sizes (7- 25 µm) and materials (platinum, carbon) were fabricated according to published protocol.[38] While platinum/iridium (Pt/Ir) alloy electrodes are

also common materials for neural applications as shown in Table B.1, their high costs and difficulty to pull into smaller wires complicates the development of miniaturized disk-shaped biosensors.

Reducing the Pt diameter favors biosensor miniaturization (Figure 3.2A) and improves current densities. Compared to 25 µm bare MEs, 10 µm MEs offered higher characterization current densities with a ratio of j_{25}/j_{10}=0.360 ± 0.057 (Figure 3.2B). Increased current density of smaller electrode sizes is attributed to enhanced mass transfer[46] and reduced capacitive current[47]. Lower capacitive currents are tied to double layer charging and iR drops which result in reduced time constants and response time.[47]

To ensure biosensor reproducibility, the roughness factor (R_f) of the bare MEs was characterized in 1M H_2SO_4 (R_f= 3.89 ± 0.3). Challenges in increasing surface roughness with mechanical polishing emerge as the electrode size is decreased[48], making it difficult to roughen electrodes further while maintaining electrode reproducibility.

Moreover, while carbon is an attractive catalytic material due to its low cost and electrical properties[49], cyclic voltammograms and chronoamperometric measurements in H_2O_2 demonstrate limited electrocatalytic activity of carbon towards H_2O_2 oxidation (Figure B.1). Pt MEs, surpass carbon electrocatalytic activity towards H_2O_2 oxidation (Figure 3.2C). CVs of 10 µm bare Pt MEs in 100 µM H_2O_2 show a H_2O_2 oxidation onset potential between 0.5-0.6 V (Figure 3.2D), also observed with 25 µm bare Pt MEs (Figure B.2). Thus for H_2O_2 amperometric detection, 0.5 V (vs. Ag/AgCl) was chosen as the oxidation potential.

Electrodeposition of the PPD layer onto the bare Pt MEs (Figure 3.2E) demonstrated increased PPD layer thickness for the smaller MEs despite using the same electrodeposi-

tion protocol (5 cycles, 0.10 Vs^{-1}, -0.10 V to 1.0 V)[34,50] as confirmed by the surface area normalized electrodeposition charge ratio (Q_{25}/Q_{10}=0.771). However, reducing the number of PPD cycles from 5 cycles to 3 cycles did not positively impact the H_2O_2 sensitivity of the PPD-modified ME (B). Following PPD deposition, PPD film stress tests of the modified Pt ME with cyclic voltammetry in 10 µM H_2O_2 demonstrated high stability to PPD film delamination (Figure 3.2E). Moreover, electrochemical cleaning post PPD deposition through cyclic voltammetry in PBS was performed to remove all the residual monomer on the PPD-modified ME surface (Figure B.3A). When stored for a period of four weeks under dry conditions at 4^oC, the PPD film is stable towards the oxidation of 10 µM H_2O_2 (Figure B.3C).

Decreasing the electrode size does not significantly impact its selectivity[51] as confirmed by the PPD-ME response to common neurological interferences tested at physiologically relevant concentrations (Figure B.4A). While the PPD layer blocks 83 % of the H_2O_2 signal, the PPD-ME exhibits a preferential capacity to detect H_2O_2 amongst the other analytes tested post-PPD modification (Figure B.4B).

3.4.2 Biosensor Calibration, Detection Reproducibility and Performance Comparison

Although the biosensor backbone was miniaturized and characterized, the eventual success of the final design was not guaranteed. This is especially true with regards to enzyme loading, instrument sensitivity and overall biosensor limit of detection. More importantly, robust

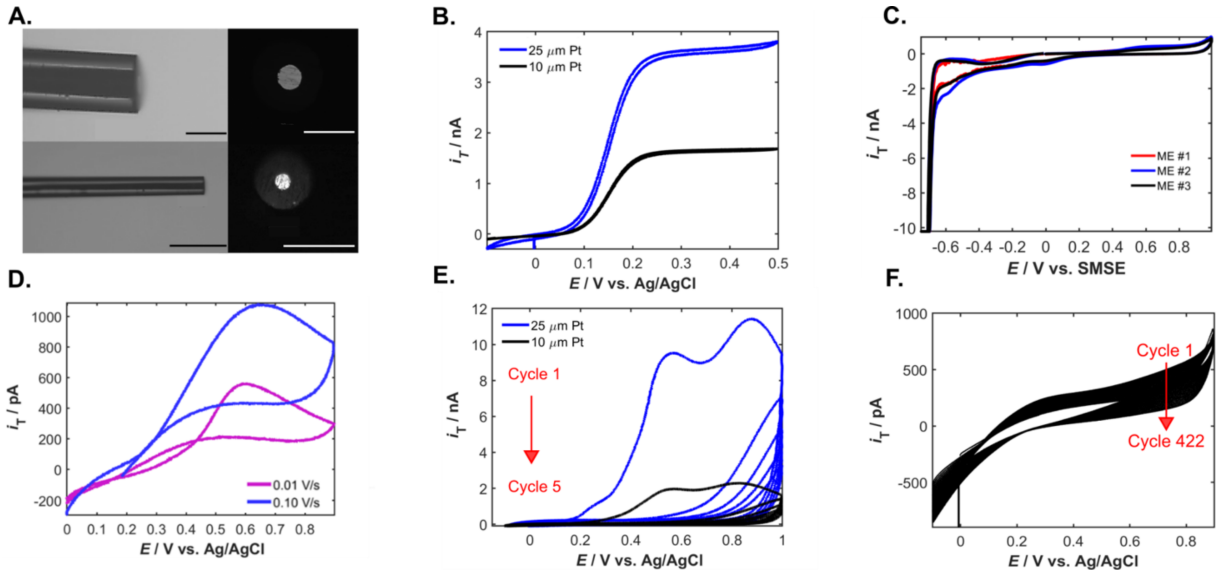

Figure 3.2: Fabrication and characterization of PPD-Pt MEs for H_2O_2 oxidation. (A) Optical micrographs show side and top views of the larger bare sensor (25 µm Pt) and the miniaturized bare sensor (10 µm Pt). All scale bars represent 50 µm. B) Characterization of the Pt MEs in 1 mM FcMeOH C) Cyclic voltammograms representing ME surface roughness characterizations in 1 M H_2SO_4. Each cyclic votammogram corresponds to a different ME. D) Oxidation of 100 µM H_2O_2 with the 10 µm Pt MEs at 0.10 Vs^{-1} (blue) and 0.01 Vs^{-1} (purple). E) Cyclic voltammograms representing the two electron electrodeposition of PPD on the Pt-ME surface. F) Stress tests of PPD-Pt 10 µm MEs in 10 µM H_2O_2 (422 cycles).

biosensor fabrication is essential for biosensor reproducibility.

The functionality and reproducibility of the final biosensor for D-serine detection was evaluated through use of fully constructed biosensors with fresh concentrated *Rg*DAAO and glutaraldehyde (Figure 3.3A). The full biosensor was fabricated and calibrated against standard solutions of 2.5 - 50 µM D-serine, a range appropriate for measurements of D-serine levels in the brain 34 (Figure 3.3B). The LOD of the biosensor was 0.361 µM ± 0.08 (n_e = 7, interelectrode RSD = 6.614 < 10 %). High biosensor reproducibility and robustness was achieved (82 % success rate, n_e = 9) using the final methodology outlined in the exper-

imental section. Importantly, the biosensor's linear and stable response was best achieved by using fresh enzyme and glutaraldehyde. Prolonged enzyme storage (>1 year) and use of glutaraldehyde solutions not prepared on the day of the biosensor fabrication, led to unstable and nonlinear behavior (B.5), likely due enzyme loss of activity . The biosensor performance was also compared to that of previous (25 µm Pt backbone) and commercial designs (DSER Probe, Sarissa Biomedical) (Figure 3.3C). It is worth nothing that biosensor current responses decrease significantly with miniaturization[34], such that the 10 µm biosensor is the miniaturization limit of biosensors with the same geometry and design.

To account for different backbone ME geometries and sizes, current was normalized to surface area and current density was used as a comparison parameter. Although the biosensor is smaller with respect to surface area, the miniaturized biosensor current density was similar to that of the 25 µm Pt backbone biosensors. The biosensor sensitivity was 283 $\pm$ 6 µA cm^{-2} mM^{-1} ($n_e = 7$), demonstrating a performance comparable with other electrode designs (Table B.1).

Moreover, optimal storage conditions for these biosensors was explored through wet and dry storage at 4^oC over a period of four days. Biosensors were calibrated in D-serine standard solutions each day and the resulting calibration curves are shown in Figure B.6. Wet storage of biosensors resulted in lack of biosensor stability (Figure B.6A) while dry storage of the biosensors resulted in a 55.2 % $\pm$ 8 % slope decrease over 24 hours of storage. A slope decrease of 68.0 $\pm$ 8 % after 72 hours of storage from the original biosensor calibration curve slope prior to application and storage was also observed (Figure B.6C).

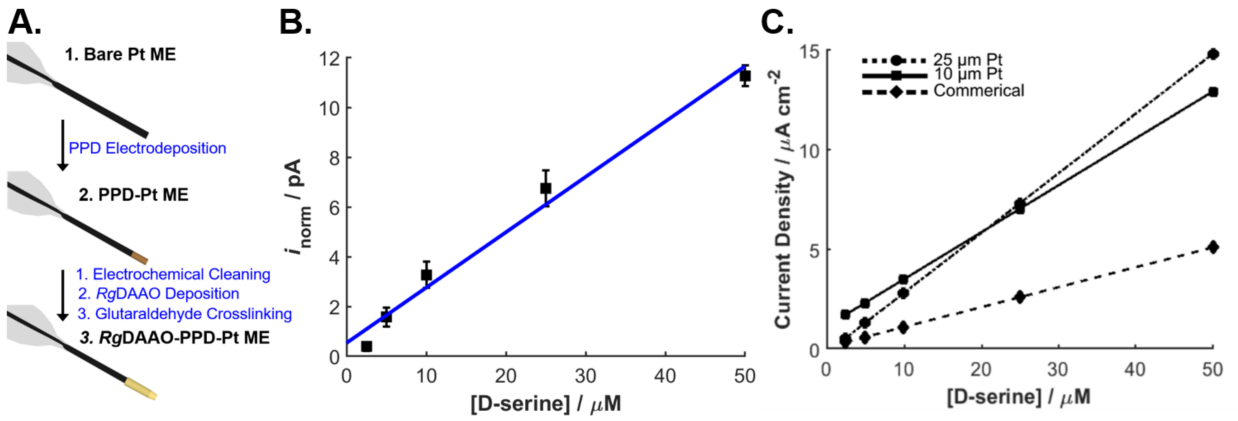

Figure 3.3: Biosensor development, *in vitro* characterization of the biosensor, and comparison to other designs. A) Schematic illustration outlining the key steps in biosensor fabrication B) Calibration curves for the steady state current corresponding to 0-50 µM D-serine. I (pA)=0.223 x C (µM) + 0.537 ; R^2=0.983, LOD= 0.361 µM ± 0.08 , LOQ=1.20 µM ± 0.03 (n=7 individual biosensors). C11urrents were measured at constant potential (0.5V). C) Current density response towards 0-50 µM D-serine was measured with a commercially available cylindrical biosensor (dashed line), the experimental disk-shaped biosensor (dotted line) and the miniaturized disk biosensor (solid line).

3.4.3 Biosensor Evaluation of Drug Candidate Inteferences Used to Evoke D-serine Release

Glutamate, acting on α-amino-3-hydroxy-5-methyl-4-isoxazolepropionic acid (AMPA) type glutamate receptors as well as adenosine triphosphate (ATP) and norepinephrine (NE) have been suggested to activate a second-messenger signaling cascade in the brain that can induce the release of endogenous D-serine.[35,52–55] The ability of AMPA, ATP and NE to drive D-serine release makes them potentially useful candidates as positive controls when using the biosensor for endogenous D-serine release detection. However, their use is contingent upon the absence of any direct interactions with the electroactive Pt portion of the biosensor or

the *Rg*DAAO enzyme itself, which would produce nonspecific readings.

The biosensor responses *in vitro* demonstrate that NE, also a redox-active molecule, is a substrate of *Rg*DAAO as noted by the increased i_{ss} representing elevated levels of H_2O_2 production (Figure 3.4). Similarly, AMPA is a substrate for *Rg*DAAO.*Rg*DAAO has a higher activity on NE than on AMPA, ruling out NE as a drug to be applied in combination with an *Rg*DAAO based biosensor. In previous work, AMPA has been used to experimentally evoke the release of D-serine[34] from the brain, but our findings in the absence of animals indicate that AMPA is a substrate for *Rg*DAAO. In contrast, ATP was not found to generate a redox signal on its own or to promote production of H_2O_2 in the presence of *Rg*DAAO enzyme, making it well suited for stimulation of endogenous D-serine release when using biosensors.

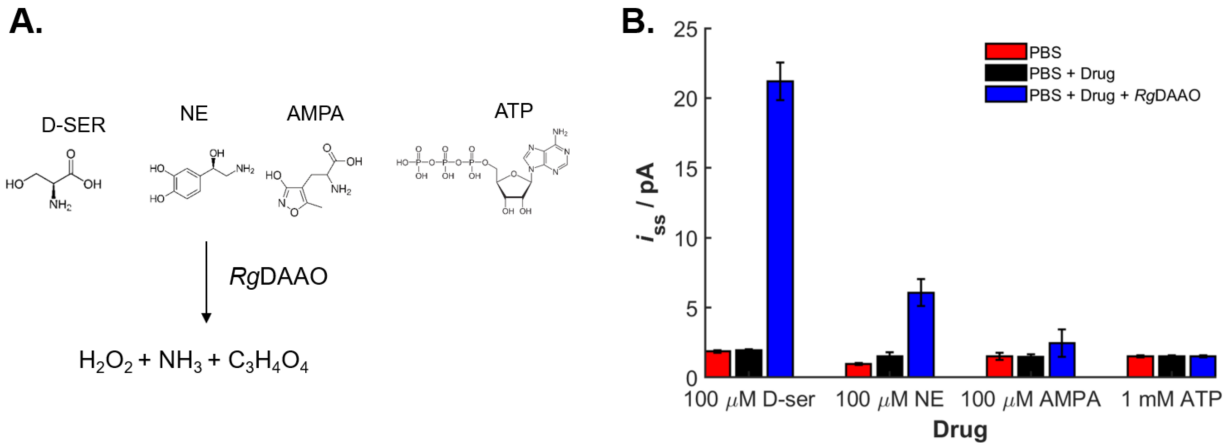

Figure 3.4: Activity of *Rg*DAAO on pharmacological drugs A) Chemical structure of tested molecules substrates of *Rg*DAAO. ATP is not a substrate for *Rg*DAAO reaction due to the large molecule size and structural dissimilarity of ATP. B) A PPD-Pt ME as used to explore the effect of pharmacological drugs on the *Rg*DAAO enzyme (0.142 mg mL^{-1}) as compared to D-serine effect on *Rg*DAAO. The steady state current was measured at 0.5 V in plain PBS (pH 7.4), after addition of the drug and of 0.142 mg mL^{-1} *Rg*DAAO (n=3, ± S.E.M.).

3.4.4 Biosensor Validation by LC-MS

To validate biosensor results, the evoked release of D-serine was measured with a biosensor as well as with LC-MS. Brains of stage 48 Xenopus tadpoles were dissected and five brains were incubated in 1 mM ATP in aCSF for 90 minutes to evoke D-serine release followed by parallel D-serine detection with LC-MS and a D-serine biosensor (Figure 3.5A).

An aliquot of the brain conditioned medium (CM) was derivatized with Marfey's reagent and subjected to chemical analysis by LC-MS. The derivatization protocol is shown in Figure 3.5B. Extracted ion chromatograms of derivatized extracts are compared against chromatograms for aCSF (Figure 3.5C), clearly indicating the presence of Marfey adducts of both L-serine (5.18 min) and D-serine (5.38 min) in the samples (m/z = 356.1). Under the same conditions, the retention time of an authentic standard of Marfey-derivatized D-serine was found to be 5.38 min (Figure 3.5D). Using this standard, a calibration curve was constructed for LC-MS quantitation of derivatized D-serine by correlating the area under the extracted ion chromatogram peak to D-serine concentration. Two independent linear ranges were observed for D-serine calibration curves obtained with LC-MS. The LC-MS calibration for concentrations ranging from 6.125 - 100 µM was used to determine the D-serine concentrations in the samples (Figure 3.5E). In addition to D-serine detection, the same methodology can be simultaneously applied for detection of additional amino acids using Marfey's derivatization (Figure B.7). Table B.2 lists several literature LC-MS methods used for the detection of amino acids, highlighting the extensive time required for sample preparation and amino acid detection as compared to biosensor detection which requires no sample

preparation.

The same sample was analyzed for D-serine by amperometric detection (Figure 3.5F): the estimated values (7.49 µM vs. 8.69 µM for the LC-MS vs. biosensor) showed a 15 % difference between the two quantification methods. These results validated the biosensor measurements since the LC-MS method is not significantly affected by any of the known interferences that could alter the amperometric responses.

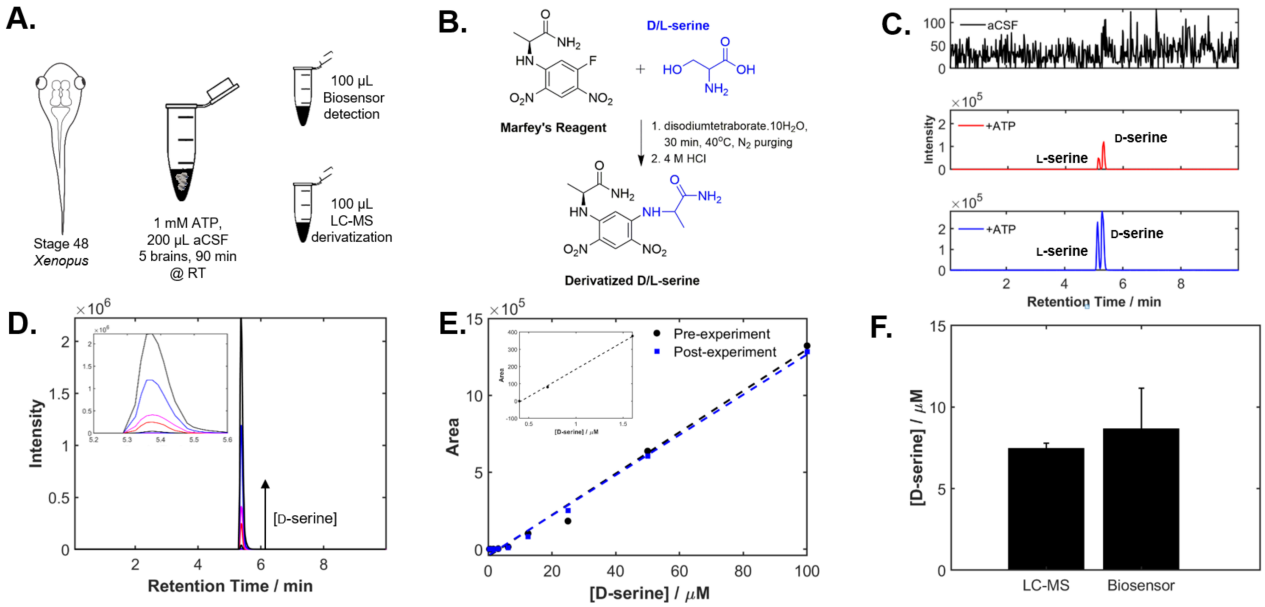

Figure 3.5: D-serine biosensor validation through detection of evoked D-serine release. A) Schematic of the experimental methodology used for biosensor validation. B) Schematic of the derivatization protocol with Marfey's reagent. C) LC-MS detection of ATP evoked D-serine release. Two samples each with five dissected brains were incubated in 1 mM ATP in aCSF for 90 min. An aliquot from each sample was extracted for derivatization with Marfey's reagent and 10 µL was subjected to LC-MS for detection. The extracted ion chromatograms corresponding derivatized aCSF (top), ATP-infused sample 1 (middle) and ATP-infused sample 2 (bottom) are shown. In the two ATP-infused brain samples, two separate peaks appear (from left to right): one for L-serine and one for D-serine. D) Extracted ion chromatograms corresponding to the LC-MS peaks for D-serine detection. The increasing intensity of the peaks corresponds to increasing D-serine concentrations. E) Calibration curve for LC-MS detection of derivatized standard D-serine solution where two linear ranges are present (0-1.5 µM and 6.25-100 µM). Calibration curve duplicates were run, one before D-serine detection with LC-MS and one following LC-MS D-serine detection. Inset: Calibration curve for the lower end of the linear range between 0-1.5 µM. F) Comparison of biosensor results (8.69 µM) with LC-MS detection of D-serine release (7.49 µM) of D-serine release under ATP stimulation.

3.4.5 Measurement of D-serine from Xenopus Brain Preparations

Prior to real-time *in vivo* D-serine detection, it was essential that the biosensor performance in a less complex biological environment be studied. As such, the biosensor was applied *ex vivo* to measure D-serine release from Xenopus. Previous research in mice provided evidence for D-serine level fluctuation as a function of wakefulness.[36] In particular D-serine levels were found to be highest after a full day of being awake. Here, we used the biosensor to explore whether a similar phenomenon exists in Xenopus tadpoles.

Stage 48 animals were sampled randomly from a group of animals raised under 12 h /12 h light-dark cycle for 7-8 days. To mitigate biosensor LOD, five brains were extracted and pooled to constitute a single sample and placed in a single Eppendorf with 200 µL room temperature aCSF. D-serine levels were measured with the biosensor in brain samples collected at various time points throughout the day (Figure 3.6A).

D-serine levels were measured following a 90-minute incubation period of the brains in the oxygen saturated aCSF. Previously calibrated biosensors were used as D-serine probes in the brain-conditioned aCSF (Figure 3.6B). Biosensors were calibrated in standard solutions of D-serine before and after D-serine detection experiments, demonstrating an operational lifetime of at least 4 h of continuous use (Figure B.8). Experiments with the null sensors were also performed to exclude the contribution of false positive signals in biosensor D-serine detection (Figure B.9). In this work, D-serine levels fluctuations as a function of Zeitgeber Time (ZT) were studied. Herein, ZT represents the light-driven environmental time cue which trigger Xenopus entrainment to a 24-hour cycle. Figure 3.6B shows a representative

result from the biosensor measurements at ZT2 and ZT5.

Comparison of D-serine levels at different dissection times reveals that D-serine levels fluctuate over a 24 h period (Figure 3.6C). D-serine levels were highest early in the light phase (ZT2) but rapidly declined until ZT5. D-serine levels were also high at the beginning of the dark phase (ZT14). In particular, significant elevations in D-serine levels were apparent during the initial switch from light-to-dark (ZT2) and dark-to-light (ZT14). Tracking the tadpole's behavior during transitions from dark to light revealed that tadpoles exhibited a higher level of swimming activity during this transition period (Figure 3.6D) consistent with the possibility that D-serine levels may increase as a function of wakefulness or locomotor activity.

To further explore the effects of light on D-serine level changes, tadpoles were raised in darkness until they reached developmental stage 48 for 1 week. One group of animals was then exposed to light for 2h between ZT0 and ZT2, while another group remained in darkness. D-serine detection from samples at ZT2 shows that D-serine levels are higher in the group of animals exposed to 2 h of light (Figure 3.6E). These results suggest that the increase in D-serine levels measured after the transition from dark to light is likely due at least in part to an increase in light-driven activity.

Moreover, ATP has been shown to activate calcium transients in astrocytes that induce transmitter release by binding to P2Y1 purinergic receptors.[56] To test whether D-serine release is evoked by pharmacological stimulation of ATP, 5 brains were incubated for 90 min 1 mM ATP at ZT 5. D-serine levels from the animal groups incubated in ATP are higher than any light driven D-serine release (Figure 3.6F), supporting the proposed role of ATP

in D-serine release mechanisms, validated with complimentary LC-MS data at ZT5 (Figure B.10). A third group used pharmacological stimulation by incubation in 1 mM ATP at ZT 5 to activate D-serine release.

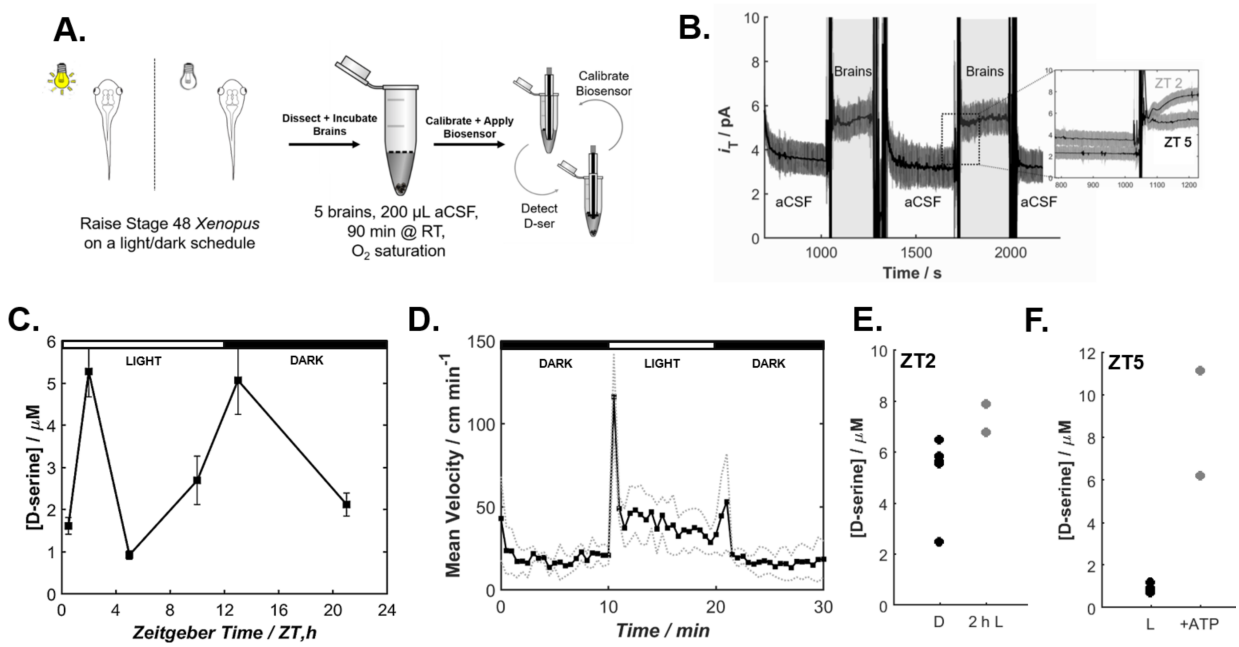

Figure 3.6: *Ex vivo* detection of D-serine release over a light-dark schedule A) Schematic of experiment protocol. B) Sample experiment. Unhighlighted portions represent the biosensor response in unconditioned aCSF. The highlighted portions represent the biosensor response in the brain-conditioned aCSF medium (CM). Expanded plot shows the difference in the current measured with the biosensor at ZT 2 and ZT 5 corresponding to a variation in D-serine levels. C) D-serine measurements in ZT0.5, ZT2, ZT5, ZT10, ZT14 and ZT22 CM (n $\geq$ 3). Error bars represent ± S.E.M. D) The average mean velocity of swimming in cm $\cdot$ s^{-1} of 5 independent experiments done with 6 tadpoles separately housed in a 6 well dish (n=30). Tadpoles were allowed to stabilize behavior for 10 min and then mean velocity was sampled every 30 seconds for alternating 10 min light and dark conditions. The dotted grey lines represent the average mean velocity ± S.D. E) D-serine measurements at ZT2 in CM from animals raised in complete darkness and then either kept in darkness (n=3), or exposed to light (n=2) for the 2 h immediately prior to sacrifice. Each point represents an individual measurement. F) D-serine measurements at ZT 5 in CM from animals raised under a 12 h L/ 12 h D schedule without (n=4) or with (n=2) the addition of 1mM ATP at the beginning of brain samples incubation in aCSF. Each point represents an individual measurement.

3.4.6 Biosensor Application *In Vivo*

Following successful biosensor *ex vivo* D-serine release studies, biosensor application in an increasingly challenging *in vivo* context for real-time local D-serine detection was explored. Biosensors were inserted into the optic tectum of intact tadpole animals. Following sensor stabilization and calibration in the perfusion chamber under animal absence, chronoamperometric recordings in Xenopus were performed to measure *in vivo* D-serine levels (n_e=4). A representative calibration curve in the perfusion chamber is shown along with the *in vivo* experiments (Figure 3.7A, Figure B.11). The *in vivo* LOD of the biosensors is 0.7 ± 0.2 µM. Under application of 0.5 V, the biosensor was allowed at least a 10 min stabilization in aCSF in the recording chamber away from the animal. The biosensor was then implanted into the ventricle space surrounding the Xenopus optic tectum (Figure 3.7B) and a 10 min baseline was measured. The ventricular space adjacent to optic tectum is a convenient location to measure extracellular D-serine levels without significant damage to the neural tissue. Subtraction of biosensor signal from the null signal resulted in the quantification of 3.73 ± 0.8 μM D-serine (Figure 3.7C). This amount may be attributed to passive diffusion of small molecules possibly assisted by the incision made in the optic tectum. Notably, video monitoring of blood flow and heart beat confirmed that the animals remained alive after the insertion of the sensor into the brain. As such, these experiments demonstrated successful biosensor application *in vivo* for real time D-serine detection enabling future work in single cell measurements of D-serine release.

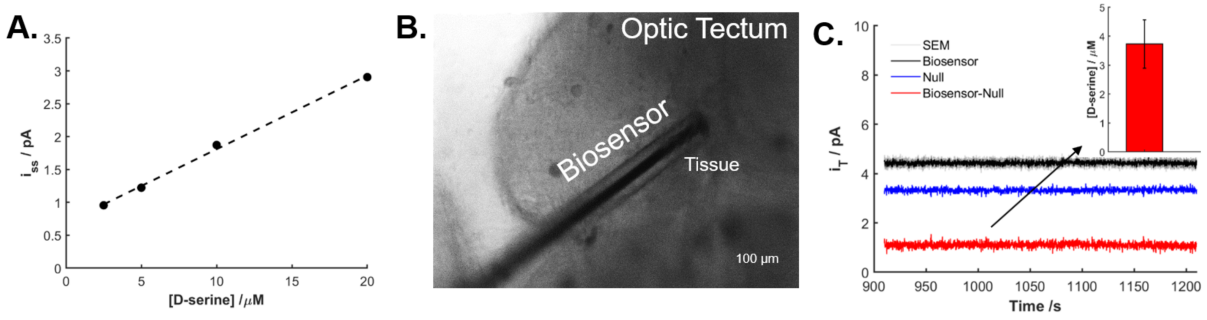

Figure 3.7: *In vivo* detection of D-serine inside the optic tectum of stage 48 Xenopus laevis tadpoles. Currents were measured at constant potential (0.5 V). A) Standard solutions of D-serine (0-20 μM) were flushed into the measurement chamber in the absence of the animal to calibrate the biosensor *in vivo* (t =20-30 min). B) Optical microscope image of the biosensor inserted inside the tissue of the optic tectum of an Xenopus laevis tadpole (Scale bar =100 μm. C) Detection of D-serine in the ventricular space representing D-serine in the cerebrospinal fluid *in vivo*. The difference in the current between the biosensor and the null was used to determine D-serine concentration. Inset: A concentration of 3.73 $\pm$ 0.8 μM D-serine was detected. Error bars represent the standard error of the mean.

3.5 Conclusion

We successfully miniaturized D-serine detecting biosensors and established their biosensing limits with regards to selectivity, sensitivity, reproducibility, stability, and practical applicability. This is the first report, to our knowledge, combining a comprehensive summary of sensor development, miniaturization, characterization as well as successful application for D-serine detection *ex vivo* and *in vivo* at the micromolar level. This study now paves the way for future application in other animal models to study D-serine at the molecular level under physiological and pathological conditions. In addition to biosensor characterization, we showed the importance of evaluating the biosensor against any pharmacological drugs prior to their application for evoked D-serine release, identifying ATP as a candidate for

application in biosensor studies to evoke D-serine release. More importantly, we also validated the hypothesis that D-serine release is a process tied to tadpole alertness and activity using a combination of biosensor D-serine detection and behavioral activity tracking experiments. Biosensor application *ex vivo* demonstrated that D-serine levels fluctuate between 1-5 μM depending on the time of the day, with the highest levels being during the initial switch from light to dark and dark to light. Tadpole locomotion experiments demonstrate that tadpole activity is highest during initial switches in light, suggesting that D-serine levels rise with increased Xenopus activity. Additionally, D-serine measurements from intact Xenopus demonstrated the first measurements of D-serine made in live Xenopus with enzymatic biosensors, without the need for brain preparation to expose cells to the biosensor. Currently, the future of these sensors includes extensive application *in vivo* for detection of sensory evoked D-serine as well as single cell D-serine release studies.

References

(1) Nishikawa, T. Analysis of Free D-Serine in Mammals and Its Biological Relevance. *J. Chromatogr. B* **2011**, *879*, 3169–3183.

(2) Hashimoto, A.; Nishikawa, T.; Hayashi, T.; Fujii, N.; Harada, K.; Oka, T.; Takahashi, K. The Presence of Free D-Serine in Rat Brain. *FEBS Lett.* **1992**, *296*, 33–36.

(3) Pollegioni, L.; Sacchi, S.; Murtas, G. Human D-Amino Acid Oxidase: Structure, Function, and Regulation. *Frontiers in Molecular Biosciences* **2018**, 1–14.

(4) Pollegioni, L.; Sacchi, S. Metabolism of the Neuromodulator D-Serine. *Cell. Mol. Life Sci.* **2010**, *67*, 2387–2404.

(5) Shleper, M.; Kartvelishvily, E.; Wolosker, H. D-Serine Is the Dominant Endogenous Coagonist for NMDA Receptor Neurotoxicity in Organotypic Hippocampal Slices. *J. Neurosci.* **2005**, *25*, 9413–9417.

(6) Mothet, J.; Parent, A.; Wolosker, H.; Brady, R.; Linden, D.; Ferris, C.; Rogawski, M.; Snyder, S. D-Serine Is an Endogenous Ligand for the Glycine Site of the N-Methyl-D-Aspartate Receptor. *PNAS* **2000**, *97*, 4926–4931.

(7) Schell, M.; Molliver, M.; Snyder, S. D-Serine, an Endogenous Synaptic Modulator: Localization to Astrocytes and Glutamate-Stimulated Release. *Neurobiology* **1995**, *92*, 3948–3952.

(8) Neame, S.; Safory, H.; Radzishevsky, I.; Touitou, A.; Marchesani, F.; Marchetti, M.; Kellner, S.; Berlin, S.; Foltyn, V.; Engelender, S.; Billard, J.; Wolosker, H. The NMDA Receptor Activation by D-Serine and Glycine Is Controlled by an Astrocytic Phgdh-Dependent Serine Shuttle. *PNAS* **2019**, *116*, 20736–20742.

(9) Hashimoto, K.; Si, T.; Baker, G.; Mackay, M.-A.; Kravtsenyuk, M.; Thomas, R.; Mitchell, N.; Dursun, S. D-Serine: Potential Therapeutic Agent and/or Biomarker in Schizophrenia and Depression? *Front. Psychiatry* **2019**, *10*, 25.

(10) Kumashiro, S.; Hashimoto, A.; Nishikawa, T. Free D-Serine in Post-Mortem Brains and Spinal Cords of Individuals with and without Neuropsychiatric Diseases. *Brain Res* **1995**, *681*, 117–125.

(11) Turpin, F.; Dallérac, G.; Mothet, J. Electrophysiological Analysis of the Modulation of NMDA-Receptors Function by d-Serine and Glycine in the Central Nervous System. *Methods Mol. Bio.l* **2012**, *794*, 299–312.

(12) Rosini, E.; D'Antona, P.; Pollegioni, L. Biosensors for D-Amino Acids: Detection Methods and Applications. *Int. J. Mol. Sci.* **2020**, *21*, 4574.

(13) Mothet, J.; Billard, J.; Pollegioni, L.; Coyle, J.; Sweedler, J. Investigating Brain D-serine: Advocacy for Good Practices. *Acta Physiol.* **2019**, *226*, 13257.

(14) Dai, X.; Zhou, E.; Yang, W.; Zhang, X.; Zhang, W.; Rao, Y. D-Serine Made by Serine Racemase in Drosophila Intestine Plays a Physiological Role in Sleep. *Nat. Commun.* **2019**, 1–10.

(15) Fukushima, T.; Kawai, J.; Imai, K.; Toyo'oka, T. Simultaneous Determination of D- and L-Serine in Rat Brain Microdialysis Sample Using a Column-Switching HPLC with Fluorimetric Detection. *Biomed. Chromatogr.* **2004**, *18*, 813–819.

(16) Biemans, E.; Verhoeven-Duif, N.; Gerrits, J.; Claassen, J.; Kuiperij, H.; Verbeek, M. CSF D-Serine Concentrations Are Similar in Alzheimer's Disease, Other Dementias, and Elderly Controls. *Neurobiol. Aging* **2016**, *42*, 213–216.

(17) Grant, S.; Shulman, Y.; Tibbo, P.; Hampson, D.; Baker, G. Determination of D-Serine and Related Neuroactive Amino Acids in Human Plasma by High-Performance Liquid Chromatography with Fluorimetric Detection. *J. Chromatogr. B Anal. Technol. Biomed. Life Sci.* **2006**, *844*, 278–282.

(18) Koval, D.; Jirásková, J.; Stříšovský, K.; Konvalinka, J.; Kašička, V. Capillary Electrophoresis Method for Determination Of D-Serine and Its Application for Monitoring of Serine Racemase Activity. *Electrophoresis* **2006**, *27*, 2558–2566.

(19) Sakamoto, T.; Kuwabara, R.; Takahashi, S.; Onozato, M.; Ichiba, H.; Iizuka, H.; Fukushima, T. Determination of D-Serine in Human Serum by LC-MS/MS Using a Triazole-Bonded Column after Pre-Column Derivatization with (S)-4-(3-Isothiocyanatopyrrolidin-1-Yl)-7- (N, N-Dimethylaminosulfonyl)-2,1,3-Benzoxadiazole. *Anal. Bioanal. Chem.* **2016**, *408*, 517–526.

(20) Howley, E. et al. Assessment of the Target Engagement and D-Serine Biomarker Profiles of the d-Amino Acid Oxidase Inhibitors Sodium Benzoate and PGM030756. *Neurochem. Res.* **2017**, *42*, 3279–3288.

(21) Zhao, S.; Yuan, H.; Xiao, D. Detection of D-Serine in Rat Brain by Capillary Electrophoresis with Laser Induced Fluorescence Detection. *J. Chromatogr. B Anal. Technol. Biomed. Life Sci.* **2005**, *822*, 334–338.

(22) Campos-Beltrán, D.; Konradsson-Geuken, Å.; Quintero, J.; Marshall, L. Amperometric Self-Referencing Ceramic Based Microelectrode Arrays for D-Serine Detection, en.

(23) Chatard, C.; Meiller, A.; Marinesco, S. Microelectrode Biosensors for in Vivo Analysis of Brain Interstitial Fluid. *Electroanal.* **2018**, *30*, 977–998.

(24) Di Pietrantonio, F.; Benetti, M.; Cannatà, D.; Verona, E.; Girasole, M.; Fosca, M.; Dinarelli, S.; Staiano, M.; Marzullo, V.; Capo, A.; Varriale, A.; D'Auria, S. A Shear Horizontal Surface Acoustic Wave Biosensor for a Rapid and Specific Detection of D-Serine. *Sensors Actuators B Chem* **2016**, *226*, 1–6.

(25) Zain, Z.; Ghani, S.; O'Neill, R. Amperometric Microbiosensor as an Alternative Tool for Investigation of D-Serine in Brain. *Amino Acids* **2012**, *43*, 1887–1894.

(26) Sacchi, S.; Rosini, E.; Caldinelli, L.; Pollegioni, L. Biosensors for D-Amino Acid Detection. *Methods Mol. Biol.* **2012**, *794*, 313–324.

(27) Yabuki, S.; Mizutani, F.; Hirata, Y. Preparation of D-Amino Acid Oxidase-Immobilized Polyion Complex Membranes. *Sens. Actuat. B Chem* **2001**, *76*, 142–146.

(28) Johansson, E.; Marko-Varga, G.; Gorton, L. Study of a Reagent- and Mediatorless Biosensor for D-Amino Acids Based on Co-Immobilized D-Amino Acid Oxidase and Peroxidase in Carbon Paste Electrodes. *J. Biomater. Appl.* **1993**, *8*, 146–173.

(29) Draghiciu, L.; Romanitan, C.; Parvulescu, C.; Tutunaru, O.; Müller, R.; Ignat, T. In *Proceedings of the International Semiconductor Conference*, Institute of Electrical and Electronics Engineers Inc: CAS, 2019, pp 263–266.

(30) Pernot, P.; Mothet, J.; Schuvailo, O.; Soldatkin, A.; Pollegioni, L.; Pilone, M.; Adeline, M.; Cespuglio, R.; Marinesco, S. Characterization of a Yeast D-Amino Acid Oxidase Microbiosensor for D-Serine Detection in the Central Nervous System. *Anal. Chem.* **2008**, *80*, 1589–1597.

(31) Maucler, C.; Pernot, P.; Vasylieva, N.; Pollegioni, L.; Marinesco, S. In Vivo D-Serine Hetero-Exchange through Alanine-Serine-Cysteine (ASC) Transporters Detected by Microelectrode Biosensors. *ACS Chem. Neurosci.* **2013**, *4*, 772–781.

(32) Papouin, T.; Haydon, P. D-Serine Measurements in Brain Slices or Other Tissue Explants. *Bio-Protocol* **2018**, *8*, 1–10.

(33) Zain, Z.; O'Neill, R.; Lowry, J.; Pierce, K.; Tricklebank, M.; Dewa, A.; Ghani, S. Development of an Implantable D-Serine Biosensor for in Vivo Monitoring Using Mammalian d-Amino Acid Oxidase on a Poly (o-Phenylenediamine) and Nafion-Modified Platinum-Iridium Disk Electrode. *Biosens. Bioelectron.* **2010**, *25*, 1454–1459.

(34) Polcari, D.; Kwan, A.; Van Horn, M.; Danis, L.; Pollegioni, L.; Ruthazer, E.; Mauzeroll, J. Disk-Shaped Amperometric Enzymatic Biosensor for in Vivo Detection of D-Serine. *Anal. Chem.* **2014**, *86*, 3501–3507.

(35) Van Horn, M.; Strasser, A.; Miraucourt, L.; Pollegioni, L.; Ruthazer, E. The Gliotransmitter D-Serine Promotes Synapse Maturation and Axonal Stabilization In Vivo. *J. Neurosci.* **2017**, *37*, 6277–6288.

(36) Papouin, T.; Dunphy, J.; Tolman, M.; Dineley, K.; Haydon, P. Septal Cholinergic Neuromodulation Tunes the Astrocyte-Dependent Gating of Hippocampal NMDA Receptors to Wakefulness. *Neuron* **2017**, *94*, 840–854.

(37) Fantinato, S.; Pollegioni, L.; Pilone, S.; Engineering, M. Expression and Purification of a His-Tagged Chimeric D-Amino Acid Oxidase from Rhodotorula Gracilis. *Enzyme Microb. Technol.* **2001**, *29*, 407–412.

(38) Danis, L.; Polcari, D.; Kwan, A.; Gateman, S.; Mauzeroll, J. Fabrication of Carbon, Gold, Platinum, Silver, and Mercury Ultramicroelectrodes with Controlled Geometry. *Anal. Chem.* **2015**, *87*, 2565–2569.

(39) Perry, S.; Gateman, S.; Sifakis, J.; Pollegioni, L.; Mauzeroll, J. Enhancement of the Enzymatic Biosensor Response through Targeted Electrode Surface Roughness. *J. Electrochem. Soc.* **2018**, *165*, 3074–3079.

(40) Fuchs, S.; De Sain-Van Der Velden, M.; De Barse, M.; Roeleveld, M.; Hendriks, M.; Dorland, L.; Klomp, L.; Berger, R.; De Koning, T. Two Mass-Spectrometric Techniques for Quantifying Serine Enantiomers and Glycine in Cerebrospinal Fluid: Potential Confounders and Age-Dependent Ranges. *Clin. Chem.* **2008**, *54*.

(41) Kandel, E.; Schwartz, J.; Jessel, T. Principles of Neural Science, es, accessed Apr 18, 2020).

(42) He, W.; Bellamkonda, R., A Molecular Perspective on Understanding and Modulating the Performance of Chronic Central Nervous System (CNS) Recording Electrodes In *Indwelling Neural Implants: Strategies for Contending with the in Vivo Environment*; CRC Press: 2007, pp 151–175.

(43) Bucur, B. Technological Barriers in the Use of Electrochemical Microsensors and Microbiosensors for In Vivo Analysis of Neurological Relevant Substances. *Curr. Neuropharmacol.* **2012**, *10*, 197–211.

(44) Van Der Vliet, A.; Janssen-Heininger, Y. Hydrogen Peroxide as a Damage Signal in Tissue Injury and Inflammation: Murderer, Mediator, or Messenger? *J. Cell. Biochem.* **2014**, *115*, 427–435.

(45) Zestos, A. Carbon Nanoelectrodes for the Electrochemical Detection of Neurotransmitters. *Int. J. Electrochem.* **2018**, 1–19.

(46) Pocaznoi, D.; Erable, B.; Delia, M.-L.; Bergel, A. Ultra Microelectrodes Increase the Current Density Provided by Electroactive Biofilms by Improving Their Electron Transport Ability. *Energy Environ. Sci.* **2012**, 5287–5296.

(47) Butson, C.; McIntyre, C. Tissue and Electrode Capacitance Reduce Neural Activation Volumes during Deep Brain Stimulation. *Clin. Neurophysiol.* **2005**, *116*, 2490–2500.

(48) Liu, Q.; Zhang, Q.; Zhu, G.; Wang, K.; Zhang, J.; Dong, C. Effect of Electrode Size on the Performances of Micro-EDM. *Mater. Manuf. Process* **2016**, *31*, 391–396.

(49) Hu, C.; Xiao, Y.; Zou, Y.; Dai, L. Carbon-Based Metal-Free Electrocatalysis for Energy Conversion, Energy Storage, and Environmental Protection. *Electrochem. Energy Rev.* **2018**, *1*, 84–112.

(50) Sadana, A.; Sadana, N., Biosensor Performance Parameters and Their Enhancement In *Fractal Analysis of the Binding and Dissociation Kinetics for Different Analytes on Biosensor Surfaces*; Elsevier: 2008, pp 19–53.

(51) Polcari, D.; Perry, S.; Pollegioni, L.; Geissler, M.; Mauzeroll, J. Localized Detection of D-Serine by Using an Enzymatic Amperometric Biosensor and Scanning Electrochemical Microscopy. *ChemElectroChem* **2017**, *4*, 920–926.

(52) Billard, J.-M. Serine Racemase as a Prime Target for Age-Related Memory Deficits. *Eur. J. Neurosci.* **2013**, *37*, 1931–1938.

(53) Sullivan, S.; Miller, R. AMPA Receptor Mediated D-Serine Release from Retinal Glial Cells. *J. Neurochem.* **2010**, *115*, 1681–1689.

(54) Salm, A.; McCarthy, K. Norepinephrine-Evoked Calcium Transients in Cultured Cerebral Type 1 Astroglia. *Glia* **1990**, *3*, 529–538.

(55) Pan, H.-C.; Chou, Y.-C.; Sun, S. P2X7 R-Mediated Ca2+ -Independent D-Serine Release via Pannexin-1 of the P2X 7 R-Pannexin-1 Complex in Astrocytes. *Glia* **2015**, *63*, 877–893.

(56) Shen, W.; Nikolic, L.; Meunier, C.; Pfrieger, F.; Audinat, E. An Autocrine Purinergic Signaling Controls Astrocyte-Induced Neuronal Excitation. *Sci. Rep.* **2017**, *7*, 1–13.

Chapter 4

Enhancing Electrochemical Biosensor Selectivity with Engineered D-amino Acid Oxidase Enzymes for D-serine and D-alanine Quantification

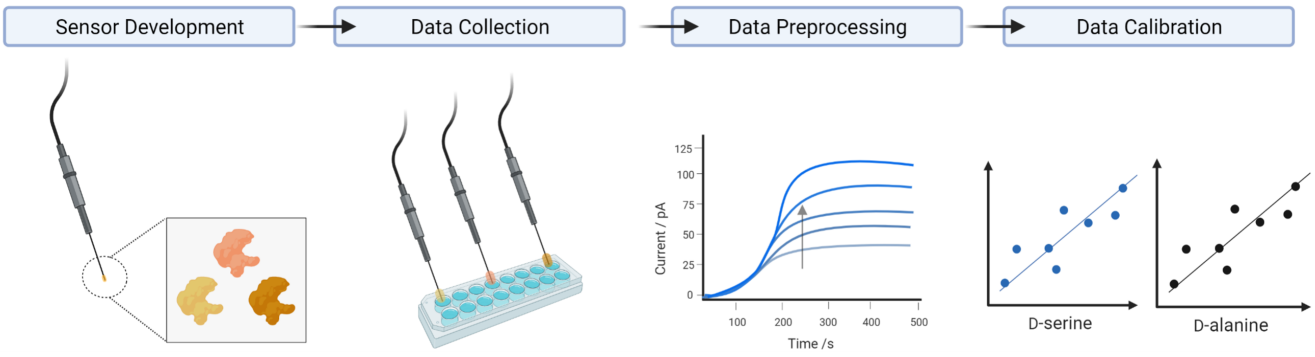

Chapter Preface

DAAO enzymes bind a range of D-amino acids with variable affinity. As such, the design of selective DAAO-based enzymatic biosensors remains a challenge for real-world biosensor application. In Chapter 4, a methodology for developing biosensors with varying substrate selectivity is presented. Challenges with DAAO-based biosensor selectivity towards D-serine are addressed by introducing point mutations into DAAO using rational design. The variants human DAAO W209R and yeast DAAO M213G were characterized for their selectivity and activity towards D-serine and D-alanine, the preferred DAAO substrates. The DAAO enzymes were also immobilized for final biosensor design, where they demonstrated selectivity comparable to free DAAO. By studying the impact of crosslinking on immobilized enzyme structure, an simple biosensor strategy was developed.

The work presented in this chapter is reproduced from:

Publication Information: The text in this chapter is reproduced from: Moussa, S., Murtas, G., Pollegioni, L., Mauzeroll J., Enhancing Electrochemical Biosensor Selectivity with Engineered D-amino acid Oxidase Enzymes for D-serine and D-alanine Quantification, *ACS Applied Biomaterials* **2021**,4(7),5598-5604.

4.1 Introduction

D-amino acids are increasingly reported for their roles in kidney function[1] and brain synaptic transmission regulation.[2] Altered D-amino acid levels, namely D-serine and D-alanine, are associated with disease prevalence such as kidney diseases[3,4], schizophrenia[5] and cancer[6,7], making D-amino acids potential disease biomarkers[8,9]. To monitor and understand the role of D-serine and D-alanine in disease diagnosis[5], management[10] and treatment[11], rapid online tracking of D-amino acid levels is essential. The most employed method for D-amino acid detection is chromatography.[12–15]While useful for trace analyte detection, chromatography entails extensive sample preparation, long detection times, and requires regular maintenance.[14,15] For clinical implementation, alternatives to chromatography should employ low-cost, rapid and high-throughput measurements.[16] Biosensors are viable low-cost alternatives for analyte detection and quantification.[17] However, remaining improvement areas in biosensor design include analyte sensitivity and selectivity. We previously demonstrated the application of DAAO biosensors for *in vivo* D-serine measurements.[18,19] These biosensors rely on DAAO surface immobilization onto a PPD-ME. DAAO is responsible for D-serine and D-alanine catalysis into equimolar amounts of hydrogen peroxide (H_2O_2),[20,21] which is oxidized at the polarized Pt surface (0.5 V). In practical application of D-serine biosensors, DAAO must preferentially detect D-serine amongst other substrates, especially in samples where D-alanine may also be present. *Rg*DAAO is the classical enzyme used to develop DAAO-based biosensors. Using *Rg*DAAO WT-based biosensors, both D-alanine and D-serine are detected simultaneously.[18,22,23] To increase DAAO-based biosensor selectivity and

sensitivity, we use DAAO from different sources (variants) generated via protein engineering to produce biosensors with a range of analytical detection properties. DAAO variants share the same catalytic and kinetic mechanism (Figure 4.1)while the rate constants associated with individual steps vary. Thus, kinetic constants for D-serine and D-alanine oxidation are impacted.

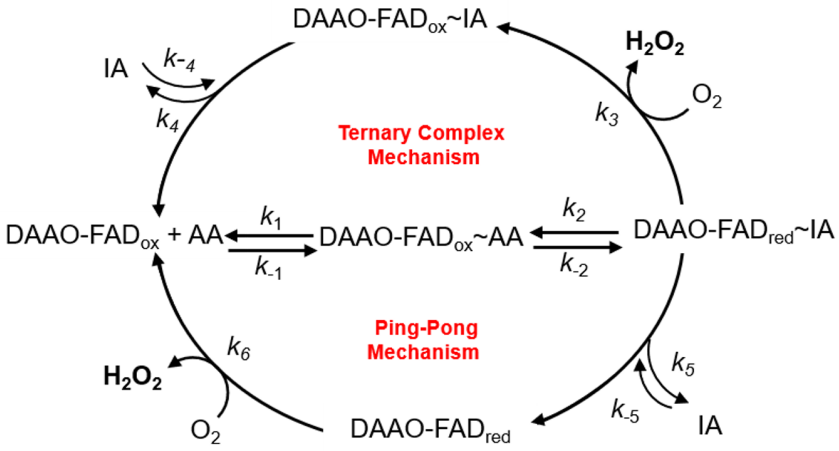

Figure 4.1: Kinetic mechanism of DAAO enzymes.[20,21] The reaction can follow two kinetic mechanisms, i.e. ternary complex or ping-pong mechanism. AA, FAD_{ox}, FAD_{red}, and IA correspond to D-amino acid, oxidized FAD, reduced FAD, imino acid respectively. The rate constants for single steps depend on the DAAO enzyme type.

Using different DAAO enzymes (wild-type, *Rg*DAAO M213G[24,25] and the W209R variant of the human counterpart (hDAAO)[24,25], we report the successful fabrication of three different biosensors with variable D-serine: D-alanine selectivity. Improving the detection properties of DAAO-based biosensors enable increased D-serine and D-alanine quantification accuracy. Moreover, we explore the mechanism in which immobilization impacts biosensor performance, noting that significant structural changes occur due to enzyme crosslinking. Finally, a unique biosensor strategy that increases biosensor lifetime is presented and the

mechanism behind the regeneration principle is discussed.

4.2 Experimental Section

4.2.1 Materials and Chemicals

Chemicals

All reagents were purchased from Fischer Scientific or Sigma-Aldrich unless otherwise noted. All solutions were prepared using Millipore MilliQ water (18.2 $M\Omega \cdot cm^{-1}$).

Enzyme Preparation

Recombinant *Rg*DAAO WT (*Rg*DAAO, EC 1.4.3.3) was prepared as reported in literature.[26] Briefly, recombinant *Rg*DAAO WT was expressed using the pT7-HisDAAO expression vector. Enzyme variants were selected by rational design. Recombinant *Rg*DAAO M213G variant was expressed using the pT7-HisDAAO M213G expression vector.[25] Recombinant hDAAO W209R was expressed using the pET11b-His hDAAO W209R expression vector.[27] Recombinant enzyme variants were produced in BL21(DE3)pLysS E.coli cells and purified to >90% purity. Enzymes were characterized using standard polarographic assays (0.253 mM O_2, 25^oC) with 28 mM D-alanine in 50 mM sodium pyrophosphate, pH 8.5 (containing 40 µM FAD for hDAAO W209R).[28] One enzyme unit is defined as the amount of enzyme that converts 1 µmol of D-amino acid per minute at 25^oC. Substrate specificity was investigated by a spectrophotometric assay based on detection of hydrogen peroxide production using a

coupled assay with peroxidase and o-dianisidine (o-DNS, ϵ=13 $mM^{-1}cm^{-1}$).[28] Pure enzymes were concentrated, stored in BSA and 1% glycerol, characterized using activity assays and then used for the development of D-amino acid detecting biosensors (Appendix C).

4.2.2 Biosensor Calibration, Storage and Regeneration

In vitro calibrations in 0-50 μM D-serine or D-alanine in PBS (0.01 M, pH 7.4) were obtained using chronoamperometry (15 min, 0.5 V vs. Ag/AgCl). Biosensors were stored at -20^{o}C dry. To test storage stability, biosensors were removed from storage, left for 10 minutes at room temperature in PBS and calibrated using D-serine standard solutions (0-50 μM). Biosensor regeneration involved the immersion of the biosensor in a solution of 1 mM D-serine for 30 s under constant potential application (0.5 V). The biosensor response was then calibrated in standard D-serine solutions. The pre- and post-regeneration calibrations were compared to quantify the impact of regeneration on the biosensor signal.

4.2.3 Characterizations of Free and Crosslinked *Rg*DAAO

Free and crosslinked *Rg*DAAO were characterized using multiple characterization methods. Transmission electron microscopy (TEM) images were acquired using a Brightfield Philips CM200 TEM at 200 kV. Circular dichroism (CD) spectra were recorded at 25^{o}C on a Jasco J-810 spectropolarimeter using a 1 cm path length cuvette. Infrared spectra were measured using a Fourier transform infrared (FTIR) spectrometer (Bruker) with attenuated total reflectance (ATR). A dynamic light spectrometer (DLS, Brookhaven instruments) was used to measure the particle size dispersion. Spectrophotometric measurements were performed

using a thermostated UV/Vis spectrophotometer (V-560, Jasco) at 25^{o}C. Detailed experimental methodology on the characterization methods is presented in (Appendix C).

4.2.4 Data Preprocessing, Analysis and Statistics

All experimental data presented is the mean of triplicate measurements unless otherwise stated. Error bars represent the standard error of the mean (±, SEM). Data was analyzed on either Excel 2013 or Python 3.7 and treated in Python 3.7. Error propagation calculations were performed on Python 3.7. All electrochemical signals were blank (PBS) signal corrected, resulting in i_{norm}. To generate the calibration curves, the steady state signals from noise-filtered data was extracted at each concentration and fit to a linear regression line. The sensitivity was calculated from the slope of the regression fit. Selectivity towards D-serine was calculated as follows:

$$Selectivity_{D-ser} = \frac{SA_{desiredproduct}}{SA_{undesiredproduct}} x100 = \frac{SA_{D-ser}}{SA_{D-ala}} x100 \tag{4.1}$$

where SA is the specific activity of the selected D-amino acid.

4.3 Results and Discussion

4.3.1 DAAO Selection Strategy, Expression and Characterization

Based on their reported kinetic properties for the free enzyme (Table 4.1),[20,21,24,27] three DAAO enzymes were selected to develop biosensors with increased D-serine selectivity. Wild-type hDAAO (hDAAO WT) has a higher D-serine:D-alanine turnover ratio (0.58) than the control *Rg*DAAO WT (0.48). The hDAAO W209R (0.61) has a higher turnover for both D-amino acids. However, the M213G variant of *Rg*DAAO, previously identified as a DAAO variant with improved catalytic activity on unnatural substrates, presents the highest D-serine:D-alanine turnover ratio (1.37).[24,25] The selectivity and activity of DAAO enzymes were assessed via spectrophotometric activity assays on D-serine, D-alanine and glycine (Figure 4.2A). The SEM of the enzyme activities are also presented in Figure 4.2B. While all enzymes have negligible activity on glycine (Figure 4.2A, 1mM), enzyme activity towards D-serine and D-alanine varies with substrate concentration (as a result of different $K_{m,app}$ values). The substrate concentration-dependent enzyme activity affects the D-serine and D-alanine specificity of the enzyme. At saturating substrate conditions (25 mM), hDAAO W209R has the highest D-serine selectivity whereas at 0.1 mM, hDAAO W209R D-serine selectivity drops from 70% to 3% (Figure 4.2C).

While not possible to assay activity at substrate concentrations lower than 0.1 mM due to o-DNS assay sensitivity limitations, the results at 0.1 mM (a concentration in the higher range of *in vivo* biosensor application) indicate that *Rg*DAAO M213G is the most D-serine

Table 4.1: Apparent DAAO kinetic parameters at 25 ^{o}C, pH=8.5.

Enzyme	D-Ala k$_{cat}$ (s^{-1})	D-Ser kcat(s^{-1})	D-Ser:D-Ala turnover ratio	Ref.
hDAAO WT	5.2	3.0	0.58	21
*Rg*DAAO WT	85	40.7	0.48	20
hDAAO W209R	11.8	7.2	0.61	27
*Rg*DAAO M213G	4.9	6.7	1.37	24

selective enzyme amongst the tested enzymes (Figure 4.2C). The superior *Rg*DAAO M213G selectivity suggests the potential of its incorporation into biosensor design for enhanced D-serine detection as compared to previously published DAAO biosensors.[18,29,30]

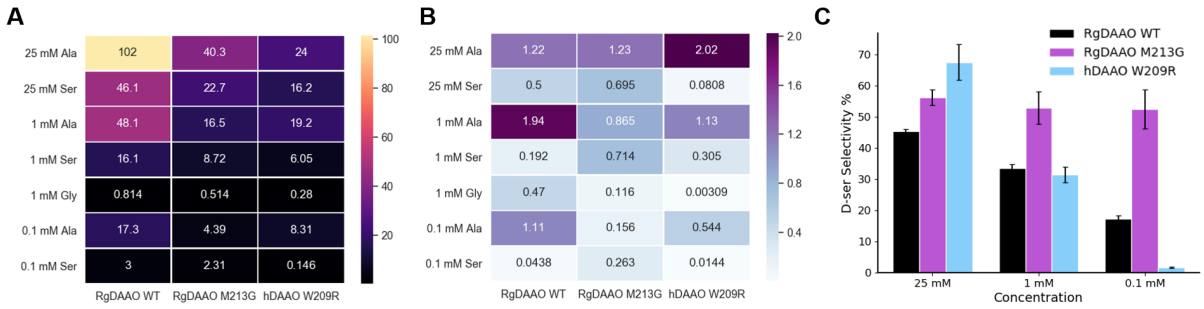

Figure 4.2: Characterization of *Rg*DAAO WT, *Rg*DAAO M213G and hDAAO W209R Using the spectrophotometric assay (pH 8.5). A) Specific activity (U mg^{-1}) values for the enzymes at various substrate concentrations of D-serine, D-alanine or glycine. B) SEM values for the specific activities as reported in panel A. C) Selectivity of enzymes towards D-serine over D-alanine. Error bars represent mean values ±S.E.M.

4.3.2 DAAO Variants for Biosensor Development

Characterization of the free enzymes highlighted the potential of *Rg*DAAO M213G use for biosensor development. Yet, to fully compare *Rg*DAAO M213G performance against other DAAO enzymes in the final biosensor architecture, the enzymes were used to build individual biosensors. DAAO enzymes were immobilized on individual PPD-Pt MEs. Initial attempts of hDAAO W209R biosensor development were unsuccessful (Figure C.2). As such, we established that enzyme concentrations > 40 mg $\cdot$ mL^{-1} are essential for biosensor design success (Figure C.2A,D). Another factor important for biosensor success is the presence of FAD. *Rg*DAAO WT and *Rg*DAAO M213G show high FAD binding affinity (K_d = 2 x 10^{-8} M for *Rg*DAAO WT)[21,25,31] resulting in a tightly bound FAD which assures the presence of the active holoenzyme during enzyme immobilization. Conversely, hDAAO has a weak FAD binding affinity (K_d= 2 x 10^{-6})[32,33], making its exogenous presence required in biosensor design to avoid the production of the inactive apoprotein form. Although FAD co-immobilization with hDAAO W209R was ineffective at generating a linear calibration curve (Figure C.2C), the presence of exogenous FAD (100 µM) in calibration solutions yielded linear calibration curves (Figure C.2B,D). Biosensors were produced using enzyme concentrations of 56.8 mg $\cdot$ mL^{-1}, 48 mg $\cdot$ mL^{-1}, 45 mg $\cdot$ mL^{-1} for *Rg*DAAO WT, *Rg*DAAO M213G and hDAAO W209R, respectively. Calibrations of all biosensors in standard D-serine and D-alanine solutions (Figure 4.3) indicate that each biosensor differs in selectivity and sensitivity towards D-serine and D-alanine (Table 4.2). Calibration curve regression parameters are listed in Table C.1. Defining *Rg*DAAO WT's response to D-alanine as 100%, the relative

response of all three biosensors towards D-serine and D-alanine is compared at 50 µM (Table 4.2). As seen in the calibrations in (Figure 4.3), the hDAAO W209R biosensor surpasses the performance of the other biosensors with respect to substrate response at 50 µM (D-ser: 80%, D-ala: 213%). Additionally, the hDAAO W209R bio-sensor supersedes the other biosensors in sensitivity (D-ala: 291 pA mM^{-1}) and D-alanine selectivity (62.4%, Table 4.2). Although the greatest in current response, sensitivity, and selectivity when immobilized, the activity of free hDAAO W209R on D-serine and D-alanine is the lowest amongst other enzymes. The difference between free and immobilized hDAAO W209R responses suggests a strong impact of immobilization on enzyme behavior.

Table 4.2: Biosensor calibration parameters for the various DAAO enzymes variants.

	*Rg*DAAO WT		*Rg*DAAO M213G		hDAAO W209R	
	D-Ser	D-Ala	D-Ser	D-Ala	D-Ser	D-Ala
Sensitivity (pA mM-1)	89.5 ± 1.52	154 ± 2.23	104 ± 5.61	117 ± 6.12	143 ± 3.42	291 ± 6.54
Relative response at 50 µM (%)	63 ± 2.4	100 ± 0.30	80 ± 2.4	82 ± 4.2	80 ± 3.5	213 ± 5.3
	D-Ser Selectivity (%)					
Biosensor	63 ± 3.10		97.6 ± 1.75		37.6 ± 2.25	
Free DAAO (100 µM)	20 ± 1.14		55 ± 6.29		3 ± 0.21	

Additionally, both free and immobilized DAAO follow a similar trend for D-serine selectivity. Both DAAO forms demonstrate that *Rg*DAAO M213G has the greatest selectivity (55% free, 97.6% biosensor), followed by *Rg*DAAO WT (20% free, 63% biosensor), and finally hDAAO W209R (3% free, 37.6% biosensor). The selectivity trend is consistent with that observed in free DAAO enzyme in 0.1 mM substrate. The results suggest that the free enzyme selectivity ratio at low substrate concentrations is a predictive parameter of biosensor selectivity. Thus, by characterizing free enzyme activity in the concentration range relevant

to biosensor application, costs associated with enzymatic biosensor optimization are reduced. The biosensor performance may also be easily predicted. Moreover, to evaluate the long term enzyme stability following immobilization, biosensors were stored at -20^{o}C. After two weeks of storage, biosensors were calibrated and generated linear calibration curves with almost no change in the slope for hDAAO W209R. The sensitivity of *Rg*DAAO M213G and *Rg*DAAO WT, on the other hand, was impacted (Figure C.3 and Table C.2).

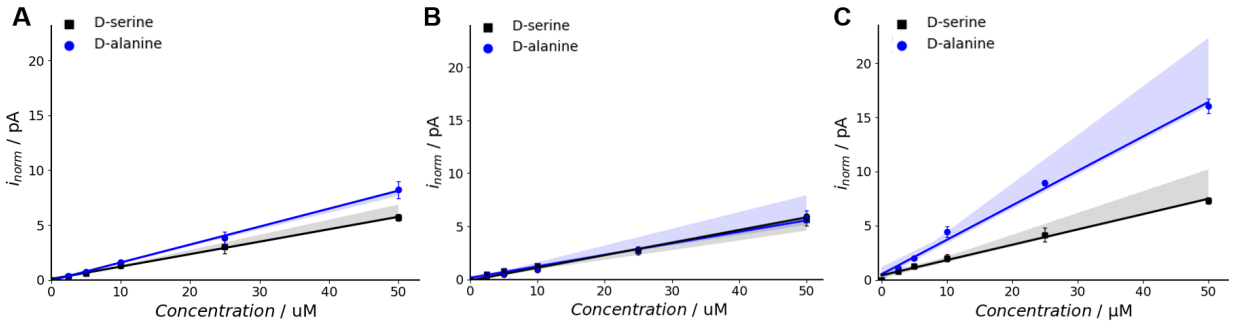

Figure 4.3: *Rg*DAAO WT (A), *Rg*DAAO M213G (B) and hDAAO W209R (C) biosensor calibration in standard solutions of 0 – 50 µM D-serine and D-alanine. Error bars represent ± S.E.M, (n=3). The shaded area represent 95% confidence interval regions.

4.3.3 Immobilization Impacts DAAO Biosensor Performance

Biosensor performance is dictated by enzyme-structure function relationships in the enzyme layer. The structure-function relationships are impacted by enzyme packing density and solvent accessibility. In our biosensors, the DAAO layer represents a mixture of crosslinked DAAO and BSA aggregates. BSA is a highly hydrophilic protein used to stabilize enzymes.[34] BSA presence has no observed effect on enzyme activity (Table C.3).

It is, however, the inter-enzyme differences that explain the reason behind hDAAO-

biosensors surpassing the performance of other biosensors. Free *Rg*DAAO is a homodimer with head-to-tail inter-actions between the monomers .[35] (Figure 4.4A), whereas free hDAAO exists as a homodimer with head-to-head interactions between the monomers (Figure 4.4B).[36] *Rg*DAAO is more hydrophilic than hDAAO (Figure 4.4A vs B), and *Rg*DAAO has more polar contacts than hDAAO.

When immobilized onto the surface, and in comparison to *Rg*DAAO, the water molecules are not as tightly packed between the hDAAO enzyme molecules, creating a larger effective enzyme concentration (Figure 4.4C). The increased hDAAO effective concentration occurs due to a concept known as molecular crowding, a common biological phenomenon, occurring typically in cells. Molecular crowding may affect the enzyme stability, packing density, and oligomerization state.[37–39] As a result of molecular crowding and increased hDAAO stability, H_2O_2 production from the enzyme reaction rises and H_2O_2 diffusion towards the bio-sensor surface increases. As such, although the activity of free hDAAO is significantly lower on both D-serine and D-alanine than *Rg*DAAO (Table C.1), hDAAO biosensors offer better limits of detection and sensitivities.

In addition, structural changes which occur with glutaraldehyde crosslinking impact the immobilized enzyme behavior. Taking *Rg*DAAO WT for instance, CD spectra in the near UV range (Figure C.4) suggest structural changes upon enzyme crosslinking. The CD spectral signals likely corresponding to phenylalanine (270-290 nm) and tryptophan (280-300 nm) residues vary between the free and the solution crosslinked DAAO. Moreover, ATR-FTIR spectra of glutaraldehyde, free *Rg*DAAO WT and crosslinked *Rg*DAAO WT demonstrate differences between the three samples (Figure C.5). The spectra for free and crosslinked

*Rg*DAAO WT demonstrate changes in peaks for selected functional groups for the latter *Rg*DAAO form. The main distinctions can be made in four spectral regions: 3800-3300 cm^{-1} (O-H stretch), 3000-2800 cm^{-1} (C-H stretch) ¬, 1700-1500 cm^{-1} (N-H bend, C=C stretch), and 1450-1000 cm^{-1} (fingerprint region). Hence, it is evident that enzyme crosslinking alters certain enzyme functional groups, resulting in enzyme structural changes and impacting enzymatic biosensor performance.

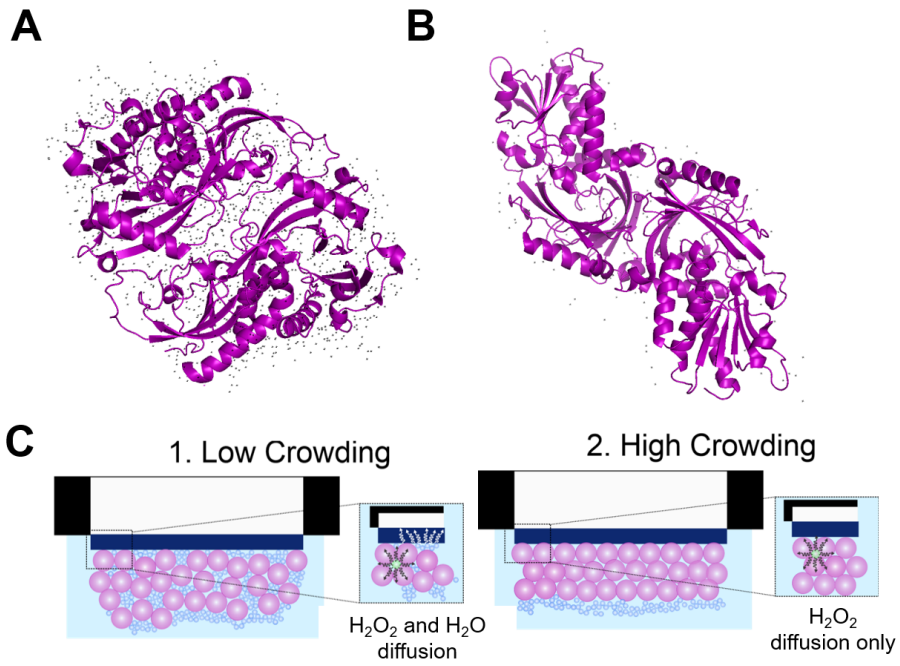

Figure 4.4: Structural representations of *Rg*DAAO WT and hDAAO WT and their interactions with surrounding non-bonded solvent molecules. The figures were prepared with PyMOL. A) Crystal structure of *Rg*DAAO WT (dimer); the black dots correspond to the non-bonded water molecules (PDB code: 1C0P). *Rg*DAAO has a calculated 47.9% solvent ac-cessible surface area. B) Crystal structure of dimeric hDAAO WT; the black dots correspond to the non-bonded water molecules (PDB code: 2DU8). hDAAO is slightly more hydrophobic than *Rg*DAAO with a 43.0% solvent ac-cessible surface area. C) (1) Effect of *Rg*DAAO enzyme immobilization onto the microelectrode surface resulting in low crowding and allowing for the diffusion of both H_2O_2 and H_2O through the PPD layer. (2) Effect of hDAAO immobilization onto the microelectrode surface resulting in high crowding and low level of solvent molecules pre-sent near the electrode surface: this allows for the diffusion of only H_2O_2 produced by the enzyme close to the PPD layer.

4.3.4 Biosensors are Regenerated with a Simple Strategy

For practical applications, biosensors must be easily regenerated after use. Regeneration is achievable through several mechanisms such as thermal heating, manual polishing, and

chemical regeneration.[33] Chemical regeneration is the most widely used approach for biosensor regeneration taking advantage of enthalpic and entropic changes in solvent environment. Changes in the solvent environment include ionic strength, pH and the presence of competitor ions, possible through the use of regeneration buffers and acidic solutions.[33–35]

Using *Rg*DAAO WT as a prototype for DAAO biosensors, a novel biosensor regeneration strategy was developed. The biosensor was placed in a solution of 1 mM D-serine for a period of 30 s under simultaneous potential application to oxidize H_2O_2 (0.5 V) (Figure 4.5A). The biosensor was regenerated and the electrochemical signal was also amplified. Regeneration resulted in a 2.5-fold amplification of calibration curve steady-state currents (Figure 4.5B). The linear range is similar for pre and post-regeneration calibrations (Table C.4).

To explain the regeneration behavior, the biosensor electrochemical response was further explored. Immersed in 100 µM of substrate in PBS buffer, a steady current response is observed with the biosensor (Figure 4.5C, top). Immersed in 1 mM of substrate, steady state current is also initially observed. However, after a period of 100 – 200 s a sudden burst in product formation occurs, characterized by over a 10-fold increase in the oxidation current (Figure 4.5C, bottom). The biosensor response at different substrate concentrations suggests microenvironment changes within the bio-sensor vicinity due to elevated H_2O_2 and H^+ ion levels around the enzyme layer (H^+ is the byproduct of H_2O_2 oxidation at the microelectrode surface), resulting in molecular crowding. The The PPD layer rejects 70-80% of the H_2O_2 produced from diffusing towards the platinum sites.[18] As such, H_2O_2 and H^+ ion presence induce a pH change in the microenvironment of the enzyme layer, affecting both BSA and *Rg*DAAO tertiary conformation and spatial arrangement on the ME

surface.[40] In solution, the electrochemical behavior of free and crosslinked *Rg*DAAO WT is dissimilar to that of the biosensor, further supporting the presence of microenvironment changes only at the biosensor's enzyme-PPD interface (Figure C.6). Moreover, dynamic light scattering (DLS) measurements of free and crosslinked *Rg*DAAO in the presence of 1 mM D-alanine demonstrate aggregation and larger particle diameters for crosslinked *Rg*DAAO WT (Figure 4.5D). Comparison of TEM images of crosslinked *Rg*DAAO incubated in D-alanine also demonstrate enzyme aggregation: the degree of aggregation, size, and morphology are tied to the D-alanine concentration (Figure 4.5E,F). Energy-dispersive X-ray spectroscopy (EDS) analysis confirmed the presence of protein in the darker regions (Figure C.8). The increased aggregation of crosslinked *Rg*DAAO suggests that enzyme aggregation plays a role in biosensor regeneration in addition to structural changes.[41,42]

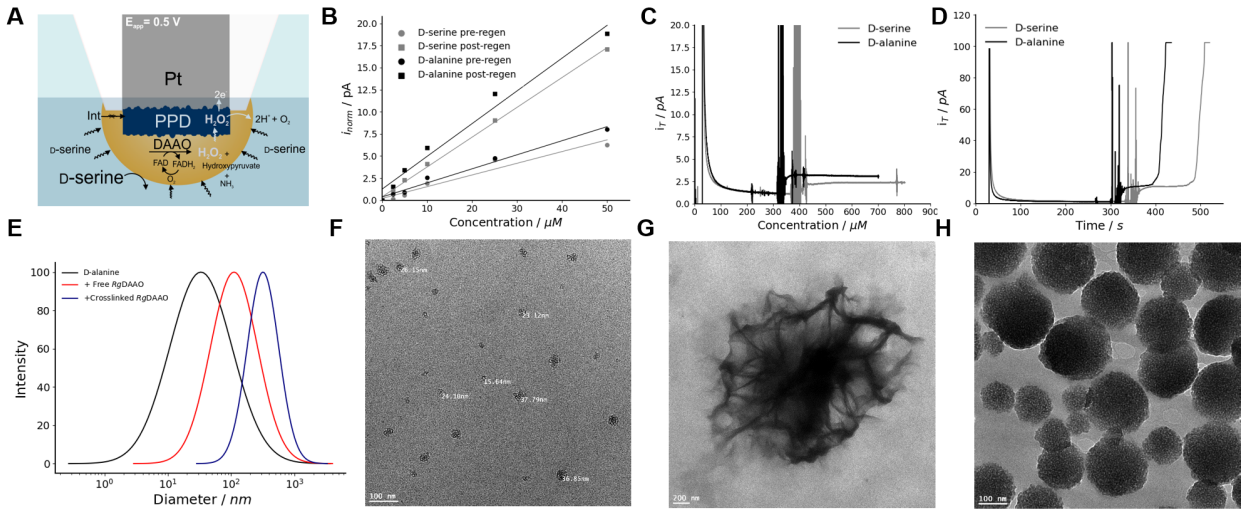

Figure 4.5: Biosensor regeneration strategy. A) Scheme of biosensor placed in a solution of D-serine and the sequentially occurring reactions underlying D-serine detection. B) Effect of biosensor regeneration on the calibration curve. C) Electrochemical response of the biosensor in solutions of PBS added of 100 µM D-serine or D-alanine (top) and of 1 mM D-serine or D-alanine (bottom). D) Laser light scattering size dispersion of 1 mM D-alanine, 0.5 µL free *Rg*DAAO in 1 mM D-alanine, or 0.5 µL crosslinked *Rg*DAAO in 1 mM D-alanine. E) TEM image of immobilized *Rg*DAAO incubated in 100 µM D-alanine; scale bar: 200 nm. F) TEM image of immobilized *Rg*DAAO incubated in 1 mM D-alanine; scale bar: 200 nm.

4.4 Conclusion

Improving D-serine and D-alanine detection using enzymatic electrochemical biosensors is important for their practical application. In this work, we altered the selectivity and specificity of the D-serine sensing element by using enzymes from different sources and variants, generated by point substitutions. The enzymes were successfully developed into DAAO-biosensors. We also demonstrated that while free enzyme activity does not necessarily define immobilized enzyme activity, it can serve as a predictive indicator for biosensor selectiv-

ity. Moreover, the crosslinking step in enzyme immobilization results in DAAO structural changes, enabling a simple biosensor regeneration strategy. Overall, this work enables the future development of DAAO biosensors with improved substrate selectivity and increased lifetimes. Future work consists of multiple biosensor application to quantify individual levels of D-serine and D-alanine in mixed substrate environments. These biosensors may be used to probe single or dual D-amino acid presence, enabling novel insights on D-amino acid function and roles in neurological disease onset and management.

References

(1) Kimura, R.; Tsujimura, H.; Tsuchiya, M.; Soga, S.; Ota, N.; Tanaka, A.; Kim, H. Development of a Cognitive Function Marker Based on D-Amino Acid Proportions Using New Chiral Tandem LC-MS/MS Systems. *Sci. Rep.* **2020**, *10*, 1–12.

(2) Yamanaka, M.; Miyoshi, Y.; Ohide, H.; Hamase, K.; Konno, R. D-Amino Acids in the Brain and Mutant Rodents Lacking D-Amino-Acid Oxidase Activity. *Amino Acids* **2012**, *43*, 1811–1821.

(3) Hesaka, A.; Sakai, S.; Hamase, K.; Ikeda, T.; Matsui, R.; Mita, M.; Horio, M.; Isaka, Y.; Kimura, T. D -Serine Reflects Kidney Function and Diseases. *Sci. Rep.* **2019**, *9*, 1–8.

(4) Kimura, T.; Hamase, K.; Miyoshi, Y.; Yamamoto, R.; Yasuda, K.; Mita, M.; Rakugi, H.; Hayashi, T.; Isaka, Y. Chiral Amino Acid Metabolomics for Novel Biomarker Screening in the Prognosis of Chronic Kidney Disease. *Sci. Rep.* **2016**, *6*, 1–7.

(5) MacKay, M.; Kravtsenyuk, M.; Thomas, R.; Mitchell, N.; Dursun, S.; D-serine, B. G. Potential therapeutic agent and/or biomarker in schizophrenia and depression? *Front. in Psychiatry* **2019**, *10*, 1–9.

(6) Bastings, J.; Eijk, H.; Damink, S.; Rensen, S. D-Amino Acids in Health and Disease: A Focus on Cancer. *Nutrients* **2019**, *11*, 2205–2223.

(7) Zhang, Z.; Liu, Y.; Liu, P.; Yang, L.; Jiang, X.; Luo, D.; Yang, D. Non-Invasive Detection of Gastric Cancer Relevant D-Amino Acids with Luminescent DNA/Silver Nanoclusters. *Nanoscale* **2017**, 19367–19373.

(8) Lin, C.; Yang, H.; Chiu, C.; Lane, H. Blood Levels of D-Amino Acid Oxidase vs. D-Amino Acids in Reflecting Cognitive Aging. *Sci. Rep.* **2017**, *7*, 1–10.

(9) Lin, C.; Yang, H.; Lane, H. D-Glutamate, D-Serine, and D-Alanine Differ in Their Roles in Cognitive Decline in Patients with Alzheimer's Disease or Mild Cognitive Impairment. *Pharmacol. Biochem. Behav.* **2019**, 185–191.

(10) Kantrowitz, J.; Malhotra, A.; Cornblatt, B.; Silipo, G.; Balla, A.; Suckow, R.; D'Souza, C.; Saksa, J.; Woods, S.; Javitt, D. High Dose D-Serine in the Treatment of Schizophrenia. *Schizophr. Res.* **2010**, *121*, 125–130.

(11) Tsai, G.; Yang, P.; Chang, Y.; Chong, M. D-Alanine Added to Antipsychotics for the Treatment of Schizophrenia. *Biol. Psychiatry* **2006**, *59*, 230–234.

(12) Furusho, A.; Koga, R.; Akita, T.; Mita, M.; Kimura, T.; Hamase, K. Three-Dimensional High-Performance Liquid Chromatographic Determination of Asn, Ser, Ala, and Pro Enantiomers in the Plasma of Patients with Chronic Kidney Disease. *Anal. Chem.* **2019**, *91*, 11569–11575.

(13) Nakano, Y.; Konya, Y.; Taniguchi, M.; Fukusaki, E. Development of a Liquid Chromatography-Tandem Mass Spectrometry Method for Quantitative Analysis of Trace D-Amino Acids. *J. Biosci. Bioeng.* **2017**, *123*, 134–138.

(14) Carenzi, G.; Sacchi, S.; Abbondi, M.; Pollegioni, L. Direct Chromatographic Methods for Enantioresolution of Amino Acids: Recent Developments. *Amino Acids* **2020**, 849–862.

(15) Xing, Y.; Li, X.; Guo, X.; Cui, Y. Simultaneous Determination of 18 D-Amino Acids in Rat Plasma by an Ultrahigh-Performance Liquid Chromatography-Tandem Mass Spectrometry Method: Application to Explore the Potential Relationship between Alzheimer's Disease and d-Amino Acid Level Alteration. *Anal. Bioanal. Chem.* **2016**, *408*, 141–150.

(16) Purohit, B.; Vernekar, P.; Shetti, N.; Chandra, P. Biosensor Nanoengineering: Design, Operation, and Implementation for Biomolecular Analysis. *Sensors Int.* **2020**, *1*, 1–19.

(17) Shoja, Y.; Rafati, A.; Ghodsi, J. Enzymatic Biosensor Based on Entrapment of d -Amino Acid Oxidase on Gold Nanofilm/MWCNTs Nanocomposite Modified Glassy Carbon Electrode by Sol-Gel

Network: Analytical Applications for d -Alanine in Human Serum. *Enzyme Microb. Technol.* **2017**, *100*, 20–27.

(18) Polcari, D.; Kwan, A.; Van Horn, M.; Danis, L.; Pollegioni, L.; Ruthazer, E.; Mauzeroll, J. Disk-Shaped Amperometric Enzymatic Biosensor for in Vivo Detection of D-Serine. *Anal. Chem.* **2014**, *86*, 3501–3507.

(19) Moussa, S.; Van Horn, M.; Shah, A.; Pollegioni, L.; Thibodeaux, C.; Ruthazer, E.; Mauzeroll, J. A Miniaturized Enzymatic Biosensor For Detection of Sensory-Evoked D-Serine Release in the Brain. *J. Electrochem. Soc.* **2021**, *168*, 1–10.

(20) Pollegioni, L.; Langkau, B.; Tischer, W.; Ghisla, S.; Pilone, M. Kinetic Mechanism of D-Amino Acid Oxidases from Rhodotorula Gracilis and Trigonopsis Variabilis. *J. Biol. Chem.* **1993**, *268*, 13850–13857.

(21) Molla, G.; Sacchi, S.; Bernasconi, M.; Pilone, M.; Fukui, K.; Pollegioni, L. Characterization of Human D-Amino Acid Oxidase. *FEBS Lett.* **2006**, *580*, 2358–2364.

(22) Pernot, P.; Maucler, C.; Tholance, Y.; Vasylieva, N.; Debilly, G.; Pollegioni, L.; Cespuglio, R.; Marinesco, S. D-Serine Diffusion through the Blood-Brain Barrier: Effect on D-Serine Compartmentalization and Storage. *Neurochem. Int.* **2012**, *60*, 837–845.

(23) Van Horn, M.; Strasser, A.; Miraucourt, L.; Pollegioni, L.; Ruthazer, E. The Gliotransmitter D-Serine Promotes Synapse Maturation and Axonal Stabilization In Vivo. *J. Neurosci.* **2017**, *37*, 6277–6288.

(24) Caligiuri, A.; D'Arrigo, P.; Rosini, E.; Tessaro, D.; Molla, G.; Servi, S.; Pollegioni, L. Enzymatic Conversion of Unnatural Amino Acids by Yeast D-Amino Acid Oxidase. *Adv. Synth. Catal.* **2006**, *348*, 2183–2190.

(25) Sacchi, S.; Lorenzi, S.; Molla, G.; Pilone, M.; Rossetti, C.; Pollegioni, L. Engineering the Substrate Specificity of D-Amino-Acid Oxidase. *J. Biol. Chem.* **2002**, *30*, 27510–27516.

(26) Fantinato, S.; Pollegioni, L.; Pilone, S.; Engineering, M. Expression and Purification of a His-Tagged Chimeric D-Amino Acid Oxidase from Rhodotorula Gracilis. *Enzyme Microb. Technol.* **2001**, *29*, 407–412.

(27) Cappelletti, P.; Piubelli, L.; Murtas, G.; Caldinelli, L.; Valentino, M.; Molla, G.; Pollegioni, L.; Sacchi, S. Structure–Function Relationships in Human d-Amino Acid Oxidase Variants Corresponding to Known SNPs. *Biochim. Biophys. Acta* **2015**, *1854*, 1150–1159.

(28) Rosini, E.; Caldinelli, L.; Piubelli, L. Assays of D-Amino Acid Oxidase Activity. *Front. Mol. Biosci.* **2018**, *4*, 1–12.

(29) Zain, Z.; O'Neill, R.; Lowry, J.; Pierce, K.; Tricklebank, M.; Dewa, A.; Ghani, S. Development of an Implantable D-Serine Biosensor for in Vivo Monitoring Using Mammalian d-Amino Acid Oxidase on a Poly (o-Phenylenediamine) and Nafion-Modified Platinum-Iridium Disk Electrode. *Biosens. Bioelectron.* **2010**, *25*, 1454–1459.

(30) Maucler, C.; Pernot, P.; Vasylieva, N.; Pollegioni, L.; Marinesco, S. In Vivo D-Serine Hetero-Exchange through Alanine-Serine-Cysteine (ASC) Transporters Detected by Microelectrode Biosensors. *ACS Chem. Neurosci.* **2013**, *4*, 772–781.

(31) Pollegioni, L.; Molla, G.; Sacchi, S.; Rosini, E.; Verga, R.; Pilone, M. Properties and Applications of Microbial D-Amino Acid Oxidases: Current State and Perspectives. *Appl. Microbiol. Biotechnol.* **2008**, *78*, 1–16.

(32) Caldinelli, L.; Iametti, S.; Barbiroli, A.; Bonomi, F.; Fessas, D.; Molla, G.; Pilone, M.; Pollegioni, L. Dissecting the Structural Determinants of the Stability of Cholesterol Oxidase Containing Covalently Bound Flavin. *J. Biol. Chem.* **2005**, *280*, 22572–22581.

(33) Pollegioni, L.; Sacchi, S.; Murtas, G. Human D-Amino Acid Oxidase: Structure, Function, and Regulation. *Frontiers in Molecular Biosciences* **2018**, 1–14.

(34) Jeyachandran, Y.; Mielczarski, J.; Mielczarski, E.; Rai, B. Efficiency of Blocking of Non-Specific Interaction of Different Proteins by BSA Adsorbed on Hydrophobic and Hydrophilic Surfaces. *J. Colloid Interface Sci.* **2010**, *341*, 136–142.

(35) Umhau, S.; Pollegioni, L.; Molla, G.; Diederichs, K.; Welte, W.; Pilone, M.; Ghisla, S. The X-Ray Structure of D-Amino Acid Oxidase at Very High Resolution Identifies the Chemical Mechanism of Flavin-Dependent Substrate Dehydrogenation. *PNAS* **2000**, *97*, 12463–12468.

(36) Kawazoe, T.; Tsuge, H.; Pilone, M.; Fukui, K. Crystal Structure of Human D-Amino Acid Oxidase: Context-Dependent Variability of the Backbone Conformation of the VAAGL Hydrophobic Stretch Located at the Si -Face of the Flavin Ring. *Protein Sci.* **2006**, *15*, 2708–2717.

(37) Kuznetsova, I.; Turoverov, K.; Uversky, V. What Macromolecular Crowding Can Do to a Protein. *International Journal of Molecular Sciences* **2014**, *12*, 23090–23140.

(38) Ellis, R. Macromolecular Crowding: Obvious but Underappreciated. *Trends in Biochemical Sciences* **2001**, *1*, 597–604.

(39) Löwe, M.; Kalacheva, M.; Boersma, A.; Kedrov, A. The More the Merrier: Effects of Macromolecular Crowding on the Structure and Dynamics of Biological Membranes. *FEBS* **2020**, *1*, 5039–5067.

(40) Gooding, J.; Pugliano, L.; Hibbert, D.; Erokhin, P. Amperometric Biosensor with Enzyme Amplification Fabricated Using Self-Assembled Monolayers of Alkanethiols: The Influence of the Spatial Distribution of the Enzymes. *Electrochem. Commun.* **2000**, *2*, 217–221.

(41) Xu, M.; Li, F.; Yu, W.; Li, R.; Zhang, Y. Combined Cross-Linked Enzyme Aggregates of Glycerol Dehydrogenase and NADH Oxidase for High Efficiency in Situ NAD+ Regeneration. *Int. J. Biol. Macromol.* **2020**, *144*, 1013–1021.

(42) Chen, Y.; Jiang, Q.; Sun, L.; Li, Q.; Zhou, L.; Chen, Q.; Li, S.; Yu, M.; Li, W. Magnetic Combined Cross-Linked Enzyme Aggregates of Ketoreductase and Alcohol Dehydrogenase: An Efficient and Stable Biocatalyst for Asymmetric Synthesis of (R)-3-Quinuclidinol with Regeneration of Coenzymes In Situ. *Catalysts* **2018**, *8*, 334–342.

Chapter 5

A High-Throughput Strategy for Glycine Oxidase Biosensor Development Reveals Glycine Release from Cultured Cells

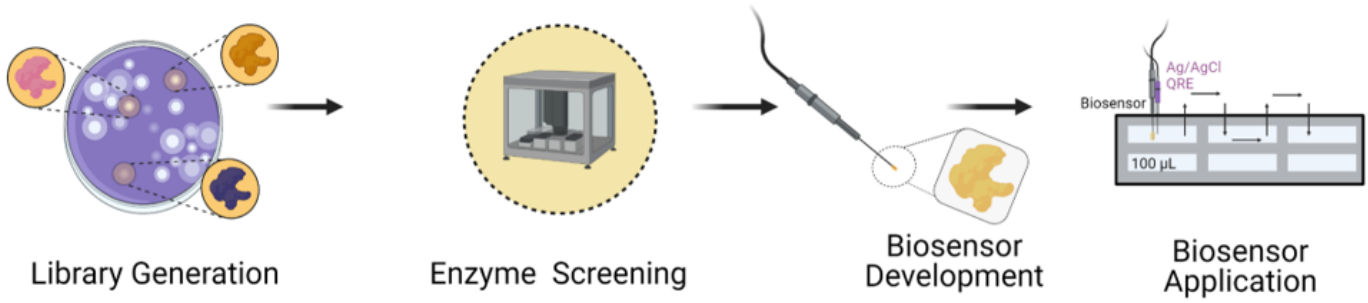

Chapter Preface

Glycine is an important biomarker in clinical analysis due to its involvement in multiple physiological processes. As such, the need for low-cost analytical tools for glycine detection is growing. As a neurotransmitter, glycine is involved in inhibitory and excitatory neurochemical transmission in the central nervous system.

Chapter 5 presents an electrochemical enzymatic biosensor for localized real time measurements of glycine. This biosensor relies on amperometric readout and does not require additional redox mediators. The biosensor was characterized and applied for real-time glycine detection from cells, mainly HEK 293 cells and primary rat astrocytes. An enzyme, glycine oxidase (GO) H244K, with increased glycine turnover was identified using mutagenesis. GO H244K was developed into a functional biosensor. Using GO H244K biosensors, glycine release of 395.7 µM ± 123 µM from primary astrocytes was measured which is ≈ 5 fold higher than from HEK 293 cells (75.4 µM ± 3.91 µM) measurements.

The work presented in this chapter is reproduced from:

Moussa, S., Rossini, E.,Chitsaz, D., Pollegioni, L., Kennedy, T., Mauzeroll J., A High-throughput Strategy for Glycine Oxidase Biosensor Development Reveals Glycine Release from Cultured Cells , *Analytical Chemistry* **2021** *(Accepted)*

Moussa, S., Mauzeroll J., Sensorlyze: A Software for Biosensor Data Analysis , *Manuscript in preparation* **2021**

5.1 Introduction

Biosensors are becoming increasingly popular for their ability to enable real-time analyte detection. The use of biosensors is revolutionizing many research areas, including neuroscience and clinical testing. Amperometric biosensors are one class of sensors that allow for quantification of concentration changes based on measured current changes.[1] One particular example case of amperometric biosensors is their successful commercialization into point of care devices as glucose test strips.[2,3] Previously, the application of amperometric enzymatic biosensors in pre-clinical studies on the detection of D-serine[4,5], an amino acid shown to be a co-agonist at excitatory NMDA receptors in the brain, was demonstrated.[6] A number of other enzymatic electrochemical probes have also been developed for neurotransmitter detection such as glutamate[7], dopamine[8] and acetylcholine[9]. No such amperometric sensors are available for localized measurements of the neurotransmitter and NMDAR co-agonist, glycine. As a neurotransmitter, glycine is involved in inhibitory and excitatory neurochemical transmission in the central nervous system.[10] Glycine release in the brain has varying overall impact depending on cellular release source.[11] It is endogenously synthesized from other amino acids, primarily in the liver and kidney, making it a non-essential amino acid.[12] Although non-essential, glycine plays other important roles in physiological function of humans and animals. In rest of the body, glycine has anti-inflammatory, cryoprotective, and immune modulating responses.[13] Previous efforts to associate glycine level measurement with diseased states have shown that low glycine levels are related to obesity, diabetes and schizophrenia.[12] Nutritionally, insufficient glycine intake may result in suboptimal growth,

impaired immune responses and other adverse effects on health and nutrient metabolism.[14] Currently, glycine levels are measured using chromatographic methods, which are expensive and time-consuming.[15–17] Glycine detecting electrochemical sensors have been developed to avoid the shortcomings of chromatography.[15,18,19]However, none of these sensors have been developed for localized glycine measurements, making it impossible to measure glycine levels associated with synaptic transmission without microdialysis.[10,11]

In Chapter 5, a rapid approach for the development of enzymatic amperometric electrochemical biosensors for real-time measurements of glycine release from localized regions is presented. To develop these sensors, a high-throughput screening (HTS) was used to identify GO variants with increased glycine activity. From a library of GO clones produced using random mutagenesis, clones with amino acidic substitutions at the H244 position were screened for enhanced glycine activity (Figure 5.1). The H244 residue on GO is localized in the active site cavity and is interesting since it is involved in optimization of the reaction catalyzed by GO without affecting the properties of the enzyme. Substitutions at the H244 position frequently result in substrate turnover number increase compared to GO WT.[20] Following the selection of clones with increased glycine activity relative to GO WT, enzymes were expressed and used for enzymatic electrochemical biosensor development.

First, the GO enzyme was immobilized onto the electrochemical sensor surface. Next, GO turned over glycine into H_2O_2. The H_2O_2 diffused through a permselective polymer layer and was subsequently oxidized at the electroactive sensor surface, where an oxidative current is measured and enabling indirect glycine quantification. To further reduce biosensor development time (≈30%), an approach using high-throughput assay techniques was devel-

oped for biosensor calibration and application. Finally, glycine levels were measured from astrocyte-conditioned media, HEK cells, and primary astrocytes. The GO H244K biosensors were found to be useful in glycine detection measurements, making them an important tool for localized glycine measurements in neurologically relevant systems.

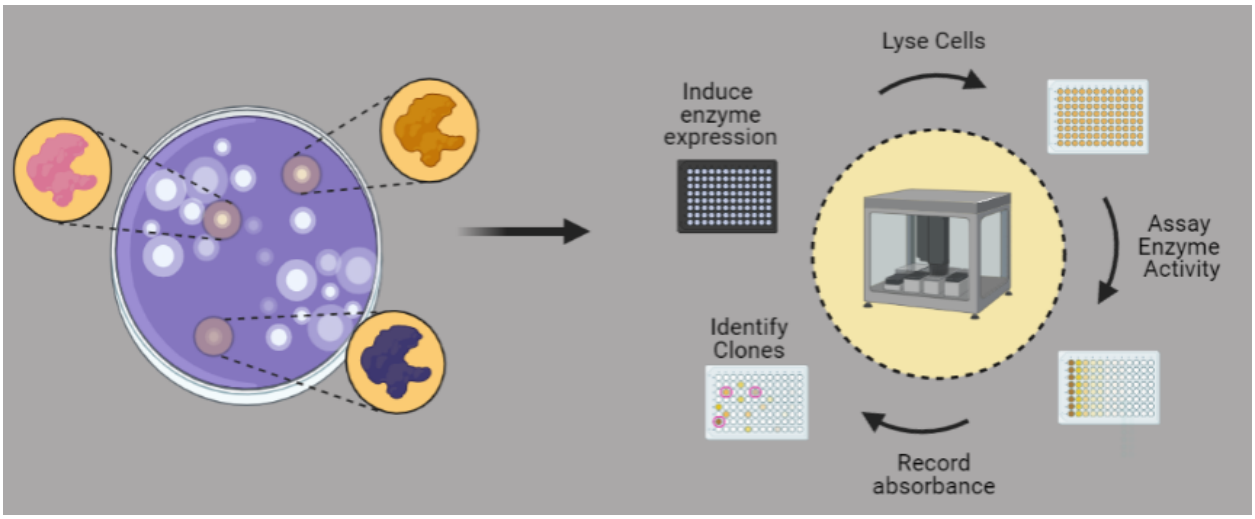

Figure 5.1: Random clone selection strategy and schematic of high-throughput screening methodology to search for variants with enhanced glycine activity.

5.2 Experimental Section

5.2.1 Materials and Chemicals

Horseradish peroxidase, amino acids, Amp, Cam, and all other compounds were purchased from Sigma unless otherwise stated. The final concentration of Amp and Cam used were 100 µg/mL and 34 µg/mL respectively.

5.2.2 Library Generation and Variant Screening

A library of GO variants was generated by site-directed mutagenesis at the H244 position using the QuikChange site-directed mutagenesis kit (Stratagene, La Jolla, CA) and the GO cDNA subcloned into the pT7(BH)-HisGO plasmid. The introduction of the mutation was confirmed by automated DNA sequencing. The PCR products were used to transform JM109 *E.*coli cells. Subsequently, the recombinant plasmids were transferred to BL21(DE3)pLysis *E.*coli cells and these clones were used for the screening procedure. The GO library was screened using a rapid colorimetric assay.[21] Briefly, the colorimetric assay is based on the quantification of hydrogen peroxide produced. Oxidase activity towards 36 mM D-serine, 36 mM D-alanine or 18 mM glycine was assayed on crude extracts of the overexpressed clones following cell lysis using an HRP and o-DNS coupled assay. The time course of the absorbance change at 450 nm was recorded at room temperature using a microtiter plate reader (Tecan). The average response was calculated and the clones which outperformed the control were selected for a repetition of the screening. Multiple reparations were performed for the screenings (n=3 replicates for each substrate). The highest activity clones were evaluated in three individual screening experiments and out of the clones selected, 6 final clones were selected for further analysis and biochemical characterization. The DNA of the interesting clones was isolated and sent for sequencing. Appendix D contains more details on the experimental methodology corresponding to the screening and clone selection.

5.2.3 Expression and Purification of His-GO WT, H244K, H244F and H244Q

The pT7(BH) expression plasmids coding for His-tagged wild type, H244K, H244F and H244Q were transferred to the host BL21(DE3)pLysS *E.*coli strain cells. Recombinant cells were grown under aerobic conditions at 37^{o}C in LB medium (20 g/L) containing Amp and Cam. Protein expression was induced in the exponential phase (at an $OD_{600nm} = 2$) by the addition of ITPG to a final concentration of 0.5 mM. The cells were then grown at 30^{o}C under agitation (130 rpm) and collected after 18 h by centrifugation and stored at -20^{o}C. Crude extracts were prepared by sonication (four cycles of 30 s each - pulsed and then continuous) of the cell paste suspended with 50 mM disodium pyrophosphate buffer, pH 8.5, containing 5 mM EDTA, 20 µM FAD, 5 mM 2-β- mercaptoethanol, 0.7 µg/ml pepstatin, and 10 µg/ml deoxyribonuclease I (2-3 ml of buffer/ gram of E.coli cells). The insoluble fraction of the lysate was removed by centrifugation. The recombinant GO proteins were purified from the crude extracts by using HiTrap chelating affinity chromatography column (GE Healthcare) previously loaded with 100 mM $NiCl_2$ and equilibrated with 50 mM disodium pyrophosphate buffer (NaPPi, pH 7.2), 1 M NaCl, 20 mM imidazole and 5% glycerol. The purified GOs were then equilibrated with 50 mM NaPPi, pH 8.5, and 10% glycerol. The final preparation of GO WT, GO H244Q and GO H244K was stored in 0.01 M PBS, pH 7.4, containing 1% glycerol. Enzyme purity was confirmed to be >90% by SDS-PAGE (Figure D.1). Enzymes were concentrated with a Centricon ultrafiltration device (MW cutoff = 30 kDa, Amicon). Protein concentration of the purified enzymes was determined using the extinction coefficient

at 450 nm (11.8 $mM^{-1}cm^{-1}$ for GO and 14.4 $mM^{-1}cm^{-1}$ for GO H244K).[20,22]

5.2.4 GO Activity Assay

Standard polarographic assays (0.253 mM O_2, 25^{o}C) for GO WT and GO H244K on 10 or 100 mM glycine in 50 mM sodium pyrophosphate (pH 8.5) were employed.[20,21] One enzyme unit is defined as the amount of enzyme that converts 1 µmol of amino acid per minute at 25^oC.[23] Substrate specificity was investigated by a colorimetric assay based on detection of hydrogen peroxide production using a coupled assay with peroxidase and o-dianisidine (o-DNS, ϵ=13 $mM^{-1}cm^{-1}$). Briefly, H_2O_2 produced from GO is reduced by horseradish peroxidase that simultaneously oxidizes o-DNS to give a colored compound with an absorption maximum at 440 nm. Different concentrations of standard D-alanine (1 mM), D-serine (1 mM) and glycine (100 µM - 25 mM) were used as substrates.

5.2.5 Electrochemical Experiments

Electrochemical measurements were performed using an Electrochemical Probe Scanner 3 (Heka Elektronik, Lambrecht, Germany; bipotentiostat model PG340). All potentials were recorded relative to an Ag/AgCl QRE (fabricated in-house, radius=0.125 mm).[24] All electrochemical solutions were prepared in phosphate-buffered saline (PBS, 0.01 M, pH 7.4). Measurements performed using chronoamperometry, involved a ME biased at 0.5 V vs. Ag/AgCl. All recorded potentials are reported against an Ag/AgCl reference.

5.2.6 GO WT and GO H244K Biosensor Fabrication

For biosensor development, the final GO WT and GO H244K preparations were concentrated to 50 mg mL^{-1} in 0.01 M PBS (pH 7.4) containing 1% glycerol and 25 mg mL^{-1} BSA using a Centricon device (MW cutoff = 30 kDa, Amicon). Platinum (Pt) disk MEs (10 µm) were prepared according to previously reported procedure.[24] Briefly, a soda-lime glass capillary was pulled and a Pt wire was inserted into the capillary, which was then sealed. The ME tip was polished until the Pt wire was exposed, revealing a disk-shaped surface geometry. The final ME was rinsed with deionized water (18.2 MΩ), 70% ethanol, and acetone. The R_g was confirmed with optical microscopy using a customized Axio Vert A1 inverted microscope (Zeiss, Oberkochen, Germany) to be between 2-3 for all MEs. A permselective polymer was then electrodeposited onto the electrode surface using cyclic voltammetry (0 to +1 V, 5 cycles) with 0.1 M m-phenylenediamine (PPD) prepared in 0.01 M PBS (pH 7.4). The full biosensors were fabricated according to a literature protocol.[25] Briefly, 2 µL of each enzyme was drop-casted onto a PDMS coated glass slide. The PPD-ME was immersed in the enzyme droplet for five seconds and then removed to dry for 4 minutes. This procedure was repeated four times, followed by enzyme crosslinking using glutaraldehyde solution (50% v/v in H2O).

5.2.7 Biosensor High-throughput Assay

Experiments were conducted in a Faraday cage positioned on a vibration dampening table (Micro 60, Halcyonics, Ames, IA, USA) to minimize noise. A custom made well plate (4 x 5 wells) was fixed to the ELP-3 sample plate (Appendix D). The biosensor was lowered to

approach the well plate using the z-piezo micro-positioner until contact was made with the solution in the well ($\approx$ 6 mm). Upon contact with the solution, an electrical connection was made and a chronoamperometric protocol was applied in which a potential of 500 mV was applied at the biosensor tip after a stabilization period of 30 s at 0 V. Following the completion of a five-minute current recording in a single microwell, the biosensor was retracted upwards to break the electrical connection, moved 6 mm in the x-direction towards the next well and the approach and record process was repeated. For each biosensor, independent chronoamps were recorded in a 4 x 5 grid. A macros protocol was written to iterate the hopping mode recording process until recording from all individual wells in each was completed. To move to the next row, the biosensor was moved 4 mm in the y direction. Currents were sampled at 10 Hz.

5.2.8 Glycine Quantification from Astrocyte Conditioned Media

Primary astrocyte cultures were obtained by mechanically dissociating and discarding non-astrocyte cell types from mixed glial cultures derived from P2 Sprague-Dawley rat pup cortices.[26] Astrocytes were cultured on 100 mm poly-d-lysine coated 100 mm dishes in DMEM containing 10% fetal bovine serum (FBS), pen/strep, and L-glutamine, and passaged at least 3 times before use. Cultures were checked with optical microscopy to ensure >95% astrocyte purity. Cells were cultured until confluency and the media was collected after 7 days and after 10 days for analysis. The astrocyte-conditioned media was filtered with 0.22 µm filters and stored at -80^oC until ready for analysis.

5.2.9 Biosensor Application for Real-Time Glycine Detection from Cells

Cultured HEK-293 cells were split and grown in separate 100 mm dishes and Dulbecco's Modified Eagle Medium (DMEM) supplemented with 9.1% fetal bovine serum (Thermo Fisher, Ottawa, ON, Canada) and 0.5 mg/mL primocin (InvivoGen, San Diego, CA, U.S.A.). Following confluency (≈ 7-8 days), the plates were scraped (STEMCELL) the cells were collected, and centrifuged for 5 mins (6000 rpm) to form a cell pellet. The cells were washed with sterile PBS twice and then resuspended in PBS buffer using a pipette tip for a buffer exchange. An aliquot of the cells was taken for cell counting to get an approximate amount of cells in solution. For any biosensor experiments, an aliquot corresponding to $1x10^6$ cells were transferred to a well on the well plate. The same protocol was repeated for null biosensor measurements and for rat-derived astrocytes.

5.2.10 LC-MS Experiments

A previously published protocol was used to prepare the LC-MS samples.[15] Briefly, 10 µL of blank samples (PBS) were diluted 1:4 with a mixture of acetonitrile/methanol/water 65/25/10. Fifteen microliters of this solution were injected into the LC–MS/MS. Gradient elution profile of the LC–MS/MS method Mobile phase "A" and "B" consisted of 0.1% formic acid in water (LC–MS grade) and methanol (LC–MS grade), respectively. The gradient elution profile at a constant flow rate of 400 l/min was chosen as follows: 0.0 min 80% A→0.2 min 80% A→3.0 min 40% A→4.0 min 40% A→4.2 min 80% A→5.0 min 80% A.

5.2.11 Data Analysis

All experimental data presented is the mean of triplicate measurements unless otherwise stated. Error bars represent the ±SEM. Data was analyzed using a inhouse developed software Sensorlyze, or Python 3.7 and treated in Python 3.7. Electrochemical signals were blank (PBS) signal corrected, resulting in i_{norm}. To generate the calibration curves, the steady state signals from noise-filtered data were extracted at each concentration and fit to a linear regression line. Selectivity towards glycine was calculated as follows:

$$Selectivity_{gly} = \frac{SA_{desiredproduct}}{SA_{undesiredproduct}} x100 = \frac{SA_{gly}}{SA_{D-ser/D-ala}} x100 \tag{5.1}$$

where SA is the specific activity of the selected amino acid.

5.3 Results and Discussion

5.3.1 Screening for GO Variant Enzymes with High Glycine Activity

Glycine is turned over by GO during the enzyme catalytic cycle, producing H_2O_2 as a byproduct. His-GO WT has a catalytic efficiency of 0.86 $s^{-1}mM^{-1}$.[22] Enzyme catalytic efficiency, a measure for enzyme specificity and turnover, can be improved through site directed mutagenesis.[27–29] To minimize discovery times associated with biocatalyst development with

enhanced efficiency for use in biosensor design, we applied a site saturation mutagenesis approach, namely mutant library generation and HTS for activity. Following the generation of a GO mutant library at the H244 position through error-prone PCR, a 96-well plate and an automated liquid handling system were used for a colorimetric assay. The signal observed from the o-DNS assay in 10 mM glycine and the crude extracts of E.coli cells expressing GO variants, corresponds to the enzyme variant activity.[21] Any alteration in the GO clone activity on glycine was monitored using a change in absorbance at $\lambda = 440$ nm (Figure 5.2A). After a final round of screenings (Figure 5.2B), 10 clones with increased glycine activity were identified. To confirm the increased activity of the 10 selected clones, one final screening was performed with only the 10 clones. The absorbance values for these clones normalized to the absorbance for GO WT is presented in Figure 1C. These clones correspond to GO variants with enhanced glycine activity (Figure 5.2C, gold), making their use for biosensor development an attractive option compared to GO WT (Figure 5.2C, purple).

The most active clones (6/10 clones from final screening, Figure 5.2C: B2,B4,C2,C4,G3) on glycine as detected via the screening procedure were identified by automatic DNA sequencing. The sequencing allowed us to identify the mutation type for each clone and eliminated the presence of false positives (3/6 clones). Asides from the false positives, three interesting variants were identified by mutant screening with possibly improved glycine activity: H244F, H244Q and H244K (Figure 5.2: C2,C3,C4). H244F, H244Q and H244K GO variants were expressed and their activity on glycine was characterized using polarographic method. From the specific activities (Table D.1, GO WT: 0.8 U mg^{-1}, GO H244F : 0.523 U mg^{-1}, GO H244K: 1.038 U mg^{-1}, GO H244Q : 0.177 U mg^{-1}) and literature activities[22], GO

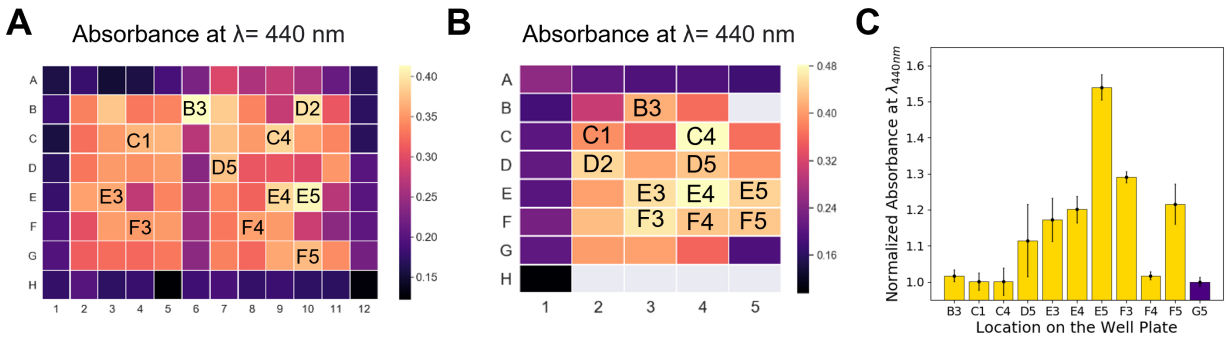

Figure 5.2: HTS Assay screening results for glycine activity following 24 hour incubation in 18 mM glycine A) Absorbance values (λ = 440 nm) for all GO clones screened in a 96 well plate. Position H11 corresponds to the clone for GO WT and position H12 corresponds to the control well with no clone present. B) Absorbance values(λ = 440 nm) for glycine oxidase clones selected from initial screening of 94 clones. screened in a 96 well plate. Position G5 corresponds to the clone for GO WT and position H1 corresponds to the control well with no clone present. Grey boxes represent empty wells. C) Normalized absorbance values (corrected for the control plate and normalized by a factor of 1 to GO WT [G5]) for the ten glycine oxidase clones (yellow) selected from the screening.

H244K had the highest glycine turnover ratio compared to GO WT (D.2, 11.22 vs 1.00). As such, GO WT and GO H244K were characterized using spectrophotometric o-DNS assays (Figure 5.3). At all tested concentrations (0.1 mM, 1 mM and 10 mM), GO H244K indeed had higher glycine activity than GO WT. Moreover, GO H244K had high activity towards glycine compared to D-serine and D-alanine (Figure 5.3C), two neurologically present amino acids which are simultaneously found in presence of glycine.[30–32]

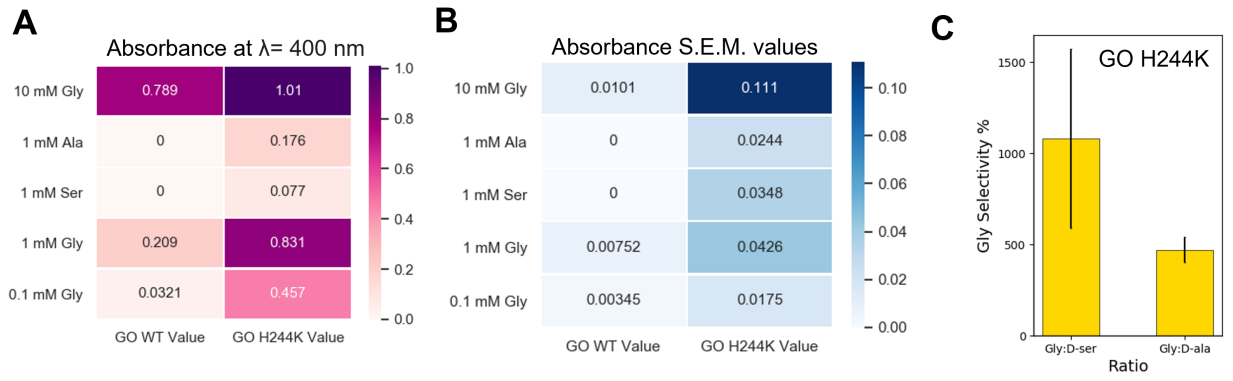

Figure 5.3: Substrate specificity of GO WT and GO H244K using the spectrophotometric assay (NaPPi buffer, pH 85). (A) Specific activity (U mg^{-1}) values for the enzymes at various substrate concentrations of D-serine, D-alanine, or glycine. (B) SEM values for the specific activities as reported in panel A. (C) Selectivity of GO H244K enzymes towards glycine over D-serine and D-alanine. Error bars represent mean values ± SEM.

5.3.2 Assessing the Performance of GO WT and GO H244K Biosensors

Using both GO H244K and GO WT, the enzymes were incorporated into biosensors. Through enzyme immobilization on PPD-Pt MEs, biosensors were fabricated and calibrated in standard solutions of glycine.[33] To rapidly generate calibration curves, Sensorlyze, a inhouse python-based software tool developed by the author, was used for biosensor performance assessment. Sensorlyze is a software that automates data processing and manipulation by converting raw data files into figures and allows users to generate calibration curves from multiple data files, provides statistics such as linear regression parameters and limits of detection and quantification. Sensorlyze was also used to extract steady state currents from multiple chronoamperograms and to average these values over a 30 second range(see Appendix D for

more detail).

The current response of GO WT and GO H244K was linearly related to the logarithmic value of the glycine concentration within the range of 50-1000 µM (Figure 5.4). GO WT at 13.3 mg.mL^{-1} resulted in calibration curves with lower sensitivity (Figure D.3A) compared to the more concentrated GO WT at 50 mg.mL^{-1} (Figure D.3B). Additionally, the non-log calibration curves for GO WT and GO H244K were non-linear as shown in Figure D.3.

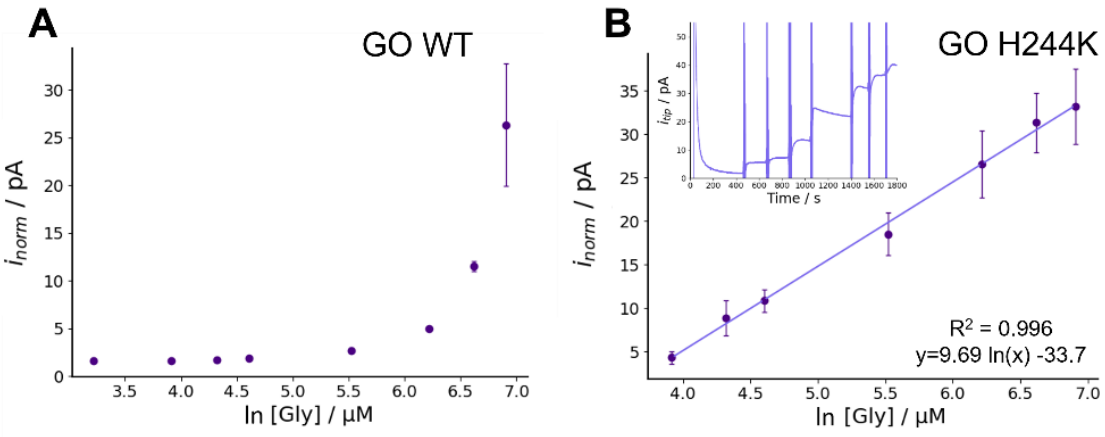

Figure 5.4: Calibration curves of (A) GO WT and (B) GO H244K-based biosensors in standard solutions of 50,75, 100, 250, 500, 750, 1000 µM glycine (PBS, pH 7.4). Inset: Raw sample current-time curve for different glycine biosensors using GO H244K enzymes. Error bars correspond to the S.E.M (n=4). LOD=16.5 µM± 2.9 µM LOQ= 55 µM± 4.2 µM.

To assess the stability of the biosensors, GO H244K and GO WT biosensors were stored at both 4^{o}C and 20^{o}C following an initial calibration. Both GO WT and GO H244K sensors lost sensitivity following two-week storage at -20^{o}C (Figure D.4A&B). GO H244K biosensors were stored dry at 4^{o}C and calibrated the following day. Dry storage at 4^{o}C resulted in linear calibration curves for GO H244K (Figure D.4C). The lack of response was due to enzyme film delamination, suggesting that the adsorption of GO requires improvement for increased

biosensor lifetime.

5.3.3 GO H244K Biosensors Detect Glycine in Astrocyte-Conditioned Media

Astrocytes are thought to be a major source of glycine[34] and were studied with GO H244K biosensors (Figure 5.5A). The biosensor was first calibrated in standard solutions of glycine spiked into DMEM buffer, which already contained 400 µM glycine (Figure 5.5B). Following astrocyte culture, media collection and filtering, and biosensor calibration, the biosensor was applied for glycine detection in 300 µL of filtered, astrocyte conditioned DMEM. Media from two sets of cultures were collected. From batch 1, the media was collected after 7 days of conditioning. From batch 2, the media was collected after 10 days of conditioning. Using the biosensor, an average of 572 µM ±113 µM glycine was measured (Figure 5.5C), suggesting glycine release of astrocytes with variability corresponding to culture time and batch-to-batch differences. Although DMEM has 400 µM glycine, it was possible to measure additional glycine levels as shown in Figure 5.5. From the biosensor readings, it is suggested that astrocytes do in fact release glycine, possibly through astrocyte glycine transporters, as shown in published literature.[34–37]

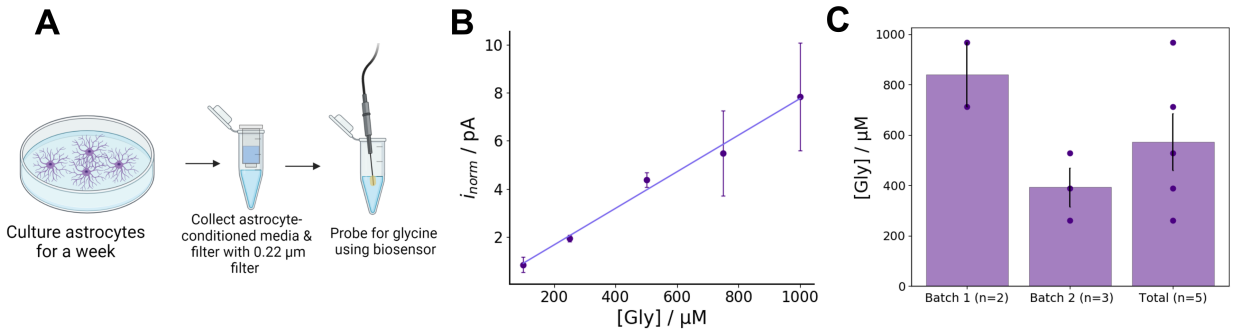

Figure 5.5: Glycine detection from cultured primary rat astrocytes using GO-H244K biosensors. (A) Schematic of experimental protocol (B) Biosensor calibration curve in standard glycine solutions prepared in DMEM (C) Concentrations obtained from biosensor calibrations for individual batches and for the batches combined. Batch 1 corresponds to media collected after 7 days. Batch two corresponds to media collected after 10 days. Total corresponds to the average of all batches. Average concentrations ±S.E.M. are displayed.

5.3.4 Achieving Real-Time Glycine Detection from Live HEK293 Cells and Astrocytes

Microelectrode biosensors are particularly useful for localized real-time quantification of analytes. To assess the performance of these biosensors in real-time glycine release measurements using an automated methodology, a custom micro-sized well plate was prepared as discussed in the experimental section. In combination with a 0.125 mm Ag/AgCl QRE, the biosensor was approached to the solution on the microwell plate using a z-piezo motor. A constant voltage of 0.5 V was applied at the biosensor tip and when the biosensor was immersed in solution, a faradaic current corresponding to the oxidation of H_2O_2 was recorded. The biosensor was moved from one well to another using a hopping mode with the ELP motor system and the current from each sample was recorded (Figure 5.6A). To evaluate real-time

glycine release, the biosensor was immersed in 100 µL of HEK 293 cells (1x 10^6 cells in PBS buffer) which were pipetted into one of the wells on the well plate. The current from the HEK 293 cells was monitored over a period of 30 minutes and the steady state current after 30 minutes was extracted from resulting chronoamperograms (Figure 5.6B purple, Figure D.5) and compared against the background signal from the biosensor in PBS buffer (Figure 5.6B yellow). The same protocol was repeated using a null biosensor (Figure 5.6B blue). The biosensor calibration curve (Figure 5.6C) was then used to convert the current responses of the biosensor in HEK 293 cells into glycine concentrations (Figure 5.6D). Similarly, glycine release from astrocytes was monitored using the active and null biosensors (Figure 5.65E purple vs blue) and the signal was compared against the biosensor response in PBS buffer (Figure 5.6E, yellow). The biosensor calibration curve (Figure 5.6F) was then used to convert the current responses of the biosensor in astrocytes into glycine concentrations (Figure 5.6G). The concentrations recorded from Figure 5.6D&G demonstrate that GO H244K biosensors are useful tools for real-time glycine detection from multiple cell types. Moreover, Figure 5.6 shows that astrocytes release significantly larger amounts of glycine (395.7 µM ± 123 µM, Figure 5.6D) compared to HEK 293 cells (75.4 µM ± 3.91 µM, Figure 5.6G). Astrocytes demonstrate ≈5 fold greater release of glycine than HEK 293 cells.

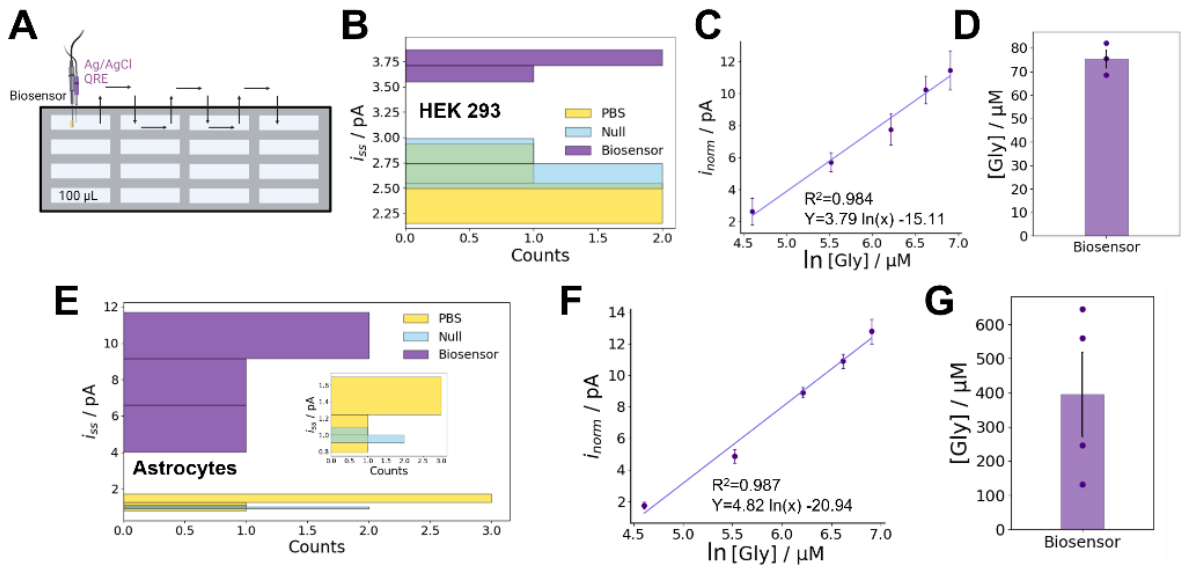

Figure 5.6: High-throughput hopping mode real-time glycine detection from multiple biological analytes. (A) Schematic of electrochemical experimental setup (B) Buffer normalized currents from HEK 293 cells using the null and enzymatic biosensors (C) Calibration curve with the GO H244K enzymatic biosensors (D) Corresponding current reading from HEK 293 cells using the biosensor. The average reading corresponds to 75.4 µM ± 3.91 µM (E) Histogram of the steady state currents from null and active biosensors immersed in buffer and astrocytes (F) Calibration curve of the biosensor prior to glycine detection from astrocytes, corresponding current readings of glycine released from astrocytes following a 30 minute biosensor incubation period. (G) The average reading corresponds to 395.7 µM ± 123 µM. Error bars correspond to ±S.E.M.

The relatively higher astrocytic glycine release is consistent with literature suggestions that astrocytes store glycine and that glycine release is mediated through the Asc-1 transporter in astrocytes, not typically found in HEK 293 cells.[34–37] Moreover, LC-MS experiments demonstrate the presence of glycine in these cell samples, confirming the release of glycine through both biosensor and LC-MS measurements (Figure D.6). Finally, the potential of using Triton X-100 and Tween-20 to lyse cells for release of stored glycine is also presented in Figure D.7. The effect of these surfactants on the biosensor response is explored in Figure

D.7 and shown to be negligible on the biosensor response.

5.4 Conclusion

In this work, we demonstrated the first enzymatic amperometric biosensor fabricated and applied for real-time glycine detection from cells based on GO H244K. Mutagenesis and HTS enzyme screening enabled the rapid discovery of enzyme variants with enhanced glycine activity. The performance of GO H244K biosensors superseded that of GO WT biosensors and GO H244K biosensors demonstrated high reproducibility. Using only 100 µL of cells, glycine was detected from both HEK 293 and astrocyte cells without the need for additional reagents. While these sensors were shown applicable for real-time detection of glycine, future work entails sensitivity improvements of such biosensors possibly through the increasing the microelectrode backbone surface roughness or the generation of a double or triple mutant enzyme with even further enhanced glycine selectivity. Given this paper's advancements in reducing enzyme discovery times, biosensor optimization, assay miniaturization and automation, as well as data analysis simplification this system can be developed with minimal effort for potentially any stable oxidase enzyme to extend the range of analytes probed with such sensors. These sensors may then be used to study glycinergic functions and mechanisms in the brain or as clinical tools for glycine analysis.

References

(1) Moussa, S.; Mauzeroll, J.-M. An Overview of Probe Development and Bioelectrochemistry Applications from 2013 to 2018. *J. Electrochem. Soc.* **2019**, 1–16.

(2) Newman, J.; Turner, A., *Home Blood Glucose Biosensors: A Commercial Perspective. Biosensors and Bioelectronics*; Biosens. and Bioelectron.: 2005, pp 2435–2453.

(3) Chen, C.; Xie, Q.; Yang, D.; Xiao, H.; Fu, Y.; Tan, Y.; Yao, S. Recent Advances in Electrochemical Glucose Biosensors: A Review. *RSC Adv.* **2013**, *14*, 4473–4491.

(4) Moussa, S.; Van Horn, M.; Shah, A.; Pollegioni, L.; Thibodeaux, C.; Ruthazer, E.; Mauzeroll, J. A Miniaturized Enzymatic Biosensor For Detection of Sensory-Evoked D-Serine Release in the Brain. *J. Electrochem. Soc.* **2021**, *168*, 1–10.

(5) Polcari, D.; Kwan, A.; Van Horn, M.; Danis, L.; Pollegioni, L.; Ruthazer, E.; Mauzeroll, J. Disk-Shaped Amperometric Enzymatic Biosensor for in Vivo Detection of D-Serine. *Anal. Chem.* **2014**, *86*, 3501–3507.

(6) MacKay, M.; Kravtsenyuk, M.; Thomas, R.; Mitchell, N.; Dursun, S.; Baker, G. D-Serine: Potential Therapeutic Agent and/or Biomarker in Schizophrenia and Depression? *Front. Psychiatry*, *5*, 1–9.

(7) Isoaho, N.; Peltola, E.; Sainio, S.; Wester, N.; Protopopova, V.; Wilson, B.; Koskinen, J.; Laurila, T. Carbon Nanostructure Based Platform for Enzymatic Glutamate Biosensors. *J. Phys. Chem. C* **2017**, *121*, 4618–4626.

(8) Njagi, J.; Chernov, M.; Leiter, J.; Andreescu, S. Amperometric Detection of Dopamine In Vivo with an Enzyme Based Carbon Fiber Microbiosensor. *Anal. Chem.* **2010**, *82*, 989–996.

(9) Moreira, F.; Sale, M.; Di Lorenzo, M. Towards Timely Alzheimer Diagnosis: A Self-Powered Amperometric Biosensor for the Neurotransmitter Acetylcholine. *Biosens. Bioelectron.* **2017**, *87*, 607–614.

(10) Zhang, W.; Herde, M.; Mitchell, J.; Whitfield, J.; Wulff, A.; Vongsouthi, V.; Sanchez-Romero, I.; Gulakova, P.; Minge, D.; Breithausen, B.; Schoch, S.; Janovjak, H.; Jackson, C.; Henneberger, C. Monitoring Hippocampal Glycine with the Computationally Designed Optical Sensor GlyFS. *Nat. Chem. Biol.* **2018**, *14*, 861–869.

(11) Harsing, L.; Matyus, P. Mechanisms of Glycine Release, Which Build up Synaptic and Extrasynaptic Glycine Levels: The Role of Synaptic and Non-Synaptic Glycine Transporters. *Brain Research Bulletin* **2013**, *1*, 110–119.

(12) Wang, W.; Wu, Z.; Dai, Z.; Yang, Y.; Wang, J.; Wu, G. Glycine Metabolism in Animals and Humans: Implications for Nutrition and Health. *Amino Acids* **2013**, *45*, 463–477.

(13) Weinberg, J.; Bienholz, A.; Venkatachalam, M., *The Role of Glycine in Regulated Cell Death*; Birkhauser Verlag AG: 2016, pp 2285–2308.

(14) Razak, M.; Begum, P.; Viswanath, B.; Rajagopal, S. Multifarious Beneficial Effect of Nonessential Amino Acid, Glycine: A Review. *Oxidative Medicine and Cellular Longevity* **2017**, 1–8.

(15) Voehringer, P.; Fuertig, R.; Ferger, B. A Novel Liquid Chromatography/Tandem Mass Spectrometry Method for the Quantification of Glycine as Biomarker in Brain Microdialysis and Cerebrospinal Fluid Samples within 5min. *J. Chromatogr. B Anal. Technol. Biomed.* **2013**, *939*, 92–97.

(16) Forgacsova, A.; Galba, J.; Mojzisova, J.; Mikus, P.; Piestansky, J.; Kovac, A. Ultra-High Performance Hydrophilic Interaction Liquid Chromatography – Triple Quadrupole Tandem Mass Spectrometry Method for Determination of Cysteine, Homocysteine, Cysteinyl-Glycine and Glutathione in Rat Plasma. *J. Pharm. Biomed. Anal.* **2019**, *164*, 442–451.

(17) Pérez-Ràfols, C.; Liu, Y.; Wang, Q.; Cuartero, M.; Crespo, G. Why Not Glycine Electrochemical Biosensors? *Sensors* **2020**, *20*, 1–19.

(18) Vidotti, M.; Torresi, S.; Kubota, L. Electrochemical Oxidation of Glycine by Doped Nickel Hydroxide Modified Electrode. *Sens. Actuat. B Chem.* **2008**, *135*, 245–249.

(19) Roushani, M.; Shamsipur, M.; Pourmortazavi, S. Amprometric Detection of Glycine, L-Serine, and L-Alanine Using Glassy Carbon Electrode Modified by NiO Nanoparticles. *J. Appl. Electrochem.* **2012**, *42*, 1005–1011.

(20) Boselli, A.; Rosini, E.; Marcone, G.; Sacchi, S.; Motteran, L.; Pilone, M.; Pollegioni, L.; Molla, G. Glycine Oxidase from Bacillus Subtilis: Role of Histidine 244 and Methionine 261. *Biochimie* **2007**, *89*, 1372–1380.

(21) Rosini, E.; Caldinelli, L.; Piubelli, L. Assays of D-Amino Acid Oxidase Activity. *Front. Mol. Biosci.* **2018**, *4*, 1–12.

(22) Rosini, E.; Piubelli, L.; Molla, G.; Frattini, L.; Valentino, M.; Varriale, A.; D'Auria, S.; L., P. Novel Biosensors Based on Optimized Glycine Oxidase. *FEBS* **2018**, *4*, 3460–3472.

(23) Sacchi, S.; Lorenzi, S.; Molla, G.; Pilone, M.; Rossetti, C.; Pollegioni, L. Engineering the Substrate Specificity of D-Amino-Acid Oxidase. *J. Biol. Chem.* **2002**, *30*, 27510–27516.

(24) Danis, L.; Polcari, D.; Kwan, A.; Gateman, S.; Mauzeroll, J. Fabrication of Carbon, Gold, Platinum, Silver, and Mercury Ultramicroelectrodes with Controlled Geometry. *Anal. Chem.* **2015**, *87*, 2565–2569.

(25) Polcari, D.; Perry, S.; Pollegioni, L.; Geissler, M.; Mauzeroll, J. Localized Detection of D-Serine by Using an Enzymatic Amperometric Biosensor and Scanning Electrochemical Microscopy. *ChemElectroChem* **2017**, *4*, 920–926.

(26) KD, M.; J, d. V. Preparation of Separate Astroglial and Oligodendroglial Cell Cultures from Rat Cerebral Tissue. *J. Cell Biol.* **1980**, *85*, 890–902.

(27) Duan, X.; Chen, J.; Wu, J. Improving the Thermostability and Catalytic Efficiency of Bacillus Deramificans Pullulanase by Site-Directed Mutagenesis. *Appl. Environ. Microbiol.* **2013**, *79*, 4072–4077.

(28) Jaouadi, B.; Aghajari, N.; Haser, R.; Bejar, S. Enhancement of the Thermostability and the Catalytic Efficiency of Bacillus Pumilus CBS Protease by Site-Directed Mutagenesis. *Biochimie* **2010**, *92*, 360–369.

(29) Molloy, S.; Nikodinovic-Runic, J.; Martin, L.; Hartmann, H.; Solano, F.; Decker, H.; O'Connor, K. Engineering of a Bacterial Tyrosinase for Improved Catalytic Efficiency towards D-Tyrosine Using Random and Site Directed Mutagenesis Approaches. *Biotechnol. Bioeng.* **2013**, *110*, 1849–1857.

(30) Mothet, J.; Billard, J.; Pollegioni, L.; Coyle, J.; Sweedler, J. Investigating Brain D-serine: Advocacy for Good Practices. *Acta Physiol.* **2019**, *226*, 13257.

(31) Murtas, G.; Sacchi, S.; Valentino, M.; Pollegioni, L. Biochemical Properties of Human D-Amino Acid Oxidase. *Front. Mol. Biosci.* **2017**, *4*, 1–11.

(32) Le Bail, M.; Martineau, M.; Sacchi, S.; Yatsenko, N.; Radzishevsky, I.; Conrod, S.; Ouares, K.; Wolosker, H.; Pollegioni, L.; Billard, J.; Mothet, J.; Snyder, S. Identity of the NMDA Receptor Coagonist Is Synapse Specific and Developmentally Regulated in the Hippocampus. *PNAS* **2015**, *112*, 204–213.

(33) Moussa, S.; Murtas, G.; Pollegioni, L.; Mauzeroll, J. Enhancing Electrochemical Biosensor Selectivity with Engineered D-Amino Acid Oxidase Enzymes for D-Serine and D-Alanine Quantification. *ACS Appl. Bio. Mater.* **2021**, *4*, 5598–5604.

(34) Shibasaki, K.; Hosoi, N.; Kaneko, R.; Tominaga, M.; Yamada, K. Glycine Release from Astrocytes via Functional Reversal of GlyT1. *J. Neurochem.* **2017**, *140*, 395–403.

(35) Holopainen, I.; Kontro, P. Uptake and Release of Glycine in Cerebellar Granule Cells and Astrocytes in Primary Culture: Potassium-Stimulated Release from Granule Cells Is Calcium-Dependent. *J. Neurosci. Res.* **1989**, *24*, 374–383.

(36) Rosenberg, D.; Artoul, S.; Segal, A.; Kolodney, G.; Radzishevsky, I.; Dikopoltsev, E.; Foltyn, V.; Inoue, R.; Mori, H.; Billard, J.-M.; Wolosker, H. Cellular/Molecular Neuronal D-Serine and Glycine

Release Via the Asc-1 Transporter Regulates NMDA Receptor-Dependent Synaptic Activity. *J. Neurosci.*, *33*, 3533–3544.

(37) Hogerton, A.; Bowser, M. Monitoring Neurochemical Release from Astrocytes Using In Vitro Microdialysis Coupled with High-Speed Capillary Electrophoresis. *Anal. Chem.* **2013**, *85*, 9070–9077.

Chapter 6

Conclusions

6.1 Summary, Conclusions, and Future Directions

6.1.1 Summary and Conclusions

MEs have been around since the 1800s, with early measurements made for dopamine detection. State of the art technology has made it possible to reduce instrumental limits of detection, all the way into the femto-scale. In particular, potentiostats, which are used in conjunction with MEs, have been refined to reduce noise and increase sensitivity. Yet, ME-based biosensors have inherent challenges that remain to be addressed. For example, ME-based biosensors often suffer from limit of detection and selectivity limitations, that even with the best performing potentiostat, cannot be improved upon. Optimizing the design of biosensors will unlock multiple opportunities, not only for their application as point of care devices, but for furthering areas of research where there is a real need for localized real-time analyte detection, such as in clinical chemistry and neuroscience.

Nevertheless, the ultimate goal of this thesis is to obtain localized and real time measurements of multiple analytes using biosensors. To achieve the goal of real-time analyte detection using biosensors, this thesis addresses challenges in the biosensor bioreceptor component. Key contributions of this thesis towards real-time analyte detection include characterization of immobilized enzyme activity, developing of a methodology to screen for enzymes with increased analyte selectivity, increasing biosensor limits of detection and selectivity, as well as demonstrating biosensor application for real-time measurements *in vitro*, *ex vivo* and *in vivo*.

Compared to state of the art biosensing technologies, which are not limited to electrochemical methods, this thesis pushes forward electrochemical-based biosensing for real time analyte quantification. While other methods such as colorimetric-based sensing are promising, electrochemical methods are reagent-free and present more cost effective solutions in the field of biosensing. A significant portion of the available literature in electrochemical based biosensing is focused on proof-of-concept biosensor development,lacking extensive application to derive useful information on biochemical levels using the developed sensors. This thesis focuses on the development and application of enzymatic biosensors, going beyond the proof-of-concept, and establishing real world applications for such biosensors. In this thesis, the first ever glycine oxidase mutant-based electrochemical biosensor was developed and appplied. Moreover, novel findings with respect to the development and application of DAAO-based electrochemical biosensors were presented. A summary of each chapter's contribution towards real-time detection of biological analytes with desired sensitivity and selectivity is discussed below.

Chapter 1 presented a summary of the existing literature on ME theory, fabrication methods, and notable applications during the 2013-2018 period. Case studies from literature were highlighted to demonstrate the many ways in which MEs were used as biosensors to obtain critical analyte information. Chapter 1 also focused on surface modifications of MEs using polymers, nanoparticles, fibers, enzymes, nucleic acids, peptides and DNA, to improve selectivity and sensitivity for real-time bioanalyte detection. Although surface modifications improve ME performance, results obtained with ME biosensors still require complementary analysis such as LC-MS to validate and ensure accurate readings.

Future direction of this work includes generating a database of developed biosensors with their surface functionalities and their successful application. The database would enable other researchers, who lack expert knowledge in this field, to select appropriate sensors for their research. Moreover, although biosensors are being applied for analyte detection in biological media, there remains room in extending their application for clinical analysis of disease biomarkers. There is significant advantage in involving clinicians during the design stage of biosensors, such that they can be applied regularly in clinical chemistry. Additionally, incorporating multiplexed sensing with MEs poses a significant advantage for real-time monitoring of multiple biomarkers simultaneously.

Chapter 2 described a ME-based electrochemical characterization approach method (MECA) to determine the true enzymatic activity of a biosensor. Typically, enzymatic assays of the nanoparticle-bound enzymes are used to determine the biosensor activity, however these assays do not consider the case immobilized enzyme on fixed supports. Thus, the activity of immobilized enzymes on biosensors, which is dependent on enzyme spatial orientation, is often grossly overestimated. Under MECA, the production of H_2O_2 from enzymes immobilized on a ME using PPD-MEs is measured by chronoamperometry. The enzyme *Rg*DAAO was used for the proof-of-concept, but this method may be generalized to any enzyme which produces a redox active species such as H_2O_2 from its catalytic cycle. The underexplored effect of immobilization on enzyme efficacy was studied using MECA. The enzymatic activity and substrate selectivity of free *Rg*DAAO and its immobilized counterpart on PPD-MEs was explored.

The study in Chapter 2 may be extended to assess the effect of different crosslinkers such

as poly(ethylene glycol) and diglycidyl ether (PEDGE) on enzyme activity. This is motivated in part by the need for milder crosslinkers that are less toxic than glutaraldehyde, which is currently the preferred crosslinkers to immobilized enzymes for biosensors. As such, MECA could be adapted to explore other aspects of enzyme immobilization in order to optimize biosensor designs in accordance with a specific application. Beyond the field of medical technology, MECA could be of interest in the development of biofuel cells. Characterization of immobilized enzyme activity is critical for efficient biofuel cell design and Chapter 2 lays some of the groundwork for extending the MECA method to biofuel cell design, particularly in optimizing reactions at the cathode and anode electrodes.

Chapter 3 extended the research in Chapter 2 by developing minituarized biosensors with *Rg*DAAO immobilized onto the ME surface and applying them for *ex vivo* and *in vivo* D-serine detection. A robust methodology for the fabrication of a reproducible miniaturized 10 µm D-serine detecting amperometric biosensor was developed. The biosensors were then used for D-serine detection from tadpole brains, where D-alanine levels are considered negligible.

Chapter 3 presented the application of ME-based biosensors to address an important ongoing question on the association of D-serine with sensory stimulation. With the help of *Rg*DAAO biosensors, it was observed that levels in the brain of *Xenopus laevis* tadpoles fluctuate with sensory experience. The application of such biosensors for real-time *in vivo* measurements was also validated. Demonstrating the feasibility of applying the biosensors for *in vivo* measurements was critical in their continued success for application in determining localized, real-time D-serine release.

The biosensors developed in Chapter 3 may be even further applied for more extensive

D-serine research. Mechanisms of D-serine release have not yet been completely deciphered. As such, observing the impact ATP-stimulated D-serine release *in vivo* would contribute to understanding D-serine release mechanisms and the overall impact of ATP on D-serine levels. Another interesting avenue, is mapping out the relationship between gut derived D-serine and brain-derived D-serine to elucidate the gut-brain relationship with respect to D-serine. Recent research shows that intestine derived D-serine plays a role in sleep regulation in *Drosophila*.[1] Using the D-serine biosensors developed in Chapter 3, it may be possible to extend this study to other model organisms, as well as understand the gut-brain relationship even further.

Chapter 4 advanced the development of D-serine detecting biosensors by identifying alternative enzymes to optimize D-serine selectivity. Inspired by Chapter 3, Chapter 4 focused on exploring DAAO enzymes to increase biosensor D-serine selectivity. Chapter 4 also studied the possibility of developing D-alanine selective biosensors with DAAO enzymes.

Through introduction of point mutations into DAAO, DAAO variants were expressed and characterized for their selectivity and activity towards D-serine and D-alanine. The structural impact of enzyme crosslinking was studied. More importantly, the biosensors were characterized and assessed for their selectivity towards D-serine and D-alanine. Chapter 4 highlighted factors critical for the success for enzymatic biosensors and their regeneration. The need to characterize free enzymes prior to biosensor development was emphasized, as this characterization would cut biosensor research time and cost significantly.

Future developments of Chapter 4 entails application of multiple biosensors for simultaneous D-serine and D-alanine detection. Multiplexed measurements would involve extensive

sample data collection to accurately predict concentrations in unknown samples. These measurements may be achieved by application of multiple individual biosensors and using chemometric methods such as partial least squares regression (PLSR) to distinguish the signal for one amino acid over the other (Figure 6.1).[2] Alternatively, developing a biosensor array where one of two enzymes are immobilized would also enable the simultaneous detection of amino acids.

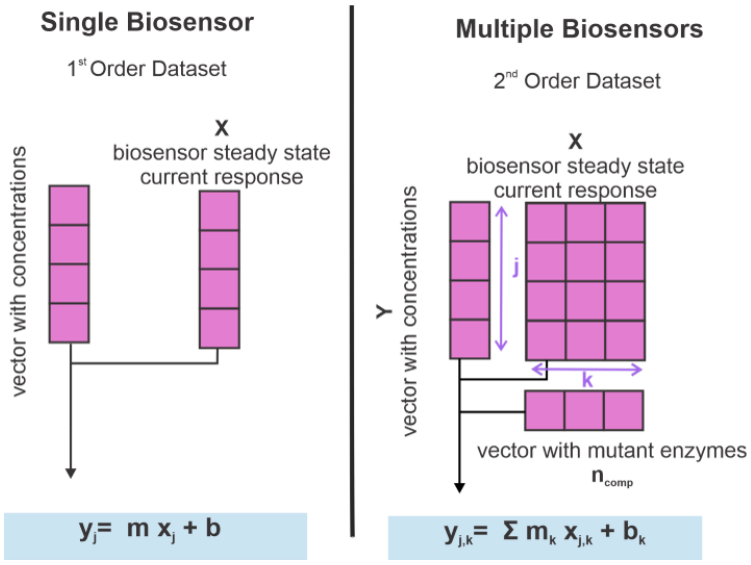

Figure 6.1: Schematic for data treatment methodology. Left: Calibration of single biosensor employs a first order dataset to generate a linear calibration curve corresponding to $y_j = mx_j + b$ where j corresponds to the sample concentration. Right: Calibration of multiple sensors against a single analyte (i.e. D-serine). A second order dataset is used to generate a calibration curve corresponding to the sum of the calibration curves at concentrations j, for k biosensors. The number of components (n_{comp}) used for the regression analysis also corresponds to the number of biosensors.

Chapter 5 is an extension of the earlier chapters by expanding the analyte scope of enzymatic electrochemical biosensors to glycine. Through replacing DAAO with an oxidase

enzyme responsible for glycine turnover, glycine is detected using the biosensor. Due to their naturally low activity on glycine, GO WT biosensors are not the primary enzymes of choice for glycine biosensor development. Rather than investing significant time and cost into finding an enzyme variant suitable for glycine turnover, a high-throughput screening strategy was applied to identify GO variants with improved glycine activity. From an enzyme activity screening, a GO variant, GO H244K, was identified as a more suitable enzyme and used for biosensor development. GO H244K biosensors were applied for real-time glycine detection from HEK293 cells and astrocyte cell cultures with a high-throughput electrochemical setup.

Additionally, since data treatment requires significant time in biosensor development and application, a python-based software developed used for data analysis of Chapter 5 data. Sensorlyze, the software, enables the rapid generation of calibration curves from chronoamperograms obtained using multiple potentiostat systems. The software provides important calibration curve statistics such as regression line parameters as well as limits of detection and quantification.

Chapter 5 may be extended through exploring the application of glycine biosensors for *in vivo* measurements as well as SECM measurements from individually cultured cells. Such measurements may require further improvements in biosensor sensitivity and limit of detection, addressable through alternative biosensor surface modifications and increasing the surface roughness.

Moreover, the functionalities of Sensorlyze may be broadened to include 1) non-linear regression for calibration curves 2) machine learning algorithms for multivariate calibration data processing 3) data analysis of biofuel cell relevant calculations, such as current density.

6.1.2 Thoughts for the Future

Much of the mentioned success of enzymatic biosensors comes from a particularly commercialized sensor: the glucometer. Bottlenecks in the successful development of biosensors have been tied to identification of stable enzymes which enable selective analyte detection. Recent years highlighted the importance of collaboration between engineers, chemists, biologists and clinicians in the successful development of biosensors which have real-world application. Future triumphs in the design and extensive application of enzymatic electrochemical biosensors relies on constant communication and iterative design of such biosensors. The growing need for biomarker monitoring led to an increased demand for biosensing.[3–5] Advancements in research will enable researchers to make more accurate decisions about key biosensor design parameters, with focused efforts on certain elements that require further modification. Additionally, while many sensors exhibit excellent properties when characterized in buffer or ideal conditions, their translation into biologically relevant environments is crucial for their success. Research efforts should be made on optimizing and testing biosensors in relevant environments. In summary, the efforts of this thesis are in designing biosensors which can be converted into point of care devices or used for pre-clinical and clinical studies. In the case of pre-clinical and clinical studies, the biosensors must be tested for their application feasibility for analysis of low volumes of body fluids such as saliva, urine or blood. While the main focus of this thesis was on real-time detection of small amino acids, the only limitation of extending the scope of biomarkers is the use of appropriate surface modifications. As such, electrode surface modification is expected to be continued area of development in biosensor

design.

References

(1) Dai, X.; Zhou, E.; Yang, W.; Zhang, X.; Zhang, W.; Rao, Y. D-Serine Made by Serine Racemase in Drosophila Intestine Plays a Physiological Role in Sleep. *Nat. Commun.* **2019**, 1–10.

(2) Olivieri, A.; Olivieri, A., Chemometrics and Multivariate Calibration In *Introduction to Multivariate Calibration*; Springer International Publishing: 2018, pp 1–17.

(3) Karimi-Maleh, H. et al. A Critical Review on the Use of Potentiometric Based Biosensors for Biomarkers Detection. *Biosens. Bioelectron.* **2021**, *184*, 1–16.

(4) Beitollahi, H.; Zia Mohammadi, S.; Safaei, M.; Tajik, S. Applications of Electrochemical Sensors and Biosensors Based on Modified Screen-Printed Electrodes: A Review. *Anal. Methods* **2020**, *12*, 1547–1560.

(5) Saylan, Y.; Özgür, E.; Denizli, A. Recent Advances of Medical Biosensors for Clinical Applications. *Med. Devices Sensors* **2021**, *4*, 1–8.

Appendix A

Supporting Information for Chapter 2

A.1 Determination of Hydrogen Peroxide Diffusion Coefficient

A.1.1 Defining the Apparent Diffusion Coefficient

For a porous system, such as the permeable PPD layer used in this work, diffusion occurs uniquely in the electrolyte present in the pore phase. Diffusive flux is proportional to the cross-sectional area and the apparent diffusion (D_{app}). Since the cross-sectional area impacts diffusional flux, D_{app} is proportional to porosity (ϕ). Moreover, tortuous path transport (τ) of the porous network microstructure impacts diffusion. As such, D_{app} is defined relative to the bulk diffusion coefficient (D_0) by factoring in both the PPD porosity and tortuosity. In this work, we discuss Dapp, taking into consideration that this value accounts for ϕ, τ and D_0.

$$D_{app} = \frac{D_0 \phi}{\tau} \tag{A.1}$$

A.2 COMSOL Simulation

A 2-D axisymmetric finite element model was built using COMSOL Multiphysics 5.3a to extract the diffusion coefficient of H_2O_2 towards the ME surface. A schematic of the geometry

is presented in A.1. The mesh was free triangular with coarse size with finer distributions at regions closer to the ME electroactive surface.

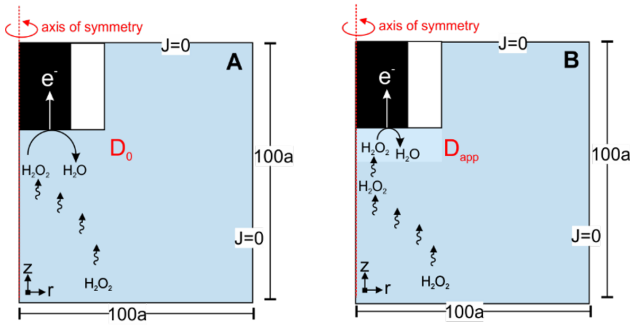

Figure A.1: COMSOL geometry where a corresponds to radius and J corresponds to flux. A) Schematic of H_2O_2 diffusion. D_o is the bulk diffusion coefficient of H_2O_2. B) Schematic of H_2O_2 diffusion through the PPD layer. D_{app} is the limiting diffusion coefficient.

A.2.1 Model Equations

Using the Transport of Diluted Species Module, a diffusion limited system was assumed for species mass transport calculations to calculate species mass transport. Migration and convection contributions were assumed to be negligible:

$$J_k = -D_k \Delta c_k \tag{A.2}$$

Where for an individual species k, J_k is the mass transport flux, D_k, bulk is the diffusion coefficient in the bulk solution and c_k is the concentration. For a single species k, the Nernst-Plank equation may be presented as follows:

$$J_k = \frac{dC}{dt} = D(\frac{d^2C}{dr^2} + \frac{1}{r} + \frac{dC}{dr} + \frac{d^2C}{dz^2}) \tag{A.3}$$

Where r and z are the model cylindrical coordinates

Using the Butler-Volmer kinetics corresponding to the irreversible oxidation of H_2O_2, the H_2O_2 flux at the ME surface is as follows:

$$J_R(x,t) = -k_{ox}C_R \tag{A.4}$$

Where

$$-k_{ox} = k_0 e^{-\alpha * f(E-E_0)} \tag{A.5}$$

and

$$f = \frac{F}{RT} \tag{A.6}$$

Where k_{tip} is the rate of the reaction at the electrode surface in $mol.m^{-2}s^{-1}$, k_0 is the standard rate constant for the rate determining step of the H_2O_2 reaction on platinum surfaces ($k_0 = 24.96x10^{-5}m.s^{-1}$) in $m.s^{-1}$, α is the mass transfer coefficient (assumed to be

0.5), E_0 is the standard formal potential in V derived from the literature (0.407 V vs. 0.1 M Ag/AgCl) and E is the applied potential in V (0.5 V vs. 0.1 M Ag/AgCl), R is the ideal gas constant, T is the temperature (assumed to be 298 K).

To calculate the current i corresponding to the irreversible oxidation of peroxide from the flux at the ME tip:

$$\int_{x=0}^{x=a} C_R k_{ox} n_{electrons} F \tag{A.7}$$

Where x is the position at the electrode surface The potential at the ME tip was stepped up from 0 V to 0.5 V at t=5 seconds using the step function to simulate the oxidation current from a chronoamperogram. Parametric sweeps in which the simulation was run at various diffusion coefficients. For an estimate of the diffusion coefficient towards the ME surface, the chronoamperometric steady state current at 300s was matched to the experimental steady state current at all concentrations. Isotropic diffusion was assumed throughout the entire model. Model initial and boundary conditions Time-dependent simulations with the ME (a=5 µm, RG= 5) were performed to model the chronoamperometric oxidation. The initial concentration and diffusion coefficient of hydrogen peroxide were 0.1 nM and $1.97x10^{-9}m^2s^{-1}$ respectively. The following initial and boundary conditions were set:

At t=0,

$$C_R(x, 0) = C_{R,bulk} \tag{A.8}$$

$$J_R(x, 0) = 0 \tag{A.9}$$

At the edges where L=100a and $0 < t$

$$C_R(L, t) = C_{R,bulk} \tag{A.10}$$

$$J_R(L, t) = 0 \tag{A.11}$$

Where C_R is the concentrations of H_2O_2 in mol/m^3 and J_r is the flux of H_2O_2 in mol/m^2.s, t is the time in s and L is the length of the electrochemical cell in cm and a is the radius of the microelectrode in cm.

A.3 Supporting Figures and Tables

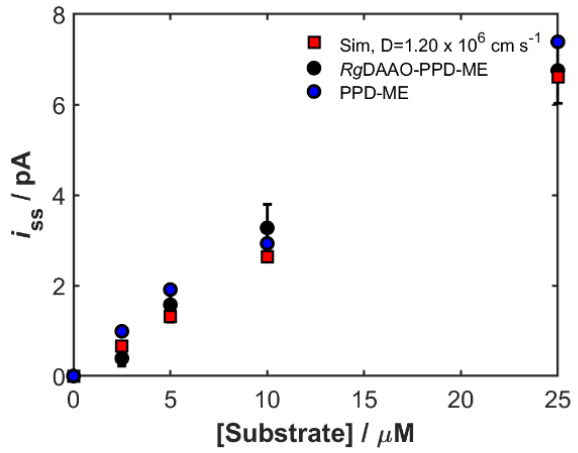

Figure A.2: Agreement of the simulation derived currents with the experimental values. The *Rg*DAAO-PPE-ME was immersed in standard solutions of D-serine in PBS (0-25 µM). The PPD-ME was immersed in standard solutions of H_2O_2. The steady state current (i_{ss}) was measured at an oxidizing potential of 0.5 V.

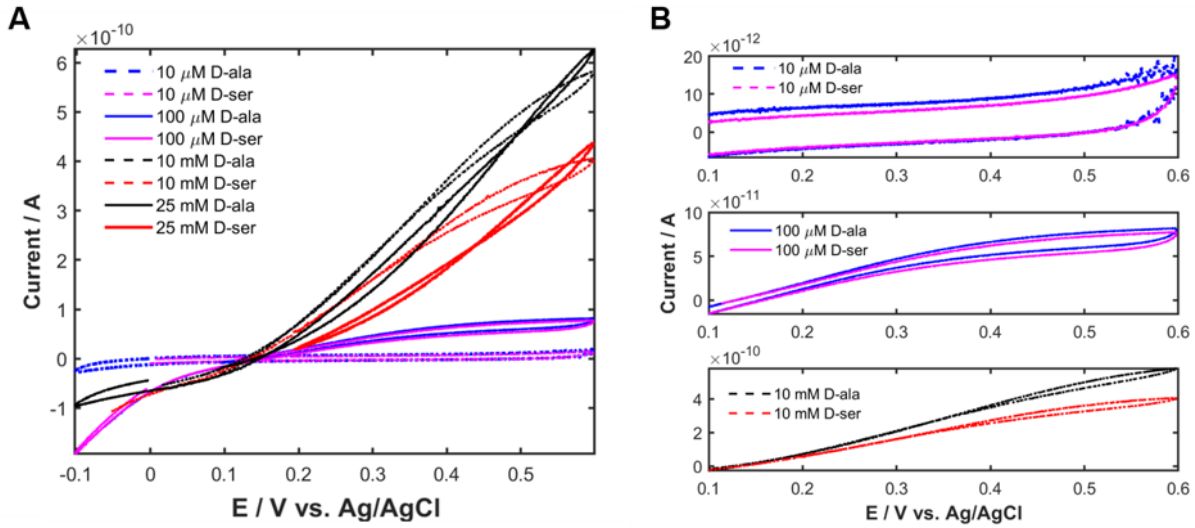

Figure A.3: Cyclic voltammograms (CVs) using an $RgDAAO_{immob}-PPD-ME$ immersed in solutions of D-serine and D-alanine (-0.1–0.6 V vs. Ag/AgCl, $0.1\text{V} \cdot s^{-1}$). A) CVs showing increasing peak current at 0.5 V for the oxidation of H_2O_2 produced from the RgDAAO reaction with the substrate solutions. B) Zoomed image of paired plots of CVs at the same substrate concentration, demonstrating a change in response ratio between D-serine and D-alanine as concentration is increased (top to bottom).

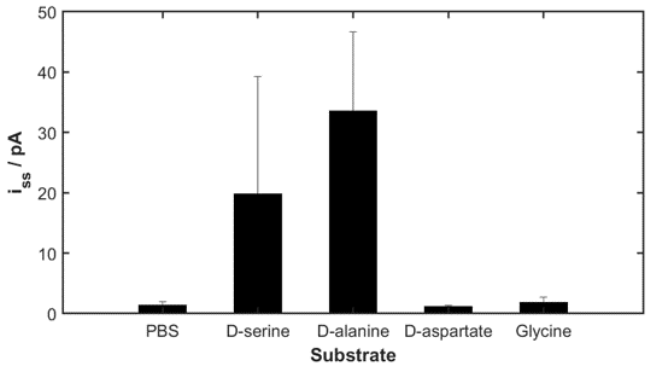

Figure A.4: The steady state current response using PPD-MEs poised at 0.5 V measured by the production of H_2O_2 from the reaction of $RgDAAO_{free}$ (1.0 µL , $58.6\text{ mg} \cdot mL^{-1}$) mixed in individual solutions solution of 200 µL of 0.1 M PBS containing 100 µM D-serine, 100 µM D-alanine, 100 µM -aspartate or 100 µM glycine. The steady state current responses demonstrate that significant H_2O_2 production from RgDAAO reaction is only apparent with -serine and -alanine as substrate. Error bars represent ±S.D.

Table A.1: Presence and Localization of D-amino acids at physiological and pathological conditions

Species	**Localization**
Concentration	**Reference**
Physiological Conditions: D-alanine	
Male mice	Cerebrum/Hippocampus/Hypothalamus/Serum
12.4/11.4/9.0/8.8 [nmol/g wet tissue]	[1]
Humans	White matter/ Grey matter
0.60/ 0.66 [µmol/g wet tissue]	[2]
Male Wilstar rats	Pituitary gland(Anterior lobe/posterior lobe)/plasma
86.4/14.7/0.6-4.8/11.6 [nmol /g wet tissue]	[3]
Humans	CSF/ Plasma
0.113/0.531 [µM]	[3]
Male Wilstar Rats (6-9 weeks)	Pituitary/ Plasma
10 [nmol/g wet tissue]/8 [µM]	[4]
Rats (6 weeks)	Pituitary Gland (male/female)
25.9 /10.7 [nmol/g tissue]	[5]
Physiological Conditions: D-serine	
Male mice	Cerebrum/Hippocampus/Hypothalamus/Serum
423.2/341.5/105.2/2.1 [nmol/g wet tissue]	[1]
Mice	Forebrain/Extracellular fluid
5-7 [µM]	[6]
Humans	CSF/ Plasma
1.165/0.761 [µM]	[7]
Humans	Serum
176.2 µmol/L	[8]
Rats (6 weeks)	Cerebrum/Hippocampus/Pineal & Pituitary Gland/Hypothalamus
210,218/231,245/5.8,10.8/	
210,215/11.6,9.7 [nmol/g wet tissue]	[5]
Pathological Conditions: D-alanine	
Male mice (no DAAO)	Cerebrum/Hippocampus/Hypothalamus/Serum
63.7/61.7/52.6/134.6 [nmol/g wet tissue]	[1]
Mice	Hippocampus/Frontal Cortex/Cerebellum
20/28/2.5 [µg/g tissue]	[9]
Pathological Conditions: D-serine	
Male Mice (no DAAO)	Cerebrum/Hippocampus/Hypothalamus/Serum
424.5/300.3/147.1/11.6 [nmol/g wet tissue]	[2]
Humans	White matter/ Grey matter
0.84/ 0.92 [µmol/g wet tissue]	[2]
Humans	Serum
203.5 µmol/L	[8]

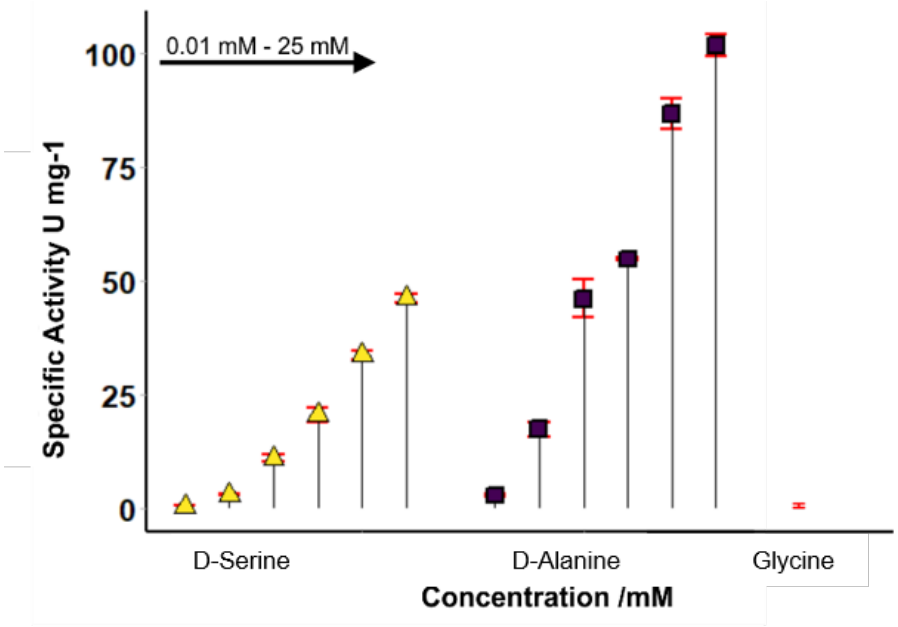

Figure A.5: Specific activity of *Rg*DAAO towards different substrates at various concentrations (0.01,0.1, 1, 2,7.5,25 mM) in NaPPI buffer (pH=8.5) using the o-DNS assay as shown in Figure 4. **Rg*DAAO was found to have no activity (< 1 U mg^{-1}) on 1 mM glycine. The average of three measurements is shown $\pm S.D.$).

A.4 Matlab Scripts

A.4.1 Brief Description of Code

In enzyme kinetics, measuring the observed reaction rate reveals the catalytic mechanism of an enzyme as well the enzyme interaction with different substrates. Michaelis–Menten kinetics are the simplest and most commonly used approximation to describe the kinetics of many enzymes. The Michaelis–Menten equation relates the initial reaction rate (v_0) to the substrate concentration (S). The resulting plot is a hyperbolic function where the maximum rate is defined as V_{max}. The Michaelis-Menten constant (K_m) is the concentration of substrate where v_0 is half of V_{max}. To determine the kinetic parameters, a set of experiments are conducted in which the substrate concentration is varied and the initial rate of product formation is measured. Non-linear regression of the Michaelis-Menten data (v_0 vs S) allow for determination of the K_m and V_{max} values. The Michaelis-Menten equation may also be linearized to measure the effect of substrate inhibition on the enzyme (Lineweaver-Burk Analysis).

Script 1: Function to Perform a least squares linear regression required for Lineweaver-Burk Analysis

```
function=[slope,intercept,stats]=lslregr(x,y,varargin)
%LSLREGR: Perform a least-squares linear regression.
%Syntax:   lslregr(x,y)
%
%    Inputs:
%          X - Independent variable array
%          Y - Dependent variable. If Y is a matrix, the i-th Y row is a
%          replicate of i-th X point. The mean value will be used.
%    Outputs:
%
%          1) Slope with standard error an 95% C.I.
%          2) Intercept with standard error an 95% C.I.
%          3) Pearson's Correlation coefficient with 95% C.I. and its adjusted form
%          4) Spearman's Correlation coefficient
%          5) Regression Standard Error
%          6) Total Variability
%          7) Variability due to regression
%          8) Residual Variability
%          9) Student's t-Test on Slope (to check if slope=0)
%          10) Student's t-Test on Intercept (to check if intercept=0)
%
%          - Plots:
%               1)  Data points, Least squares regression line ,
%                   Red dotted lines: 95% Confidence interval of regression
%                   Green dotted lines: 95% Confidence interval of new y value from this
  regression.
%               2)  Residuals plot
%
%   [Slope,Intercept,stats]= returns a structure of slope and intercept
%   containing value, standard error, lower and upper bounds 95% C.I
%   and returns a STATS structure with stats info


%Handling Input Errors
par = inputParser;
addRequired(par,'x',@(x) validateattributes(x,{'numeric'},{'row','real','finite','
  nonempty'}));
addRequired(par,'y',@(x) validateattributes(x,{'numeric'},{'2d','real','finite','nonempty
  '}));
addOptional(par,'avgm',1, @(x) isnumeric(x) && isreal(x) && isfinite(x) && isscalar(x) &&
   (x==0 || x==1));
parse(par,x,y,varargin{:});
avgm=par.Results.avgm; %mean value for Y matrix
```

```
alpha=0.05;
clear par
x=x(:);
if isvector(y)
ymean=y(:); %columns vectors
else
ymean=mean(y)'; %find the mean of y
end
assert(length(x)==length(ymean),'X and Y arrays must have equal column numbers.'); %
  confirm equal array length

un=unique(x);
if length(un)~=length(x)
uny=zeros(num(un));
for N=1:length(un)
col=sum(x==un(N));
if col==1
uny(N)=ymean(x==un(N));
else
uny(N)=mean(ymean(x==un(N)));
end
end
x=un(:); ymean=uny(:);
clear uy I
end
clear ux

%regress function input
xtemp=[x ones(length(x),1)];
ytemp=ymean;

%regression coefficients
[par,pINT,R,int] = regress(ytemp,xtemp);

%outlier presence check
outlierx=find(ismember(sign(int),[-1 1],'rows')==0);
if ~isempty(outlierx)
disp('These points are outliers at 95% fiducial level')
disp(array2table([xtemp(outlierx) ytemp(outlierx)],'VariableNames',{'X' 'Y'}))
ques= input('Do you want to delete outliers? Y/N [Y]: ', 's');
disp(' ')
if isempty(ques) || upper(ques)=='Y'
ytemp(outlierx)=[]; xtemp(outlierx,:)=[];
[par,pINT,R] = regress(ytemp,xtemp);
end
end

xtemp(:,2)=[]; %delete column 2
%save coefficients
```

```
N(1)=par(1); q(1)=par(2);

%standard error of regression coefficients
%Student's critical value
num=length(xtemp);
xmean=mean(xtemp); xstd=std(xtemp);


if isvector(y)
criv=tinv(0.975,num-2);
else
criv=tinv(0.975,sum(num(y))-3);
end
N(2)=(pINT(3)-par(1))/criv; %slope standard error
N=[N pINT(1,:)]; %add slope 95% C.I.
q(2)=(pINT(4)-par(2))/criv; %intercept standard error
q=[q pINT(2,:)]; %add intercept 95% C.I.

slope.value=N(1); slope.se=N(2); slope.lv=N(3); slope.uv=N(4);
intercept.value=q(1); intercept.se=q(2); intercept.lv=q(3); intercept.uv=q(4);

%Pearson's Correlation coefficient
[rp,pr,rlow,rupper]=corrcoef(xtemp,ytemp);
rval(1)=rp(2); rval(2)=realsqrt((1-rval(1)^2)/(num-2)); rval(3)=rlow(2); rval(4)=rupper
  (2);

%Adjusted Pearson's Correlation coefficient
rval(5)=sign(rval(1))*(abs(rval(1))-((1-abs(rval(1)))/(num-2)));

%Spearman's Correlation coefficient
[rvalx]=tiedrank(xtemp);
[rvaly]=tiedrank(ytemp);
diff=rvalx-rvaly;
spearman=1-(6*sum(diff.^2)/(num^3-num));
rs=[spearman NaN tanh(atanh(spearman)+[-1 1].*(1.96/realsqrt(num-3))) NaN];


%Total Variability
yavg=polyval(par,xmean);
vtot=sum((ytemp-yavg).^2);

%Regression Variability
ystart=ytemp-R;
vregress=sum((ystart-yavg).^2);

%Residual Variability
vresidual=sum(R.^2);

%regression standard error (RSE)
```

```
if isvector(y)
RSE=realsqrt(vresidual/(num-2));
else
if ~isempty(outlierx) && (isempty(reply) || upper(reply)=='Y')
y2=y; y2(outlierx)=[];
RSE=realsqrt((vresidual+sum(sum((y2-repmat(ytemp',num(y,1),1)).^2)))/(sum(num(y2))-3));
else
RSE=realsqrt((vresidual+sum(sum((y-repmat(ymean',num(y,1),1)).^2)))/(sum(num(y))-3));
end
end

%Confidence interval at 95% of regression
sumy=RSE*realsqrt(1/num+(((xtemp-xmean).^2)/((num-1)*xstd^2)));
cir=[ystart+criv*sumy ystart-criv*sumy];

%Confidence interval at 95% of a new observation (this is the confidence
%interval that should be used when you evaluate a new y with a new observed x)
%sumy2=realsqrt(sumy.^2+RSE^2);
%cir2=[ystart+criv*sumy2 ystart-criv*sumy2];

%stats.rse=RSE; stats.criv=criv; stats.num=num;
%stats.xm=mean(x); stats.ym=yavg; stats.sse=sum((xtemp-xmean).^2); stats.r=rval;

%display results
if avgm==1
div=repmat('-',1,80);
disp('REGRESSION SETTING X AS INDEPENDENT VARIABLE')
disp(div)
disp(array2table([N;q],'RowNames',{'Slope','Intercept'},'VariableNames',{'Value','
  Standard_Error','Lower_bound','Upper_bound'}))
fprintf('\t\t\tCorrelation Coefficients\num')
disp(div)
disp(array2table([rval;rs],'RowNames',{'Pearson','Spearman'},'VariableNames',{'Value','
  Standard_Error','Lower_bound','Upper_bound','Adjusted'}))
fprintf('\t\t\tVariability\num')
disp(div)
disp(array2table([RSE vtot vregress vregress/vtot*100 vresidual vresidual/vtot*100],'
  RowNames',{'Regr_SE'},'VariableNames',{'Value','Total','By_Regression','Percent1','
  Residual','Percent2'}))
disp(' ')

%test on slope
stregress=cell(2,5);
stregress{1,1}=abs(N(1)/N(2)); %Student's t
stregress{1,2}=criv; stregress{1,3}=pr(2);
if stregress{1,1}>stregress{1,2}
stregress{1,5}='slope ~= 0';
stregress{1,4}=1-tcdf(tinv(1-alpha,num-2) - stregress{1,1},num-2);%Power estimation.
else
```

```
stregress{1,5}='slope = 0';
stregress{1,4}=tcdf(stregress{1,1} - tinv(1-alpha,num-2),num-2);%Power estimation.
N(1)=0;
end
stregress{2,1}=abs(q(1)/q(2)); %Student's t
stregress{2,2}=criv; stregress{2,3}=(1-tcdf(stregress{2,1},num-2))*2; %p-value
if stregress{2,1}>stregress{2,2}
stregress{2,5}='intercept ~= 0';
stregress{2,4}=1-tcdf(tinv(1-alpha,num-2) - stregress{2,1},num-2);%Power estimation.
else
stregress{2,5}='intercept = 0';
stregress{2,4}=tcdf(stregress{2,1} - tinv(1-alpha,num-2),num-2);%Power estimation.
q(1)=0;
end


% Regression Plot
figure('Color',[1 1 1],'outerposition',get(groot,'ScreenSize'));
subplot(2,1,1);
if isvector(y)
plot(x,ymean,'ko',xtemp,ystart,xtemp,cir,'b',xtemp,cir2,'r');
else
hold on
plot(x',ymean,'LineStyle','none','Marker','o','MarkerEdgeColor','r')
plot(xtemp,ystart,'k',xtemp,cir,'b',xtemp,cir2,'r');
hold off
end
text=sprintf('Blue dotted lines: 95%% Confidence interval of regression\nRed dotted lines
  : 95%% Confidence interval of new y value based on the regression');
title(text)

Script #2: Function to transform initial velocity values into Michaelis-Menten (non-
  linear regression) and Lineaweaver Burk plots (linear regression)

function michmout=michmin(S,v)
%
%
% Syntax:  michmout=michmin(S,v)
%
% Inputs:
%          S - data array of substrate concentrations
%          v - data array of measured initial velocities
% Outputs:
%  - Vmax and Km estimation by
%          - Tables of:
%    1) Michaelis-Menten non linear regression
%          2) Lineweaver-Burk Linear Regression
%     - A plot of the Michaelis-Menten Non-Linear Fit with the estimated Km and Vmax
  parameters
```

```
%
%
%
% To run this function, another function called lslregr is required. Please save it in
  the same working folder.


%%%%% Stats and Regression

%Input Error handling
par=inputParser;
addRequired(par,'S',@(x) validateattributes(x,{'numeric'},{'vector','real','finite','
  nonnan','nonnegative','row','increasing'}));
addRequired(par,'v',@(x) validateattributes(x,{'numeric'},{'vector','real','finite','
  nonnan','nonnegative','row','increasing'}));
parse(par,S,v)
assert(length(S)==length(v))
clear par

%set the constants
num=length(S); % # data points
vcrit=tinv(0.95,num-2); %confidence interval critical value
div=repmat('-',1,100); %divisor
txtlbl={'Michaelis & Menten Non Linear Fit' '[S]' 'v';
   sprintf('Lineweaver-Burk\n(x=1/S; y=1/v)') '1/[S]' '1/V'}

KM=NaN(2,4); VMAX=KM;
disp(div)
fprintf('Lineweaver-Burk Model (x=1/S; y=1/v => Vmax=1/q; Km=m/q)...\n')
disp(div)

[x,Yval]=sort(1./S); y=1./v(Yval);
[slope, intercept, stats]=lslregr(x,y,0);
VMAX(1,1:2)=[1/intercept.value intercept.se/intercept.value^2]; VMAX(1,3:4)=VMAX(1,1)+[-1
   1].*vcrit*VMAX(1,2);
KM(1,1:2)=[slope.value/intercept.value realsqrt((intercept.value*slope.se)^2+(slope.value
  *intercept.se)^2)/intercept.value^2]; KM(1,3:4)=KM(1,1)+[-1 1].*vcrit*KM(1,2);
%disppar(1)
clear x y slope intercept stats
disp(' ')

%Michaelis and Menten non linear hyperbolic fit
xfit = S(:); yfit = v(:)

%Check if x and y are valid
valid = isfinite(xfit) & isfinite(yfit);
if ~all(valid)
warning( 'GenerateMFile:IgnoringNansAndInfs', ...
'Ignoring NaNs and Infs in data' );
```

```
end

%set fitting options:
fitt = fitoptions('method','NonlinearLeastSquares','Robust','On','Lower',[0 0],'
  DiffMaxChange',9.999999999999995475e-07);
%Set the Michaelis & Menten equation
set(fitt,'Startpoint',[KM(1,1) VMAX(1,1)]);

ftmodel = fittype('(Vmax*x)/(Km+x)',...
'dependent',{'y'},'independent',{'x'},...
'coefficients',{'Km', 'Vmax'});

% Fit this model using the x and y values
[cf, goodness] = fit(xfit(valid),yfit(valid),ftmodel,fitt);

%Display the results
disp(div)
fprintf('Michaelis & Menten Nonlinear Fit...\n')
fprintf('\tR = \t%0.4f\n',sqrt(goodness.rsquare))
disp(cf)
disp(div)
disp(' ')

par=coeffvalues(cf); KM(2,1)=par(1); VMAX(2,1)=par(2);
par=confint(cf); KM(2,3:4)=par(1,:)'; VMAX(2,3:4)=par(2,:)';
KM(2,2)=(KM(2,4)-KM(2,1))/vcrit;
VMAX(2,2)=(VMAX(2,4)-VMAX(2,1))/vcrit;
clear par st fitt ft cf goodness

disp(array2table(KM,'VariableNames',{'KM','Std_Err','Lower_bound','Upper_bound'},...
'Rownames',{'Lineweaver_Burk','Michealis_Menten_Fit'}));

disp(array2table(VMAX,'VariableNames',{'VMAX','Std_Err','Lower_bound','Upper_bound'},...
'Rownames',{'Lineweaver_Burk','Michealis_Menten_Fit'}));

if nargout
michmout.KM=KM;
michmin.VMAX=VMAX;
end



%%%%Plotting

%%Michaelis & Menten Non Linear Plot
x=S; y=v;
[~,xtick,ytick]=kingraph(1,VMAX(2,1),KM(2,1));
H=text(5*xtick,VMAX(2,1)+3*ytick,['Vmax = ' num2str(VMAX(2,1))]); set(H,'Color','b')
H=text(KM(2,1)+5*xtick,VMAX(2,1)/2,['Km = ' num2str(KM(2,1))]); set(H,'Color','b')
```

```
function [out1,out2,out3]=kingraph(P,m,q,lbls) % main plot function
xtick=range(x)/50; ytick=range(y)/50;

%Plot the data points

plot(x(1:end),y(1:end),'Marker','o','MarkerEdgeColor','b','MarkerFaceColor','b','
  MarkerSize',10,'LineStyle','none')
hold on

% %Plot the regression line (black)

hold on
xs=linspace(0,max(x),500); ys=(m.*xs)./(q+xs);
plot(xs,ys,'k','Linewidth',2)


as=axis;   out2=xtick;

if nargout
out1=as;
out3=ytick;

end
hold on

plot(as(1:2),[m m],'k--') %plot the Vmax asymptote
plot([0 q],[m m]./2,'k--',[q q],[0 m/2],'k--') %plot the Km coordinates

axis square

% %set the labels
xlabel(txtlbl(1,2))
ylabel(txtlbl(1,3))

end

set(gca,'fontsize',16,'linewidth',1.5); %setting the font size of axis
eginnaxis tight
 end
Script #3: Determine the Km value using the enzyme kinetic profile measured with
  chronoamperometry

%Microelectrode Shape: Disk
%Microelectrode Diameter: 10 micron
%iss=4*B*n*F*D*C*a
D=1.2E-6 %cm^2/s
F=96485.33 %C.mol-1= A*s/mol
B=1.04 %Rg value=5
```

```
a=5 %Microelectrode radius in micron
a=5*10^-4 %cm
n=1 % Number of electrons
C=56.8 %enzyme concentration in U/mg
di=input('Please input the di value in picoamps')
dt=input('Please input the dt value in seconds')
di=di*10^-12 %in pA
dt=dt/60 %in mins
didt=di/dt
k=1 %convert cm^3 into mL factor
EA=didt/(4*n*F*D*B*a)%[mol/mL.min]
EA=EA*10^6 %[micromol/mL.min]
Vtot=input('Please input the total volume in uL')
Venz=input('Please input the enzyme volume in uL')
SEA=EA*((Vtot+Venz)/Venz)*(1/C)
```

References

(1) Morikawa, A.; Hamase, K.; Inoue, T.; Konno, R.; Niwa, A.; Zaitsu, K. Determination of free D-aspartic acid, D-serine and D-alanine in the brain of mutant mice lacking D-amino-acid oxidase activity. *J. Chromatogr. B Biomed. Sci. Appl.* **2001**, *5*, 119–125.

(2) D'Aniello, A.; Vetere, A.; Fisher, G.; Cusano, G.; Chavez, M.; Petrucelli, L. Presence of d-alanine in proteins of normal and Alzheimer human brain. *Brain Res.* **1992**, *2*, 44–48.

(3) Morikawa, A.; Hamase, K.; Zaitsu, K. Determination of D-alanine in the rat central nervous system and periphery using column-switching high-performance liquid chromatography. *Anal. Biochem.* **2003**, *1*, 66–72.

(4) Karakawa, S.; Miyoshi, Y.; Konno, R.; Koyanagi, S.; Mita, M.; Ohdo, S. Two-dimensional high-performance liquid chromatographic determination of day-night variation of D-alanine in mammals and factors controlling the circadian changes. *Anal. Bioanal. Chem.* **2013**, *405*, 8083–8091.

(5) Hamase, K.; Homma, H.; Takigawa, Y.; Fukushima, T.; Santa, T.; Imai, K. Regional distribution and postnatal changes of D-amino acids in rat brain. *Biochim. Biophys. Acta* **1997**, *15*, 214–222.

(6) Wolosker, H.; Panizzutti, R.; De, M. J. Neurobiology through the looking-glass: D-serine as a new glial-derived transmitter. *Neurochem. Int.* **2002**, *41*, 327–32.

(7) Visser, W.; Verhoeven-Duif, N.; Ophoff, R.; Bakker, S.; Klomp, L.; Berger, R. A sensitive and simple ultra-high-performance-liquid chromatography-tandem mass spectrometry based method for the quantification of D-amino acids in body fluids. *J. Chromatogr. A* **2011**, *7*, 7130–7136.

(8) Hashimoto, K.; Fukushima, T.; Shimizu, E.; Komatsu, N.; Watanabe, H.; Shinoda, N. Decreased serum levels of D-serine in patients with schizophrenia: Evidence in support of the N-methyl-D-aspartate receptor hypofunction hypothesis of schizophrenia. *Arch Gen. Psychiatry* **2003**, *1*, 572–576.

(9) MacKay, M.; Kravtsenyuk, M.; Thomas, R.; Mitchell, N.; Dursun, S.; D-serine, B. G. Potential therapeutic agent and/or biomarker in schizophrenia and depression? *Front. in Psychiatry* **2019**, *10*, 1–9.

Appendix B

Supporting Information for Chapter 3

B.1 Supporting Figures and Tables

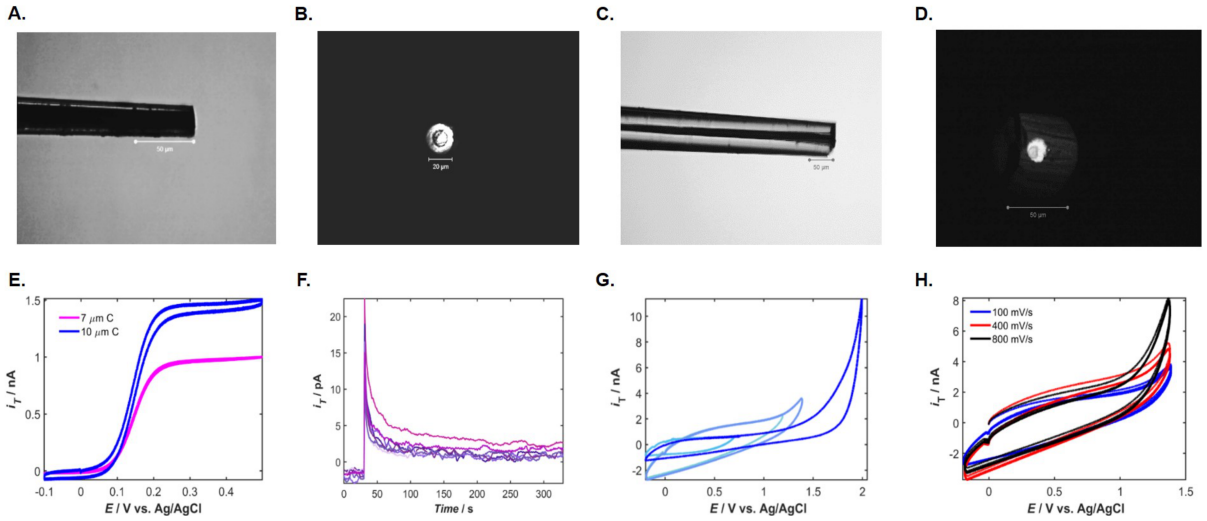

Figure B.1: Carbon Fibre Microelectrode (CFME) fabrication and H_2O_2 electrochemical detection. A) Side view of optical microscope image of 7 µm CFME (scale bar = 50 µm). B) Top view 7 µm CFME (scale bar = 20 µm). C) Side view of optical microscope image of 10 µm CFME (scale bar = 50 µm). D) Top view 7 µm CFME (scale bar = 50 µm). E) Characterization of CFMEs with cyclic voltammetry (CV) in 1mM FcMeOH (-0.1 V to 0.5 V vs. Ag/AgCl, 0.10 Vs^{-1}). F) Chronoamperograms representing the oxidation of H_2O_2 (0, 2.5, 5, 10, 20 µM) at 0.5 V with 7 µm CFMEs. G) CVs (0.10 Vs^{-1}) with 10 µm CFMEs of H_2O_2 at various reversal potentials (E_{rev}). H) CVs at various scan rates with 10 µm CMEs in H_2O_2 (- 0.1 V to 1.4 V vs. Ag/AgCl).

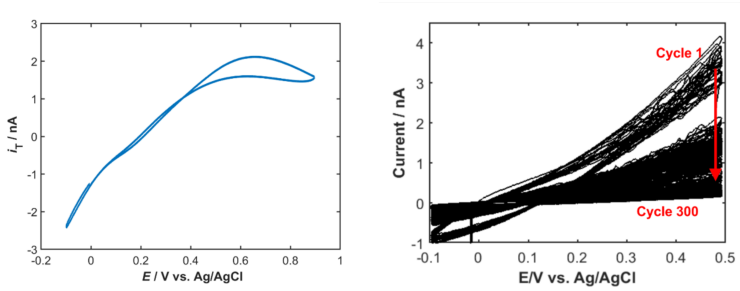

Figure B.2: Oxidation of H_2O_2 at Pt MEs. A) CV representing the oxidation of 750 µM H_2O_2 at bare 25 µm Pt MEs (-0.1 V – 0.9 V, 0.1 Vs^{-1}). B) Stress test of the PPD-Pt ME in 100 mM H_2O_2 using CVs (0.10 Vs^{-1}). Arrow represents the direction of increasing cycle number.

Table B.1: Comparison of D-serine biosensors based on DAAO.

Geometry (µm) & Material Reference	DAAO Origin	Sensitivity (µA $cm^{-2}mM^{-1}$)	LOD (µM)	Cost($-$$$)
10 Pt Disk Experimental	Rhodotorula gracilis	236	0.43	$
25x 150 Pt/Ir, Cylindrical [1]	Rhodotorula gracilis	87 ± 27	0.016	$$
125 µm Pt/Ir (90%/10%), Disk [2]	Porcine kidney	54 ± 1	20 ± 1nM	$$
125 x 1000 Pt/Ir, Cylindrical [2]	Porcine kidney	61 ± 7	N/A	$$
25x 150 Pt/Ir , Cylindrical [3]	Rhodotorula gracilis	212 ± 119	0.0009	$$
3000 Glassy carbon, Disk [4]	Porcine kidney	0.08	2	$
25 Pt, Disk [5]	Rhodotorula gracilis	276 ± 6	0.6	$
25x 150 Pt/Ir, Cylindrical [6]	-	128 ± 5	0.007	$$$

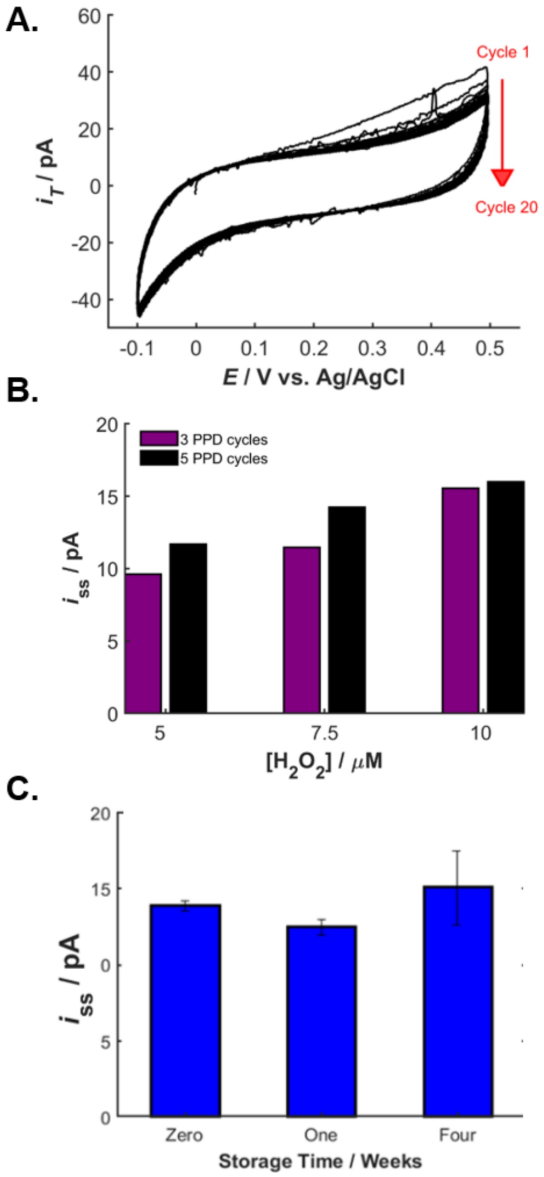

Figure B.3: Optimization of PPD layer. A) Electrochemical treatment of the PPD-Pt ME in PBS (0.1 M, pH 7.4) to remove residual monomer on the PPD-Pt ME surface (20 cycles). B) Effect of 3 PPD cycles vs 5 PPD cycles on the sensor response to H_2O_2. C) Stability of stored Pt-PPD MEs. MEs were stored dry at 4^{o}C and the response towards the oxidation of 10 µM H_2O_2 (E_{app}=0.5 V) is shown (n=6).

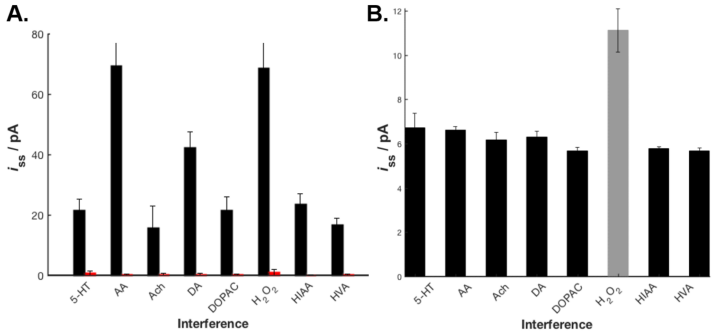

Figure B.4: Selectivity of the non-functionalized biosensor towards 10 µM serotonin (5-HT), 100 µM ascorbic acid (AA), 10 µM acetylcholine (Ach), 10 µM dopamine (DA), 50 µM 3,4-dihyroxylphenylacetic acid (DOPAC), 10 µM H_2O_2, 50 µM 5-hydroxyindoleactic acid (5-HIAA) and 10 µM homovanillic acid (HVA). The current was recorded at 0.50 V vs. Ag/AgCl. Error bars represent the SEM (n=3). A) Biosensor selectivity before PPD electrodeposition (black) and after PPD electrodeposition (red). B) Expanded view of the biosensor selectivity after PPD electrodeposition demonstrating highest selectivity of the PPD layer towards H_2O_2 (grey) amongst the other analytes (black). Approximately 4 pA of current is due to the non-faradic current contribution for all measured currents.

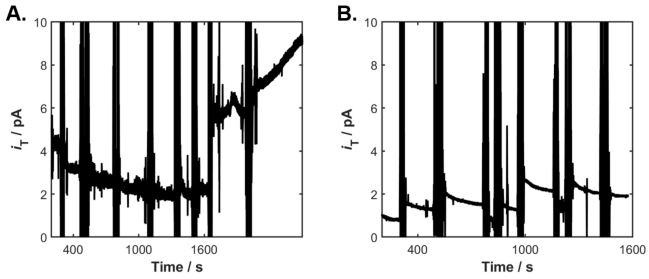

Figure B.5: Steady state response of different biosensors towards standard D-serine solutions. A) D-serine detection with biosensors fabricated using enzyme stored >1 year in 0-200 µM standard D-serine solutions. B) D-serine detection with biosensors fabricated with old glutaraldehyde in 0-100 µM standard D-serine solutions. No clear linear change in the current is observed under both conditions.

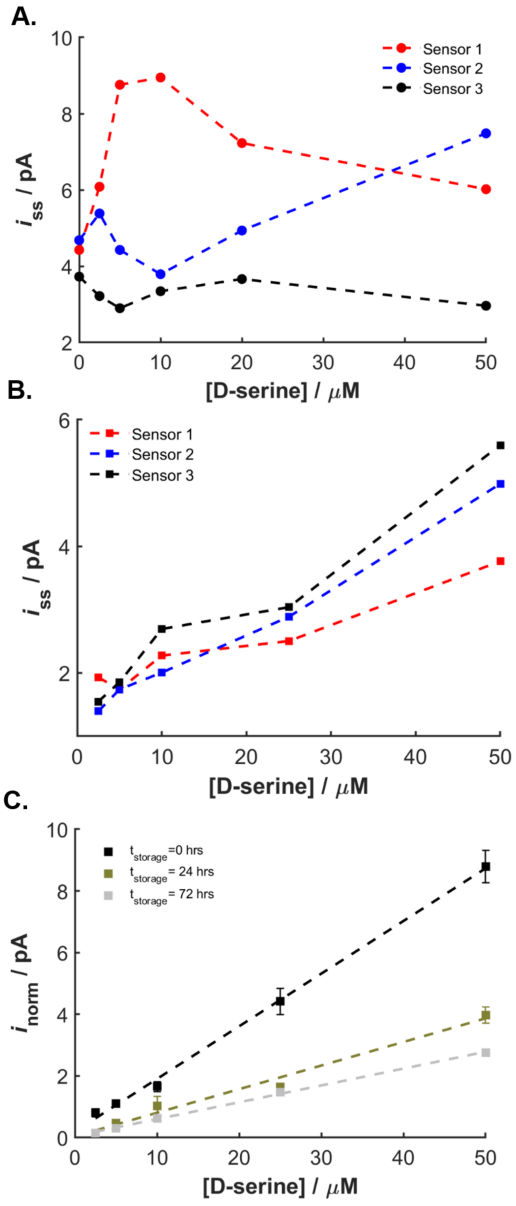

Figure B.6: Effect of biosensor storage on biosensor response towards standard D-serine solutions (2.5-50 µM). A) Calibration curves of biosensors stored wet in PBS at 4^{o}C. B) Individual calibration curves of biosensor stored dry in PBS at 4^{o}C after 24h of storage. C) Biosensor calibration curve over a 72 hour storage period : t=0 , I(pA) =0.1707 C (µM) + 0.1971, R^2 =0.998 / t=24 , I(pA) =0.0765 C (µM) + 0.0406, R^2 =0.982 / t=72 , I(pA) =0.0546 C (µM) + 0.0537, R^2 =0.998.

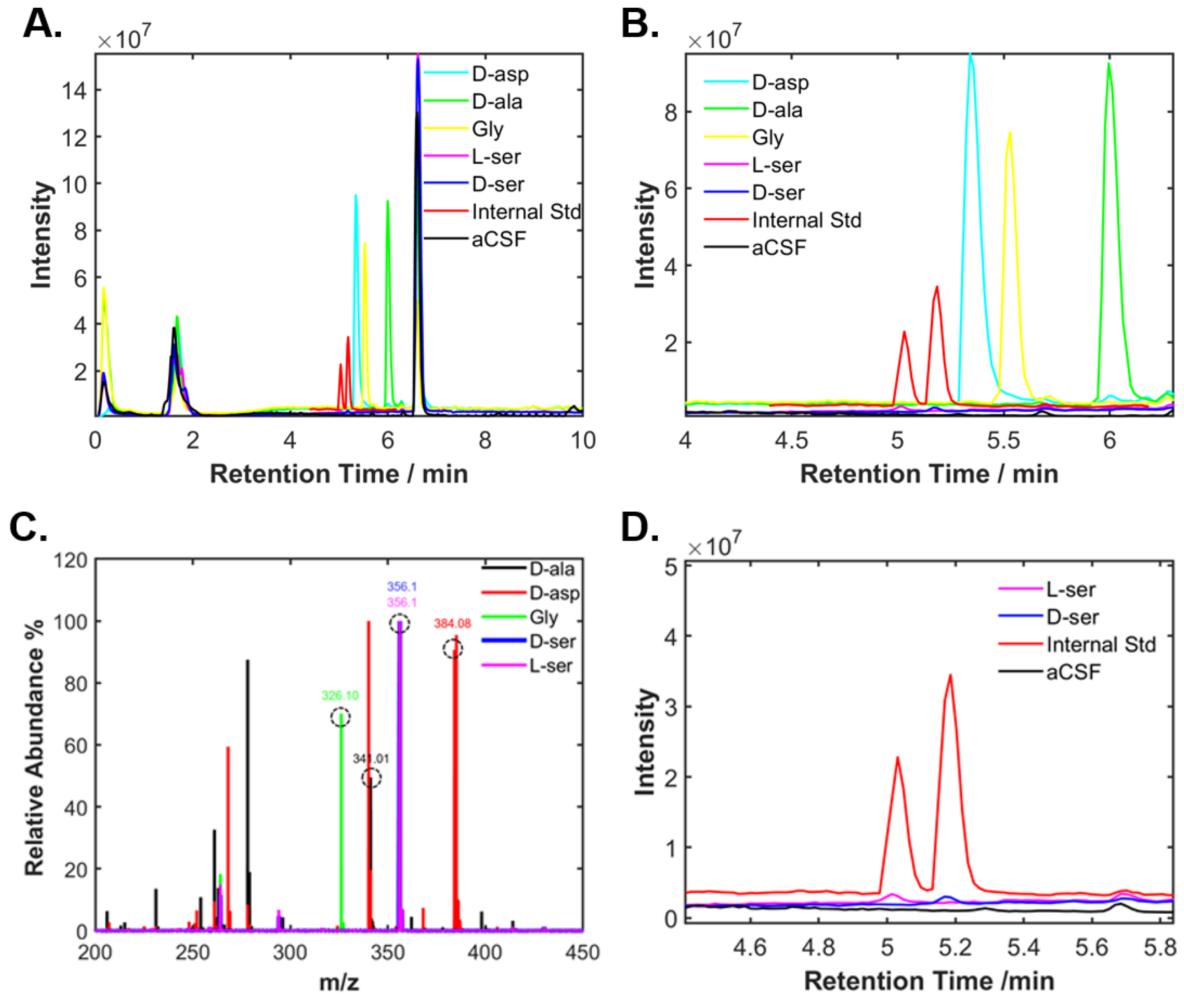

Figure B.7: LC-MS data for the detection of various amino acids. A) Chromatograms for various amino acids derivatized with Marfey's reagent demonstrating different retention times for various amino acids (D-aspartate, D-alanine, glycine, D/L-serine internal standard: 600 µM, D-serine and L-serine 100 µM) using LC-MS and the presence of none of the amino acids in aCSF. B) Close up of the chromatograms in Fig. S7A). C) Spectra for the amino acids showing peaks corresponding to the molecular weight of the derivatized amino acids. D) Zoom of the chromatograms for D- and L-serine (100 µM) as well as an internal standard with a mixture of D- and L-serine (600 µM). L-serine eluted at a shorter retention time than D-serine.

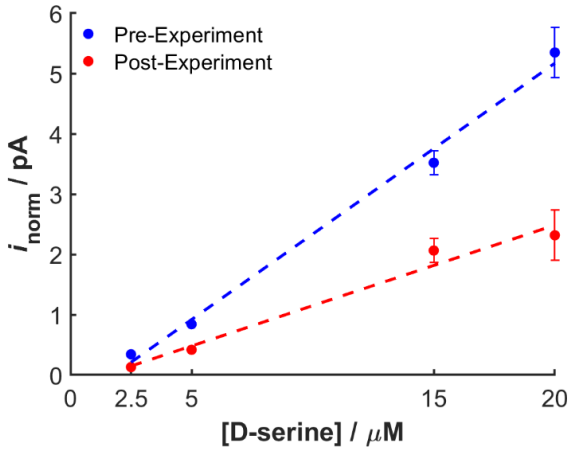

Figure B.8: Sample pre and post- experiment calibration curves. Pre-experiment calibration: I (pA) = 0. 13357 × C (μM) - 0.1867; R^2 = 0.993 ; LOD = 0.278 μM Post-experiment calibration: I (pA) = 0. 28344 × C (μM) - 0.4985; R^2 = 0.975 ; LOD = 0.0873 four hours after the initial pre-experiment calibration.

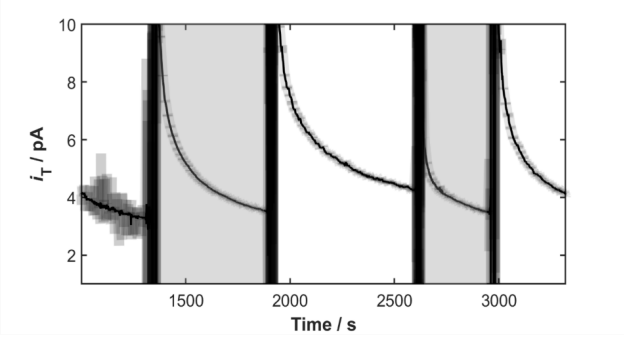

Figure B.9: *Ex vivo* measurements using a null sensor. Measurements were noise reduced using a smoothing digital filter. Unhighlighted portions correspond to the null response in aCSF whereas highlighted portions correspond to the null response in the CM. The lack of increase in current when the sensor is placed in CM exhibits no significant electroactive interference in the current response.

Table B.2: Literature reporting LC-MS based D-serine detection.

Mode, pH	Linear Range	LOD (µM)	Retention Time	Reference
Negative Mode, 6.5	0-800 x 10^{-6}	2.5 x 10^{-6}	12.65	[7]
Negative Mode, 7.5	0.1– 72	0.1	3.07	[8]
Negative Mode, 6.5	0-100	0.2 - 22	12	[9]

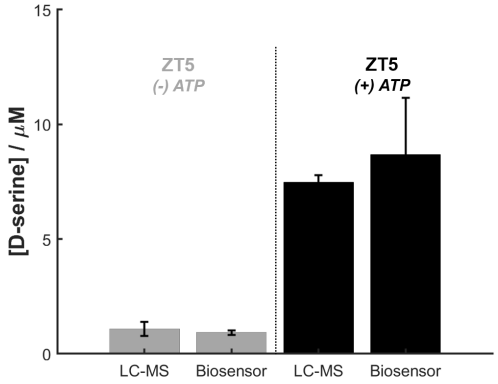

Figure B.10: Comparison of LC-MS and biosensor results for D-serine levels at ZT5, n=2 (1.09 ± 0.30 µM vs 0.93 ± 0.10 µM) and at ZT5 following 1 mM ATP incubation, n=2 (7.49 ± 0.30 µM vs 0.87 ± 2.5 µM). A significant difference in D-serine levels associated with ATP incubation is present ($p < 0.05$).

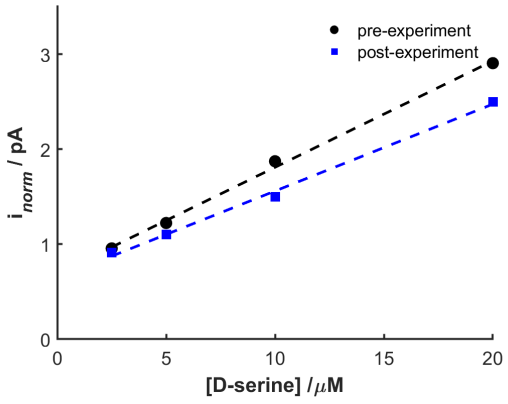

Figure B.11: Biosensor calibration curves pre- (I (pA) = 0. 1120 × C (μM) - 0.6897) and post (I (pA) = 0. 0914 × C (μM) - 0.6452) *in vivo* measurements in standard D-serine solutions performed in the *Xenopus* perfusion chamber.

References

(1) Pernot, P.; Mothet, J.; Schuvailo, O.; Soldatkin, A.; Pollegioni, L.; Pilone, M.; Adeline, M.; Cespuglio, R.; Marinesco, S. Characterization of a Yeast D-Amino Acid Oxidase Microbiosensor for D-Serine Detection in the Central Nervous System. *Anal. Chem.* **2008**, *80*, 1589–1597.

(2) Zain, Z.; O'Neill, R.; Lowry, J.; Pierce, K.; Tricklebank, M.; Dewa, A.; Ghani, S. Development of an Implantable D-Serine Biosensor for in Vivo Monitoring Using Mammalian d-Amino Acid Oxidase on a Poly (o-Phenylenediamine) and Nafion-Modified Platinum-Iridium Disk Electrode. *Biosens. Bioelectron.* **2010**, *25*, 1454–1459.

(3) Vasylieva, N.; Barnych, B.; Meiller, A.; Maucler, C.; Pollegioni, L.; Lin, J.-S.; Barbier, D.; Marinesco, S. Covalent Enzyme Immobilization by Poly(Ethylene Glycol) Diglycidyl Ether (PEGDE) for Microelectrode Biosensor Preparation. *Biosens. Bioelectron.* **2011**, *26*, 3993–4000.

(4) Nieh, C.; Kitazumi, Y.; Shirai, O.; Kano, K. Sensitive D-Amino Acid Biosensor Based on Oxidase/Peroxidase System Mediated by Pentacyanoferrate-Bound Polymer. *Biosens. Bioelectron.* **2013**, *47*, 350–355.

(5) Polcari, D.; Kwan, A.; Van Horn, M.; Danis, L.; Pollegioni, L.; Ruthazer, E.; Mauzeroll, J. Disk-Shaped Amperometric Enzymatic Biosensor for in Vivo Detection of D-Serine. *Anal. Chem.* **2014**, *86*, 3501–3507.

(6) Sarissa Biomedical Ltd - Novel Biosensors for the Measurement of Neuroactive Chemical Products, en, accessed Nov 21, 2018.

(7) Ayon, N.; Deep Sharma, A.; Gutheil, W. LC-MS/MS-Based Separation and Quantification of Marfey's Reagent Derivatized Proteinogenic Amino Acid DL-Stereoisomers. *J. Am. Soc. Mass Spectrom.* **2018**, 448–458.

(8) Berna, M.; Ackermann, B. Quantification of Serine Enantiomers in Rat Brain Microdialysate Using Marfey's Reagent and LC/MS/MS. *J. Chromatogr. B Anal. Technol. Biomed. Life Sci.* **2007**, *846*, 359–363.

(9) Fuchs, S.; De Sain-Van Der Velden, M.; De Barse, M.; Roeleveld, M.; Hendriks, M.; Dorland, L.; Klomp, L.; Berger, R.; De Koning, T. Two Mass-Spectrometric Techniques for Quantifying Serine Enantiomers and Glycine in Cerebrospinal Fluid: Potential Confounders and Age-Dependent Ranges. *Clin. Chem.* **2008**, *54*.

Appendix C

Supporting Information for Chapter 4

C.1 Experimental Methodology

C.1.1 Enzyme Preparation

Enzyme Purification and Concentration

All enzymes were purified by HiTrap chelating chromatography (GE Healthcare Bio-sciences). Purification of hDAAO W209R was carried out with the exogenous FAD (40 µM) addition to all purification buffers. The final preparation of *Rg*DAAO WT and *Rg*DAAO M213G was stored in 20 mM Tris-HCl, pH 8.0, 100 mM NaCl, 10% glycerol, and 5 mM 2-β-mercaptoethanol. The final preparation of hDAAO W209R was stored in 20 mM Tris-HCl, pH 8.0, 100 mM NaCl, 10% glycerol, 5 mM 2-β-mercaptoethanol and 40 µM FAD. Enzyme purity was confirmed by SDS-PAGE. Enzymes were concentrated with a centricon ultrafiltration device (MW cutoff = 30 kDa, Amicon). Protein concentration of the purified enzymes was determined using the extinction coefficient at 450 nm (12.6 mM^{-1} cm^{-1} for *Rg*DAAO enzymes and 12.2 for hDAAO enzymes).[1–3]

Biochemical Activity Assay Enzyme Characterization

Standard polarographic assays (0.253 mM O_2, 25^oC) for *Rg*DAAO WT, *Rg*DAAO M213G and hDAAO W209R with 28 mM D-alanine in 50 mM sodium pyrophosphate, pH 8.5 (containing 40 µM FAD for hDAAO W209R) were employed. One enzyme unit is defined as the amount of enzyme that converts 1 µmol of D-amino acid per minute at 25^oC. Substrate specificity was investigated by a spectrophotometric assay based on detection of hydrogen

peroxide production using a coupled assay with peroxidase and o-dianisidine (o-DNS, ϵ=13 $mM^{-1}cm^{-1}$).[4] Briefly, H_2O_2 produced from DAAO is reduced by horseradish peroxidase that simultaneously oxidizes o-DNS to give a colored compound with an absorption maximum at 440 nm. Different concentrations of standard D-alanine (10 µM - 25 mM), D-serine (10 µM - 25 mM) and glycine (100 µM - 1 mM) were tested as substrates.

Enzymatic Biosensor Preparation

For biosensor development, the final *Rg*DAAO WT was concentrated to 56.8 mg mL^{-1} in 0.01 M PBS, pH 7.4 containing 1% glycerol and 25 mg mL^{-1} BSA. The final *Rg*DAAO M213G solution of was concentrated to 48 mg mL^{-1} in 0.01 M PBS, pH 7.4, containing 1% glycerol and 23 mg mL^{-1} BSA. The final hDAAO W209R solution of was concentrated to 45 mg mL^{-1} protein using a centricon device (MW cutoff = 10 kDa, Amicon) and stored in 0.01 M PBS, pH 7.4, containing 1% glycerol and 23 mg mL^{-1} BSA. Pt disk MEs (10 µm) were prepared according to previously reported procedure.[5] Briefly, a soda-lime glass capillary was pulled and a Pt wire was inserted into the capillary, which was then sealed. The ME tip was polished until the Pt wire was exposed, revealing a disk-shaped surface geometry. The final ME was rinsed with deionized water (18.2 MΩ), 70% ethanol, and acetone. The R_g is the ratio of the glass sheath to the diameter of the electroactive surface and was confirmed with optical microscopy using a customized Axio Vert A1 inverted microscope (Zeiss, Oberkochen, Germany) to be between 2-3 for all MEs. A permselective polymer was then electrodeposited onto the electrode surface using cyclic voltammetry (0 to +1 V, 5 cycles) with 0.1 M PPD prepared in 0.01 M PBS (pH 7.4). The full biosensors were

fabricated according to a literature protocol.[6] Briefly, 2 µL of each enzyme was drop-casted onto a PDMS coated glass slide. The PPD-ME was immersed in the enzyme droplet for five seconds and then removed to dry for 4 minutes. This procedure was repeated four times, followed by enzyme crosslinking using glutaraldehyde solution (50% v/v in H_2O). Scheme Figure C.1 shows the complete biosensor development approach with all enzymes.

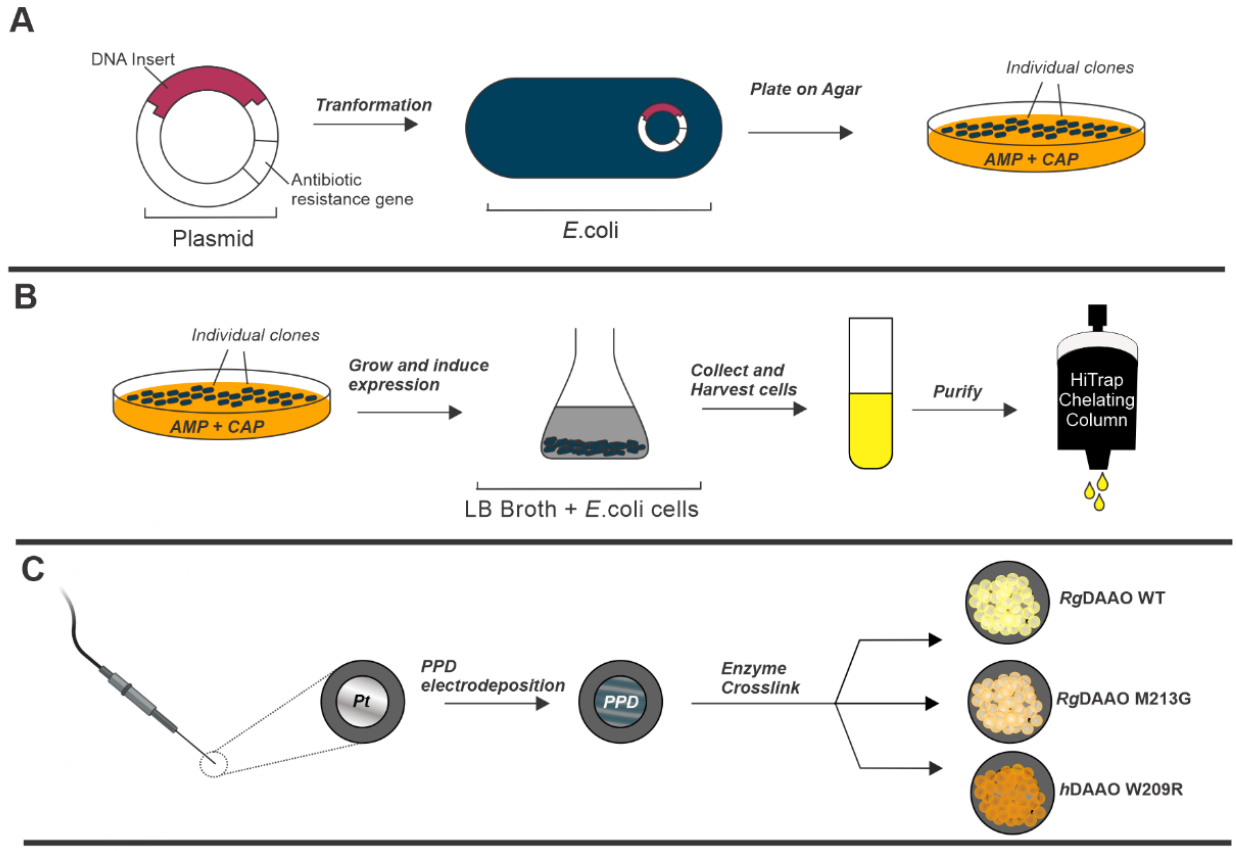

Figure C.1: Approach to multiple biosensor development. A) To express a select enzyme, *E.*coli cells are transformed with a plasmid containing the gene encoding the enzyme and the gene for antibiotic resistance. The cells are then plated on agar in the presence of AMP and CAP to obtain individual cell clones. B) The clones are used to inoculate LB broth and protein expression was induced with IPTG. Following growth, cells are harvested by centrifugation and the enzyme was purified by HiTrap chelating chromatography. C) Following enzyme concentration, the enzymes are deposited into the surface of different PPD-modified Pt MEs.

C.1.2 Instrumentation

Spectrophotometric measurements were performed using a thermostated UV/Vis spectrophotometer (V-560, Jasco) at 25 ^{o}C. Electrochemical measurements were performed using an

Electrochemical Probe Scanner 3 (Heka Elektronik, Lambrecht, Germany). All potentials were recorded relative to a Ag/AgCl QRE (fabricated in-house, radius=0.125 mm).[5] All electrochemical solutions were prepared in phosphate-buffered saline (PBS, 0.01 M, pH 7.4). Measurements performed using chronoamperometry, involved a ME biased at 0.5 V vs. Ag/AgCl. All recorded potentials are reported against an Ag/AgCl reference.

C.1.3 Characterizations of Free and Crosslinked RgDAAO

TEM Characterization

TEM images were acquired using a Brightfield Philips CM200 TEM at 200 kV. One µL of *Rg*DAAO was dropcasted onto the TEM carbon coated copper grid (TED PELLA, Inc.), left to dry and crosslinked with glutaraldehyde. The enzyme film was rinsed with PBS to remove unbound protein (0.01 M, pH 7.4) and exposed to either PBS or 0.1 or 1 mM -alanine for 5 minutes before rinsing with PBS, air drying and acquiring TEM images.

Electrochemical Characterization

Chronoamperograms were recorded using an *Rg*DAAO biosensor. Following immersion in a PBS solution, the biosensor was placed in solutions of 0.1 mM and 1 mM D-serine and D-alanine individually. The current profile corresponding to the oxidation of H_2O_2 produced by the enzymatic reaction was followed for a period of 15 min. To compare the behavior of the final biosensor to the soluble crosslinked *Rg*DAAO and free *Rg*DAAO, chronoamperograms were recorded in 1 mM D-alanine. *Rg*DAAO solution crosslinking was achieved placing the

enzyme in a glutaraldehyde desiccator.

Circular Dichroism Characterization

CD spectra were recorded at 25 ^{o}C on a Jasco J-810 spectropolarimeter using a 1 cm path length cuvette.[7] Temperature was kept constant using a Peltier unit. Spectra were recorded from 230 to 350 nm, at a response time of 4.0 s with three spectra acquisitions. The enzyme concentration of the free and self-crosslinked samples was 0.2 mg mL^{-1} in 0.1 M PBS, pH 7.4.

FTIR Characterization

Infrared spectra were measured using an FTIR spectrometer (Bruker) with attenuated total reflectance (ATR). Seven scans corrected for PBS were collected per spectrum; the resolution was 4 cm^{-1}. Two µL of each sample were drop casted onto the detector.

DLS Characterization

A DLS spectrometer (Brookhaven instruments) was used to measure the particle size dispersion. Measurements were recorded with a 90 angle degree light with a wavelength of 659 nm using a square polystyrene cell, at 25^{o}C. Measurements were recorded for 120 seconds with an equilibration time. A dust filter for <10 nm particles was applied. Three measurements for each sample were taken. Measurements were completed at pH 7.4 where the real refractive index of the particles was set to 1.590 assuming uniform spheres. Baseline normalization was applied.

C.1.4 Structural Analysis and Calculations

All structure figures in the manuscript were prepared with PyMOl. To calculate the % surface solvent accessible surface area, the percent ratio of solvent accessible surface area to molecular surface area was computed on PyMOL. The non-polar contacts were found using PyMOL by displaying solvent non-polar interactions with the enzymes.

C.2 Supporting Figures and Tables

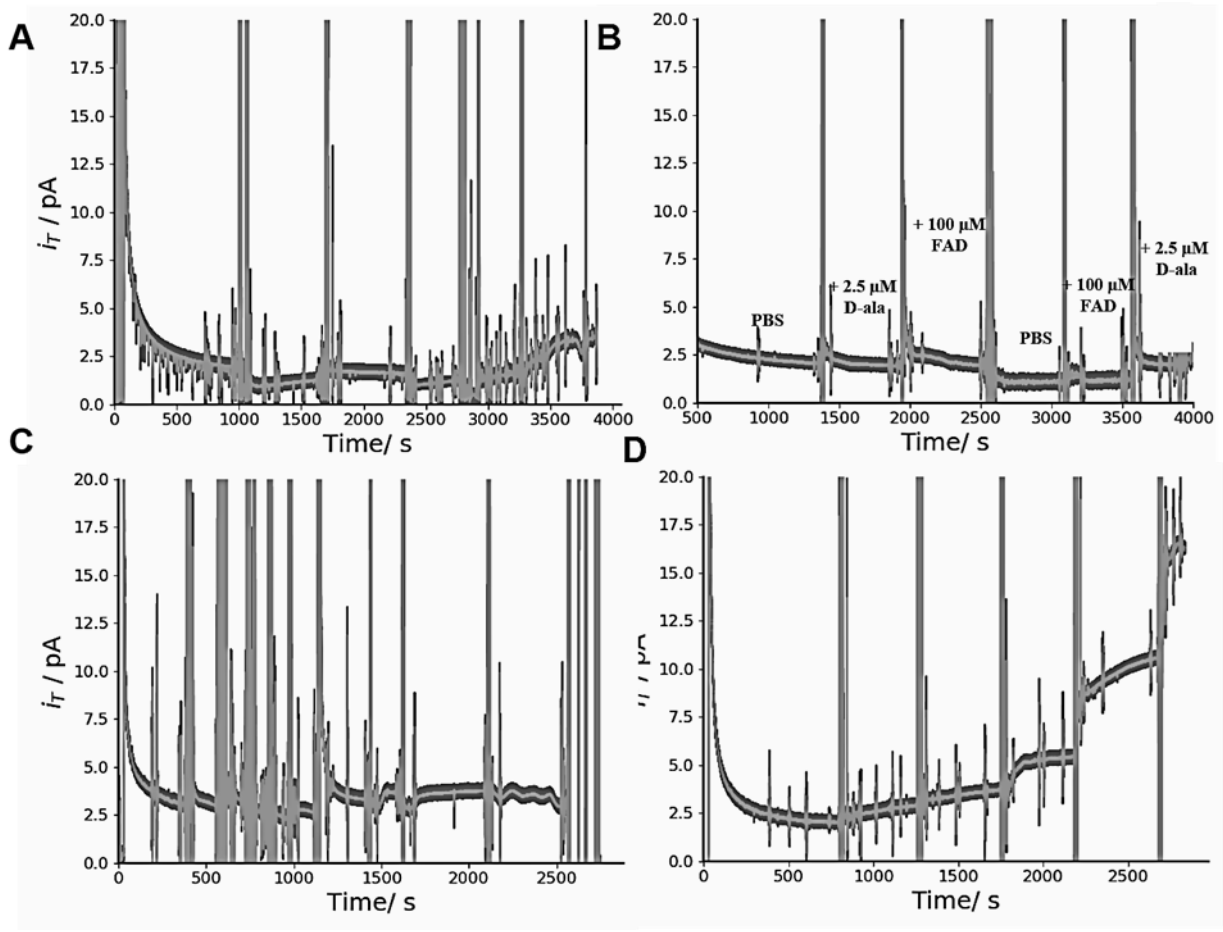

Figure C.2: Development of hDAAO W209R biosensors where the steady-state current responses at various concentrations of standard D-alanine solutions are shown. A) Unconcentrated hDAAO W209R (9 mg mL^{-1}) in 0-50 µM D-alanine solutions. B) Concentrated hDAAO (45 mg mL^{-1}). The biosensor was placed in PBS buffer, 2.5 µM D-alanine with 100 µM FAD. As a control to evaluate the lack of FAD electrochemical activity, the order was also reversed. C) Concentrated hDAAO W209R (45 mg mL^{-1}) co-immobilized with 100 µM FAD. D) Concentrated hDAAO (45 mg mL^{-1}) where 100 µM FAD is present in all of the D-alanine solutions.

Table C.1: Biosensor calibration curve regression parameters.

	*Rg*DAAO WT		*Rg*DAAO M213G		hDAAO W209R	
	D-ser (n=3)	D-ala (n=3)	D-ser (n=3)	D-ala (n=3)	D-ser (n=3)	D-ala (n=3)
R^2	0.997	0.999	0.993	0.999	0.986	0.984
m	0.090	0.154	0.104	0.117	0.143	0.291
b	0.039	0.120	0.124	-0.123	0.442	0.789

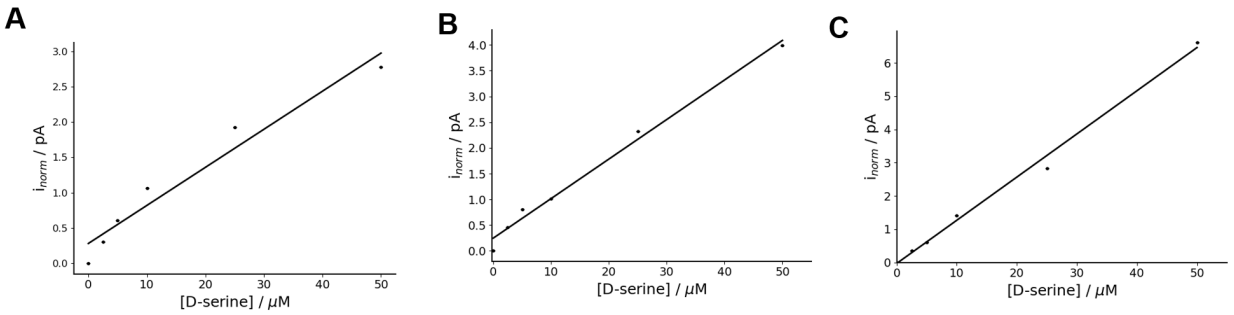

Figure C.3: Calibration of biosensors stored for 2 weeks dry at -20 ^{o}C. Calibrations were carried out using standard solutions of 0–50 µM D-serine and: A) *Rg*DAAO WT; B) *Rg*DAAO M213G; C) hDAAO W209R.

Table C.2: Effect of storage at -20 ^{o}C for two weeks on the linearity and slope of the biosensor calibration curves.

Data	*Rg*DAAO WT	*Rg*DAAO M213G	hDAAO W209R
Pre-Storage	I=0.0895x +0.120	I=0.104x+0.124	I=0.143x +0.442
	R^2=0.997	R^2=0.990	R^2=0.990
Post-Storage	I = 0.054 x + 0.281	I = 0.0768 x + 0.248	I = 0.130 x - 0.298
	R^2=0.950	R^2=0.988	R^2=0.990
Slope Decrease (%)	39.66	26.15	9.09

Table C.3: Effect of BSA on the specific activity of *Rg*DAAO WT. The activity, expressed as U $\cdot$ mg^{-1} protein, was assessed on 25 mM of substrate using the o-DNS assay (pH 8.5).

*Rg*DAAO	D-alanine	D-serine
With BSA	105	48
Without BSA	103	48

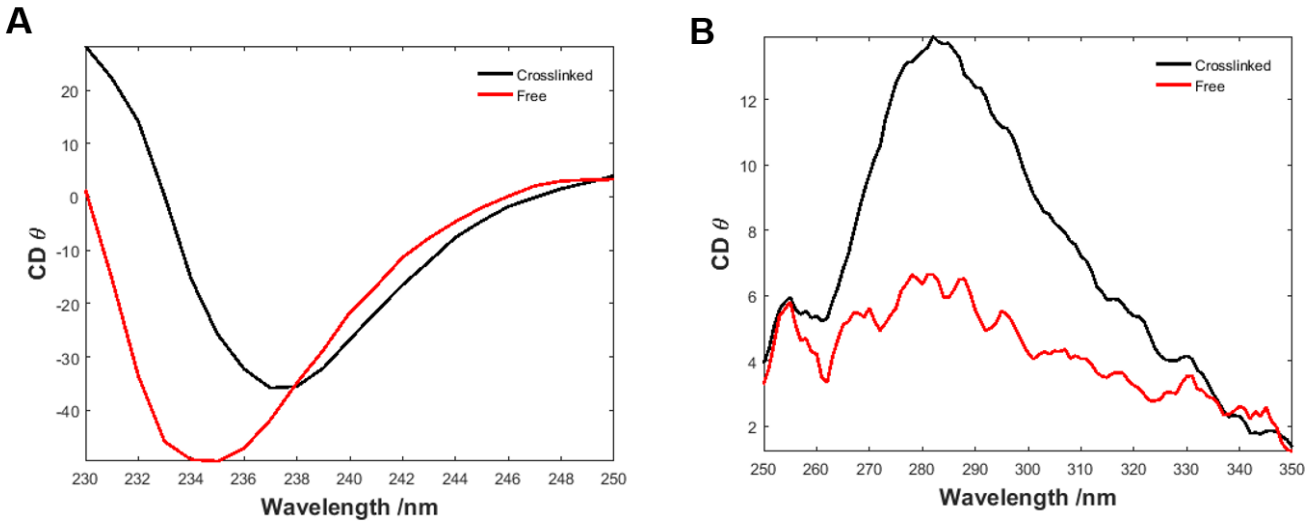

Figure C.4: Circular dichroism spectra of free (red) and crosslinked (black) *Rg*DAAO WT where the degree of ellipticity is shown as a function of wavelength. A) Spectra in the far-UV range. B) Spectra in the near-UV range.

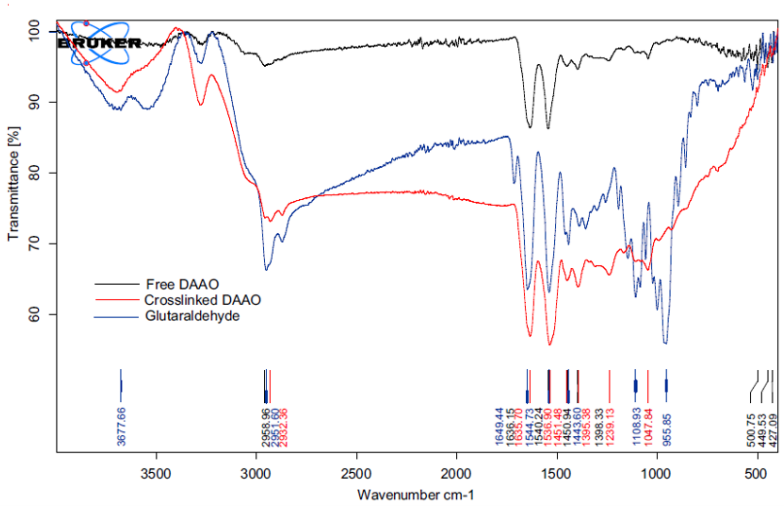

Figure C.5: FTIR spectra of free (black) and crosslinked (red) *Rg*DAAO WT as well as glutaraldehyde (blue). The major differences in the spectra between the free and crosslinked *Rg*DAAO correspond to the peaks representative of glutaraldehyde (3677.66, 2951.50, 1544.73, 1443.50, 1108.93 and 995.85 cm^{-1})

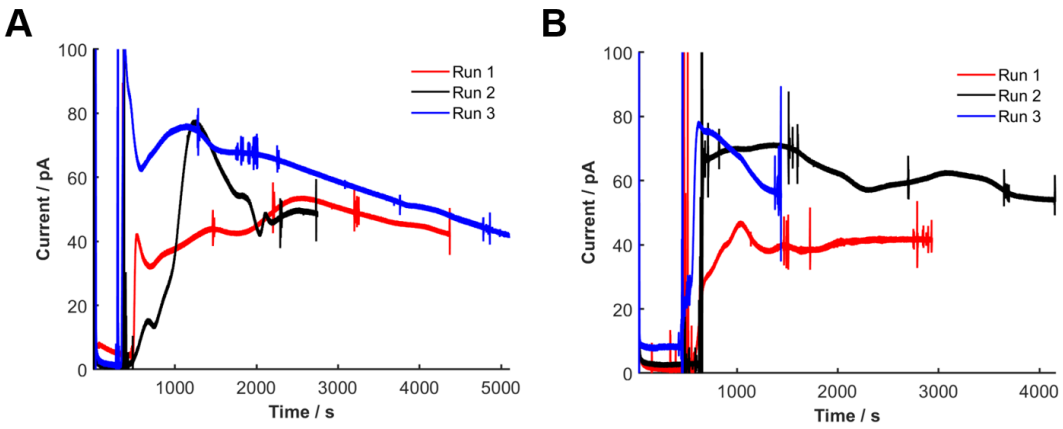

Figure C.6: Chronoamperograms measured with a PPD-ME poised at 0.5 V vs. Ag/AgCl. The electrochemical current response of DAAO incubated in 1 mM D-alanine was measured. The PPD-ME was immersed in 1 mM D-alanine, to which the following was added: A) 0.5 µL of free *Rg*DAAO; B) 0.5 µL of glutaraldehyde-crosslinked *Rg*DAAO. Each run corresponds to a different measurement. DAAO was added at approximately 400 s for each run.

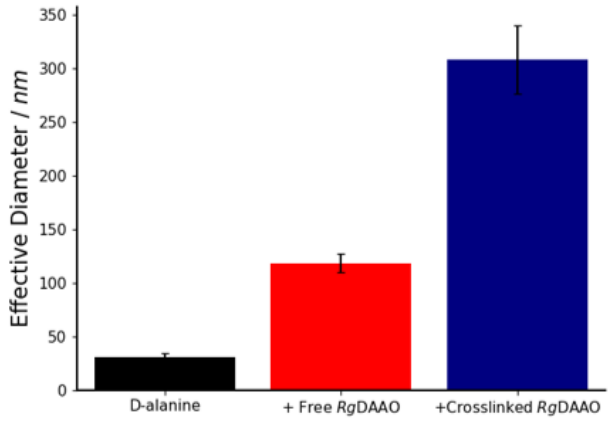

Figure C.7: Effective diameter determined from DLS measurements for D-alanine, free *Rg*DAAO in the presence of D-alanine and crosslinked *Rg*DAAO in the presence of D-alanine.

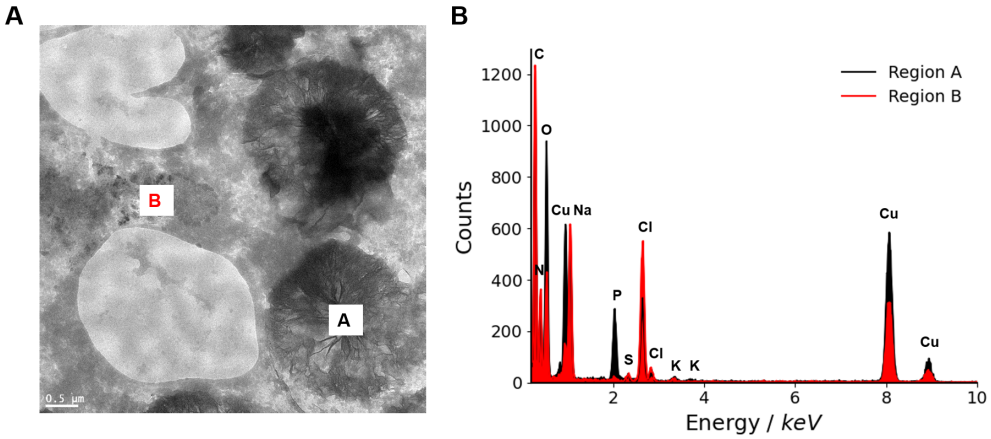

Figure C.8: TEM images showing the presence of DAAO/BSA mixture. A) TEM images of crosslinked DAAO/BSA mixture onto the copper grid (scale bar = 0.5 µm) where region A corresponds to protein presence and region B protein absence. B) EDS measurements on the two different regions.

Table C.4: Effect of biosensor regeneration on its calibration, reported as equation of the corresponding fit.

Data	D-serine	D-alanine
Pre-Regeneration	I=0.133x +0.205 R^2=0.943	I=0.159x+0.367 R^2=0.982
Post-Regeneration	I = 0.338 x + 0.373 R^2=0.998	I = 0.371 x + 1.246 R^2=0.976
Slope Increase (%)	153	133

References

(1) Fantinato, S.; Pollegioni, L.; Pilone, S.; Engineering, M. Expression and Purification of a His-Tagged Chimeric D-Amino Acid Oxidase from Rhodotorula Gracilis. *Enzyme Microb. Technol.* **2001**, *29*, 407–412.

(2) Sacchi, S.; Lorenzi, S.; Molla, G.; Pilone, M.; Rossetti, C.; Pollegioni, L. Engineering the Substrate Specificity of D-Amino-Acid Oxidase. *J. Biol. Chem.* **2002**, *30*, 27510–27516.

(3) Cappelletti, P.; Piubelli, L.; Murtas, G.; Caldinelli, L.; Valentino, M.; Molla, G.; Pollegioni, L.; Sacchi, S. Structure–Function Relationships in Human d-Amino Acid Oxidase Variants Corresponding to Known SNPs. *Biochim. Biophys. Acta* **2015**, *1854*, 1150–1159.

(4) Rosini, E.; Caldinelli, L.; Piubelli, L. Assays of D-Amino Acid Oxidase Activity. *Front. Mol. Biosci.* **2018**, *4*, 1–12.

(5) Danis, L.; Polcari, D.; Kwan, A.; Gateman, S.; Mauzeroll, J. Fabrication of Carbon, Gold, Platinum, Silver, and Mercury Ultramicroelectrodes with Controlled Geometry. *Anal. Chem.* **2015**, *87*, 2565–2569.

(6) Polcari, D.; Perry, S.; Pollegioni, L.; Geissler, M.; Mauzeroll, J. Localized Detection of D-Serine by Using an Enzymatic Amperometric Biosensor and Scanning Electrochemical Microscopy. *ChemElectroChem* **2017**, *4*, 920–926.

(7) Caldinelli, L.; Molla, G.; Bracci, L.; Lelli, B.; Pileri, S.; Cappelletti, P.; Sacchi, S.; Pollegioni, L. Effect of Ligand Binding on Human D-Amino Acid Oxidase: Implications for the Development of New Drugs for Schizophrenia Treatment. *Protein Sci.* **2010**, *19*, 1500–1512.

Appendix D

Supporting Information for Chapter 5

D.1 Experimental Methodology

D.1.1 DNA Sequencing of Clones

The DNA of the interesting clones was isolated using gel extraction and PCR cleanup (Macherey Nagel). Briefly, 10-50 µL of crude extracts were inoculated in 3 mL LB with Amp and Cam. DNA from 1.5 mL of the cultures was isolated and agarose gel electrophoresis was used to extract the band corresponding to the pT7 DNA. The DNA was excised and eluted with 50 mL AE buffer. Ultracompetent E.coli JM109 cells were transformed using 5-10 µL of the DNA and the pT7 expressing cells were plated on AMP and CAM containing LB agar plates. A single colony from each plate was picked for inoculation of the cells in 10 mL LB (with AMP and CAM). The pT7 plasmid DNA was extracted from the ultracompetent cells, eluted with 50 µL mQ water and sent for sequencing (Milan, Italy). Prior to sequencing, gel electrophoresis was performed (Figure D.1) to check for DNA presence in the sample.

D.1.2 Well Plate Preparation

Well plates were prepared by cleaning a microscope glass slide. The glass slide was modified with adhesive tape which had 4x5 rectangular grids printed on the surface. The modified glass slide was coated in PDMS and stored in an oven overnight at 120^{o}C. After 24 hours, a surgical knife was used to remove the PDMS from the regions within the rectangular boxes, creating evenly spaced wells with hydrophobic walls to contain liquid within.

D.1.3 Null Experiments with PPD-ME and Glycine Oxidase

PPD-MEs were immersed in a solution of PBS buffer. A constant potential of 0.5V was applied at the tip of the PPD-MEs and the current was monitored. After a period of 5 minutes, a cell suspension of HEK 293 cells was transferred to the well plate and the current at 0.5 V from the cell suspension was measured. After a period of 10 mins, 2 µL GO H244K enzyme was added to the cell suspension and the consumption of glycine released from HEK 293 cells was monitored indirectly through hydrogen peroxide production.

D.1.4 Interference Effect of Triton X-100 and Tween-20

GO H244K biosensors were immersed in 200 µL buffer. A constant potential of 0.5V was applied at the tip of the biosensors and following recording baseline currents in PBS, 2 µL Triton X-100 was added to the buffer solution. The same experimental protocol was repeated with Tween-20.

D.2 Supporting Figures and Tables

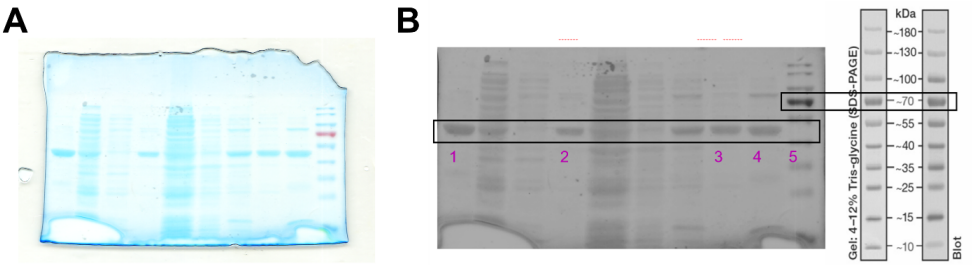

Figure D.1: Sample SDS gel confirming purity of protein in sample (A) unmodified SDS page (B) Black and white image of SDS page for better visualization clarity. Numbers correspond to enzyme/ marker (1. GO WT, 2. H244K, 3. H244Q, 4. H244F, 5. Marker)

Table D.1: Specific Activity (U.mg^{-1}) of GO wild-type and GO Variants.

GO Mutant	[Glycine]	Specific activity (U.mg^{-1})
WT	100 mM	0.80
H244F	100 mM	0.523
H244K	100 mM	1.038
H244Q	100 mM	0.177

Table D.2: Kinetic parameters for GO variants of interest.

	k_{cat}	$K_{M,app}$	$k_{cat,app}(mM)/K_{M,app}s^{-1}mM^{-1}$	Turnover Ratio (Enzyme:GO WT)
His-GO WT	0.60 ± 0.03	0.70 ± 0.10	0.86	1.00
His-GO H244Q	1.21± 0.06	0.90 ± 0.04	1.34	1.55
His-GO H244K	1.35 ± 0.05	0.14 ± 0.02	9.65	11.22

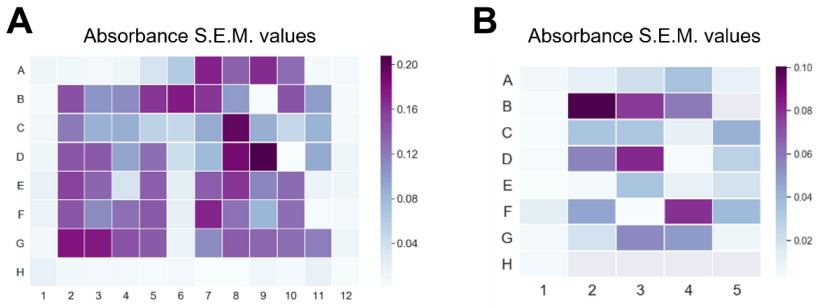

Figure D.2: Corresponding S.E.M. values for the absorbance measurements as reported in the manuscript. (A) SEM values for reported absorbances in Figure 1A. Position H11 corresponds to the clone for GO WT and position H12 corresponds to the control well without cells. (B) SEM values for reported absorbances in Figure 1B. Position G5 corresponds to the clone for GO WT and position H1 corresponds to the control well without cells. Grey boxes represent empty wells.

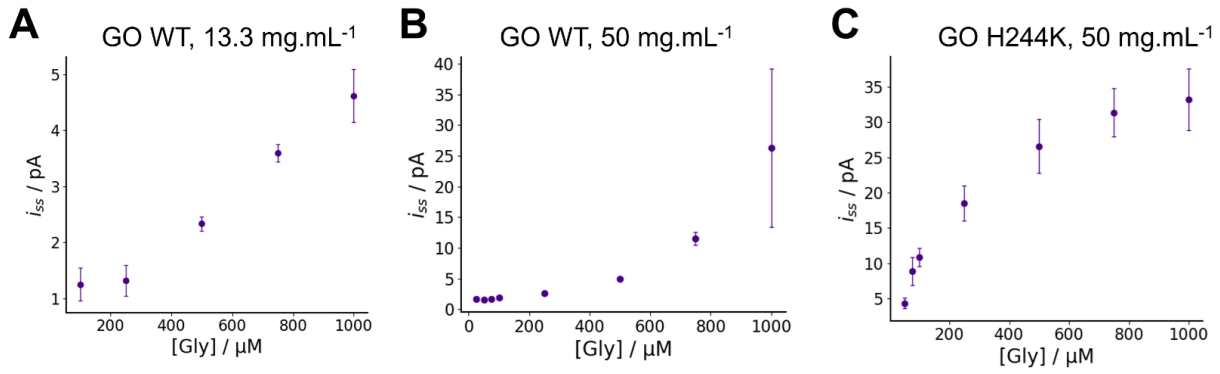

Figure D.3: Calibrations of GO biosensors in standard solutions of glycine (A) 13.3 mg.mL-1 GO WT biosensors in 100, 250, 500, 750, 1000 µM glycine. (B) 50 mg.mL-1 GO WT biosensors in 25,50,75,100, 250, 500, 750, 1000 µM glycine. (C) 50 mg.mL-1 GO H244K biosensors in 50,75,100, 250, 500, 750, 1000 µM glycine.

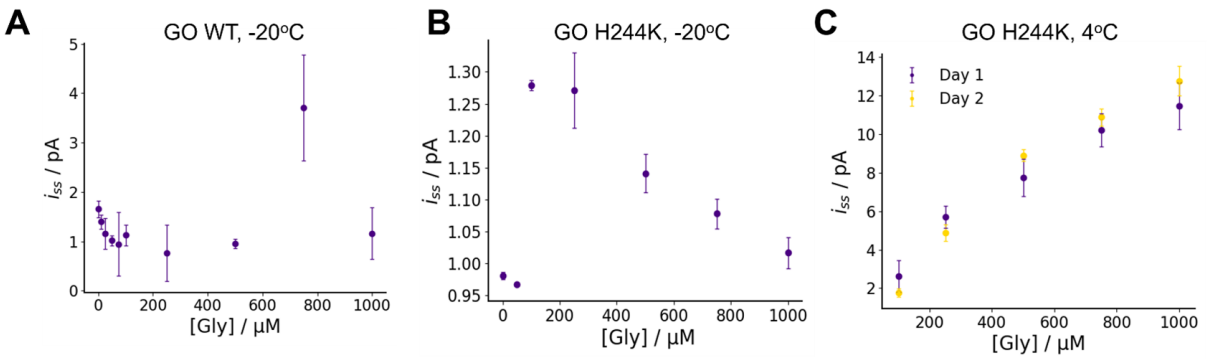

Figure D.4: Calibrations of stored GO biosensors in standard solutions of glycine (A) GO WT after 2 weeks of storage at 20^{o}C in 0,25,50,75,100, 150, 250, 500, 750, 1000 µM glycine. (B) GO H244K after 2 weeks of storage at 20oC in 0,50,100, 250, 500, 750, 1000 µM glycine. CB) GO H244K after one day of storage at 4^{o}C in 100, 250, 500, 750, 1000 µM glycine.

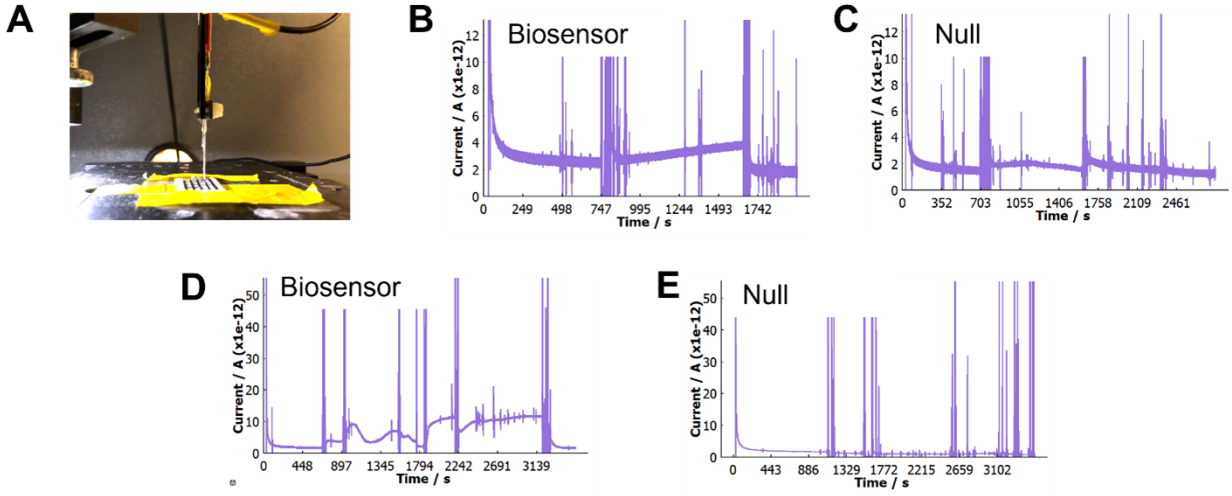

Figure D.5: Application of GO H244K biosensors for real-time detection of glycine(A) Photograph of experimental setup (B) Representative experimental curve from the biosensor placed in PBS, followed by HEK 293 cells, followed by PBS (C) Representative experimental curve from the null sensor placed in PBS, followed by HEK 293 cells, followed by PBS (D) Representative experimental curve from the biosensor placed in PBS, followed by astrocytes, followed by PBS (E) Representative experimental curve from the null sensor placed in PBS, followed by astrocytes, followed by PBS.

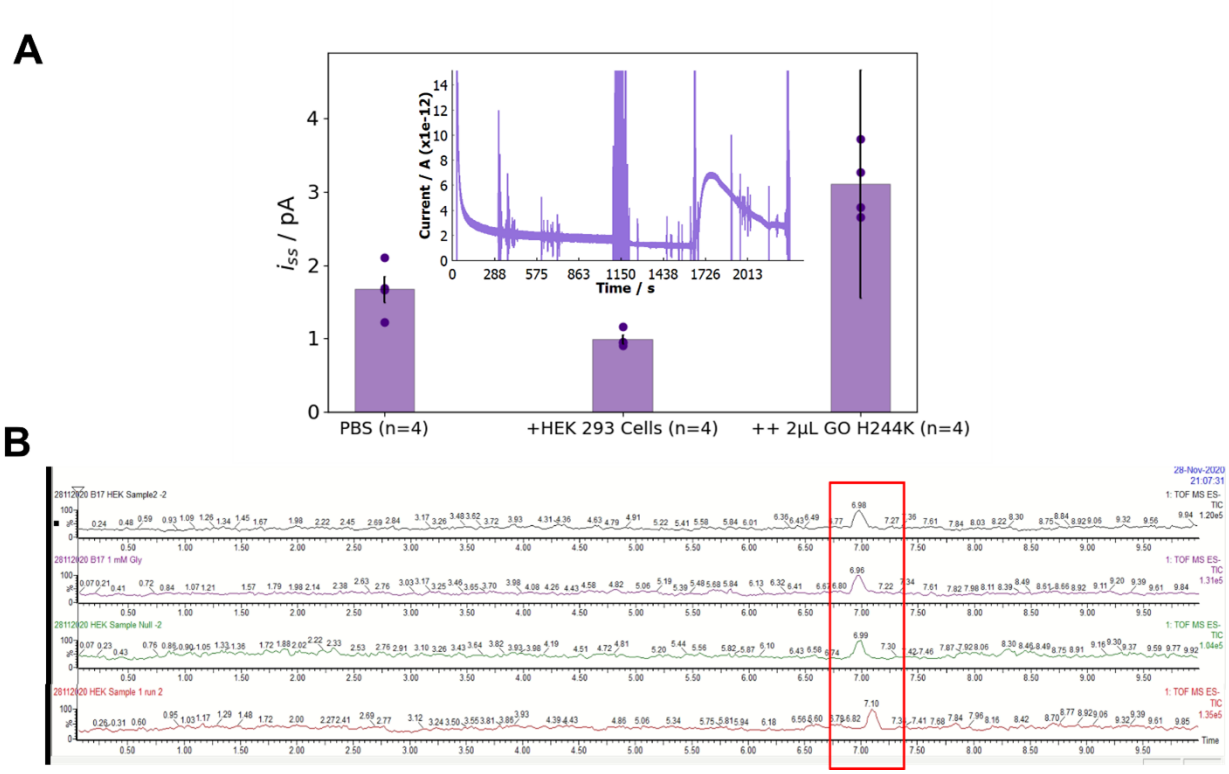

Figure D.6: Validation of biosensor measurements with (A) the PPD-ME immersed in PBS, followed by cells and followed by the addition of 2 µL GO H244K enzyme. The current corresponding to the application of 0.5V was monitored throughout the entire length of the experiment (Inset). The steady state current was extracted and demonstrates glycine turnover by the addition of GO H244K to the HEK 293 cells. Calibrations of GO biosensors in standard solutions of glycine (B) LC-MS experiments where the peak at 6.90-7.00 min corresponds to the glycine presence. Top to bottom: aliquot of HEK 293 sample (1), 1 mM standard glycine, HEK 293 sample (2), HEK 293 sample (3).

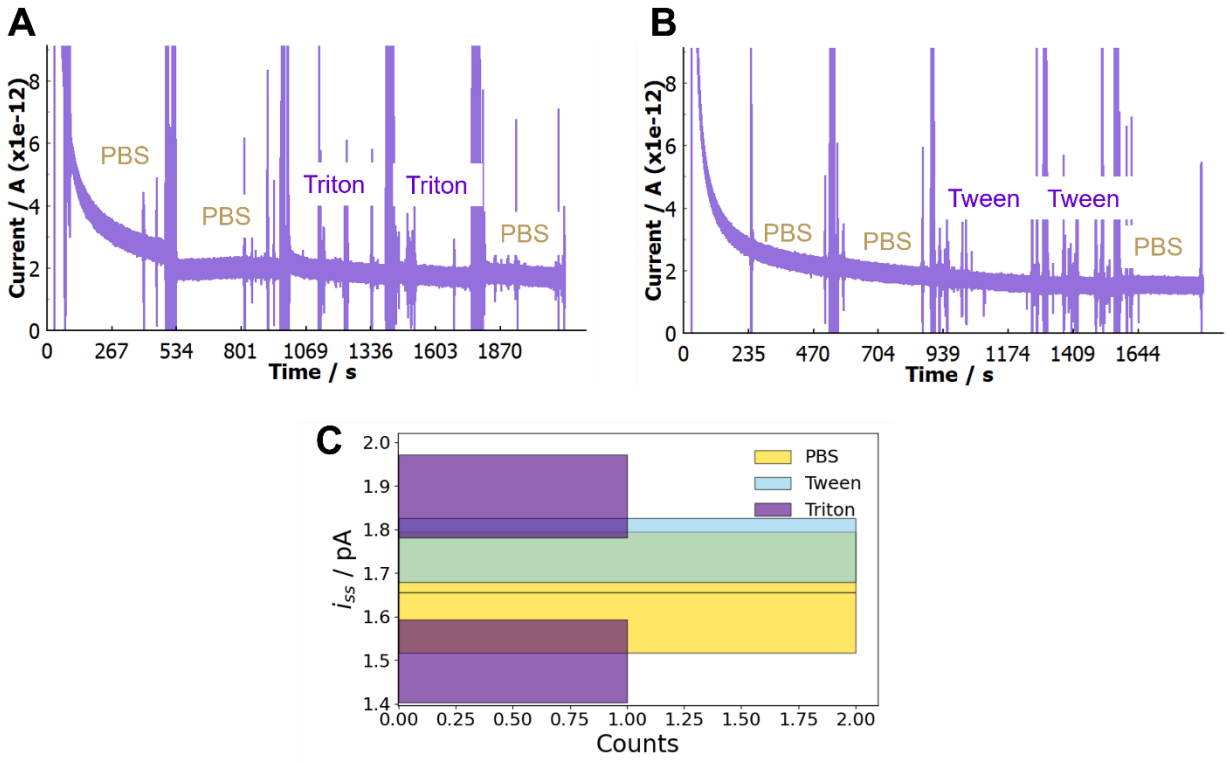

Figure D.7: Effect of the addition of (A) 1% Triton-X 100 (B)1% Tween-20 in PBS on the current response measured with GO biosensors immersed in PBS (C) Histogram showing steady state currents for biosensor immersed in surfactants. No increase in the steady state current is observed, confirming that both surfactants do not interfere with the oxidation current.

D.3 Sensorlyze: A Biosensor Data Analysis Software

D.3.1 Motivation

Chronoamperometric measurements using biosensors allow for quantification of analyte concentrations in biological media. While relatively simple, chronoamperometric measurements include a large number of data points and depending on the signal measurements, are prone to being impacted by noise. These is no simple and easy platform that has the capacity for data processing and filtering in the context of electrochemical biosensor data to generate calibration curves and enable analyte quantification. Moreover, extracting useful information from biosensor data points can be particularly challenging, especially from data of in vivo biosensor measurements. Blips and spikes in data can occur and if they are not accurately processed and electrical or thermal noise may easily be misinterpreted as a signal. Additionally, each experiment is controlled by a large number of parameters set by either the experimenter or the biosensor (i.e. according to the stimuli applied or the state of the biological system in study). Based on the amount of data collected in this thesis, the next logical step was to develop a tool to reduce time invested in data analysis and publication ready figure generation. Sensorlyze is a graphical user interface (GUI) with four key main modules/features: single sensor calibration, multiple sensor calibration, quantification and data visualization. The development of this graphical user interface is key in enabling access to beginners to the field of biosensors or even users, who do not have the preliminary understanding of biosensor data programming protocols. The Sensorlyze manual is readily

available at https://sibamoussa.github.io/sensorlyze/manual/. Additionally, Sensorlyze is data format flexible. That is, it allows for functionality of importing multiple data formats from different manufacturers, which not possible with commonly used electrophysiology software applied in neuroscience sensor-based research.

D.3.2 Software Development

Sensorlyze was built using Python 3.7 and Qt5. The following python packages were used: numpy, pandas, scikitlearn, matplotlib, PyQT5, pyqtgraph, sklearn, seabornmatplotlib, statistics, openpyxl, and xlwt. The software was designed to import files from a variety of potentiostat manufacturers. Currently supported formats include: Excel (.xlsx), HEKA Elektronik (.asc) ,Biologic (.txt), CH Instruments (.txt), and Sensolytics (.dat). PyQT was chosen for building the GUI model because of its efficient and comprehensive framework, with the optionality to connecting the GUI to a database, making it better performing than Tkinter, despite its increased development complexity. Sensorlyze can run within Python or as a standalone executable. It is currently only accessible for Windows (.exe). Output data from Sensorlyze is exported as .xlsx and figures as .jpg /.tiff.

D.3.3 Sensorlyze User Manual

1. **Getting Started: Installing Sensorlyze**

   Two options are available for running Sensorlyze:

   - A standalone executable file

   - The open-source python code for the software

   Both options are available on github.

2. **Running the executable file:**

   The .exe file is available for downloading. This version is currently only windows compatible.

3. **Running the open-source python code:**

   To run the python script, download the guisensorlyze.py file and supporting .py files. Make sure that the supporting files are in the same folder as the main script. To prompt the GUI, run guisensorlyze.py. The following packages are required to run the script:

   numpy, pandas, scipy, scikit, matplotlib, pyqt, sklearn

4. **Using Sensorlyze : Start and Experiment Selection**

   Once the software is prompted to run either by running the source code or by clicking on the icon of the .exe file, a window will appear, prompting the user to start or exit Sensorlyze. Sensorlyze contains four modules, defined as experiments. Selecting start

will prompt a new window [select experiment] to open (Figure D.8). Click on the grey box to see a list of options. To perform the correct analysis, the user can navigate through the options and select the option which matches best with the user analysis needs.

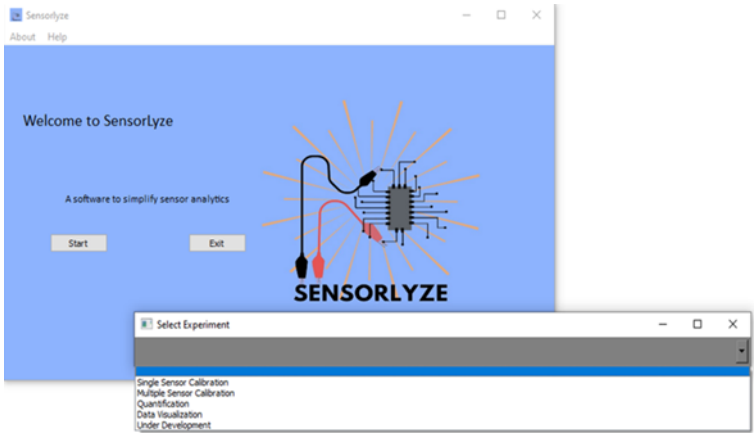

Figure D.8: Screenshot of the main window pop up open prompting of the software to open up and the experiment type selection window.

5. **Analysis Options:**

Single Sensor Calibration

This window is split into two main tabs. To go through the data analysis follow the steps outlined for specified tab:

Tab 1: Single Sensor Analytics

a. Import a data file to visualize: To import, select the file in the directory of choice.

b. Select the Manufacturer and file type: The import file option currently supports files from the following manufacturers: HEKA, Biologic, CH Instruments, Excel Select

the desired file type to proceed.

c. Plot File: Current-time data within the selected file will be plotted.

d. Apply Noise Reduction Filter: Checking the box will apply the noise reduction filter. The data is filtered using a first-degree polynomial Savitzky-Golay filter. The Savitzky-Golay filter uses convolution-based filtering, i.e. fitting sub-sets of data points with a low degree polynomial using linear least squares. Unchecking the box will remove the noise filtered data and the original data will reappear.

e. Clear Plot: Clicking this button will clear the plot of the raw or filtered data.

f. Save Plot: The plot will be saved in the directory of choice. Current supported file formats for saving graphics are: *.jpg and *.tiff file formats

g. Select Points: Checking the select points box will allow to extract the mean of the current values over a time period of 30 seconds. Once the checkbox for select points is chosen, a blue bar will appear. The blue bar is automatically set to average data over a range of 30s. The range can be changed by moving either xmin or the xmax limit of the bar further or closer (hover over the limit under a red vertical line appears and then drag the line) Select points (with or without noise-reduction filter- range is automatically set to 30 seconds, but can be modified) To select multiple points, click in the middle of the bar, and drag the bar to the region(s) of interest.

h. Please input all concentrations with a space in between: Once the points of interest are selected, to build a calibration curve, enter the concentrations corresponding to each selection. Make sure to enter the concentrations in μM and with a space in between each value.

i. Done: When concentrations have been entered, click on the button done to proceed.

j. Export Data: Clicking on export data will export the mean currents from the selected regions and the concentration corresponding to each region. The data is automatically exported into an excel sheet named "Results" in the same working directory as the software files.

- To export points only and no concentrations, enter a range of indices instead of concentrations - To export the points and concentrations, click export data after including the right concentration corresponding to each mean current.

k. Plot Calibration: Clicking on plot calibration will allow to visualize the current-time calibration profile Clicking on plot calibration with cause the calibration profile to appear along with three other options:

- Save Plot: Save the graphic in *.tiff or *.jpg file formats

- Clear Calibration Plot: Clear the calibration plot

- Export Calibration: The data will export to an excel sheet called Results in the same working directory as the software If the regress data? box is checked, then the regression parameters will also export to the same excel sheet.

l. Normalize Plot?: Checking the box for normalize plot will normalize to the baseline through background current substraction. i.e. the first selected set of points using select points correspond to the current from the background signal. All following mean currents are substracted from this baseline signal.

m. Plot Normalized Calibration: Clicking on plot normalized calibration will allow to visualize the current-time calibration profile Clicking on plot normalized calibration

will allow the calibration profile to appear along with three other options:

- Save Plot: Save the graphic in *.tiff or *.jpg file formats

- Clear Normalized Calibration: Clear the calibration plot

- Export Normalized Calibration: The data will export to an excel sheet called Results in the same working directory as the software If the regress data? box is checked, then the regression parameters will also export to the same excel sheet.

n. Regress Data?: Checking the box for regress data will cause the following regression parameters to appear in a textbox above the calibration plot: - Slope, Intercept, R^2 To show the regression data for the unnormalized calibration curve, make sure that the checkbox for for normalize plot is unchecked. To show the regression data for the normalized calibration curve, make sure that the checkbox for for normalize plot is checked.

o. Export all Data: Clicking on export data will allow to export all data obtained from this module into a single excel files consisting of multiple sheets.

- To export the data correctly, please ensure that the data is regressed for both the unnormalized and normalized calibrations.

Exporting the data will generate an excel file with three sheets which consist of:

- Raw current-time series data

- Calibration data including the mean current values for each concentration and the regression parameters

- Normalized calibration data including the mean current values for each concentration and the regression parameters

Multiple Sensor Calibration This window is split into two main tabs. To go through the data analysis follow the steps outlined for each tab:

Tab 1: Analytics- Point Selection

a. Import a data file to visualize: To import, select the file in the directory of choice.

b. Select the Manufacturer and file type: The import file option currently supports files from the following manufacturers: HEKA, Biologic, CH Instruments, Excel Select the desired file type to proceed.

c. Plot File: Current-time data within the selected file will be plotted.

d. Please input the sampling range over which the values are to be averaged (seconds): This option will allow the user to enter a sampling range (in seconds) over which the current data is averaged. For example, if the user would like to get the mean current for a 30 second sampling frequency, enter 30 into the textbox. The current data over a range of 30s will be extracted from the plot each time the blue bar is moved. These values will be averaged over time range to provide a mean current value.

e. Done: When the user has entered a value to change the sampling range, click on done A blue bar will appear on the plot. This blue bar can be moved to different regions of the data so that the data over the length of the bar is averaged and saved each time it is moved.

f. Apply Noise Reduction Filter: Checking the box will apply the noise reduction filter. The data is filtered using a first-degree polynomial Savitzky-Golay filter. The Savitzky-Golay filter uses convolution-based filtering, i.e. fitting sub-sets of data points

with a low degree polynomial using linear least squares. Unchecking the box will remove the noise filtered data and the original data will reappear. To select points from the noise filtered plot, the points exported will not contain the original raw data. Instead, for the specific file, the mean currents from the noise filtered data are presented.

g. Done Point Selection: When selecting all regions of interest in the plot is completed, click on done point selection.

h. Export Selected Points:

Clicking on export selected points will export the following to an excel file called QuantSelectedPoints:

- Table 1 [Time Points(first,last)]: A row with range of time points for each selection made in the data file (i.e. for each time the blue bar was dragged from one region to another). Only the first and last time point for each selected region are recorded. A row above with the corresponding point indices is also included.
- Table 2 [Current Values(first,last)]) : A row with first and last current reading collected from the range of time points for each selection made in the data file (i.e. for each time the blue bar was dragged from one region to another). Only the first and last time current reading for each selected region are recorded. A row above with the corresponding point indices is also included.
- Table 3 [Mean Currents (A)]: A row with the mean current from the average of current values across the range of time points for each selection made in the data file. (i.e. if the length of the blue bar was 30s, the first index would include the average of currents measured for 30s corresponding to the first region the blue bar was moved

to). A row above with the corresponding point indices is also included.

Notes:

- All indexing begins at zero.

- The data is automatically exported into an excel sheet named ‘QuantSelectedPoints‘ in the same working directory as the software files.

i. Clear Selections:

Clicking on clear selections will remove the blue bar and allow to select a different sampling range and a new set of points to be exported.

Tab 2: Analytics- Calibration Statistics

a. Plot Calibration: Clicking on plot calibration will show a plot of the calibration along with the following regression parameters: - R^2, Slope, Intercept, LOD, and LOQ

* LOD is the limit of detection, defined as 3 times the standard deviation of the blank signal divided by the slope of the regression line.

* LOQ is the limit of quantification, defined as 10 times the standard deviation of the blank signal divided by the slope of the regression line.

Note: Values will show to 3 decimal places. If a value of 0 appears, exporting the data will show the real value.

b. Save Calibration Plot:

Clicking on save calibration will allow to save the plot in the directory of choice. Current supported file formats for saving graphics are: *.jpg and *.tiff file formats

c. Export Calibration Data:

Clicking on export calibration data will automatically save the calibration data in an excel file named Calibration located in the same working directory as the software. The data exported data will consist of two tables in the same sheet:

- Table 1: Columns with the 1) concentration, 2) average currents from all the data files for each concentration , 3) standard deviation for the currents used to calculate the mean current , standard error of the mean (SEM) for each mean current value

- Table 2: Calibration regression statistics [R^2, Intercept, Slope, LOD, and LOQ]

d. Plot Normalized Calibration:

Clicking on plot normalized calibration will show a plot of the normalized calibration along with the following regression parameters: - R^2, Slope, Intercept, LOD, and LOQ

Notes: - Values will show to 3 decimal places. If a value of 0 appears, exporting the data will show the real value. - Normalized currents are background signal subtracted current values.

e. Save Normalized Calibration Plot: Clicking on save normalized calibration will allow to save the plot in the directory of choice. Current supported file formats for saving graphics are: *.jpg and *.tiff file formats

e. Export Normalized Calibration Data: Clicking on export normalized calibration data will automatically save the calibration data in an excel file named Normalized Calibration located in the same working directory as the software. The data exported data will consist of two tables in the same sheet:

- Table 1: Columns with the 1) concentration, 2) background subtracted average cur-

rents (normalized average currents) from all the data files for each concentration , 3) standard deviation of the normalized currents used to calculate the mean current, standard error of the mean (SEM) for each normalized mean current value -

Table 2: Calibration regression statistics [R^2, Intercept, Slope, LOD, LOQ, Standard Deviation of the Blank**]

For each set of currents obtained for a single data file, the currents are normalized by subtracting the background current from each current value. Once this has been completed for each file, the mean current for each concentration from the different files is calculated and displayed in the table. The standard deviation for the baseline (zero) concentration will always be zero.

The standard error of the mean for the baseline (zero) concentration will always be zero.

*** For LOD and LOQ calculations, the the standard deviation of the blank used is the standard deviation of the unnormalized current readings for the blank signals.

Quantification

This window is split into two main tabs. To go through the data analysis follow the steps outlined for each tab:

Tab 1: Analytics- Point Selection

a. Import a data file to visualize: To import, select the file in the directory of choice.

b. Select the Manufacturer and file type:

The import file option currently supports files from the following manufacturers: HEKA,

Biologic, CH Instruments, Excel Select the desired file type to proceed.

c. Plot File: Current-time data within the selected file will be plotted.

d. Please input the sampling range over which the values are to be averaged (seconds):

This option will allow to enter a sampling range (in seconds) over which the current data is averaged.

For example, if the user would like to get the mean current for a 30 second sampling frequency, enter 30 into the textbox. The current data over a range of 30s will be extracted from the plot each time the blue bar is moved. These values will be averaged over time range to provide a mean current value.

e. Done: When a value to change the sampling range is entered, click on done A blue bar will appear on the plot. This blue bar can be moved to different regions of the data so that the data over the length of the bar is averaged and saved each time it is moved.

f. Apply Noise Reduction Filter: Checking the box will apply the noise reduction filter. The data is filtered using a first-degree polynomial Savitzky-Golay filter. The Savitzky-Golay filter uses convolution-based filtering, i.e. fitting sub-sets of data points with a low degree polynomial using linear least squares. Unchecking the box will remove the noise filtered data and the original data will reappear. If points from the noise filtered plot are selected, the points exported will not contain the original raw data. Instead, for the specific file, the mean currents from the noise filtered data are presented.

g. Done Point Selection: When selecting all regions of interest in the plot is complete, click on done point selection

h. Export Selected Points: Clicking on export selected points will export the following to an excel file called QuantSelectedPoints:

- Table 1 [Time Points(first,last)]: A row with range of time points for each selection made in the data file (i.e. for each time the blue bar was dragged from one region to another). Only the first and last time point for each selected region are recorded. A row above with the corresponding point indices is also included.
- Table 2 [Current Values(first,last)]) : A row with first and last current reading collected from the range of time points for each selection made in the data file (i.e. for each time the blue bar was dragged from one region to another). Only the first and last time current reading for each selected region are recorded. A row above with the corresponding point indices is also included.
- Table 3 [Mean Currents (A)]: A row with the mean current from the average of current values across the range of time points for each selection made in the data file. (i.e. if the length of the blue bar was 30s, the first index would include the average of currents measured for 30s corresponding to the first region the blue bar was moved to). A row above with the corresponding point indices is also included.

Notes:

- All indexing begins at zero.

- The data is automatically exported into an excel sheet named ‘QuantSelectedPoints‘ in the same working directory as the software files.

i. Clear Selections: Clicking on clear selections will remove the blue bar and allow to select a different sampling range and a new set of points to be exported.

Tab 2: Analytics- Analyte Quantification

a. Please input the regression line slope: Input the slope of the regression line. This could be a slope obtained through earlier analysis using the Analytics- Point Selection tab.

b. Please input the regression line intercept: Input the intercept for the same regression line as the one used for the slope input.

c. Please input the current value: Input the current reading. Make sure that the calibration regression line parameters correspond to the same sensor used for experimental measurements.

d. Done: Once all fields are complete in the textboxes above this button, click on Done. Clicking on done will add the entered values into the table displayed on the window.

e. Calculate concentration: After clicking on done, click on calculate concentration to calculate analyte concentration from the current reading and the regression parameters. The calculated concentration will appear in the concentration row in the table. Steps a-e can be repeated multiple times, with either the same regression parameters or varying regression parameters, to calculate the concentration for multiple sensor readings from the current values. Currently, the table can hold up to 12 measurements/readings.

f. Export table: Clicking on export table will allow to export the table to an excel file. The file can be named and saved in the directory of choice as a .xslx file.

g. Clear table: Clicking on clear table will clear all tabular values. It is possible to re-populate the table by inserting new values into the textboxes in the window.

Data Visualization This window consists of solely one tab. To go through the data analysis follow the steps outlined:

Tab 1: Visualize Data

a. Import a data file to visualize: To import, select the file in the directory of choice. It is possible to import one file or multiple files simultaneously by clicking the ctrl button and the filename.

b. Select the Manufacturer and file type: The import file option currently supports files from the following manufacturers: HEKA and Biologic Select the desired file type to proceed.

c. Select X-Axis: From the drop down menu, select the desired x-axis. For HEKA files, use one of the following: Emon ,Imon, Time For Biologic files, use one of the following: Time, Ewe, I

* Emon and Ewe correspond to the **Potential** header for HEKA and Biologic files respectively

** Imon and I correspond to the **Current** header for HEKA and Biologic files respectively

d. Select Y-Axis: From the drop down menu, select the desired x-axis. For HEKA files, use one of the following: Emon ,Imon, Time For Biologic files, use one of the following: Time, Ewe, I

* Emon and Ewe correspond to the **Potential** header for HEKA and Biologic files respectively

** Imon and I correspond to the **Current** header for HEKA and Biologic files respectively

e. Plot File: The data with the selected x and y-axes will be plotted. If more than one file was selected, data for all files and their chosen x-and y-axes will be plotted. A legend is available to identify the files displayed.

f. Save Plot: The plot will be saved in the directory of choice. Current supported file formats for saving graphics are: *.jpg and *.tiff file formats

g. Clear Plot: Data from the most currently plotted file will be cleared from the window. Clicking on plot file will cause the data to reappear.

Under Development

Future releases will include plot formatting functionality as well as other data treatment processes.

D.3.4 Data Processing

Sensorlyze performs multiple manipulations on the datasets. These manipulations include averaging for steady state readings, noise reduction filtering, data regression, and normalization of calibrations. Below is a short explanation of each of these manipulations.

Noise Reduction Filtering

Sensorlyze provides the option to apply a filter to the dataset at hand for noise reduction. The filter is a one-dimensional first order polynomial Savitzky-Golay filter, applied only to the y-axis data. The Savitzky-Golay filter is a convolution based digital filter typically

applied for the purpose of smoothing data without distorting the signal.

Data Averaging

Sensorlyze finds the mean y-value, typically the current, over a range of 30 data points for each region selected. For example, for a dataset with a sampling frequency of 1 second/data point, Sensorlyze calculates the mean current over a range of 30 seconds and presents that mean value as a single data point which can be used for calibration curves.

Data Regression

Linear regression is the sole type of regression currently available for these calibration plots. The software fits the mean values to the concentration inputs based on a linear relationship as follows:

$$i_{ss} = m[Concentration] + b \tag{D.1}$$

Where i_{ss} is the steady state current, typically averaged over a range of 30 seconds, m is the slope of the calibration curve and b is the y-intercept. To assess the fit of the linear regression line to the data, the coefficient of determination (also known as the R2 value) is calculated. A value as close as possible to one is desired and any value below 0.98 demonstrates a poor fit.

Normalized Calibration

To remove the contribution of the non-faradaic current to the biosensor readings, the calibration curve can be normalized by the baseline signal (typically signal from the buffer). As such the normalized currents are calculated as follows to generate a normalized calibration curve with regression line parameters that remove the baseline signal contribution:

$$i_{norm} = i_{ss} - i_{background} \tag{D.2}$$

Where i_{norm} is the normalized current and $i_{background}$ is background current contribution of the buffer.

D.3.5 Future Features

In Appendix D, the development of a Python based GUI, Sensorlyze, is reported. Sensorlyze can be used for electrochemical biosensor data processing and analysis. The GUI can import data from different data acquisition systems regardless of their format and can output the data into a standardized .xlsx format. Sensorlyze provides further options for data plotting and statistics. Future work of Sensorlyze includes expanding its functionality to include differential pulse voltammetry data processing, current density calculations, non-linear regression as well as chemometric data analysis.

CCC Marketplace™

Order Date	04-Aug-2021	**Type of Use**	Republish in a thesis/dissertation
Order License ID	1138301-1		
ISSN	1945-7111	**Publisher**	IOP Publishing
		Portion	Chapter/article

LICENSED CONTENT

Publication Title	Journal of the Electrochemical Society	**Country**	United States of America
		Rightsholder	IOP Publishing, Ltd
Author/Editor	Electrochemical Society.	**Publication Type**	e-Journal
Date	01/01/1948	**URL**	http://www.scitation.org/JES
Language	English		

REQUEST DETAILS

Portion Type	Chapter/article	**Rights Requested**	Main product and any product related to main product
Page range(s)	1-30		
Total number of pages	30	**Distribution**	Worldwide
Format (select all that apply)	Electronic	**Translation**	Original language of publication
Who will republish the content?	Academic institution	**Copies for the disabled?**	No
Duration of Use	Life of current edition	**Minor editing privileges?**	No
Lifetime Unit Quantity	Up to 499	**Incidental promotional use?**	No
		Currency	USD

NEW WORK DETAILS

Title	Electrochemical Sensor Development for Robust Amino Acid Sensing	**Institution name**	McGill University
		Expected presentation date	2021-08-31
Instructor name	Siba Moussa		

ADDITIONAL DETAILS

Order reference number	N/A	**The requesting person / organization to appear on the license**	Siba Moussa

REUSE CONTENT DETAILS

Title, description or numeric reference of the portion(s)	10.1149/2.0741906jes	**Title of the article/chapter the portion is from**	microelectrodes: an overview of probe development and bioelectrochemistry applications from 2013 to 2018
Editor of portion(s)	N/A	**Author of portion(s)**	Electrochemical Society.
Volume of serial or monograph	N/A	**Issue, if republishing an article from a serial**	N/A
Page or page range of portion	1-10	**Publication date of portion**	1948-01-01

RIGHTSHOLDER TERMS AND CONDITIONS

These special terms and conditions are in addition to the standard terms and conditions for CCC's Republication Service and, together with those standard terms and conditions, govern the use of the Works. As the User you will make all reasonable efforts to contact the author(s) of the article which the Work is to be reused from, to seek consent for your intended use. Contacting one author who is acting expressly as authorised agent for their co-author(s) is acceptable. User will reproduce the following wording prominently alongside the Work: the source of the Work, including author, article title, title of journal, volume number, issue number (if relevant), page range (or first page if this is the only information available) and date of first publication; and a link back to the article (via DOI); and if practicable, and IN ALL CASES for new works published under any of the Creative Commons licences, the words "© The Electrochemical Society. Reproduced by permission of IOP Publishing Ltd. All rights reserved" Without the express permission of the author(s) and the Rightsholder of the article from which the Work is to be reused, User shall not use it in any way which, in the opinion of IOP Publishing Ltd, could: (i) distort or alter the author(s)' original intention(s) and meaning; (ii) be prejudicial to the honour or reputation of the author(s); and/or (iii) imply endorsement by the author(s) and/or the Rightsholder and/or IOP Publishing Ltd. This licence does not apply to any article which is credited to another source and which does not have the copyright line '© The Electrochemical Society'. User must check the copyright line of the article from which the Work is to be reused to check that the Electrochemical Society and IOP Publishing Ltd has all the necessary rights to be able to grant permission. User is solely responsible for identifying and obtaining separate licences and permissions from the copyright owner for reuse of any such third party material/figures which the Rightsholder is not the copyright owner of. The Rightsholder shall not reimburse any fees which User pays for a republication license for such third party content. This licence does not apply to any material/figure which is credited to another source in the Rightsholder's publication or has been obtained from a third party. User must check the Version of Record of the article from which the Work is to be reused, to check whether any of the material in the Work is third party material. Third party citations and/or copyright notices and/or permissions statements may not be included in any other version of the article from which the Work is to be reused and so cannot be relied upon by the User. User is solely responsible for identifying and obtaining separate licences and permissions from the copyright owner for reuse of any such third party material/figures where the Rightsholder is not the copyright owner. The Rightsholder shall not reimburse any fees which User pays for a republication license for such third party content. User and CCC acknowledge that IOP Publishing Ltd and/or the Rightsholder may, from time to time, make changes or additions to these special terms and conditions without express notification, provided that these shall not apply to permissions already secured and paid for by User prior to such change or addition. User acknowledges that the Rightsholder and IOP Publishing Ltd (which includes companies within its group and third parties for whom it publishes its titles) may make use of personal data collected through the service in the course of their business. If User is the author of the Work, User may automatically have the right to reuse it under the rights granted back when User transferred the copyright in the article to the Rightsholder. User should check the copyright form and the relevant author rights policy to check whether permission is required. If User is the author of the Work and does require permission for proposed reuse of the Work, User should select 'Author of requested content' as the Requestor Type. The Rightsholder shall not reimburse any fees which User pays for a republication license. If User is the author of the article which User wishes to reuse in User's thesis or dissertation, the republication licence covers the right to include the Version of Record of the article, provided it is not then published commercially. User must include citation details and, for online use, a link to the Version of Record of the article on the IOPscience website. User may need to obtain separate permission for any third party content included within the article. User must check this with the copyright owner of such third party content. User may not include the article in a thesis or dissertation which is published by ProQuest. Any other commercial use of User's thesis or dissertation containing the article would also need to be expressly notified in writing to the Rightsholder at the time of request and would require separate written permission from the Rightsholder. As well as CCC, the Rightsholder and IOP Publishing Ltd shall have the right to bring any legal action that they deem necessary to enforce their rights should they consider that the Work infringes those rights in any

way. For content reuse requests that qualify for permission under the STM Permissions Guidelines, which may be updated from time to time, the STM Permissions Guidelines supplement the terms and conditions contained in this license.

SPECIAL RIGHTSHOLDER TERMS AND CONDITIONS

When you transferred the copyright in your article to The Electrochemical Society you were granted back certain rights, including the right to include the Final Published Version of the article within any thesis or dissertation. Please note you may need to obtain separate permission for any third party content you included within your article. Please include citation details, "© The Electrochemical Society. Reproduced with permission. All rights reserved" and for online use, a link to the Version of Record. The only restriction is that if, at a later date, you wanted your thesis/dissertation to be published commercially, further permission would be required.

CCC Terms and Conditions

1. Description of Service; Defined Terms. This Republication License enables the User to obtain licenses for republication of one or more copyrighted works as described in detail on the relevant Order Confirmation (the "Work(s)"). Copyright Clearance Center, Inc. ("CCC") grants licenses through the Service on behalf of the rightsholder identified on the Order Confirmation (the "Rightsholder"). "Republication", as used herein, generally means the inclusion of a Work, in whole or in part, in a new work or works, also as described on the Order Confirmation. "User", as used herein, means the person or entity making such republication.

2. The terms set forth in the relevant Order Confirmation, and any terms set by the Rightsholder with respect to a particular Work, govern the terms of use of Works in connection with the Service. By using the Service, the person transacting for a republication license on behalf of the User represents and warrants that he/she/it (a) has been duly authorized by the User to accept, and hereby does accept, all such terms and conditions on behalf of User, and (b) shall inform User of all such terms and conditions. In the event such person is a "freelancer" or other third party independent of User and CCC, such party shall be deemed jointly a "User" for purposes of these terms and conditions. In any event, User shall be deemed to have accepted and agreed to all such terms and conditions if User republishes the Work in any fashion.

3. Scope of License; Limitations and Obligations.

    3.1. All Works and all rights therein, including copyright rights, remain the sole and exclusive property of the Rightsholder. The license created by the exchange of an Order Confirmation (and/or any invoice) and payment by User of the full amount set forth on that document includes only those rights expressly set forth in the Order Confirmation and in these terms and conditions, and conveys no other rights in the Work(s) to User. All rights not expressly granted are hereby reserved.

    3.2. General Payment Terms: You may pay by credit card or through an account with us payable at the end of the month. If you and we agree that you may establish a standing account with CCC, then the following terms apply: Remit Payment to: Copyright Clearance Center, 29118 Network Place, Chicago, IL 60673-1291. Payments Due: Invoices are payable upon their delivery to you (or upon our notice to you that they are available to you for downloading). After 30 days, outstanding amounts will be subject to a service charge of 1-1/2% per month or, if less, the maximum rate allowed by applicable law. Unless otherwise specifically set forth in the Order Confirmation or in a separate written agreement signed by CCC, invoices are due and payable on "net 30" terms. While User may exercise the rights licensed immediately upon issuance of the Order Confirmation, the license is automatically revoked and is null and void, as if it had never been issued, if complete payment for the license is not received on a timely basis either from User directly or through a payment agent, such as a credit card company.

    3.3. Unless otherwise provided in the Order Confirmation, any grant of rights to User (i) is "one-time" (including the editions and product family specified in the license), (ii) is non-exclusive and non-transferable and (iii) is subject to any and all limitations and restrictions (such as, but not limited to, limitations on duration of use or circulation) included in the Order Confirmation or invoice and/or in these terms and conditions. Upon completion of the licensed use, User shall either secure a new permission for further use of the Work(s) or immediately cease any new use of the Work(s) and shall render inaccessible (such as by

deleting or by removing or severing links or other locators) any further copies of the Work (except for copies printed on paper in accordance with this license and still in User's stock at the end of such period).

3.4. In the event that the material for which a republication license is sought includes third party materials (such as photographs, illustrations, graphs, inserts and similar materials) which are identified in such material as having been used by permission, User is responsible for identifying, and seeking separate licenses (under this Service or otherwise) for, any of such third party materials; without a separate license, such third party materials may not be used.

3.5. Use of proper copyright notice for a Work is required as a condition of any license granted under the Service. Unless otherwise provided in the Order Confirmation, a proper copyright notice will read substantially as follows: "Republished with permission of [Rightsholder's name], from [Work's title, author, volume, edition number and year of copyright]; permission conveyed through Copyright Clearance Center, Inc. " Such notice must be provided in a reasonably legible font size and must be placed either immediately adjacent to the Work as used (for example, as part of a by-line or footnote but not as a separate electronic link) or in the place where substantially all other credits or notices for the new work containing the republished Work are located. Failure to include the required notice results in loss to the Rightsholder and CCC, and the User shall be liable to pay liquidated damages for each such failure equal to twice the use fee specified in the Order Confirmation, in addition to the use fee itself and any other fees and charges specified.

3.6. User may only make alterations to the Work if and as expressly set forth in the Order Confirmation. No Work may be used in any way that is defamatory, violates the rights of third parties (including such third parties' rights of copyright, privacy, publicity, or other tangible or intangible property), or is otherwise illegal, sexually explicit or obscene. In addition, User may not conjoin a Work with any other material that may result in damage to the reputation of the Rightsholder. User agrees to inform CCC if it becomes aware of any infringement of any rights in a Work and to cooperate with any reasonable request of CCC or the Rightsholder in connection therewith.

4. Indemnity. User hereby indemnifies and agrees to defend the Rightsholder and CCC, and their respective employees and directors, against all claims, liability, damages, costs and expenses, including legal fees and expenses, arising out of any use of a Work beyond the scope of the rights granted herein, or any use of a Work which has been altered in any unauthorized way by User, including claims of defamation or infringement of rights of copyright, publicity, privacy or other tangible or intangible property.

5. Limitation of Liability. UNDER NO CIRCUMSTANCES WILL CCC OR THE RIGHTSHOLDER BE LIABLE FOR ANY DIRECT, INDIRECT, CONSEQUENTIAL OR INCIDENTAL DAMAGES (INCLUDING WITHOUT LIMITATION DAMAGES FOR LOSS OF BUSINESS PROFITS OR INFORMATION, OR FOR BUSINESS INTERRUPTION) ARISING OUT OF THE USE OR INABILITY TO USE A WORK, EVEN IF ONE OF THEM HAS BEEN ADVISED OF THE POSSIBILITY OF SUCH DAMAGES. In any event, the total liability of the Rightsholder and CCC (including their respective employees and directors) shall not exceed the total amount actually paid by User for this license. User assumes full liability for the actions and omissions of its principals, employees, agents, affiliates, successors and assigns.

6. Limited Warranties. THE WORK(S) AND RIGHT(S) ARE PROVIDED "AS IS". CCC HAS THE RIGHT TO GRANT TO USER THE RIGHTS GRANTED IN THE ORDER CONFIRMATION DOCUMENT. CCC AND THE RIGHTSHOLDER DISCLAIM ALL OTHER WARRANTIES RELATING TO THE WORK(S) AND RIGHT(S), EITHER EXPRESS OR IMPLIED, INCLUDING WITHOUT LIMITATION IMPLIED WARRANTIES OF MERCHANTABILITY OR FITNESS FOR A PARTICULAR PURPOSE. ADDITIONAL RIGHTS MAY BE REQUIRED TO USE ILLUSTRATIONS, GRAPHS, PHOTOGRAPHS, ABSTRACTS, INSERTS OR OTHER PORTIONS OF THE WORK (AS OPPOSED TO THE ENTIRE WORK) IN A MANNER CONTEMPLATED BY USER; USER UNDERSTANDS AND AGREES THAT NEITHER CCC NOR THE RIGHTSHOLDER MAY HAVE SUCH ADDITIONAL RIGHTS TO GRANT.

7. Effect of Breach. Any failure by User to pay any amount when due, or any use by User of a Work beyond the scope of the license set forth in the Order Confirmation and/or these terms and conditions, shall be a material breach of the license created by the Order Confirmation and these terms and conditions. Any breach not cured within 30

days of written notice thereof shall result in immediate termination of such license without further notice. Any unauthorized (but licensable) use of a Work that is terminated immediately upon notice thereof may be liquidated by payment of the Rightsholder's ordinary license price therefor; any unauthorized (and unlicensable) use that is not terminated immediately for any reason (including, for example, because materials containing the Work cannot reasonably be recalled) will be subject to all remedies available at law or in equity, but in no event to a payment of less than three times the Rightsholder's ordinary license price for the most closely analogous licensable use plus Rightsholder's and/or CCC's costs and expenses incurred in collecting such payment.

8. Miscellaneous.

8.1. User acknowledges that CCC may, from time to time, make changes or additions to the Service or to these terms and conditions, and CCC reserves the right to send notice to the User by electronic mail or otherwise for the purposes of notifying User of such changes or additions; provided that any such changes or additions shall not apply to permissions already secured and paid for.

8.2. Use of User-related information collected through the Service is governed by CCC's privacy policy, available online here:https://marketplace.copyright.com/rs-ui-web/mp/privacy-policy

8.3. The licensing transaction described in the Order Confirmation is personal to User. Therefore, User may not assign or transfer to any other person (whether a natural person or an organization of any kind) the license created by the Order Confirmation and these terms and conditions or any rights granted hereunder; provided, however, that User may assign such license in its entirety on written notice to CCC in the event of a transfer of all or substantially all of User's rights in the new material which includes the Work(s) licensed under this Service.

8.4. No amendment or waiver of any terms is binding unless set forth in writing and signed by the parties. The Rightsholder and CCC hereby object to any terms contained in any writing prepared by the User or its principals, employees, agents or affiliates and purporting to govern or otherwise relate to the licensing transaction described in the Order Confirmation, which terms are in any way inconsistent with any terms set forth in the Order Confirmation and/or in these terms and conditions or CCC's standard operating procedures, whether such writing is prepared prior to, simultaneously with or subsequent to the Order Confirmation, and whether such writing appears on a copy of the Order Confirmation or in a separate instrument.

8.5. The licensing transaction described in the Order Confirmation document shall be governed by and construed under the law of the State of New York, USA, without regard to the principles thereof of conflicts of law. Any case, controversy, suit, action, or proceeding arising out of, in connection with, or related to such licensing transaction shall be brought, at CCC's sole discretion, in any federal or state court located in the County of New York, State of New York, USA, or in any federal or state court whose geographical jurisdiction covers the location of the Rightsholder set forth in the Order Confirmation. The parties expressly submit to the personal jurisdiction and venue of each such federal or state court.If you have any comments or questions about the Service or Copyright Clearance Center, please contact us at 978-750-8400 or send an e-mail to support@copyright.com.

v 1.1

SPRINGER NATURE LICENSE
TERMS AND CONDITIONS

Aug 03, 2021

This Agreement between McGill University -- Siba Moussa ("You") and Springer Nature ("Springer Nature") consists of your license details and the terms and conditions provided by Springer Nature and Copyright Clearance Center.

License Number	5121431067379
License date	Aug 03, 2021
Licensed Content Publisher	Springer Nature
Licensed Content Publication	Analytical and Bioanalytical Chemistry
Licensed Content Title	Quantitative measurements of free and immobilized RgDAAO Michaelis-Menten constant using an electrochemical assay reveal the impact of covalent cross-linking on substrate specificity
Licensed Content Author	Siba Moussa et al
Licensed Content Date	Apr 1, 2021
Type of Use	Thesis/Dissertation
Requestor type	academic/university or research institute
Format	print and electronic
Portion	full article/chapter

Will you be translating?	no
Circulation/distribution	100 - 199
Author of this Springer Nature content	yes
Title	Electrochemical Sensor Development for Robust Amino Acid Biosensing
Institution name	McGill University
Expected presentation date	Aug 2021
Order reference number	021659
Requestor Location	McGill University 3420 Rue University Office 111 Montréal,, QC H3A 0C7 Canada Attn: McGill University
Total	0.00 USD

Terms and Conditions

Springer Nature Customer Service Centre GmbH
Terms and Conditions

This agreement sets out the terms and conditions of the licence (the **Licence**) between you and **Springer Nature Customer Service Centre GmbH** (the **Licensor**). By clicking 'accept' and completing the transaction for the material (**Licensed Material**), you also confirm your acceptance of these terms and conditions.

1. Grant of License

1. 1. The Licensor grants you a personal, non-exclusive, non-transferable, world-wide licence to reproduce the Licensed Material for the purpose specified in your order only. Licences are granted for the specific use requested in the order and for no other

use, subject to the conditions below.

1. 2. The Licensor warrants that it has, to the best of its knowledge, the rights to license reuse of the Licensed Material. However, you should ensure that the material you are requesting is original to the Licensor and does not carry the copyright of another entity (as credited in the published version).

1. 3. If the credit line on any part of the material you have requested indicates that it was reprinted or adapted with permission from another source, then you should also seek permission from that source to reuse the material.

2. Scope of Licence

2. 1. You may only use the Licensed Content in the manner and to the extent permitted by these Ts&Cs and any applicable laws.

2. 2. A separate licence may be required for any additional use of the Licensed Material, e.g. where a licence has been purchased for print only use, separate permission must be obtained for electronic re-use. Similarly, a licence is only valid in the language selected and does not apply for editions in other languages unless additional translation rights have been granted separately in the licence. Any content owned by third parties are expressly excluded from the licence.

2. 3. Similarly, rights for additional components such as custom editions and derivatives require additional permission and may be subject to an additional fee. Please apply to Journalpermissions@springernature.com/bookpermissions@springernature.com for these rights.

2. 4. Where permission has been granted **free of charge** for material in print, permission may also be granted for any electronic version of that work, provided that the material is incidental to your work as a whole and that the electronic version is essentially equivalent to, or substitutes for, the print version.

2. 5. An alternative scope of licence may apply to signatories of the STM Permissions Guidelines, as amended from time to time.

3. Duration of Licence

3. 1. A licence for is valid from the date of purchase ('Licence Date') at the end of the relevant period in the below table:

Scope of Licence	Duration of Licence
Post on a website	12 months
Presentations	12 months
Books and journals	Lifetime of the edition in the language purchased

4. Acknowledgement

4. 1. The Licensor's permission must be acknowledged next to the Licenced Material in print. In electronic form, this acknowledgement must be visible at the same time as the figures/tables/illustrations or abstract, and must be hyperlinked to the journal/book's homepage. Our required acknowledgement format is in the Appendix below.

5. Restrictions on use

5. 1. Use of the Licensed Material may be permitted for incidental promotional use and minor editing privileges e.g. minor adaptations of single figures, changes of format, colour and/or style where the adaptation is credited as set out in Appendix 1 below. Any other changes including but not limited to, cropping, adapting, omitting material that affect the meaning, intention or moral rights of the author are strictly prohibited.

5. 2. You must not use any Licensed Material as part of any design or trademark.

5. 3. Licensed Material may be used in Open Access Publications (OAP) before publication by Springer Nature, but any Licensed Material must be removed from OAP sites prior to final publication.

6. Ownership of Rights

6. 1. Licensed Material remains the property of either Licensor or the relevant third party and any rights not explicitly granted herein are expressly reserved.

7. Warranty

IN NO EVENT SHALL LICENSOR BE LIABLE TO YOU OR ANY OTHER PARTY OR ANY OTHER PERSON OR FOR ANY SPECIAL, CONSEQUENTIAL, INCIDENTAL OR INDIRECT DAMAGES, HOWEVER CAUSED, ARISING OUT OF OR IN CONNECTION WITH THE DOWNLOADING, VIEWING OR USE OF THE MATERIALS REGARDLESS OF THE FORM OF ACTION, WHETHER FOR BREACH OF CONTRACT, BREACH OF WARRANTY, TORT, NEGLIGENCE, INFRINGEMENT OR OTHERWISE (INCLUDING, WITHOUT LIMITATION, DAMAGES BASED ON LOSS OF PROFITS, DATA, FILES, USE, BUSINESS OPPORTUNITY OR CLAIMS OF THIRD PARTIES), AND
WHETHER OR NOT THE PARTY HAS BEEN ADVISED OF THE POSSIBILITY OF SUCH DAMAGES. THIS LIMITATION SHALL APPLY NOTWITHSTANDING ANY FAILURE OF ESSENTIAL PURPOSE OF ANY LIMITED REMEDY PROVIDED HEREIN.

8. Limitations

8. 1. ***BOOKS ONLY:***Where **'reuse in a dissertation/thesis'** has been selected the following terms apply: Print rights of the final author's accepted manuscript (for clarity, NOT the published version) for up to 100 copies, electronic rights for use only on a personal website or institutional repository as defined by the Sherpa guideline

(www.sherpa.ac.uk/romeo/).

8. 2. For content reuse requests that qualify for permission under the STM Permissions Guidelines, which may be updated from time to time, the STM Permissions Guidelines supersede the terms and conditions contained in this licence.

9. Termination and Cancellation

9. 1. Licences will expire after the period shown in Clause 3 (above).

9. 2. Licensee reserves the right to terminate the Licence in the event that payment is not received in full or if there has been a breach of this agreement by you.

Appendix 1 — Acknowledgements:

For Journal Content:
Reprinted by permission from [**the Licensor**]: [**Journal Publisher** (e.g. Nature/Springer/Palgrave)] [**JOURNAL NAME**] [**REFERENCE CITATION** (Article name, Author(s) Name), [**COPYRIGHT**] (year of publication)

For **Advance Online Publication papers:**
Reprinted by permission from [**the Licensor**]: [**Journal Publisher** (e.g. Nature/Springer/Palgrave)] [**JOURNAL NAME**] [**REFERENCE CITATION** (Article name, Author(s) Name), [**COPYRIGHT**] (year of publication), advance online publication, day month year (doi: 10.1038/sj.[JOURNAL ACRONYM].)

For Adaptations/Translations:
Adapted/Translated by permission from [**the Licensor**]: [**Journal Publisher** (e.g. Nature/Springer/Palgrave)] [**JOURNAL NAME**] [**REFERENCE CITATION** (Article name, Author(s) Name), [**COPYRIGHT**] (year of publication)

Note: For any republication from the British Journal of Cancer, the following credit line style applies:

Reprinted/adapted/translated by permission from [**the Licensor**]: on behalf of Cancer Research UK: : [**Journal Publisher** (e.g. Nature/Springer/Palgrave)] [**JOURNAL NAME**] [**REFERENCE CITATION** (Article name, Author(s) Name), [**COPYRIGHT]** (year of publication)

For **Advance Online Publication** papers:
Reprinted by permission from The [**the Licensor**]: on behalf of Cancer Research UK: [**Journal Publisher** (e.g. Nature/Springer/Palgrave)] [**JOURNAL NAME**] [**REFERENCE CITATION** (Article name, Author(s) Name), [**COPYRIGHT**] (year of publication), advance online publication, day month year (doi: 10.1038/sj.[JOURNAL ACRONYM])

For Book content:
Reprinted/adapted by permission from [**the Licensor**]: [**Book Publisher** (e.g. Palgrave Macmillan, Springer etc) [**Book Title**] by [**Book author**(s)] [**COPYRIGHT**] (year of publication)

Other Conditions:

Version 1.3

Questions? customercare@copyright.com or +1-855-239-3415 (toll free in the US) or +1-978-646-2777.

CCC Marketplace™

Order Date	04-Aug-2021	**Type of Use**	Republish in a thesis/dissertation
Order License ID	1138300-1		
ISSN	1945-7111	**Publisher**	IOP Publishing
		Portion	Chapter/article

LICENSED CONTENT

Publication Title	Journal of the Electrochemical Society	**Rightsholder**	IOP Publishing, Ltd
		Publication Type	e-Journal
Article Title	Editors' Choice—A Miniaturized Enzymatic Biosensor For Detection of Sensory-Evoked D-serine Release in the Brain	**Start Page**	025502
		Issue	2
		Volume	168
		URL	http://www.scitation.org/JES
Author/Editor	Electrochemical Society.		
Date	01/01/1948		
Language	English		
Country	United States of America		

REQUEST DETAILS

Portion Type	Chapter/article	**Rights Requested**	Main product
Page range(s)	1-10	**Distribution**	Worldwide
Total number of pages	10	**Translation**	Original language of publication
Format (select all that apply)	Print, Electronic	**Copies for the disabled?**	No
Who will republish the content?	Academic institution	**Minor editing privileges?**	No
Duration of Use	Life of current edition	**Incidental promotional use?**	No
Lifetime Unit Quantity	Up to 499	**Currency**	USD

NEW WORK DETAILS

Title	Electrochemical Sensor Development for Robust Amino Acid Biosensing	**Institution name**	McGill University
		Expected presentation date	2021-08-02
Instructor name	Siba Moussa		

ADDITIONAL DETAILS

Order reference number	N/A

The requesting person / organization to appear on the license	Siba Moussa / McGill University

REUSE CONTENT DETAILS

Title, description or numeric reference of the portion(s)	Thesis Chapter	**Title of the article/chapter the portion is from**	Editors' Choice—A Miniaturized Enzymatic Biosensor For Detection of Sensory-Evoked D-serine Release in the Brain
Editor of portion(s)	Moussa, Siba; Van Horn, Marion; Shah, Aryan; Pollegioni, Loredano; Thibodeaux, Christopher; Ruthazer, Edward; Mauzeroll, Janine	**Author of portion(s)**	Moussa, Siba; Van Horn, Marion; Shah, Aryan; Pollegioni, Loredano; Thibodeaux, Christopher; Ruthazer, Edward; Mauzeroll, Janine
Volume of serial or monograph	168		
Page or page range of portion	025502	**Issue, if republishing an article from a serial**	2
		Publication date of portion	2021-02-15

RIGHTSHOLDER TERMS AND CONDITIONS

These special terms and conditions are in addition to the standard terms and conditions for CCC's Republication Service and, together with those standard terms and conditions, govern the use of the Works. As the User you will make all reasonable efforts to contact the author(s) of the article which the Work is to be reused from, to seek consent for your intended use. Contacting one author who is acting expressly as authorised agent for their co-author(s) is acceptable. User will reproduce the following wording prominently alongside the Work: the source of the Work, including author, article title, title of journal, volume number, issue number (if relevant), page range (or first page if this is the only information available) and date of first publication; and a link back to the article (via DOI); and if practicable, and IN ALL CASES for new works published under any of the Creative Commons licences, the words "© The Electrochemical Society. Reproduced by permission of IOP Publishing Ltd. All rights reserved" Without the express permission of the author(s) and the Rightsholder of the article from which the Work is to be reused, User shall not use it in any way which, in the opinion of IOP Publishing Ltd, could: (i) distort or alter the author(s)' original intention(s) and meaning; (ii) be prejudicial to the honour or reputation of the author(s); and/or (iii) imply endorsement by the author(s) and/or the Rightsholder and/or IOP Publishing Ltd. This licence does not apply to any article which is credited to another source and which does not have the copyright line '© The Electrochemical Society'. User must check the copyright line of the article from which the Work is to be reused to check that the Electrochemical Society and IOP Publishing Ltd has all the necessary rights to be able to grant permission. User is solely responsible for identifying and obtaining separate licences and permissions from the copyright owner for reuse of any such third party material/figures which the Rightsholder is not the copyright owner of. The Rightsholder shall not reimburse any fees which User pays for a republication license for such third party content. This licence does not apply to any material/figure which is credited to another source in the Rightsholder's publication or has been obtained from a third party. User must check the Version of Record of the article from which the Work is to be reused, to check whether any of the material in the Work is third party material. Third party citations and/or copyright notices and/or permissions statements may not be included in any other version of the article from which the Work is to be reused and so cannot be relied upon by the User. User is solely responsible for identifying and obtaining separate licences and permissions from the copyright owner for reuse of any such third party material/figures where the Rightsholder is not the copyright owner. The Rightsholder shall not reimburse any fees which User pays for a republication license for such third party content. User and CCC acknowledge that IOP Publishing Ltd and/or the Rightsholder may, from time to time, make changes or additions to these special terms and conditions without express notification, provided that these shall not apply to permissions already secured and paid for by User prior to such change or addition. User acknowledges that the Rightsholder and IOP Publishing Ltd (which includes companies within its group and third parties for whom it publishes its titles) may make use of personal data collected through the service in the course of their business. If User is the author of the Work, User may automatically have the right to reuse it under the rights granted back when User transferred the copyright in the article to the Rightsholder. User should check the copyright form and the relevant author rights policy to check whether permission is required. If User is the author of the

Work and does require permission for proposed reuse of the Work, User should select 'Author of requested content' as the Requestor Type. The Rightsholder shall not reimburse any fees which User pays for a republication license. If User is the author of the article which User wishes to reuse in User's thesis or dissertation, the republication licence covers the right to include the Version of Record of the article, provided it is not then published commercially. User must include citation details and, for online use, a link to the Version of Record of the article on the IOPscience website. User may need to obtain separate permission for any third party content included within the article. User must check this with the copyright owner of such third party content. User may not include the article in a thesis or dissertation which is published by ProQuest. Any other commercial use of User's thesis or dissertation containing the article would also need to be expressly notified in writing to the Rightsholder at the time of request and would require separate written permission from the Rightsholder. As well as CCC, the Rightsholder and IOP Publishing Ltd shall have the right to bring any legal action that they deem necessary to enforce their rights should they consider that the Work infringes those rights in any way. For content reuse requests that qualify for permission under the STM Permissions Guidelines, which may be updated from time to time, the STM Permissions Guidelines supplement the terms and conditions contained in this license.

SPECIAL RIGHTSHOLDER TERMS AND CONDITIONS

When you transferred the copyright in your article to The Electrochemical Society you were granted back certain rights, including the right to include the Final Published Version of the article within any thesis or dissertation. Please note you may need to obtain separate permission for any third party content you included within your article. Please include citation details, "© The Electrochemical Society. Reproduced with permission. All rights reserved" and for online use, a link to the Version of Record. The only restriction is that if, at a later date, you wanted your thesis/dissertation to be published commercially, further permission would be required.

CCC Terms and Conditions

1. Description of Service; Defined Terms. This Republication License enables the User to obtain licenses for republication of one or more copyrighted works as described in detail on the relevant Order Confirmation (the "Work(s)"). Copyright Clearance Center, Inc. ("CCC") grants licenses through the Service on behalf of the rightsholder identified on the Order Confirmation (the "Rightsholder"). "Republication", as used herein, generally means the inclusion of a Work, in whole or in part, in a new work or works, also as described on the Order Confirmation. "User", as used herein, means the person or entity making such republication.

2. The terms set forth in the relevant Order Confirmation, and any terms set by the Rightsholder with respect to a particular Work, govern the terms of use of Works in connection with the Service. By using the Service, the person transacting for a republication license on behalf of the User represents and warrants that he/she/it (a) has been duly authorized by the User to accept, and hereby does accept, all such terms and conditions on behalf of User, and (b) shall inform User of all such terms and conditions. In the event such person is a "freelancer" or other third party independent of User and CCC, such party shall be deemed jointly a "User" for purposes of these terms and conditions. In any event, User shall be deemed to have accepted and agreed to all such terms and conditions if User republishes the Work in any fashion.

3. Scope of License; Limitations and Obligations.

    3.1. All Works and all rights therein, including copyright rights, remain the sole and exclusive property of the Rightsholder. The license created by the exchange of an Order Confirmation (and/or any invoice) and payment by User of the full amount set forth on that document includes only those rights expressly set forth in the Order Confirmation and in these terms and conditions, and conveys no other rights in the Work(s) to User. All rights not expressly granted are hereby reserved.

    3.2. General Payment Terms: You may pay by credit card or through an account with us payable at the end of the month. If you and we agree that you may establish a standing account with CCC, then the following terms apply: Remit Payment to: Copyright Clearance Center, 29118 Network Place, Chicago, IL 60673-1291. Payments Due: Invoices are payable upon their delivery to you (or upon our notice to you that they are available to you for downloading). After 30 days, outstanding amounts will be subject to a service charge of 1-1/2% per month or, if less, the maximum rate allowed by applicable law. Unless otherwise specifically set forth in the Order Confirmation or in a separate written agreement signed by CCC, invoices are due and payable on "net 30" terms. While User may exercise the rights licensed immediately upon issuance of

the Order Confirmation, the license is automatically revoked and is null and void, as if it had never been issued, if complete payment for the license is not received on a timely basis either from User directly or through a payment agent, such as a credit card company.

3.3. Unless otherwise provided in the Order Confirmation, any grant of rights to User (i) is "one-time" (including the editions and product family specified in the license), (ii) is non-exclusive and non-transferable and (iii) is subject to any and all limitations and restrictions (such as, but not limited to, limitations on duration of use or circulation) included in the Order Confirmation or invoice and/or in these terms and conditions. Upon completion of the licensed use, User shall either secure a new permission for further use of the Work(s) or immediately cease any new use of the Work(s) and shall render inaccessible (such as by deleting or by removing or severing links or other locators) any further copies of the Work (except for copies printed on paper in accordance with this license and still in User's stock at the end of such period).

3.4. In the event that the material for which a republication license is sought includes third party materials (such as photographs, illustrations, graphs, inserts and similar materials) which are identified in such material as having been used by permission, User is responsible for identifying, and seeking separate licenses (under this Service or otherwise) for, any of such third party materials; without a separate license, such third party materials may not be used.

3.5. Use of proper copyright notice for a Work is required as a condition of any license granted under the Service. Unless otherwise provided in the Order Confirmation, a proper copyright notice will read substantially as follows: "Republished with permission of [Rightsholder's name], from [Work's title, author, volume, edition number and year of copyright]; permission conveyed through Copyright Clearance Center, Inc. " Such notice must be provided in a reasonably legible font size and must be placed either immediately adjacent to the Work as used (for example, as part of a by-line or footnote but not as a separate electronic link) or in the place where substantially all other credits or notices for the new work containing the republished Work are located. Failure to include the required notice results in loss to the Rightsholder and CCC, and the User shall be liable to pay liquidated damages for each such failure equal to twice the use fee specified in the Order Confirmation, in addition to the use fee itself and any other fees and charges specified.

3.6. User may only make alterations to the Work if and as expressly set forth in the Order Confirmation. No Work may be used in any way that is defamatory, violates the rights of third parties (including such third parties' rights of copyright, privacy, publicity, or other tangible or intangible property), or is otherwise illegal, sexually explicit or obscene. In addition, User may not conjoin a Work with any other material that may result in damage to the reputation of the Rightsholder. User agrees to inform CCC if it becomes aware of any infringement of any rights in a Work and to cooperate with any reasonable request of CCC or the Rightsholder in connection therewith.

4. Indemnity. User hereby indemnifies and agrees to defend the Rightsholder and CCC, and their respective employees and directors, against all claims, liability, damages, costs and expenses, including legal fees and expenses, arising out of any use of a Work beyond the scope of the rights granted herein, or any use of a Work which has been altered in any unauthorized way by User, including claims of defamation or infringement of rights of copyright, publicity, privacy or other tangible or intangible property.

5. Limitation of Liability. UNDER NO CIRCUMSTANCES WILL CCC OR THE RIGHTSHOLDER BE LIABLE FOR ANY DIRECT, INDIRECT, CONSEQUENTIAL OR INCIDENTAL DAMAGES (INCLUDING WITHOUT LIMITATION DAMAGES FOR LOSS OF BUSINESS PROFITS OR INFORMATION, OR FOR BUSINESS INTERRUPTION) ARISING OUT OF THE USE OR INABILITY TO USE A WORK, EVEN IF ONE OF THEM HAS BEEN ADVISED OF THE POSSIBILITY OF SUCH DAMAGES. In any event, the total liability of the Rightsholder and CCC (including their respective employees and directors) shall not exceed the total amount actually paid by User for this license. User assumes full liability for the actions and omissions of its principals, employees, agents, affiliates, successors and assigns.

6. Limited Warranties. THE WORK(S) AND RIGHT(S) ARE PROVIDED "AS IS". CCC HAS THE RIGHT TO GRANT TO USER THE RIGHTS GRANTED IN THE ORDER CONFIRMATION DOCUMENT. CCC AND THE RIGHTSHOLDER DISCLAIM ALL

OTHER WARRANTIES RELATING TO THE WORK(S) AND RIGHT(S), EITHER EXPRESS OR IMPLIED, INCLUDING WITHOUT LIMITATION IMPLIED WARRANTIES OF MERCHANTABILITY OR FITNESS FOR A PARTICULAR PURPOSE. ADDITIONAL RIGHTS MAY BE REQUIRED TO USE ILLUSTRATIONS, GRAPHS, PHOTOGRAPHS, ABSTRACTS, INSERTS OR OTHER PORTIONS OF THE WORK (AS OPPOSED TO THE ENTIRE WORK) IN A MANNER CONTEMPLATED BY USER; USER UNDERSTANDS AND AGREES THAT NEITHER CCC NOR THE RIGHTSHOLDER MAY HAVE SUCH ADDITIONAL RIGHTS TO GRANT.

7. Effect of Breach. Any failure by User to pay any amount when due, or any use by User of a Work beyond the scope of the license set forth in the Order Confirmation and/or these terms and conditions, shall be a material breach of the license created by the Order Confirmation and these terms and conditions. Any breach not cured within 30 days of written notice thereof shall result in immediate termination of such license without further notice. Any unauthorized (but licensable) use of a Work that is terminated immediately upon notice thereof may be liquidated by payment of the Rightsholder's ordinary license price therefor; any unauthorized (and unlicensable) use that is not terminated immediately for any reason (including, for example, because materials containing the Work cannot reasonably be recalled) will be subject to all remedies available at law or in equity, but in no event to a payment of less than three times the Rightsholder's ordinary license price for the most closely analogous licensable use plus Rightsholder's and/or CCC's costs and expenses incurred in collecting such payment.

8. Miscellaneous.

    8.1. User acknowledges that CCC may, from time to time, make changes or additions to the Service or to these terms and conditions, and CCC reserves the right to send notice to the User by electronic mail or otherwise for the purposes of notifying User of such changes or additions; provided that any such changes or additions shall not apply to permissions already secured and paid for.

    8.2. Use of User-related information collected through the Service is governed by CCC's privacy policy, available online here:https://marketplace.copyright.com/rs-ui-web/mp/privacy-policy

    8.3. The licensing transaction described in the Order Confirmation is personal to User. Therefore, User may not assign or transfer to any other person (whether a natural person or an organization of any kind) the license created by the Order Confirmation and these terms and conditions or any rights granted hereunder; provided, however, that User may assign such license in its entirety on written notice to CCC in the event of a transfer of all or substantially all of User's rights in the new material which includes the Work(s) licensed under this Service.

    8.4. No amendment or waiver of any terms is binding unless set forth in writing and signed by the parties. The Rightsholder and CCC hereby object to any terms contained in any writing prepared by the User or its principals, employees, agents or affiliates and purporting to govern or otherwise relate to the licensing transaction described in the Order Confirmation, which terms are in any way inconsistent with any terms set forth in the Order Confirmation and/or in these terms and conditions or CCC's standard operating procedures, whether such writing is prepared prior to, simultaneously with or subsequent to the Order Confirmation, and whether such writing appears on a copy of the Order Confirmation or in a separate instrument.

    8.5. The licensing transaction described in the Order Confirmation document shall be governed by and construed under the law of the State of New York, USA, without regard to the principles thereof of conflicts of law. Any case, controversy, suit, action, or proceeding arising out of, in connection with, or related to such licensing transaction shall be brought, at CCC's sole discretion, in any federal or state court located in the County of New York, State of New York, USA, or in any federal or state court whose geographical jurisdiction covers the location of the Rightsholder set forth in the Order Confirmation. The parties expressly submit to the personal jurisdiction and venue of each such federal or state court.If you have any comments or questions about the Service or Copyright Clearance Center, please contact us at 978-750-8400 or send an e-mail to support@copyright.com.

v 1.1

Enhancing Electrochemical Biosensor Selectivity with Engineered d-Amino Acid Oxidase Enzymes for d-Serine and d-Alanine Quantification

Author: Siba Moussa, Giulia Murtas, Loredano Pollegioni, et al

Publication: ACS Applied Bio Materials

Publisher: American Chemical Society

Date: Jul 1, 2021

PERMISSION/LICENSE IS GRANTED FOR YOUR ORDER AT NO CHARGE

This type of permission/license, instead of the standard Terms and Conditions, is sent to you because no fee is being charged for your order. Please note the following:

- Permission is granted for your request in both print and electronic formats, and translations.
- If figures and/or tables were requested, they may be adapted or used in part.
- Please print this page for your records and send a copy of it to your publisher/graduate school.
- Appropriate credit for the requested material should be given as follows: "Reprinted (adapted) with permission from {COMPLETE REFERENCE CITATION}. Copyright {YEAR} American Chemical Society." Insert appropriate information in place of the capitalized words.
- One-time permission is granted only for the use specified in your RightsLink request. No additional uses are granted (such as derivative works or other editions). For any uses, please submit a new request.

If credit is given to another source for the material you requested from RightsLink, permission must be obtained from that source.

BACK CLOSE WINDOW